Technische Universität München
TUM School of Natural Sciences

Measuring distances in the near-Universe: systematic effects and observational tests for Type II supernovae and Cepheid variables

Géza Attila Csörnyei

Vollständiger Abdruck der von der TUM School of Natural Sciences der Technischen Universität München zur Erlangung eines

Doktors der Naturwissenschaften (Dr.rer.nat.)

genehmigten Dissertation.

Vorsitz:

Prof. Dr. Stephan Paul

Prüfende der Dissertation:

1. Hon.-Prof. Dr. Wolfgang Hillebrandt
2. Prof. Dr. Sherry Suyu

Die Dissertation wurde am 28.02.2024 bei der Technischen Universität München eingereicht und durch die TUM School of Natural Sciences am 16.04.2024 angenommen.

Abstract

The ongoing and well-known Hubble tension calls for rigorous checks on existing cosmic distance estimation techniques. We test and showcase the precision of a recently established Type II supernova-based method, which offers a one-step measurement of the Hubble constant, and investigate the pulsation of Cepheid stars, uncovering a potential systematic effect. The supernova method, which makes use of radiative transfer modelling, is tested in two complementary ways. First, we apply the modelling to pairs of well-observed supernovae that exploded in the same galaxy. For each of the four pairs, we find good agreement between the distances, indicating a high degree of internal consistency of the approach. Second, we showcase the precision and potential of the method by estimating the distance of M 51 through a Type II supernova and Cepheid variable stars, finding consistent results across these independent indicators. A comparison with literature distances measured from the tip of the red-giant branch, however, reveals a discrepancy and shows the importance of direct cross-checks. We complete our investigation on distance estimation techniques by an analysis of Cepheid variables, revealing fluctuations in their periods, which could affect their accuracy as distance indicators. Our studies add to the ever-growing field of cosmic distance estimation and will help to determine the significance of the Hubble tension.

Zusammenfassung

Die seit Jahren weithin bekannte Hubble-Kontroverse erfordert eine strenge Überprüfung der bestehenden Techniken zur kosmischen Entfernungsabschätzung. Wir überprüfen und demonstrieren die Genauigkeit einer kürzlich etablierten Methode basierend auf Typ-II-Supernovae, die eine Messung der Hubble-Konstanten in einem einzigen Schritt ermöglicht, und untersuchen die Pulsation von Cepheidensternen, wobei wir einen potenziellen systematischen Effekt aufdecken. Die Supernova-Methode, die auf der Modellierung des Strahlungstransports basiert, wird auf zwei komplementäre Weisen getestet. Als Erstes wenden wir die Modellierung auf Paare gut beobachteter Supernovae an, die in derselben Galaxie explodiert sind. Für jedes der vier Paare stellen wir eine gute Übereinstimmung zwischen den Entfernungen fest, was auf eine hohe interne Konsistenz des Ansatzes hinweist. Als Zweites demonstrieren wir die Genauigkeit und das Potenzial der Methode, indem wir die Entfernung von M 51 mit Hilfe einer Typ-II-Supernova und Cepheidensternen abschätzen, wobei wir konsistente Ergebnisse über diese unabhängigen Indikatoren hinweg finden. Ein Vergleich mit Entfernungen aus der Literatur, die anhand der Spitze des Roten Riesenasts bestimmt wurden, zeigt jedoch eine Diskrepanz und betont die Wichtigkeit direkter Quervergleiche. Wir schließen unsere Untersuchung der Techniken zur Entfernungsbestimmung durch eine Analyse von Cepheidensternen ab, wobei wir Schwankungen in ihren Perioden aufdecken, die ihre Genauigkeit als Entfernungsindikatoren beeinträchtigen könnten. Unsere Studien leisten einen Beitrag zum stetig wachsenden Gebiet der kosmischen Entfernungsabschätzung und werden dabei helfen, die Signifikanz der Hubble-Kontroverse zu bestimmen.

Contents

List of Figures

List of Tables

Part I

Introduction and methology

1 Reaching to the stars: measuring distances in the Universe

Ever since the birth of civilization, measuring distances has been a crucial part of the life of humankind. Let it be just questions related to everyday life, such as the distance to a freshwater lake on a hot summer day, to a thunderstorm cloud on the horizon to seek shelter from, or to other cities on a long day of travel, the question of *"how far"* was uttered multiple times. Owing to the knowledge gathered over centuries, we mastered measuring distances on Earth and started looking beyond it. And as such, measuring distances in the cosmos has also become possible.

Similarly as on Earth, measuring cosmic distances is equally crucial to our proper understanding of the Universe. Nothing shows this better than last century's *Great Debate*,[1] or the Shapley-Curtis argument in 1920. During this conference, astronomers discussed nothing less than the scale of the known Universe; this was the time when they sought to answer whether the spiral galaxies, or spiral nebulae, as known at that time, were part of the Milky Way, or were outside of it. Ultimately, discovering a way to measure distances to other galaxies and unravelling the concept of "cosmic redshift" settled the debate.

These results showed that our cosmos was far greater than previously thought and indicated the surprising fact that the Universe was expanding, with the redshift acting as the tracker of the expansion. The effect of the expansion is illustrated in Fig. 1.1, which shows a picture taken of the Hubble Ultra Deep Field. In the figure, besides the bright foreground objects, a number of faint and farther away galaxies are also visible, which appear redder to us, due to the redshifting of their light. Following this discovery, many astronomers dedicated their work to measuring the scale of this expansion, the Hubble−Lemaître constant H_0. Over the subsequent years, it was revealed that this parameter plays a crucial role in cosmology, and it provides a straightforward way to investigate the nature of the Universe itself by observational means. However, as newer and newer methods were established for the measurement of H_0, and as the precision of these measurements increased, it became apparent that they yield different predictions; predictions, that are, in fact, in tension with each other today. To date, this tension is one of the main driving forces for ongoing investigations into the expansion of the Universe.

In this thesis, I discuss my contributions to the fast-changing field of near-universe distance measurements from two aspects: through providing empirical tests for a newly established and still developing class of cosmic distance indicators, Type II supernovae (SNe II), and by investigating the nature and a possible systematic effect for Classical

[1] https://apod.nasa.gov/debate/debate20.html

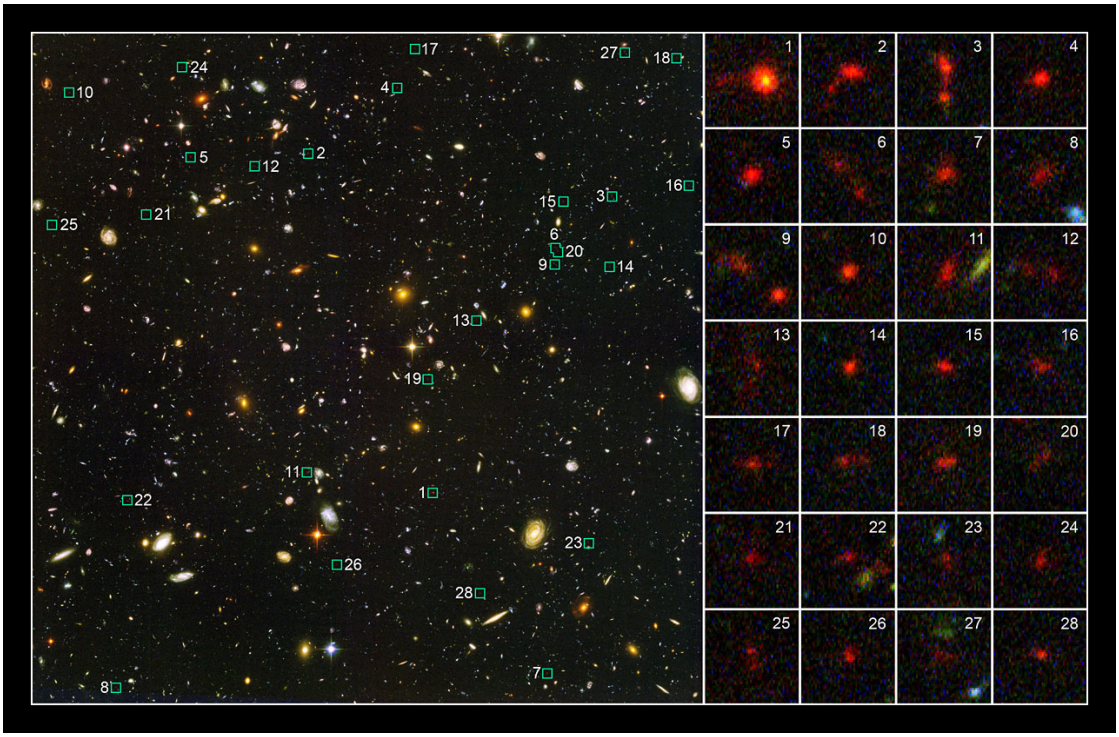

Figure 1.1: Image taken of the Hubble Ultra Deep Field by the Hubble Space Telescope. Beyond the colourful set of relatively nearby galaxies, dozens of reddened objects are also visible. These are far-away galaxies, whose observed light was emitted billions of years ago. On their way towards us, the wavelength of the emitted photons stretched due to the expansion of the space in between, which caused the light of the galaxies to shift towards redder colours. This effect is the so-called cosmological redshift. Figure credit: NASA, ESA, R. Bouwens and G. Illingworth (University of California, Santa Cruz, USA)

Cepheid variable stars, which have for long been used as the most versatile and reliable way to measure distances to nearby galaxies. To build the frame for such a discussion, I first give a brief introduction to the history of distance measurements until today's Hubble tension in Sect. 1.1. After the scene is set, I turn my attention to the various techniques that allow us to measure distances into the Hubble flow and are widely used by the community: the Cepheid variable stars (Sect. 2.1), the Tip of the Red Giant Branch (Sect. 2.2), the concept of the cosmic distance ladder (Sect. 2.3) and finally, the Type II supernovae (Sect. 2.4). Throughout this overview, I pay specific attention to systematics affecting the individual techniques.

After the summary, I present my empirical works, which aim to assess and quantify how much of an effect these systematics may have in the distance measurements through the various methods. In Part II, I demonstrate the internal consistency of the SN II-based distance measurements by applying the method to objects that exploded in the same galaxy and hence should be at the same distance. This project showcased that

assumed uncertainties are realistic and that the obtained distances are not only precise but also robust against the variations in the physical parameters of the supernovae. Following this, in Part III, I describe an investigation into the agreement between different near-Universe distance indicators by estimating a Cepheid and SN II distance to M 51, then comparing them directly to the already published Tip of the Red Giant Branch (TRGB) based value. This work demonstrated that SNe II provide distances that are competitive in terms of precision with that of the other methods. It also highlighted the need for additional comparisons to ensure that the near-Universe distance estimators yield consistent results. Finally, in Part IV, I present an analysis conducted on Cepheid variable stars, proving that these variable stars do not behave as precise clocks but fluctuate instead, which puts an upper limit on the accuracy of Cepheid distances. Having presented my results in the field of distance estimations, I conclude the thesis by providing a brief outlook on the future of Hubble constant estimations and my immediate plans beyond my dissertation.

1.1 Early geometrical means

Measuring distances to objects in the sky is a question that has fascinated astronomers for a long time. The earliest known attempts at measuring cosmic distances were performed by Hipparchus and Aristarchus, as described in detail by Clark & Clark (2004). Based on the excerpts remaining from their books titled *"On the sizes and distances"*, they were the first to discover the geometrical means to infer the distances to both the Moon and the Sun. According to a reconstruction presented by Toomer (1974), they made use of the parallax[2] and the changing phase of the Moon, along with solar eclipses. With this technique, they obtained a reasonable estimate for the Moon and followed it up with a subsequent calculation for the Sun. Although the calculated distance for the Moon was close to today's known values, the Sun's estimate fell short of reality due to the measurement uncertainties.

Taking the next step to infer an accurate distance to the Sun took many years until the end of the 18th century. Given the brightness of the Sun, the parallax method was not feasible; the Sun was just too bright for the background. For a solution to come, one had to wait until Johannes Kepler and Isaac Newton laid the foundations for describing orbital motions. The establishment of these laws provided the solution through the other planets. On one hand, it was possible to determine their distance from Earth based on the parallax method, which, combined with the Kepler laws, could yield the Sun's distance. Moreover, astronomers also realized, that one may use the timing of the Venus transits as measured from different sites on Earth as a proxy for parallax, then combine them with the Kepler formula to obtain the distance of the Sun (Jones 1944). The first such measurement was performed following the Venus transit in 1761. Following this success, astronomers did not have to wait for long to obtain a distance to another star; given the advancements in the field of instrumentation and discovering the

[2] The parallax refers to the effect that when viewed from different locations on Earth, the Moon appears in front of different backgrounds due to it being closer.

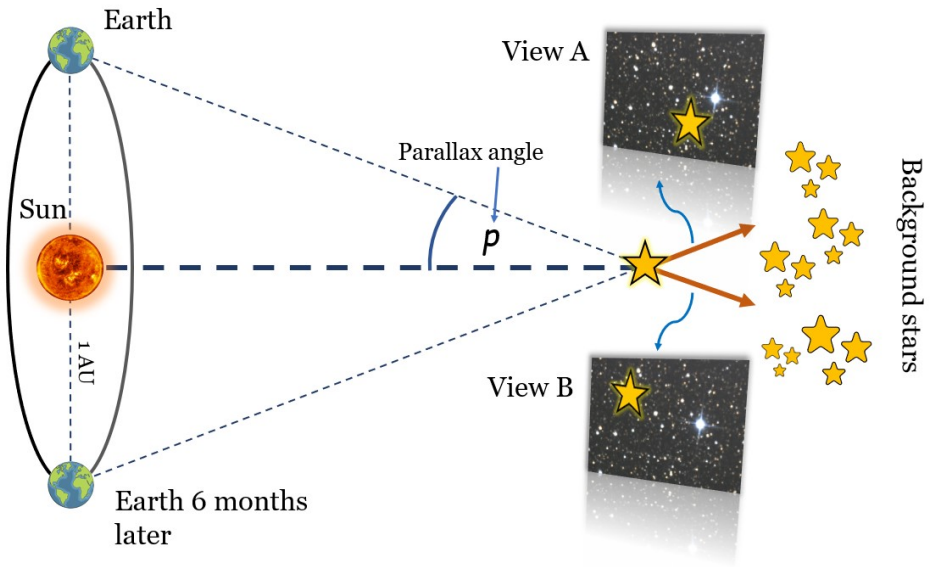

Figure 1.2: Illustration of the stellar parallax. Owing to the revolution of the Earth around the Sun, stars seem to be drifting back and forth over the year, depending on their distance from us. Hence, measuring their position on specific dates with respect to the farther-away background allows for estimating their distance.

concept of modern telescopes, it soon became possible to measure the parallax of stars precisely.

When generalized, the parallax angle in astronomy usually refers to the angle between the Earth at one time of year and the Earth six months later, as measured from a nearby star (see Figure 1.2). Owing to the motion of the Earth, stars during this time are seen as moving in front of the background of farther away stars, similarly as in the Earth-based parallax method; however, due to the longer baseline, the method can reach longer distances. Following Fig. 1.2, one may find the distance d to a star through the

$$d\ [\mathrm{pc}] = \frac{1\ [\mathrm{AU}]}{p\ [”]} \tag{1.1}$$

formula, where p denotes the parallax angle. The first published stellar parallax was determined by Bessel in 1838, who measured the distance of 61 Cygni for the first time (Webb, 1999).[3] In the years to follow, the number of stars with known parallaxes grew steadily. By the early 20th century, the number of stars with measured parallaxes had reached a few hundred, mainly owing to the steady work of Jacobus Kapteyn (Kapteyn & de Sitter, 1909; Kapteyn, 1914, 1918). In the next century, astronomers, assisted by the improvements in observing tools and techniques, gradually grew the catalogues of stars

[3]It is worth mentioning that the first known parallax measurements were carried out by John Henderson for Alpha Centauri decades before. However, these results were only published after those of Bessell.

with known distances: for example, Schlesinger et al. (1924) published a catalogue of 2000 stars with known distances, which was then extended by Jenkins (1952) to about 6000 stars by 1952, and to over 8000 stars by 1995 following the work of van Altena et al. (1995). However, due to the limitations imposed by the Earth's atmosphere on angular resolution, the parallax method could only offer accurate distances in the nearest hundred of light years in the Solar Neighbourhood.

The situation changed significantly with the launch of the Hipparcos satellite in 1989. Throughout its lifetime, Hipparcos surveyed over 120,000 objects in the Milky Way, creating the largest parallax catalogue of the time (Perryman et al., 1997a) and providing accurate distances out to one thousand parsecs. As a successor of this mission, two decades later, the *European Space Agency* launched its *Gaia* satellite to survey an even greater fraction of stars in the Milky Way and obtain accurate positional and kinematic data for them (Gaia Collaboration et al., 2016). The mission has already surveyed 1.8 billion stars, for which the data has been published in three data-releases so far (Gaia Collaboration, 2018; Lindegren et al., 2021; Riello et al., 2021). Even though *Gaia* has been able to map out the spatial distribution of the stars in the Milky Way, the parallax technique is insufficient to go beyond it. To reach other galaxies a new technique was required; and the breakthrough just came at the right time for the *Great Debate* in 1924, the discussion over the size of the Universe itself.

1.2 First extragalactic measurements

The solution required for extragalactic distances was found in Cepheid stars - pulsating red giant variable stars - through the work of Leavitt (1908) and Leavitt & Pickering (1912). They were the first to be able to isolate and observe 25 Cepheid variable stars in the Large Magellanic Cloud (Leavitt, 1908), and the first to draw attention to the "fact that the brighter variables have longer periods" (Leavitt & Pickering, 1912). The relationship they observed took the form of

$$m = a + b \log P, \tag{1.2}$$

where m is the mean observed magnitude of the Cepheid, P is its pulsation period (usually measured in days), and a and b are fitting constants. The existence of a relation for apparent magnitudes implied a similar relationship between absolute magnitudes and the period, meaning that Cepheids are standard candles[4]. If one calibrates this relation, it can be used to measure distances simply by measuring Cepheid brightness and pulsation period values. This relationship was subsequently named the period-luminosity relation, or Leavitt law (see Fig. 1.3). Whereas the existence of a relation was clear, given that the distance to the Large Magellanic Cloud was not known in 1912, calibrating it has proven difficult. Fernie (1969) summarizes the early attempts at measuring the zero point for the relationship, such as inferring distances to Milky Way Cepheids through statistical parallaxes (Hertzsprung, 1913), initial semi-empirical approaches and

[4]Standard candle: an astronomical object for which luminosity can determined accurately.

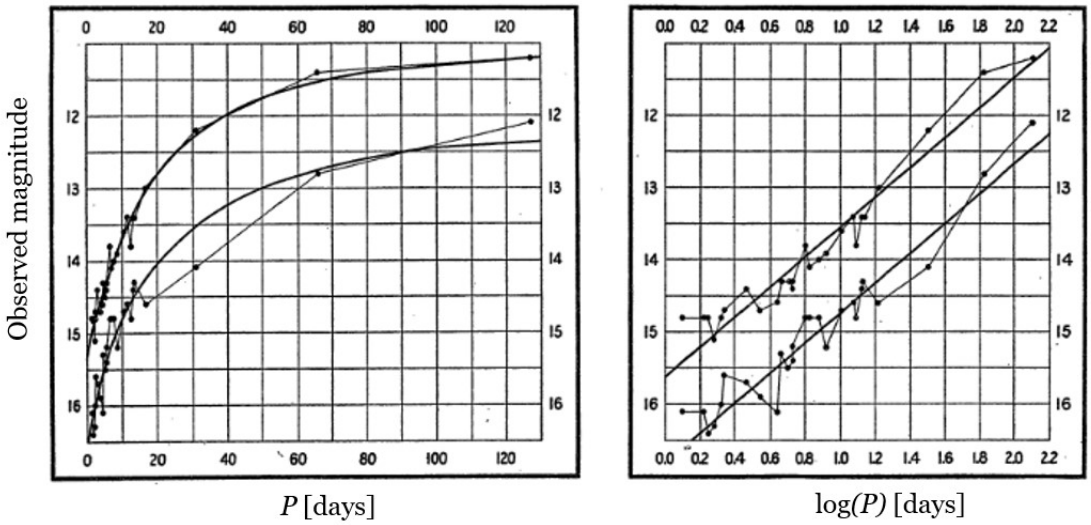

Figure 1.3: Period-luminosity relation as discovered by Leavitt & Pickering (1912). The left plot shows the period against the minimal and maximal magnitudes of the Cepheids, and the plot on the right shows the same relationship with the logarithm of the pulsation period used for the x axis. The figures depict the existence of a relationship between the two properties of Cepheids, which marks the discovery of the period-luminosity relation.

attempting to standardize Cepheids based on their colour (Shapley, 1927), or through using radial velocity curves to estimate the distance (Wesselink, 1946a). The struggle to calibrate the method lasted for several decades, with astronomers disagreeing on the general nature and cause of the brightness change of Cepheids in the 1950s as well (Fernie, 1969). However, it is noteworthy that the existence of the relation was discovered significantly earlier than the founding of the theoretical background, and it put the nearby Galaxies within reach for the instrumentation available at that time.

Following this discovery, in 1923, Edwin Hubble took this step and identified Cepheid variables in the Andromeda galaxy, which were then subsequently used to measure its distance (Hubble, 1925a). In the following years, he expanded the sample with further observations of extragalactic Cepheids, namely through observing NGC 6822 (Hubble, 1925b) and the Triangulum galaxy M 33 (Hubble, 1926a). A shortcoming of Cepheids is, however, that they are not bright enough to be detected out to sufficiently large distances: their absolute magnitudes vary between -3 and -6 mag, which makes them only detectable in more nearby galaxies. Even today's Cepheid studies, which can make use of the Hubble Space Telescope, are limited to a distance range shorter than 20 Mpc from the Milky Way. To circumvent this issue, Hubble (1926b) assumed that stars present in the "spiral nebulae" (as astronomers referred to galaxies at that time) are directly comparable to the stars in the Milky Way. Given this assumption, he then calibrated the brightnesses of the brightest stars present in the observed galaxies, and that of the entire galaxies as well in Hubble (1926b), in the very same paper, where he

introduced the renowned morphological classifications of these galaxies. As a subsequent step, Hubble measured the distances of 42 galaxies, with the Cepheids providing the necessary calibration for these measurements.[5] With this, he showed that the "spiral nebulae" are too far to be within the Milky Way, hence providing significant proof for the *Great Debate*. However, to take the first-ever step towards quantitative cosmology, additional parallel efforts were required, in the form of redshift measurements.

In physics, redshift refers to an increase in the wavelength and corresponding decrease in the frequency and photon energy of electromagnetic radiation due to the recessing movement of the source. The name of the effect refers to the optical wavelengths shifting towards redder colours or even the infrared range at suitably high velocities (see e.g. Stuart 2011). The exploration of the phenomena related to this effect began with the theoretical establishment of the Doppler effect, the frequency shift of sound waves emitted by moving sources, devised by Christian Doppler in the 18th century. Doppler then subsequently predicted that a similar effect should hold for all types of waves, hence electromagnetic radiation as well.[6] The subsequent years saw many observational evidences for the Doppler shift through observations of nearby stars.

Advancing these measurements to an extragalactic scale was carried out decades later, primarily by Vesto Slipher. In 1913, Slipher published the first measurements of the shift present in the spectral lines of the Andromeda galaxy (Slipher, 1913). The number of galaxies with available optical spectra grew steadily owing to the subsequent works of Slipher (1913, 1915, 1917, 1921), which provided a steady supply of extragalactic redshift values. By the time Hubble performed his Cepheid distance measurements, this catalogue counted 41 objects, the overwhelming majority of which were recessing away from the Milky Way. This alone provided (at that time perplexing) evidence for cosmology and towards the expansion of the Universe, as it was suggested by Eddington (1923) too.

Around this time, from a theoretical perspective, the Universe was assumed to be static and infinite. This picture changed through the introduction of special and general relativity (Einstein, 1908, 1915), which raised the possibility of a dynamic and expanding cosmos. Initially, this was not favoured by Einstein himself; after realizing that his equations would propose an initially stationary Universe to collapse due to gravity, he introduced a repulsive term to his set of equations, the cosmological constant (Einstein, 1917). The sole purpose of this constant was to stabilize the Universe, however, as Eddington (1930) pointed out, the resulting system would be unstable and prone to collapse or expand on the slightest perturbation.[7] The first models for a dynamic Universe were introduced by Friedmann (1922, 1924), which included models of an expanding Universe,

[5] It is worth noting, that this approach is the first application of the distance ladder formalism, which is widely used today as well; see Sect. 2.3.

[6] Initially, this seemed like a reasonable explanation for the different colours of stars seen in the sky. It was suspected, that the colour differences correspond to different recession radial velocities as measured from Earth (O'Connor & Robertson, 1998). However, it was later verified, that this difference is mainly driven by the temperatures of the stars, not by motion.

[7] This constant, however, became of utmost importance later when evidence for the accelerating expansion of the Universe was discovered (Riess et al., 1997).

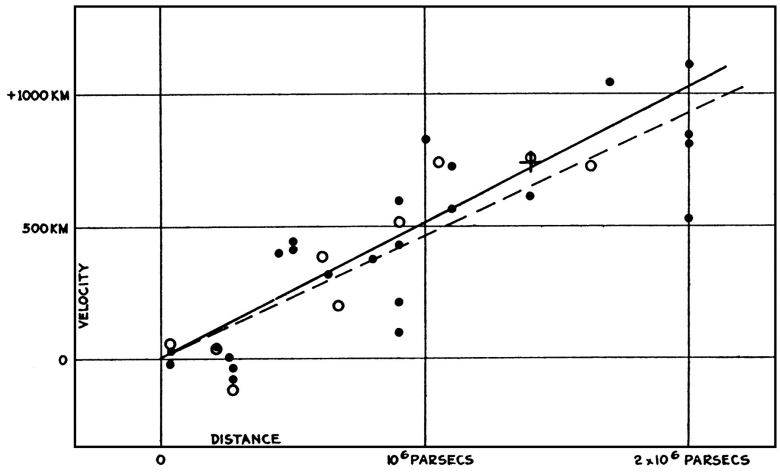

Figure 1.4: The original Hubble diagram as published by Hubble (1929) and reproduced by Kirshner (2004). The diagram shows the radial velocities of galaxies (measured in km/s) against their distances from the Milky Way. The filled circles indicate the individual measurements available for 24 sample galaxies, the open circles represent clustering of the same data in velocity and distance and the cross mark denotes the average values for the 22 objects for which the individual measurements were not feasible. The data shows an approximate linear connection between the two properties, both when fitted to the individual datapoints (solid line) and the clustered data (dashed line) as well.

along with the prediction that the redshift of the galaxies should increase the further away they are from us. This paradigm shift in theory happened at the right time for the interpretation of Hubble's and Slipher's observations.

The first person to formulate the right solution based on the evidences was Georges Lemaître, who combined the observations of redshifts and distances of other galaxies and explained them in the context of the relativistic expansion of the Universe (Lemaître, 1927). In his work, Lemaître estimated an expansion rate of about 680 km/s/Mpc based on the mean recession velocities and distances published by Stromberg (1925) and Hubble (1926b) respectively. Initially, the community did not note and recognize the breakthrough, and it took multiple decades for the results to be rediscovered. Instead, Hubble's results were causing the shift in the paradigm. The evidence, which ultimately decided the *Great Debate*, revealing the world beyond the Milky Way, showing that we are living in an expanding Universe was the Hubble diagram (Fig. 1.4, Hubble 1929). This diagram depicted the relation between the distance and redshift of galaxies, revealing a linear relationship between these two properties, which was subsequently confirmed in an independent study by Hubble & Humason (1931). Following this study, the community named the estimated expansion rate the Hubble parameter and dubbed the relationship

the Hubble law. Later, to commemorate Lemaître's independent efforts as well, the relation was renamed the Hubble-Lemaître law, as we know it today.[8]

1.3 Basics of cosmology and the Hubble law

To understand the importance of the Hubble parameter for measuring the cosmos, I attempt here to provide a quick basic overview of the theoretical background of the expansion of the Universe. For a more thorough and rigorous introduction to cosmology, I refer the reader to the manuscript of Hogg (1999) or the books of Peebles (1993) and Frei & Patkós (2005).

According to the cosmological principle, the Universe is, on average, homogenous and isotropic. Isotropy refers to the fact that there are no special viewing directions, while homogeneity means that all points within the Universe are equivalent. Homogeneity itself follows directly from isotropy, as long one assumes that it holds for all points within (Hogg, 1999). The distribution of galaxies and the on-average homogeneity of the cosmic microwave background (CMB) proves that the Universe is at first glance isotropic (Planck Collaboration et al., 2014a). These observations provide the most crucial foundation to modern cosmology.[9] This, in turn, restricts the range of models applicable to the evolution of the Universe. In this setting, the dynamics of spacetime are described with a single scalar parameter - the $a(t)$ scale factor - which establishes how the proper distance l measured between two objects in the Universe changes due to its expansion or contraction in time t:

$$l = l_0 \cdot a(t), \tag{1.3}$$

where l_0 denotes the proper distance measured for current times; hence, per definition, the scale factor at the current time equals unity: $a(t_0) = 1$. In this setting, the galaxies are fixed to the cosmic expansion (they are comoving with it), with their relative distances changing only due to it.

As described in earlier paragraphs, this expansion leads to a shift in photon wavelengths, similar to the Doppler effect for sounds, which can be observed for galaxies (see Fig. 1.5). This effect is the so-called cosmological redshift of radiation, which Slipher (1913) detected in his spectroscopic observations. By definition, the redshift refers to

[8] The initial name remained unchanged in the past century. However, in a recent symposium, the International Astronomical Union in 2018 voted to recognize Lemaître's contributions to the field by renaming the law: https://www.iau.org/news/pressreleases/detail/iau1812/

[9] There have been numerous indicators that may challenge the assumption of the cosmological principle, which were recently reviewed by Kumar Aluri et al. (2023). As outlined in that work, going beyond the scale on which the cosmological principle works would lead to tensions. Multiple such tensions have been detected, the Hubble tension being one of them. In addition, the homogeneity and isotropy of the Universe are further challenged by the existence of Gpc scale structures, such as the Hercules-Corona Borealis Great Wall or the Giant GRB Ring (Horvath et al., 2024). On the other hand, numerous results yield consistency with the cosmological principle on these scales too (such as Tiwari & Jain 2019, using polarimetry of high redshift active galactic nuclei).

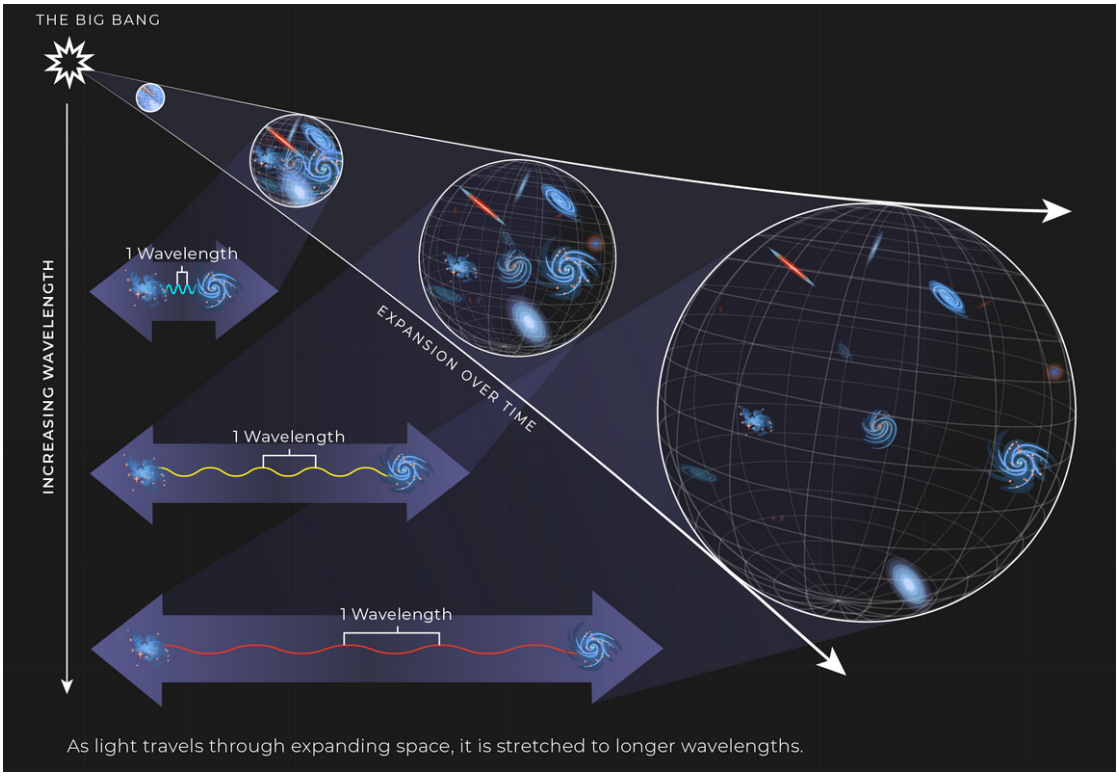

Figure 1.5: Illustration of the effects of cosmological redshift. The further away galaxies are from each other, the redder their colour becomes due to the expansion of the Universe. Image credit: NASA, ESA, Leah Hustack (STScI).

the difference between the emitted and observed wavelength of a photon normalized by its restframe wavelength:

$$z \equiv \frac{\lambda_\mathrm{o} - \lambda_\mathrm{e}}{\lambda_\mathrm{e}} = \frac{\lambda_\mathrm{o}}{\lambda_\mathrm{e}} - 1, \tag{1.4}$$

where λ_o denotes the observed, λ_e the emitted wavelengths. Furthermore, as discussed in Peebles (1993) and summarized in Vogl (2020), assuming a metric for space-time and making use of the wave representation for photons one may show that the wavelength can be related to the scale parameters valid at the emission and observation:

$$\frac{\lambda_\mathrm{o}}{\lambda_\mathrm{e}} = \frac{a(t_0)}{a(t_\mathrm{e})} \tag{1.5}$$

where t_0 and t_e denote the time of observation and emission, respectively (which correspond to different positions as well). To measure this quantity, astronomers usually use prominent emission or absorption lines of known atomic transitions (and hence with known restframe wavelengths) that stand out among other spectral features. Combining the above two equations, one obtains

$$1 + z = \frac{a(\mathrm{to})}{a(t_\mathrm{e})} \tag{1.6}$$

which shows that the farther away the galaxies are, the higher their redshift. Hence, for distant galaxies, the redshift can take values that may even make identification of emission lines troublesome, as it happened at the discovery of 3C 273, the first classified quasar at a redshift of $z = 0.158$ (Schmidt, 1963).

The redshift can be expressed in terms of the recession velocity v and the speed of light c, in the form of a special relativistic Doppler shift:

$$z = \sqrt{\frac{1 + v/c}{1 - v/c}} \approx \frac{v}{c} \tag{1.7}$$

for small values of v. When dealing with a single observed redshift measurement, it is usually impossible to discern the cosmological recession velocity that is due to the expansion of the Universe, owing to the peculiar motion of galaxies. This kinetic component arises from the motion of galaxies within local gravitational fields, and it modifies the redshift of the galaxy:

$$1 + z = (1 + z_\mathrm{cosmo.}) \cdot (1 + z_\mathrm{pec.}), \tag{1.8}$$

where $z_\mathrm{cosmo.}$ is the redshift component arising due to the galaxy comoving with the expanding space and $z_\mathrm{pec.}$ is the component due to peculiar motions. For nearby galaxies, for which the effects of redshift are small, the above expression can be approximated with

$$z = z_\mathrm{cosmo.} + z_\mathrm{pec.} \tag{1.9}$$

The peculiar velocities of galaxies usually amount to $300 - 400$ km/s (Léget et al. 2018), and hence they contribute with an additional ± 0.001 redshift term to the observation. This can contribute significantly to the error budget of cosmological analyses that are based on nearby galaxies only. For more distant galaxies, the peculiar motion adds less uncertainty (typically $2-3\%$ at z = 0.04). However, it is essential to investigate whether the galaxy is part of a compact cluster, as their peculiar velocities can be a factor of $3-4$ larger (Léget et al., 2018).

If the effect of peculiar velocities is negligible or has been corrected, then one can make use of the redshift measurements for a precise measurement of the expansion velocity of the Universe through the Hubble-Lemaître law. This linear proportionality is a direct consequence of Eq. 1.6, which connects the scale factor to the redshift. To obtain the theoretical form for the relationship, one has to define the Hubble parameter $H(t)$ as the relative rate of expansion of the Universe:

$$H(t) = \frac{\dot{a}(t)}{a(t)}. \tag{1.10}$$

The name Hubble parameter here refers to the general quantity; when dealing with observations, one measures its present value, the Hubble constant $H_0 = H(t_0)$. In the

limit of small distances, or the nearby Universe, one can use linear approximations to arrive at the law Hubble found in 1929: for small distances (and hence small temporal and scale differences) one may approximate the derivative term using differentials: $\dot{a}(t_e) \approx (a(t_e) - a(t_0))/(t_e - t_0)$. Reorganizing Eq. 1.10 then leads to

$$a(t_e) \approx a(t_0)(1 + (t_e - t_0)H(t_0)) \tag{1.11}$$

To obtain the relationship between the redshift and the Hubble parameter, we can substitute the above to Eq. 1.6:

$$z = \frac{a(t_0)}{a(t_e)} - 1 \approx \frac{1}{1 + (t_e - t_0)H(t_0)} - 1 \approx (t_0 - t_e)H(t_0) \tag{1.12}$$

After replacing the $(t_0 - t_e)$ with the corresponding distance using $D = c(t_0 - t_e)$,[10] one arrives at the Hubble-Lemaître law:

$$cz = H(t_0)D \qquad \text{or} \qquad v = H(t_0)D \tag{1.13}$$

where v denotes the recession velocity of the galaxy. This was the relationship Hubble and Lemaître found in the last century. The Hubble constant is one of the most fundamental parameters for cosmology, and obtaining a precise value for it in the low-redshift range assists in limiting the possible cosmological models that can explain the Universe.

1.4 Evolution of Hubble constant measurements

Whereas the findings of Hubble (1929) settled the debate concerning whether the "spiral nebulae" are outside the Milky Way and proved that the Universe is expanding, finding a precise value for the expansion velocity still had a long way to go. The initial result – with a value of 558 km/s/Mpc (Hubble, 1929) – was prone to several biases and was almost one order of magnitude larger than the value favoured today. The first to raise doubts about the result was Oort (1931). He argued that assuming the expansion rate and distances calculated by Hubble, the Milky Way must be significantly larger than the overwhelming majority of the galaxies, which he found unlikely. This remark led to a sequence of follow-up works that aimed to investigate this issue.

In the subsequent decades, astronomers found two issues that caused major biases in the Hubble constant. The first came from the side of variable stars: Baade (1956) discovered the existence of multiple stellar populations, Population I and II, which made him realize that the Cepheids used in the analysis of Hubble might not be homogenous. As he noted, "there was no a priori reason to expect that two Cepheids of the same period, the one a member of Population I, the other of Population II, should have the same luminosity" (Baade, 1956). Separating the Cepheids according to their populations

[10] It is worth mentioning that there are multiple ways of measuring distances, such as the proper or comoving distance l, or the so-called light-travel distance D. These are summarized in detail by Peebles (1993). Given, however, that these distances are different only in factors of $(1 + z)$, in the low-redshift limit, they are approximately equivalent.

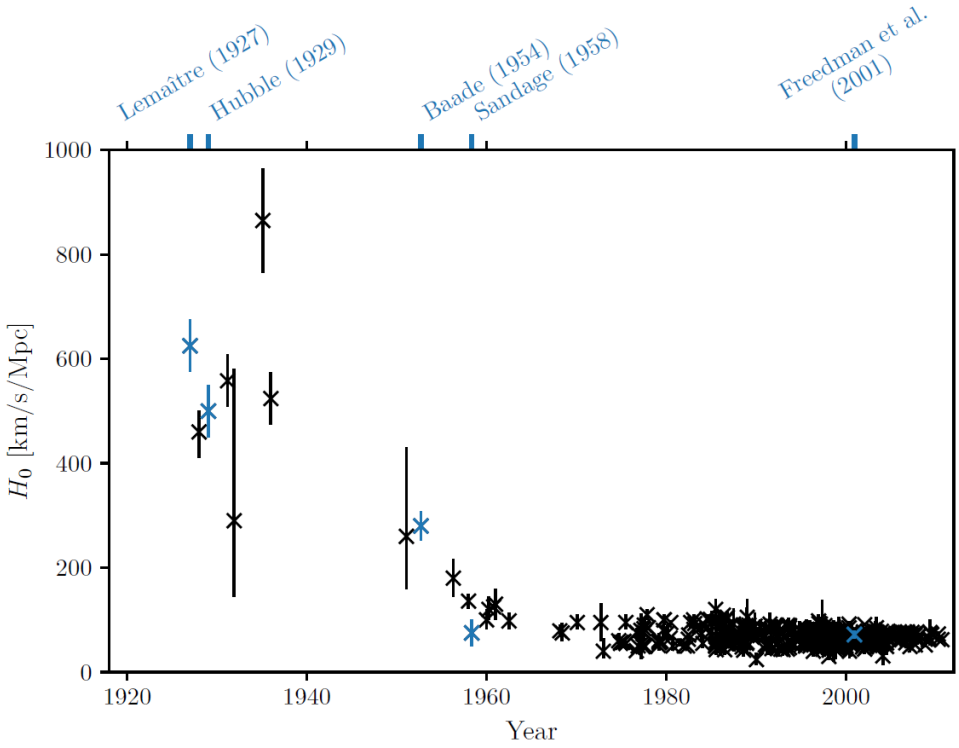

Figure 1.6: Published measurements of the Hubble constant between 1927 and 2010. The plot was reproduced in the PhD thesis of Christian Vogl (Vogl, 2020) using the data assembled by John Huchra as part of the NASA/HST Key Project on the Extragalactic Distance Scale. The most important measurements and changes highlighted in the main text, namely the ones from Lemaître (1927), Hubble (1929), Baade (1956), Sandage (1958) and Freedman et al. (2001) are marked with blue on the figure.

and recalibrating the period-luminosity relation nearly doubled the measured distance to other galaxies. The discovery of the second issue came two years later, by Sandage (1958). According to Sandage (1958), Hubble mistook bright star formation regions for the brightest stars in those galaxies, which caused all the distances to be systematically and significantly underestimated. These two issues combined accounted for an order of magnitude of difference in the Hubble constant. Once dealt with, the value of the Hubble parameter decreased to 75 km/s/Mpc, which is well in the range of the value accepted today.

In the decades to follow, the subsequent work mainly achieved the reduction of the uncertainty on the Hubble constant, however, the results still scattered in a considerable range (Fig. 1.6). The main improvement in this regard came with the launch of the Hubble Space Telescope (*HST*) in 1990 and its quest towards estimating a higher precision H_0: out of its three key projects, one was dedicated exclusively to bringing down the measurement uncertainties under 10% (Freedman et al., 1994). To this end, a more reliable sample of extragalactic Cepheids was obtained and then used to calibrate

new distance indicators, such as Type Ia supernovae (SNe Ia), the Tully-Fisher relation, surface brightness fluctuations and planetary nebulae. As a result of this effort, Freedman et al. (2001) published the updated value of $H_0 = 72 \pm 8$ km/s/Mpc. However, the puzzling story of the Hubble parameter did not end here; as the number of ways to estimate it grew and the precision increased, inconsistencies between various methods emerged. This led to a disagreement, which, due to its scale, was subsequently dubbed the Hubble tension, and which again started to drive a grand debate among astronomers.

1.5 Crisis in the cosmos: the Hubble tension

The Hubble tension is the observed discrepancy between the Hubble constants estimated using early and late Universe probes. Given the efforts the astronomical community already invested into it and the yet elusive nature of the solution, this tension became one of the biggest problems for present-day astrophysics. The tension itself has been subject to numerous reviews in recent years as well: for example, Cervantes-Cota et al. (2023) recently summarized the observational side of the H_0 tension, while Di Valentino et al. (2021) provided an overview of the theoretical side with the possible solutions to it.

The severity of the Hubble tension comes from the fact that it is not explainable through well-motivated cosmological means. The issue can be traced back to the fact that to estimate H_0 using early-Universe means, one has to assume a cosmological model to bridge the distance between us and the high-redshift regime.[11] To this end, astronomers so far used the so-called flat–ΛCDM model, which assumes a spatially flat Universe comprised of baryonic matter, cold dark matter, and a dark energy component described by a non-variable factor, the cosmological constant Λ (Hogg, 1999). In the past decades, this model performed outstandingly in explaining the Universe in various aspects: it simultaneously explained various probes, such as the formation of the large-scale structure (Davis et al., 1985), predicted the baryonic acoustic oscillations (Eisenstein & Hu, 1998), or the Big Bang nucleosynthesis (Boesgaard & Steigman, 1985), and more. These made the flat–ΛCDM an extremely successful cosmological model; however, the tensions present today may point beyond it.[12]

The tension was discovered between the Hubble constants estimated through the cosmic distance ladder, employing Cepheids and SNe Ia in a similar setting to what Hubble did (SH0ES project, Riess et al. 2022), and the one based on CMB anisotropies (Planck Collaboration et al., 2020). Although these are not the only combinations of early and

[11] Strictly speaking this is necessary for near-Universe estimates as well, however, given the small redshifts, the correction factors make only negligible changes compared to the linear Hubble law.

[12] Although it points beyond the scope of this thesis, we mention that the Hubble tension is not the only problem that challenges ΛCDM. A similarly severe tension was found in the clustering of galaxies, which tracks the clumpiness of the dark matter, and which is referred to as the σ_8 tension (Verde et al., 2019). Here, the results found by the weak-lensing experiments measured inconsistent clusterings compared to what is expected based on ΛCDM-based simulation. Recent results published by the eRosita collaboration, however, found results to be consistent with ΛCDM, which points to significant inconsistencies between the different observational means (Ghirardini et al., 2024).

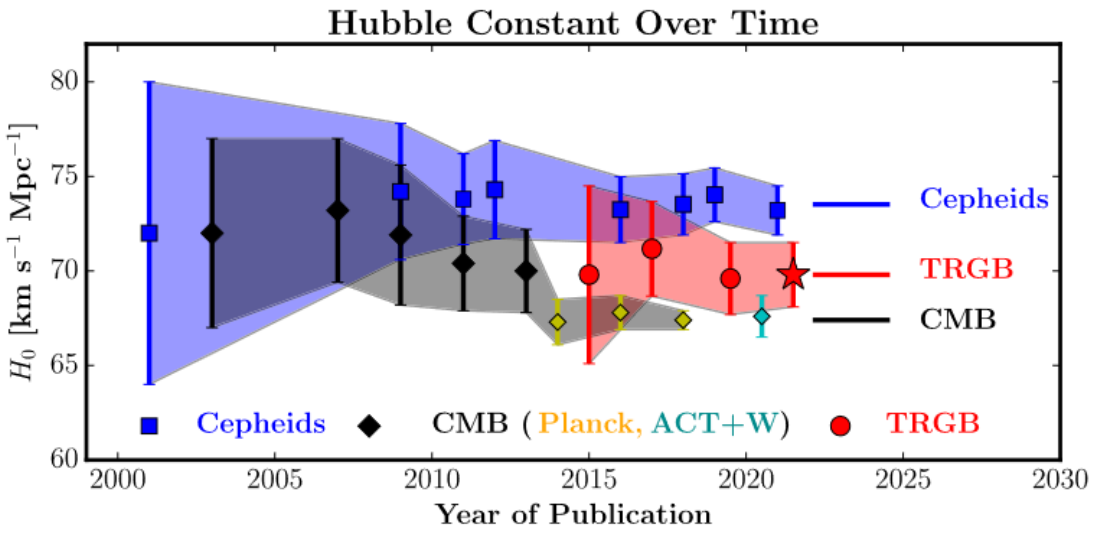

Figure 1.7: The evolution of the Hubble constants estimated through different methods, and the emergence of the Hubble tension in parallel with the shrinking of the uncertainties. The image was compiled by Freedman (2021). It shows well that as time progressed, the Cepheid (blue) and CMB-based (black) values became progressively discrepant, culminating in the tension in the last decade, even though the first measurements were in perfect agreement. The tension first emerged with the 2013 data release of the Planck Satellite (Planck Collaboration et al., 2014b). Currently, there is a 5σ tension between the latest CMB (Planck Collaboration et al., 2020) and Cepheid (Riess et al., 2022) measurements. It adds to the ambiguity that with certain calibrations, such as the one published in Freedman (2021), the TRGB (red) measurement falls in between these two estimates. We will discuss the possible systematics that may affect these results in later sections.

late Universe estimates that are discrepant or in tension with one another, the Cepheid and CMB-based techniques possess the highest precision to date. The current day significance of the tension between these two indicators is 5σ: the latest near-Universe estimate of the SH0ES project is 73.30 ± 1.04 km/s/Mpc (Riess et al., 2022), which lies significantly above the Planck estimate of 67.36 ± 0.54 km/s/Mpc (Planck Collaboration et al., 2020). Adding alternative distance indicators to the picture blurs the tension, as the discrepancy appears less significant for certain calibrations, such as the TRGB method (Freedman, 2021). The comparison and evolution of the discrepancy are displayed in Fig. 1.7.

The efforts performed by the community in the last decade showed that the tension is not limited to differences between Cepheids and the CMB anisotropies alone (Di Valentino et al., 2021). Instead, independent measures reinforced both sides already, painting the same picture of a tension. In the near-Universe, apart from different variants of the cosmic distance ladder (for example, Riess et al. 2022), relatively large values of the Hubble constant were measured through lensing time-delays (Wong et al., 2020a) and water masers as well (Pesce et al., 2020). On the other hand, analyses based on

Baryonic Acoustic Oscillations (BAOs, see, for example, Addison et al. 2018 or Macaulay et al. 2019) also confirmed the Planck results. Although the BAOs probe the Universe not at a redshift of a thousand but around $z \approx 1$, it is closer in terms of methodology and cosmological model dependence to the CMB measurements than to the near-Universe probes.[13]

Multiple theoretical explanations were proposed, to solve the tension. Without striving for a complete list, these include the possible presence of early dark energy which affects the clustering of dark matter (Herold & Ferreira, 2023), a dark energy component with a time-varying equation of state (Zhao et al., 2017) or with different parametrization and more degrees of freedom within ΛCDM (e.g. Li & Shafieloo 2019), additional unknown modes of interaction between dark matter and dark energy (Wang et al., 2016; Pan & Yang, 2023), and many more, along with theories and investigation outside the ΛCDM model (see the Sigmoid Dark Energy description of Torres-Arzayus et al. 2023 or the ηCDM model of Lapi et al. 2023 for recent examples). Apart from theoretical solutions, the question of underestimated measurement uncertainties for the estimated Hubble parameters was raised (e.g. Wang et al. 2024) and investigated by multiple authors in the past (Scolnic et al., 2020; Riess et al., 2020). For a complete review of the systematics and the range of solutions, we refer the reader to Di Valentino et al. (2021).

At the same time, it is essential to note that not all estimates are inconsistent and imply tension, as one can find a pair of early and late-Universe Hubble constant estimates that are in agreement. The variants of the distance ladder that use the TRGB as the rung that calibrates the SNe Ia demonstrate this well. While the calibration of Freedman (2021) yields a Hubble constant that is consistent with the Planck CMB measurement (69.8 ± 2.2 km/s/Mpc), the alternative calibrations of Anand et al. (2022) and Anderson et al. (2023) resulting in 71.5 ± 1.8 km/s/Mpc and 71.8 ± 1.5 km/s/Mpc respectively yield more inconsistent match-ups. A similar difference exists for Cepheids as well, primarily between the calibrations devised by the SH0ES and the CCHP teams, where the former takes the metallicity dependence of the period-luminosity relation into account (see, for example, Breuval et al. 2022), while the latter finds no statistical evidence for the need of such corrections (Madore & Freedman, 2023). Fig. 1.8 depicts a set of different Hubble constant estimates published up until recently. It shows that there are multiple possible pairings that paint different pictures of the Hubble tension; for some, the mismatch between the estimates indicates the tension, while for others no inconsistency is observed.

The Hubble tension, its possible implications, and the scale of disagreements between near-Universe measures call for detailed and meticulous checks on how we estimate distances and the Hubble constant. To this end, it is essential to delve deeper into how the existing estimators work and devise new methods that one can apply independently of the others. These can allow for disentangling previously unknown systematic effects of the various techniques. The community has spent significant effort to perform this test for the two most widely used near-Universe distance indicators, the Cepheids and the TRGB, along with the distance ladder built on them. In the following sections, we will review these methods and investigations, then extend the discussion with a third

[13] Although the BAOs as a measurement tool are not completely decoupled from the CMB anisotropies.

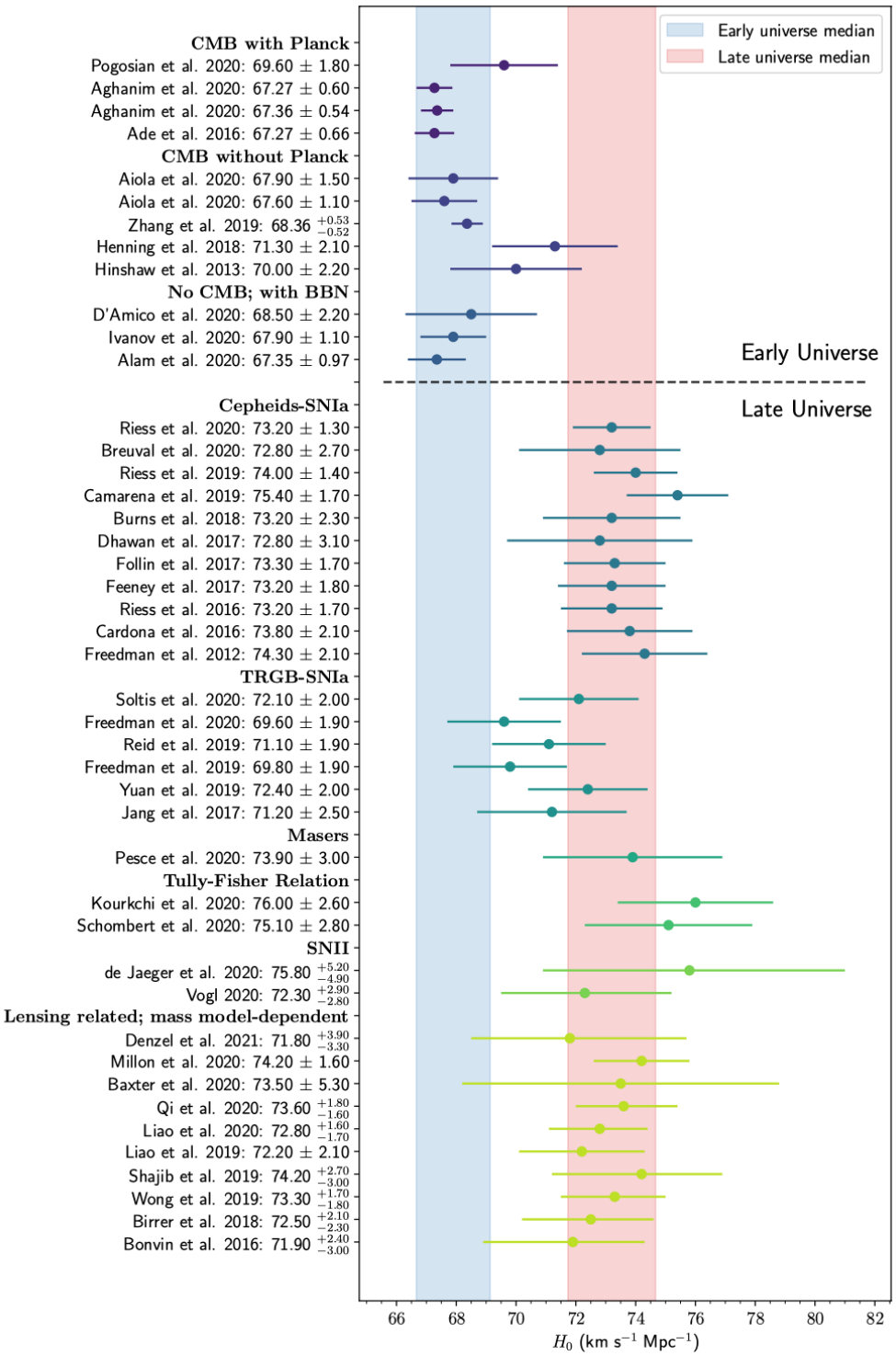

Figure 1.8: Differences between the Hubble parameters obtained through various means. On the plot, every errorbar corresponds to a particular analysis noted on the y axis next to it, which either employs a new technique, a different calibration, or simply a new dataset. Figure based on the data of Di Valentino et al. (2021), adapted by Alexander Holas.

indicator, Type II supernovae (SNe II), which can be utilized independently of the other methods (Vogl, 2020). An important aspect is, that both of these three methods track the same populations, the evolved, red giant stars. As such, they can be applied to the same galaxies in parallel, providing grounds for direct cross-comparisons that can help resolve inconsistencies, as we will expand on in later chapters.

2 Near-Universe means to measure distances

In this chapter, I will review the currently most widely used probes for estimating distances in the near-Universe. The list is meant not to include all methods: providing an in-depth overview of all existing techniques would gravely exceed the scope of this thesis. As such, the current discussion will not touch upon techniques based on masers, eclipsing binaries and lensing. Instead, here I will review methods that arise from nearly the same population of young and massive stars, and which can easily be cross-checked in practice as well: pulsating stars, such as Cepheids; specific features of a stellar population, such as TRGB; and exploding hydrogen-rich massive stars, SNe II.

2.1 Cepheids and the Leavitt law

Cepheids are one of the longest known[1] and arguably the most important type of variable stars owing to their period-luminosity relation discovered by Leavitt & Pickering (1912). These variables are evolved radially pulsating stars, which cross the instability strip during their post-main-sequence evolution. The cause of their radial pulsation is the so-called κ or γ mechanisms, which were first theoretically proposed by Eddington (1918). In these mechanisms, the pulsation is explained through the change in the opacity of partially ionized zones of He and H, which operate as a piston at a given temperature: at higher temperatures, they trap the produced radiation, which, however, exerts pressure, and expands the star. The expansion, however, results in the temperature, and hence the opacity dropping in the partially ionized zones, due to which the trapped radiation is released. As a result, the pressure drops, and the star heats and contracts back into the initial stage, starting the cycle again from the beginning (Catelan & Smith, 2015).

This mechanism requires specific temperatures and can only operate within a tight region on the Hertzsprung–Russel diagram (HRD), the so-called instability strip (see, for example, Tammann et al. 2003; Anderson et al. 2016). As a result, stars only turn into Cepheids when they cross this instability strip during their post-main-sequence evolution once they exhaust their hydrogen core. This is shown in Fig. 2.1 as well, where the stellar evolution models of Georgy et al. (2013) are plotted for different initial masses of stars, along with the position of the instability strip as well. Due to the rapid evolution of these stars, they cross the instability strip and cease to pulsate relatively fast; the Cepheid phase of the stellar evolution lasts only a few million years. However, a star may enter this region multiple times during the blue loop (De Somma et al., 2020).

[1] Edward Pigott was the first to discover the light variability of a Cepheid, η Aql (Pigott, 1785), hence, this variable star class has been known for more than two centuries.

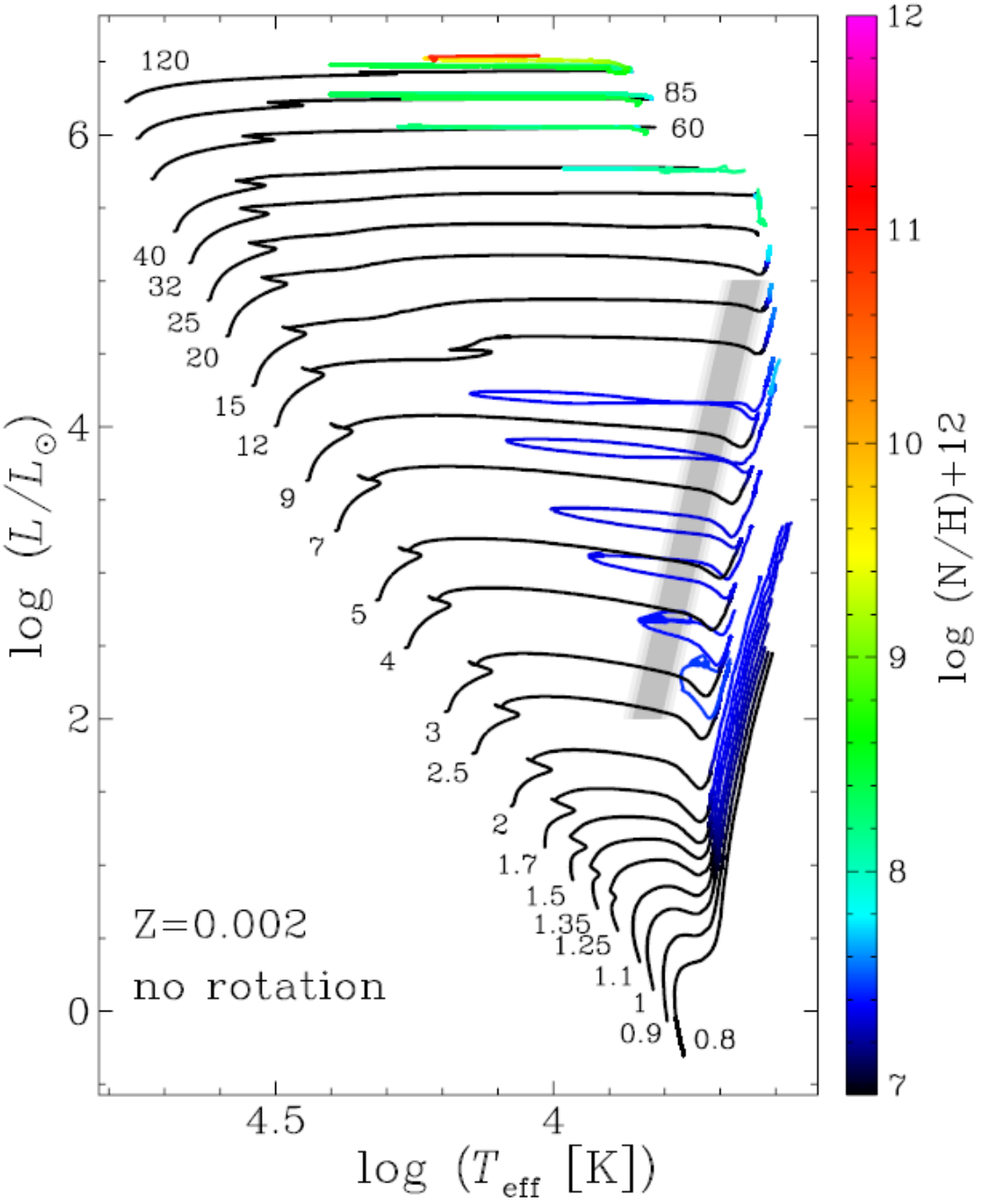

Figure 2.1: Stellar evolution models and the position of the instability strip. The figure was created by Georgy et al. (2013). The instability strip boundaries were calculated by Tammann et al. (2003), within which the evolved stars begin to pulsate. The plot shows that stars reside in the instability strip only during a brief phase of their post-main-sequence evolution. The colours indicate the surface abundance of nitrogen for the evolving stars.

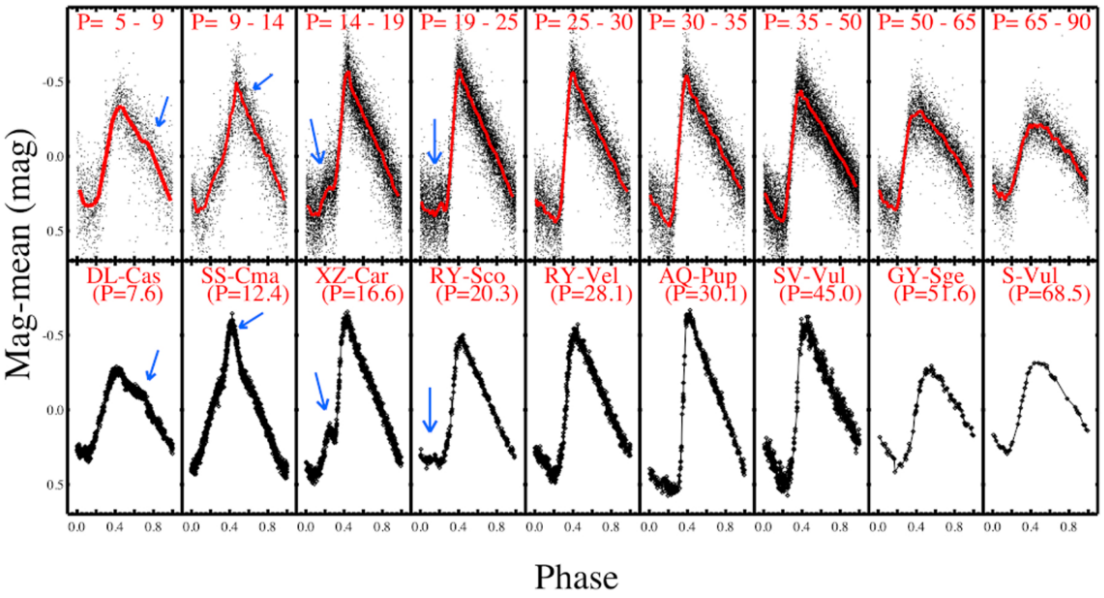

Figure 2.2: Hertzsprung progression as drawn out by Galactic and Extragalactic Cepheids from Riess et al. (2022). The top row shows the light curves of extragalactic Cepheids observed by the *HST* and binned in accordance with their pulsation period, while the bottom row shows a well-known Milky Way Cepheid in each of these ranges for comparison. Both rows show the travelling bump (marked by the blue arrows) of the Hertzsprung progression (Hertzsprung, 1926). The red curve is a fitted cubic spline, which follows the average of the light curves in each bin.

The onset of pulsation within the instability strip gives rise to the striking oscillation of the light curve with a remarkable periodicity. Figure 2.2 displays the light curve shapes that arise for Cepheids for various pulsation periods. One important feature is that the light curves of Cepheids are not the same across all period ranges, but they show a remarkable trend owing to the Hertzsprung-progression (Hertzsprung, 1926). This effect shows up as a bump on the light curve, which appears at different phases for different pulsation period lengths. The physical explanation for this phenomenon was proposed to be either a resonance effect between the different modes of pulsation (Bono et al., 2000) or pressure echoes being reflected from the stellar core (Gastine & Dintrans, 2008). Whichever theory may be correct, significant information is embedded in the light curve shape, which can help estimate the physical parameters to a higher detail than possible based on the period length alone (Bellinger et al., 2020).

The possibility to constrain physical parameters based on the light curve and the entire period-luminosity relation boils down to the fact that the instability strip is very narrow, as it is only a few hundred Kelvins wide (e.g. Anderson et al. 2016). As a result, a strong relationship arises between the pulsation period and the mean stellar density $< \rho >$ of the Cepheids, as expressed by Ritter's equation:

$$P\sqrt{< \rho >} = Q \tag{2.1}$$

where P is the period, $< \rho >$ is the mean stellar density and Q is the pulsation constant (Cox, 1980). Given this equation,[2] one may express Stefan–Boltzmann's law ($L = 4\pi R^2 \sigma T_{\mathrm{eff}^4}$, where L is the luminosity, R is the stellar radius, σ is the Stefan-Boltzmann constant and T_{eff} is the effective stellar temperature) in terms of M_{bol} bolometric absolute magnitudes:

$$\log P + 0.5 \log \mathcal{M} + 0.3 M_{\mathrm{bol}} + 3 \log T_{\mathrm{eff}} + \mathrm{const.} = \log Q \tag{2.2}$$

which already shows the desired $M_{\mathrm{bol}} \propto \log P$ proportionality. Assuming that the stellar mass $\mathcal{M}$ is proportional to the absolute magnitude M_{bol} we may merge those terms and express the temperature through the colour of the star to obtain the general period-luminosity-colour relationship, which is used for pulsating variables (Catelan & Smith, 2015):

$$M_{\mathrm{V}} = \alpha \log P + \beta (B - V)_0 + \delta \tag{2.3}$$

where $(B-V)_0$ is the mean, dereddened colour of the Cepheid, and α, β and δ are fitting constants. The relationship was first found by Leavitt & Pickering (1912), and it has subsequently become one of the best-known ways of measuring extragalactic distances. The colour term in the relationship depends significantly on the chosen wavelength range: for longer wavelengths, the observed luminosity depends less and less on the temperature of the star (Jameson, 1986).[3] As such, the pulsation amplitudes decrease steadily towards the near-infrared. This makes reconstructing the accurate P-L relation simpler, even through a single infrared observational epoch per Cepheid, once the periods of the stars are known (e.g. McGonegal et al. 1982; Freedman & Madore 2010; Catelan & Smith 2015). Due to this reason, the nature of infrared period-luminosity relations is subject to very detailed investigations (Storm et al., 2011).

When attempting to estimate the distance of a galaxy, one has to determine the value for the offset parameter γ by fitting the period-luminosity relation. For this fitting, it is usually assumed that the slope of the period-luminosity relation is the same in all galaxies (see Riess et al. 2022, which demonstrates that this assumption holds within measurement uncertainties). However, several systematics affect the comparability of period-luminosity relations of Cepheid samples from different galaxies. The most significant and limiting systematic effect is the reddening originating either within the Milky Way or the observed host galaxy. The first affects the offset of the observed P-L relation, while the second increases the scatter among the data points, ultimately giving rise to uncertainties. Since the effect of dust is stronger the shorter the wavelengths are, it would be a handy choice to move observations to the infrared range to mitigate the problems of reddening as well (Freedman & Madore, 2010). However, no observatory

[2] Along with making use of the definition of the mean density, $< \rho >= \frac{\mathcal{M}}{4\pi/3R^3}$, where $\mathcal{M}$ denotes the stellar mass

[3] For Cepheids, the maximum of the Planck curve is in the optical range, hence as longer and longer wavelength ranges are chosen, one steadily moves away from the peak. For example, for K-band observations, we already probe the Rayleigh-Jeans tail of the Planck function, where the flux is largely insensitive to variations in the temperature (Catelan & Smith, 2015).

possessed the resolution required in the NIR/MIR wavelength range for precise Cepheid measurements: even *HST* possesses only a 0.1" resolution in the NIR range, and hence, the resulting photometry is significantly impacted by crowding effects for farther away galaxies. Due to this, past Cepheid distance estimations made use of infrared observations only as an extension to optical data.[4]

The method used to mitigate the effects of reddening is the so-called Wesenheit formalism (Madore, 1982). Within this, instead of using the observed magnitudes, one has to derive a "dereddened magnitude" defined as

$$m_H^W = m_H - R(m_V - m_I), \tag{2.4}$$

where m_H, m_V, and m_I are magnitudes measured in different bands, and R is the extinction coefficient valid for the selected band combination. As described in Appendix B and C of Madore & Freedman (1991), this combination of magnitudes mitigates the effects of reddening as long as the correct extinction law is assumed. For example, in Riess et al. (2022) the $m_H = F160W$, $m_V = F555W$ and $m_I = F814W$ *HST* bands are used along with $R = A_H/(A_V - A_I)$. The effect of using infrared data and the Wesenheit indices instead of optical magnitudes is shown in Fig. 2.3. It is, however, important to emphasize that the Wesenheit magnitudes nevertheless depend on an extinction law, which might bias the final measurements. There is an ongoing discussion on how one may use this formalism to compare Cepheids from host galaxies that obey different extinction laws (for an overview, see Follin & Knox 2018). According to a recent analysis presented by Mörtsell et al. (2022), differences in the extinction laws of different host galaxies may cause significant shifts to the estimated Hubble constant, hence correctly assessing the effect of reddening is crucially important for this formalism as well.

Another frequently discussed systematic effect for Cepheids is that of metallicity. As shown by multiple previous studies, the metal content of Cepheids significantly affects the way they pulsate, which in turn affects their period-luminosity relation (Bono et al., 2008) and finally may cause biases for the final distance estimation (Bono et al., 2010; Riess et al., 2019; Breuval et al., 2022). To account for this effect, one has to add a metallicity dependent $\gamma \cdot [\mathrm{O/H}]$ term to Eq. 2.3, where [O/H] denotes the oxygen abundance that acts as a proxy for the metallicity, while γ is the correction coefficient. However, instead of measuring the metallicity of the Cepheids, it is a common procedure to establish the [O/H] gradient of the host galaxy, then assign a metallicity value to the Cepheids based on their position (see Hoffmann et al. 2016; Riess et al. 2022). The reason behind this is that one would otherwise need to obtain spectra of extragalactic Cepheids to measure their metallicity, which is not possible with the current instrumentation, or, as another alternative, detect Cepheids that pulsate in multiple modes simultaneously, then estimate their chemical composition based on their light curve parameters (Alcock et al., 1995; Kovtyukh et al., 2016).[5] Due to the difficulty of finding such objects, Riess

[4] Given the recent commission of *JWST*, it is now possible to measure distances based on IR data alone, owing to the increase in angular resolving power.

[5] The latter method however only provides a good handle on the average metallicity unless sufficient amount of multi-mode Cepheids are observed across the host galaxy.

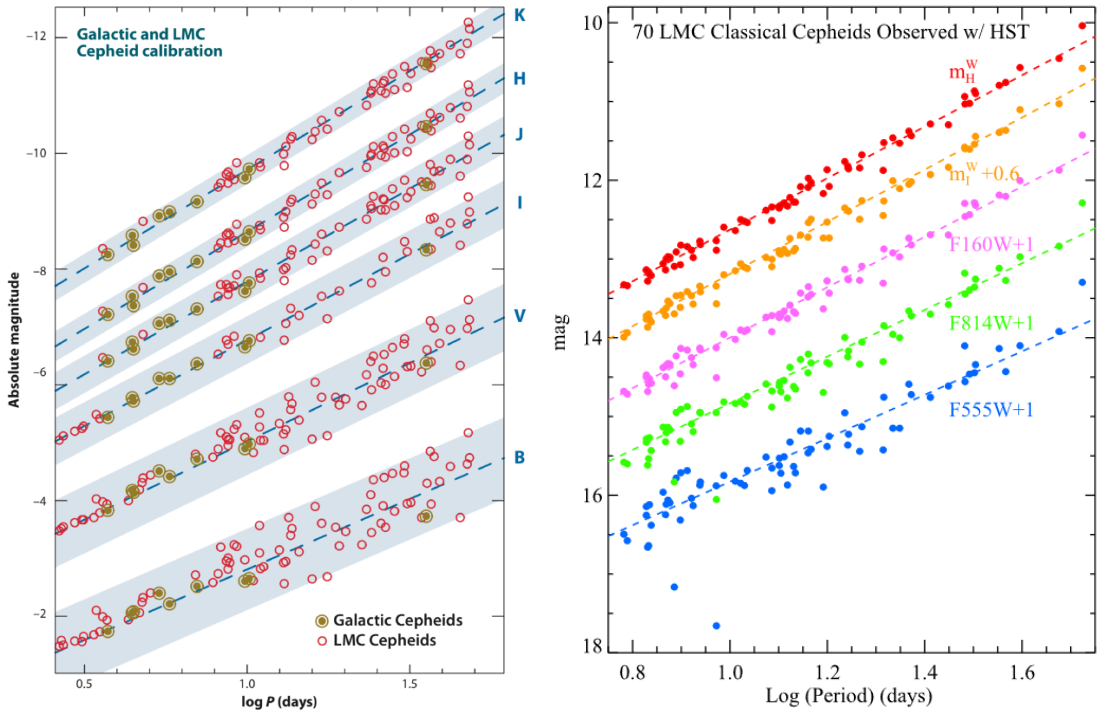

Figure 2.3: Scatter of the period-luminosity relation across different wavelengths. On the left figure, from Freedman & Madore (2010), the period-luminosity relation of Galactic and LMC Cepheids are shown in the $BVIJHK$ magnitude bands. The same is plotted on the right for LMC Cepheids and with the HST magnitudes, along with the Wesenheit indices (Riess et al., 2019). The figures show perfectly that the scatter of the period-luminosity relations steadily decreases towards longer wavelengths, and the best precision is achieved when Wesenheit formalism is used.

et al. (2019, 2022) instead resorted to measuring the metallicity of star-forming HII regions within galaxies, which are significantly brighter.[6]

The exact value of γ, or its necessity is hotly debated for the Cepheid community. Recently, Breuval et al. (2022) presented a thorough overview of the metallicity term: as outlined in the work, the majority of the theoretical models favour a positive ($\gamma > 0$) term, which would imply that more metal-rich Cepheids are fainter than the metal-poor ones. Among these are the studies using nonlinear convective models such as that of Marconi et al. (2005), Bono et al. (2008) or De Somma et al. (2022) or the results based on the stellar evolution models of Anderson et al. (2016). On the other hand, most empirical studies that measure the distances to these objects independently of the P-L relation find a negative coefficient ($\gamma < 0$), such as Storm et al. (2011) and Gieren et al. (2018)

[6]It is worth mentioning that there are multiple calibrations for the metallicity determination: the Zaritsky et al. (1994) and Bresolin et al. (2004) scales. When measuring Cepheid distances, it has to be ensured that the same scale is used for all galaxies, otherwise, they will impose biases on the analysis. This effect and the possible biases are discussed in detail by Riess et al. (2022).

through pulsation radial velocity-based distances, or as Groenewegen (2018) and Riess et al. (2021a) through parallaxes, among many others. Breuval et al. (2022) analyzed the currently existing datasets of *Gaia* and *Spitzer* to explore the wavelength dependence of the metallicity correction, finding that it globally takes the same negative value, concluding that the main influence of the metallicity is in the brightness, not the colour. At the same time, however, an independent analysis by Madore & Freedman (2023) found no statistical evidence for the metallicity dependence of Cepheid brightnesses.

Beyond the above two systematic effects, as discussed by Freedman & Madore (2023), stellar crowding may cause an additional bias term for the Cepheid-based distance estimation. This may include the effects arising due to the insufficient resolving power of the telescope, the Cepheid residing within its birth cluster or it being in a binary system[7] (Anderson & Riess, 2018). Previously, this was investigated through artificial star tests (such as done in Conroy et al. 2018 or Riess et al. 2019), but the pulsation of the Cepheids also provides a way to verify crowding effects, as shown by Riess et al. (2020). Recently, it was also shown, that the crowding issue is not causing significant offsets for the Cepheid P-L relation through *JWST* observations (Riess et al., 2024).

In addition to the previous systematics, it is an important question to consider not only the systematics that affects not the brightness of the Cepheid but its measured period. One such bias is the time dilation caused by the relative radial motion of the hosts of extragalactic Cepheids. However, this can only cause biases well below the per cent level in the periods (Anderson, 2019). It is, however, interesting to investigate how trustworthy the measured pulsation periods are; during distance estimations, they are assumed to be of pinpoint precision, even though multiple studies have shown that Cepheids are not perfect clocks: high-cadence photometric studies revealed that they exhibit short term fluctuations (Derekas et al., 2017; Süveges & Anderson, 2018; Plachy et al., 2021), which can put a lower limit on the accuracy of the measured pulsation period. Finally, as I will expand on in Part. IV, these fluctuations are indeed generally present, which may affect the distance estimations in certain cases.

Although it expands beyond the scope of this thesis, it is worth mentioning that not only Classical Cepheids possess a period-luminosity relation. All pulsating variable stars obey one such relation, such as Miras (Bhardwaj et al., 2016), RR Lyraes (Groenewegen, 2023), Type II Cepheids (Matsunaga et al., 2009) or even long secondary period variables as well (Trabucchi, 2023) (see Fig. 2.4). These provide semi-independent tests for Cepheids and help verify their usage as distance indicators. However, it is important to note that the longer the pulsation period, the more significant the fluctuation-based systematics may become, highlighting the need for further validation and bias testing.

2.2 Tip of the Red Giant Branch

The tip of the red giant branch (TRGB) method is a technique that utilizes a particular feature of the Hertzsprung-Russel diagram to establish the distance to a stellar popu-

[7] Given that more than half of the known Cepheids are within binary systems (see, for example, Pilecki et al. 2021), binarity may have a significant effect on the measured brightnesses.

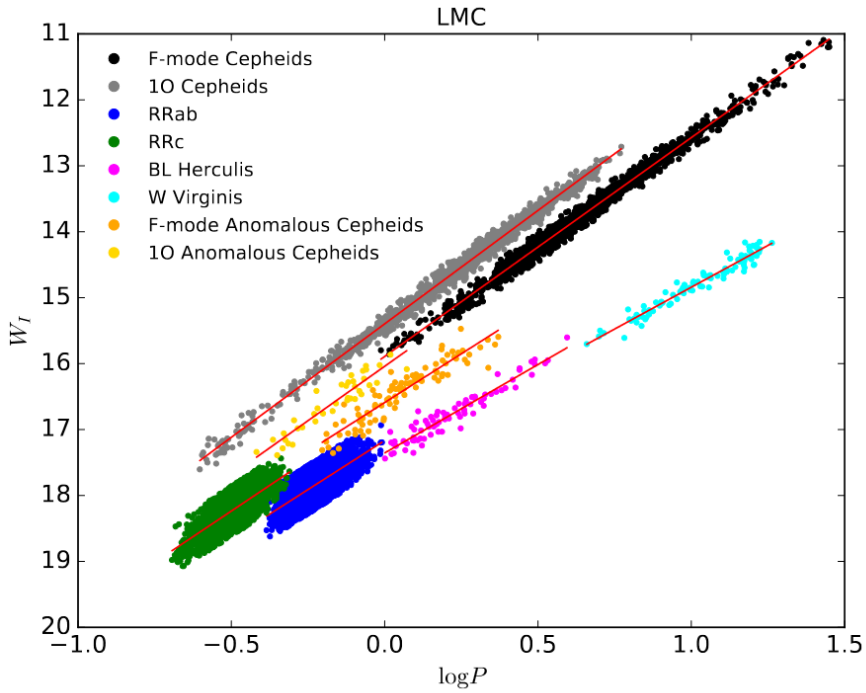

Figure 2.4: Period-luminosity relations of other, non-Classical Cepheid pulsating variable stars in the LMC by Iwanek et al. (2018).

lation. The method itself is fundamentally very close to Hubble's original method of calibrating the brightest stars in the galaxies. The tip marks a specific phase in the evolution of low-mass red giant stars, during which they abruptly transition from the red giant branch (RGB) to the lower-luminosity horizontal branch (Chiosi, 1998). This transition is initiated by the helium flash, at a thermal runaway event, when the degeneracy of the helium core is lifted, and the helium-burning process can begin, which settles the star to a lower luminosity. This process creates an upper limit for the luminosity of the red giant stars, which is theoretically well-understood (Bildsten et al., 2012; Serenelli et al., 2017). Given the extremely short timescale of the flash, we always observe RGB stars at a lower luminosity compared to where the flash occurs. This creates a feature distinctive enough to be used as a distance indicator (Rizzi et al., 2007; Freedman et al., 2020). An empirical illustration of the TRGB is shown in Fig. 2.5.

The first establishment of the TRGB as a distance indicator came mainly from two papers: the first, Da Costa & Armandroff (1990), applied the technique to Milky Way globular clusters to show that the brightness of the tip is remarkably robust, while Lee et al. (1993) laid out the method itself by investigating the systematics and introducing the Sobel filter, an edge detection technique, for deriving the tip magnitude based on the

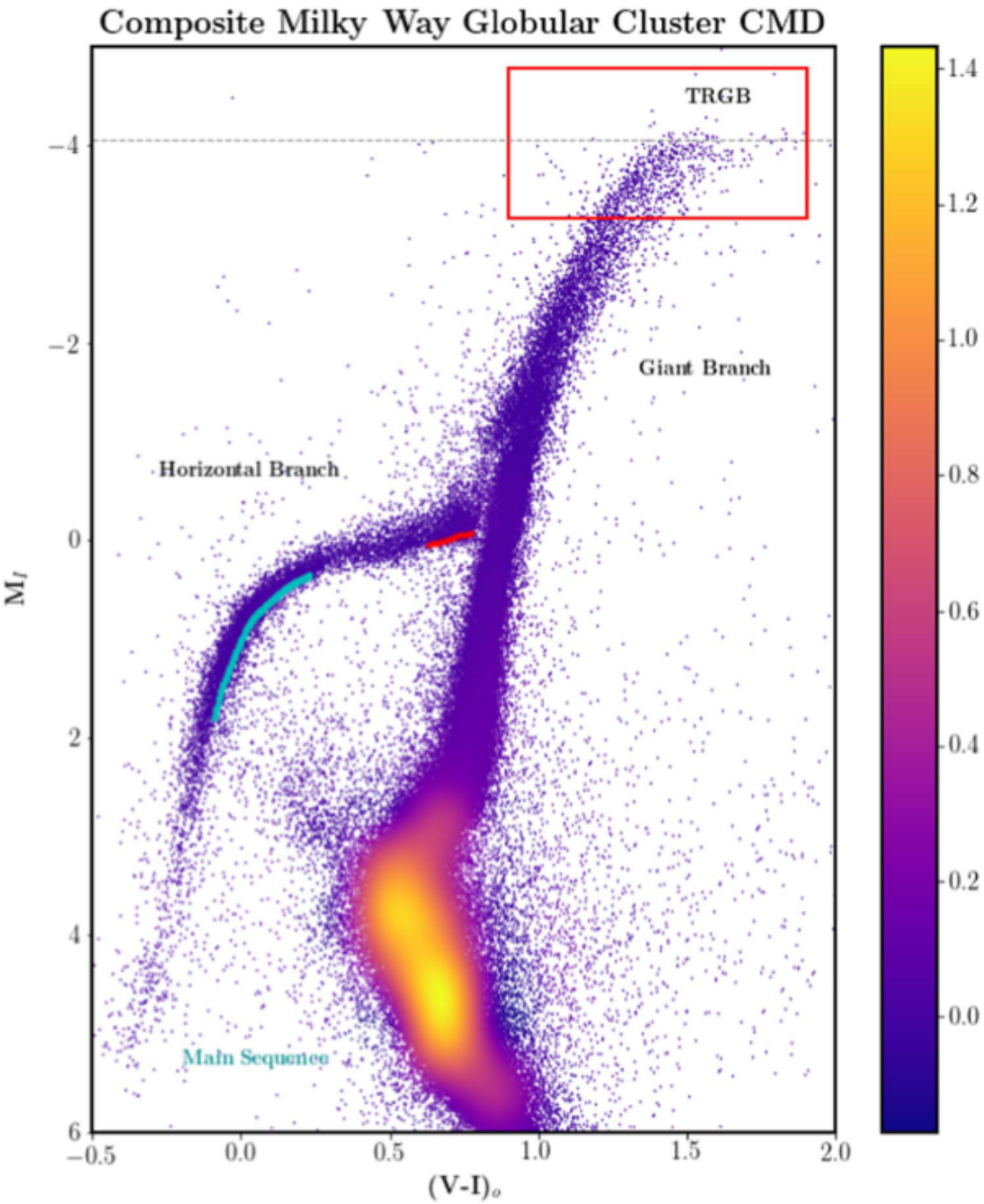

Figure 2.5: Illustration of the TRGB by Freedman (2021). The plot shows the composite CMD of 46 Galactic globular clusters. The colour of the points shows the number density of the stars in a given region of the plot. The horizontal grey line indicates the tip brightness according to Cerny et al. (2020).

observed luminosity function.[8] Fig. 2.6 depicts this procedure. It is worth noting that since the introduction of additional edge-detection techniques have also been used, such as maximum likelihood estimation (Méndez et al., 2002), or more modern kernels that employ self-consistent smoothing in the luminosity function (Madore et al., 2023). The methodology and possible uncertainties of the method have been recently outlined by Freedman & Madore (2023) and Madore et al. (2023), and Freedman (2021) also provides a thorough summary of how one makes use of TRGB measurements in cosmology. The main advantage of this method, beyond its well-understood theory, is its observational efficiency: one is required to obtain a single sufficiently deep exposure of the halo of the target galaxy (see McQuinn et al. 2017; Freedman 2021), which are multitudes easier to perform than, for example, setting up a sequence of observations for Cepheids with the correct time coverage and sampling (Freedman et al., 1994). A drawback for the TRGB for a long time has been its calibration: while Cepheids can be straightforwardly calibrated through either parallax (within the Milky Way) or by the detached eclipsing binary distance to the Magellanic Clouds or the Andromeda galaxy (Riess et al., 2022), the calibration of the TRGB was more difficult (due to the lack of Galactic calibrators, or, for long, that of independent anchors.[9]) Due to this, TRGB for long has for a long time been intertwined with other distance scales (see, for example, the calibration of Rizzi et al. 2007) and could not act as a completely independent distance estimator, for example, for the metallicity studies (Breuval et al., 2022). However, a recently published work demonstrated that the photometry and resolution of JWST are more than sufficient to measure the TRGB adequately in farther away galaxies, demonstrating it can precisely calibrate the method for absolute distances (Anand et al., 2024). In the future, an increasing number of *JWST* observations will be aimed dedicatively at the TRGB (Freedman et al., 2021; Riess et al., 2023).

It is also worth mentioning that the advent of *JWST* further widened the possibility of using features on the HRD for distance measurements by covering the wavelength range required for the J-Band Asymptotic Giant Branch method (JAGB). This method is based on a colour-selected subset of carbon-rich AGB stars, which are found to have tightly constrained luminosities in the near-infrared and are reviewed in Madore & Freedman (2020). At its core, this method is very similar to TRGB, and its use has already been demonstrated empirically recently (Zgirski et al., 2021; Lee et al., 2022). While the review of this method is beyond the scope of this thesis, it is essential to highlight that this method can provide crucial cross-checks for TRGB, such as the secondary pulsators

[8] The Sobel filter edge-detection algorithm is a spatial gradient operator which works on 2D images (Sobel, 2014). Essentially, it performs the discrete differentiation to approximate the gradient. For the TRGB setting, one has to compute the luminosity function of the stellar sample, and then apply the Sobel filter to the resulting distribution.

[9] Given the proximity of LMC and the Andromeda galaxy, to achieve a representative sample of RGB stars and to obtain a reliable TRGB calibration, observations of multiple halo fields are necessary. This, however, made observations increasingly expensive, hence such studies were only made possible in recent years (Górski et al., 2018). Given the lack of field-to-field comparisons, the calibrations were more subject to field-to-field variation uncertainties, which directly contributed to the distance biases.

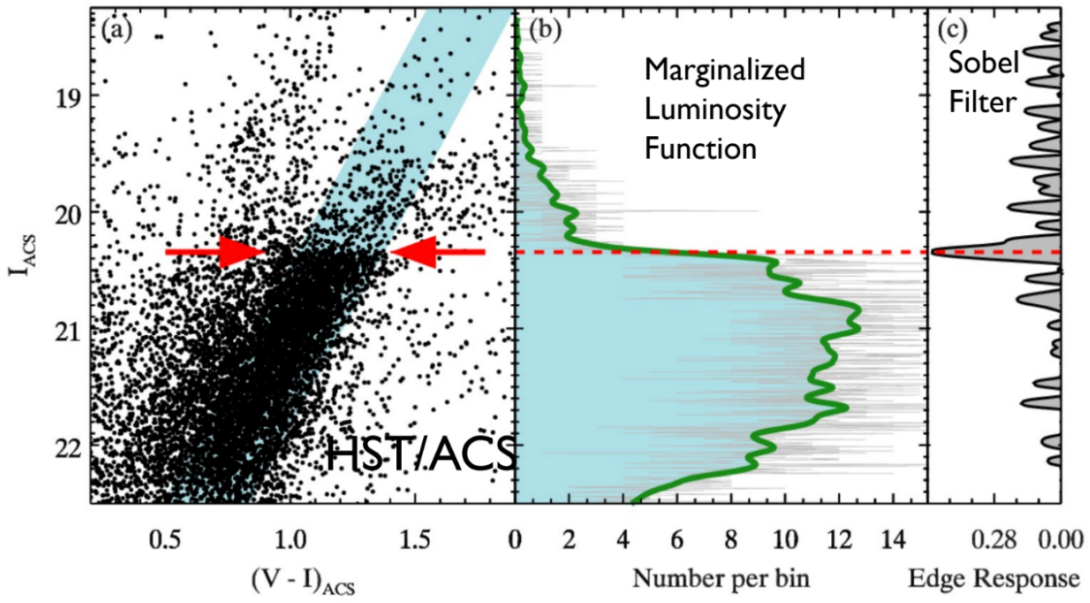

Figure 2.6: I-band TRGB and its detection procedure from Madore et al. (2023). The left panel shows the CMD of the IC 1613 galaxy along with the termination of the red giant branch. The middle panel shows the luminosity function for the red giant stars within the blue-shaded region, while the right panel shows the result of applying the Sobel filter to this distribution.

do for Cepheids. Moreover, this also opens up the possibility of jointly using TRGB and JAGB for distance estimation, putting exciting HRD-based studies within reach.

Just as for Cepheids, the list of systematics present for the TRGB method includes multiple aspects, which were discussed in detail by Madore & Freedman (2023). One of the systematic effects is the reddening, however, the TRGB possesses two advantages in this regard. On the one hand, TRGB is performed on stars that lie in the halos of other galaxies, where the problem of reddening internal to the host galaxy is less significant as in the disk (McQuinn et al., 2017). In addition, the TRGB measurements are performed in the *HST* $F814W$ band, which is less susceptible to reddening than bluer bands.

Beyond reddening, metallicity is also causing measurable changes for the TRGB, similar to Cepheids. In the past, the treatment of this metallicity difference was up to the choice of the astronomer: in some studies, the tip brightness was considered to be insensitive to this when selecting the oldest subset of stars (Madore et al., 2018), while in other studies authors employed corrections that account for this variation (Freedman, 2021; Hoyt, 2023). However, it was shown by multiple studies that halos of nearby galaxies, such as that of M 31, indeed show metallicity gradients (Gilbert et al., 2014; Ibata et al., 2014). Some studies also found metallicity gradients in the halos of elliptical galaxies, an effect that is less understood (Greene et al., 2013). Hence, metallicity corrections may be needed. Depending on the mean colour of the sample stars, both versions may differ even on a level of ~ 0.1 mag (Anderson et al., 2023). Given the disagreement between

the different approaches, the question of metallicity corrections for TRGB is still a focus of studies.

The absolute calibration of TRGB, even without the question of metallicity dependence, is also subject to particular investigations. As Anderson et al. (2023) summarized recently, the absolute calibrations used by different teams (Freedman, 2021; Rizzi et al., 2007; Soltis et al., 2021; Anand et al., 2022) vary on the scale of $\sim$ 0.06 mag, and the origin of the differences is unclear. Albeit such a difference may seem small, it directly transits to the Hubble constant when the distance ladder formalism (detailed in Sect. 2.3) is employed. Investigating this effect, Anderson et al. (2023) showed that all stars close to the tip are small amplitude variable stars (OGLE Small Amplitude Red Giants, *OSARGs*, Wray et al. 2004, Fig. 2.7), which was not taken into account in previous calibrations. Accounting for this variability results in a calibration that is 0.05 mag fainter than the ones usually adopted for cosmological studies (Freedman, 2021; Anderson et al., 2023).

Although the calibration of the tip brightness has certain uncertainties on its own, the way the tip is found can also be problematic. Several such problems have been investigated in a recent work of Scolnic et al. (2023), such as how the TRGB region used for distance estimation is selected on the CMD. This includes parameters such as the width of the red giant branch or also the way the resulting luminosity function is smoothed afterwards. Other detailed studies on the edge detection methods are presented in Beaton et al. (2018). As described in Scolnic et al. (2023), one can find a per cent level scatter for the final tip brightness among the variants. It is also worth noting that the treatment of photometric uncertainties is not uniform across different analyses, with multiple variants existing, such as the ones presented in Freedman (2021) or Anand et al. (2022). The most significant analysis choice is the way the smoothening is applied to the luminosity function and how the contrast of the tip is evaluated (which is defined as the ratio of the stars below and over the detected edge). As Anand et al. (2024) noted, certain types of smoothening may cause artefacts and biases in the analysis. In parallel, Wu et al. (2022) also concluded that the contrast of the tip significantly affects the recovered tip brightness (also confirmed by Scolnic et al. 2023), based on the analysis of multiple TRGB fields of a nearby galaxy. Fig. 2.8 shows the correlation found between the tip contrast and the magnitude residuals for the fields, which all belong to the same galaxy. The correlation was also confirmed by Scolnic et al. (2023) in an independent analysis.

One of the effects that can cause changes to the contrast of the tip and bias the distance measurement is the selection of the field used for the analysis, as also described in Jang et al. (2021) or Madore et al. (2023). As presented in Jang et al. (2021), choosing the field for the TRGB analysis that overlaps with active star formation regions can bias the measurements. For those fields, AGB and red helium-burning stars can significantly contaminate the position of the tip on the CMD (Beaton et al., 2018; McQuinn et al., 2019). Given that AGB stars can reach magnitudes much brighter than the tip (Habing & Olofsson, 2003; Rosenfield et al., 2014, 2016), they pose a significant possibility for biases. The fact that the progenitors for AGB stars are of the red giant sequence further makes them a source of risk (Beaton et al., 2018). Using disk fields also increases the

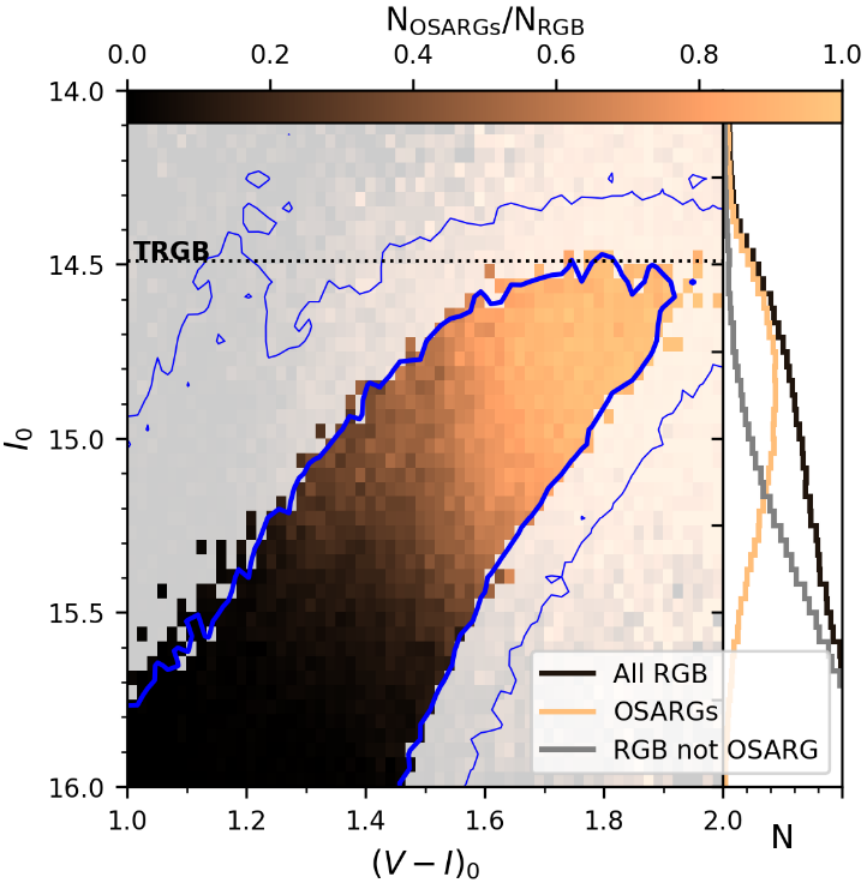

Figure 2.7: Variability fraction on the TRGB compiled by Anderson et al. (2023). The colouring of the coarsely-binned CMD indicates what fraction of the stars falling into a given bin are OSARGs. The blue contours indicate regions with 70% (thicker) and 20% (thinner) of all stars in the OGLE photometric catalogue (Udalski et al., 2008). The fraction of variables increases steadily upwards the TRGB, indicating that nearly all stars are variable on the tip.

metallicity variation on the CMD owing to the inclusion of more Population I stars (Jang et al., 2021). Finally, fields closer to or on top of the disks of galaxies are more crowded, making the photometry more uncertain, and it also increases the risks of it being affected by reddening. The comparison of two past papers highlights the potential differences in this regard well; in two independent studies on the disk field TRGB of NGC 4258 Macri et al. (2006) and Rizzi et al. (2007) found tip magnitudes that were different by ~ 0.1 magnitude, which incurs significant biases in the end. To this end, using older metal-poor populations in the halo fields is a safer way to estimate the tip brightness Jang et al. (2021). Furthermore, one may safely check the field for possible

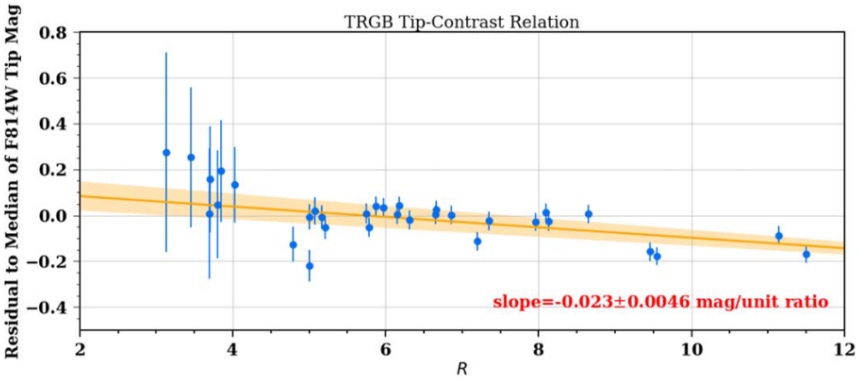

Figure 2.8: Correlation between the contrast and the brightness of the tip found by Wu et al. (2022). The individual points correspond to individual fields within the same galaxy that exhibit varying contrast values. According to the fitted relationship, the more constrastful CMD branches yield a brighter tip.

star formation to ensure no contamination from younger populations by using ultraviolet observations (McQuinn et al., 2017).

Interestingly, many of these issues become more significant towards even redder wavelengths as discussed by McQuinn et al. (2019): even though the tip becomes about two magnitudes brighter, which enables an increased dynamic range for the sample (through offering a more complete view on the fainter stars on the RGB, giving a more firm handle on the slope of the RGB), it also becomes more sensitive to stellar age and metallicity, making it a less desirable distance indicator in the near-infrared. On the other hand, the recent analysis by Anand et al. (2024) showed that *JWST* measurements on the TRGB can also be well calibrated.

2.3 The distance ladder

As we have touched upon in the previous sections, the most troublesome part of using both Cepheids and the TRGB for distance estimation is the calibration of their brightnesses. Even though there have been attempts to estimate absolute brightnesses of both already (see, for example, Ngeow et al. 2012 for Cepheids and Serenelli et al. 2017 for TRGB), the community prefers to base the analyses on the empirical grounds due to the wide range of systematics that may enter the investigation otherwise. Moreover, as of today, neither the Cepheid nor the TRGB method can reach far enough out into the Hubble flow that the peculiar velocities will not add significant uncertainty to the redshift. Instead, to reach out far enough one should employ the distance ladder.

The name distance ladder refers to the fact that instead of using a single technique to reach other galaxies, one employs a series of calibrations to build a ladder to bridge farther distances, such as shown in Freedman et al. (2001), Riess et al. (2019) or Riess et al. (2022). Figure 2.9 displays one example setup from Riess et al. (2022). In the

distance ladder setting one first estimates absolute distances to objects that can be used to measure distances farther away either through parallaxes (e.g. through the measurements of the *Gaia* space telescope for Cepheids, Lindegren et al. 2021, Riess et al. 2021b), detached eclipsing binaries (e.g. Ribas et al. 2005 for M 31, Bonanos et al. 2006 for M 33 and Pietrzyński et al. 2019 for the LMC) or a megamaser (for NGC 4258 by Reid et al. 2019, for both Cepheids and TRGB, as shown in the works of Hoffmann et al. 2017 and Jang et al. 2021). These allow for directly estimating the zero-point offset for Cepheids and the absolute brightness of the TRGB. For example, for the latest analysis of the SH0ES collaboration, Riess et al. (2022) used the distance determinations to LMC, SMC, M 31 and NGC 4258 to establish the fit parameters of the Cepheid P-L relation, then used this relation to calibrate a further reaching technique, SNe Ia.

Even though Cepheids and the TRGB can be used to probe galaxies further away than our local cosmic neighbourhood, they are still not suitable for reaching the Hubble flow. As a solution, the Cepheid and TRGB distances are instead used for calibrating the brightnesses of, for example, supernovae, which are then capable of reaching far enough for cosmological studies. For this purpose, most studies employ SNe Ia (see e.g. Freedman 2021; Riess et al. 2022). However, some other types of transients can be utilized as standardizable candles once one can determine the correct set of parameters for the standardization. The advantage of SNe Ia over the other types of transients is that they are relatively frequent and bright (with absolute magnitudes ranging from -18 to -19.5, Maguire 2017), allowing them to be observed suitably far away, and are standardizable through the use of a few easily estimable parameters (Wright & Li, 2018; Riess et al., 2022). It is worth mentioning at this point that SNe II also offer a way of standardization. However, due to the smaller sample of calibrator objects and the generally poorer standardization make these objects less advantageous for distance ladder-based approaches (Hamuy & Pinto, 2002; de Jaeger et al., 2022).

According to our current understanding, SNe Ia are thermonuclear explosions of white dwarf stars. Whereas the community largely agrees on the type of progenitor star for this explosion, there is a currently ongoing debate concerning the different explosion mechanisms or the combinations of these various channels that may lead to SNe Ia. The various scenarios are discussed in detail in, for example, Hillebrandt & Niemeyer (2000), Maoz & Mannucci (2012) and Livio & Mazzali (2018). Most of SNe Ia exhibit remarkably similar spectral evolutions and light curves (except for the more peculiar members of the population belonging to the 91T-like or 91bg-like SNe Ia, as described in detail by Taubenberger 2017), which set the base for their standardization (Riess et al., 1996; Tripp, 1998). Owing to this property, SNe Ia have long been used as distance indicators, which resulted in the discovery of the accelerated expansion of the Universe (Riess et al., 1997) and later the Hubble tension as well (Riess et al., 2012, 2022). To standardize SNe Ia, given their overall similarity, one only has to take a look at their light curves: as it was pointed out first by Rust (1974) and Pskovskii (1977), more luminous SNe Ia display slower declining light curves, a relationship that was robustly formulated later by Phillips (1993). According to this work, the B-band peak magnitude and the decline rate, parametrized by the drop in the same band magnitude 15d after the peak $\Delta m_{15}(B)$, exhibit a very tight correlation. Along the same line of ideas, Perlmutter et al.

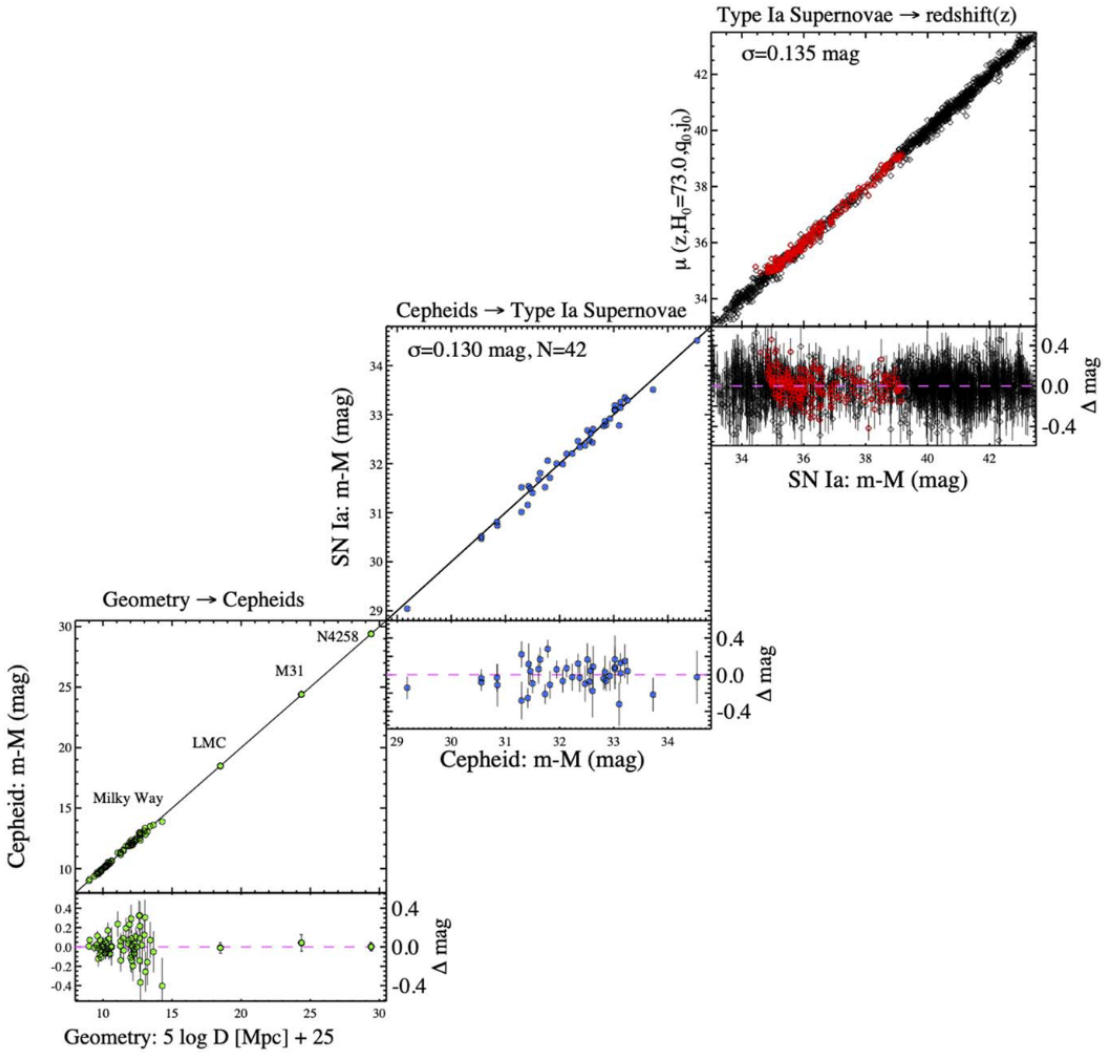

Figure 2.9: Distance ladder built out of Cepheids and SNe Ia from Riess et al. (2022). In this setting, successive further-reaching methods are calibrated one after another starting from absolute distances. For the distance ladder of the SH0ES project (Riess et al., 2022) two calibration steps are employed: in the first step, the Cepheid period-luminosity is calibrated through parallaxes in the Milky Way, detached eclipsing binaries in the LMC and M31, and the megamaser of NGC 4258. This is shown on the bottom left panel. Then, in the second step, the calibrated Cepheids are used in nearby galaxies to standardise SNe Ia. After this standardisation, these supernovae are then used at higher redshifts to probe the Hubble flow.

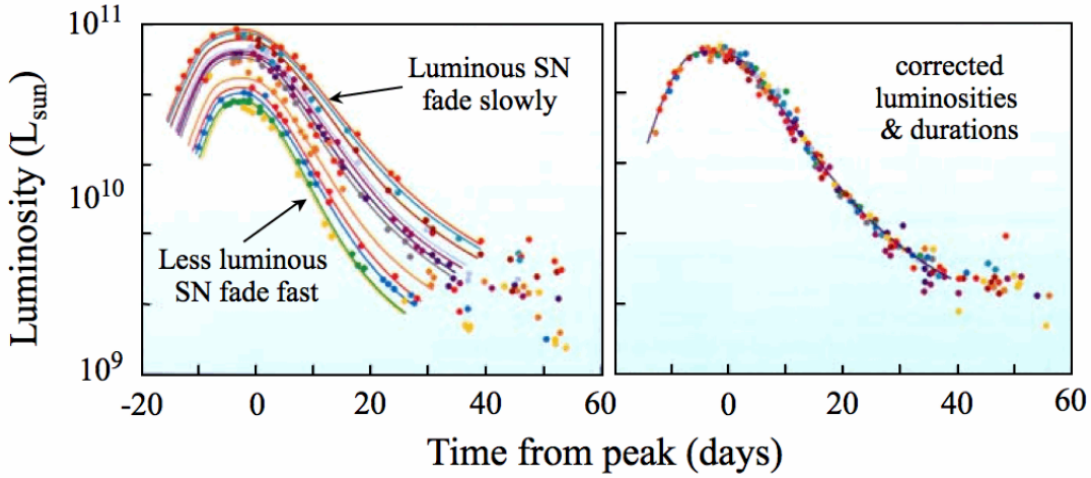

Figure 2.10: Standarization of SN Ia light curves. The left panel shows the observed SN Ia light curves which exhibit various decline rates and peak magnitudes. The right panel shows the light curves after standardization using the stretch factor. Image credit: Durham University Department of Physics (https://johnlucey.webspace.durham.ac.uk/bridge/n2015m-bridge/).

(1997) introduced the so-called stretch-factors, proposed as the required transformation factors for bringing the SN Ia light curves into an agreement through stretching or compressing them along the time axis. Early standardizations utilized only the B-band, but modern light curve fitters, such as SALT2 (Guy et al., 2007), SALT3 (Kenworthy et al., 2021), MLCS (Riess et al., 1998; Jha et al., 2006) or BayeSN (Thorp et al., 2021; Mandel et al., 2022) perform this based on multiband light curves or even spectra. Even though the light-curve stretch-based calibration performed well given the agreement of the light curve shapes (Fig. 2.10), the increase in precision revealed that SN Ia intrinsic colours correlate with the peak brightnesses, which necessitated the introduction of an additional colour term in the standardization equations (see, for example, Rose et al. 2020). Moreover, Rose et al. (2021) recently found that there might be an additional brightness term associated with the star formation rate of the host galaxy, which might cause biases tied to the type (i.e. elliptical or spiral) of the host galaxies (see Fig. 2.11). After this standardization, the distance ladder is complete and allows for probing the Universe to a redshift of $z \approx 2$.

Apart from the variant using SNe Ia, one may build a distance ladder that uses SBF alternatively, which yields Hubble constant values mostly in agreement with the SH0ES results. The overwhelming majority of past H_0 determinations use the distance ladder, which, as shown above, requires multiple steps and allows for several possibilities for systematic offsets to arise. Hence, there is a need for methods that can operate in a single step, not requiring external calibrations by other methods, yet being able to measure distances out in the Hubble flow. One such method is that of SNe II, which I will describe in the next section.

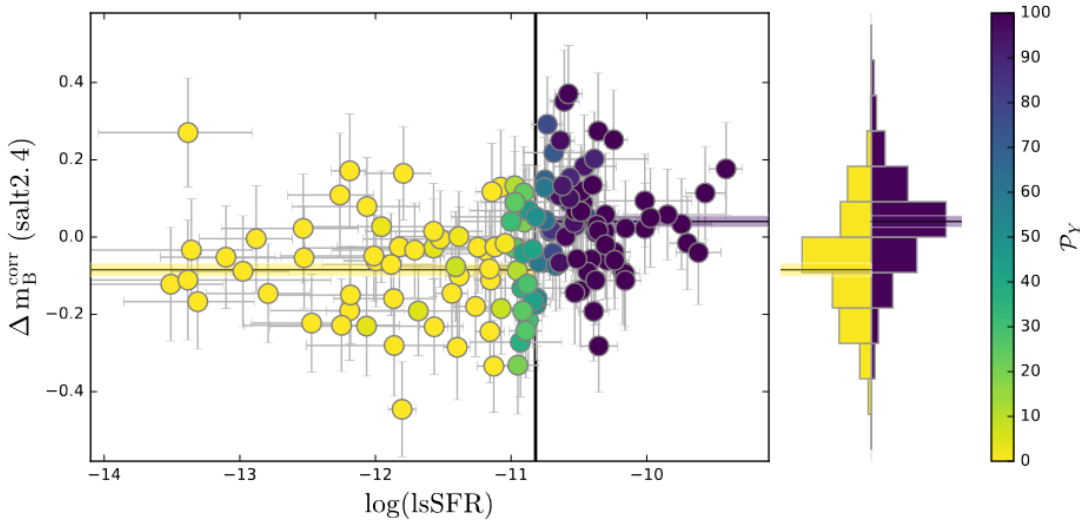

Figure 2.11: Dependency of SN Ia brightnesses on the star-formation rate of the host (Rigault et al., 2020). As shown, SNe Ia exploding in more actively star-forming galaxies are systematically brighter. Given that SNe Ia are calibrated in star-forming galaxies (since Cepheids track young stellar populations), it is important to use SNe Ia from similar galaxies in the last rung of the distance ladder as well, to avoid biases.

2.4 Type II supernovae as an alternative path

SNe II are exploding supergiant stars, first termed as a separate class by Minkowski (1941), who discovered that these transients exhibit prominent features of hydrogen, which SNe Ia do not. Thanks to the presence of hydrogen in the outer layers of the supernova, a well-defined photosphere forms, which radiates like a dilute blackbody during the first few weeks post-explosion. Below the photosphere, the material of the supernova is optically thick, thus, the escape of photons without reprocessing is unlikely. Hence, the regions above the photosphere are largely responsible for the observed parameters. As a result, while the photosphere resides within the hydrogen layer of the ejecta, the nature of the emission is relatively simple compared to other types of transients.

For SNe II, we distinguish between five main classes: IIP, IIL, IIn, IIb and 87A-likes (Arcavi, 2017). Of all supernovae, half of the transients are SNe II, among which 80% belong to the IIP/L class (Li et al., 2011). This class refers to the quote-unquote normal class of SNe II. Out of the remaining types, SNe IIb refers to the explosions of stripped-envelope supergiant stars, which retain only a thin part of their original hydrogen envelope, having lost the rest during their evolution, which is often explained through binarity (see, for example, Dessart et al. 2024). At the same time, SNe IIn are explosions engulfed within the local dust previously emitted through major mass-loss events of the progenitor star (Schlegel, 1990). These two classes are regarded as more exotic classes of SNe II, which are not as suited for distance determinations as their more

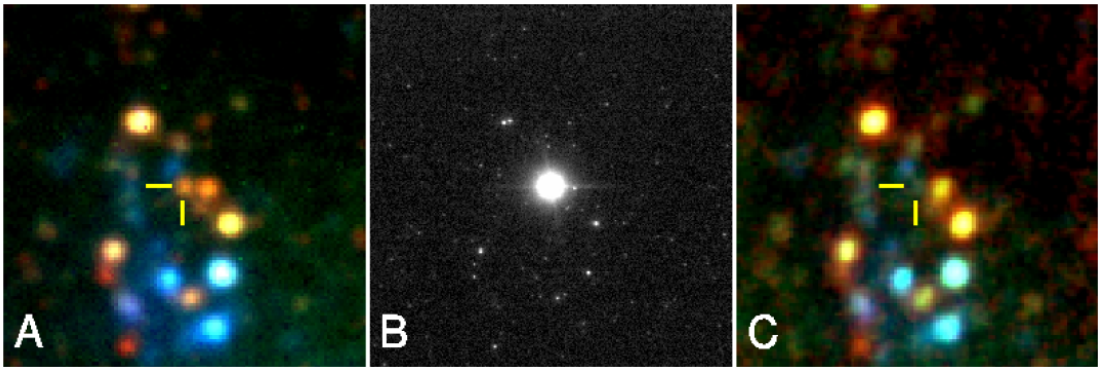

Figure 2.12: Direct observations of the disappearance of a star from Mattila et al. (2010). The panels show three phases of the explosion of the supernova; the first panel shows the supernova site before the explosion as observed by VLT, with the soon-to-explode star marked with the yellow arrows, a red supergiant progenitor star (A); the middle panel shows the resulting supernova, SN2008bk, which outshines all the stellar surroundings (B); the last panel shows the stellar field years later, after the supernova has faded (C), which clearly displays the disappearance of the progenitor star.

normal counterparts due to the need for more complex modelling (although there were already several attempts for them in the literature, see, for example, the works of Takáts & Vinkó 2012 or Blinnikov et al. 2012). Finally, 87A-like events are rare explosions of blue supergiant stars, which exhibit a very long rise, however, their scarcity limits their utility as distance indicators (Tartaglia et al., 2016).

The remaining class, SNe IIP/L (from here on, SNe II) are the explosions of red or yellow supergiant stars ($M > 8M_{\odot}$), which is confirmed through direct progenitor detections (Smartt 2009; Mattila et al. 2010; Van Dyk 2017, see Fig. 2.12) and indirect means (e.g. Tinyanont et al. 2022). These progenitors have extensive hydrogen envelopes, with radii of a few hundred to a thousand times that of the Sun (Levesque et al., 2005). During their lifetime, these stars develop massive iron cores through chains of fusion channels, which are supported by electron-degeneracy pressure during the life of the stars. However, as the mass of this core approaches the critical Chandrasekhar mass, the mounting density decreases the number of free electrons through the increasing rate of electron capture and photodissociation; essentially removing the support of the core itself. This results in positive feedback, or runaway process, which ultimately results in the explosion of the star: the star collapses onto a forming neutron star or black hole, releasing gravitational energy on the scale of 10^{53} ergs (Foglizzo et al., 2015). This energy is the order of magnitude higher than what is needed to unbind the material of the star (e.g. Ugliano et al. 2012). According to the current paradigms, the energy is then transported to the outer layers with the help of neutrinos to fuel the expansion (see the summary of Janka 2017).

The further distinction between the P (plateau) and L (linear) subclasses is observational, referring to the shapes of the light curves. Namely, the P subtype supernovae

exhibit a plateau on their light curve, while that of the L subclass can be described by a linear decline (e.g. Patat et al. 1994; Faran et al. 2014). Initially, these two subtypes were thought to be completely distinct but recent studies pointed out the continuous distribution of events covering the range between the P and L continuously both in terms of light curves (Anderson et al., 2014) and spectroscopy (Gutiérrez et al., 2014, 2017).

The light curve evolution of SNe II can be divided into multiple subsequent phases. Following the explosion, the material of the progenitor star begins to expand and fly apart, with the supernova ejecta doubling its size on less-than-day timescales. During this phase, the bolometric light curve reaches its peak rapidly in hours or a few days after the explosion as described by Shussman et al. (2016). For the optical bands, this rise is slower, 4 to 7 days post-explosion, due to the supernova spectral energy distribution (SED) being excessively blue in the beginning (González-Gaitán et al., 2015). At maximum, the absolute brightness of SNe II normally can reach -16 to -18 magnitudes (Anderson et al., 2014); however, low luminosity members of the population can have peak brightnesses as low as -14 magnitudes (Zampieri et al., 2003), while the brightest ones can reach even -19 magnitudes (Pessi et al., 2023). The rapid rise of the supernova is normally followed by a short decline in the luminosity (at a rate of 3 mag/100 days in the V band) before the supernova settles to a plateau (Anderson et al., 2014). In the plateau phase, the hydrogen recombination commences in the ejecta as described, for example, in Dessart et al. (2013). During this phase, the photosphere begins closely tracking the recombination front.[10] As a result, the light curves and spectra of these supernovae evolve barely until the recombination front reaches the helium-rich layer. This leads to a drop in the light curve, after which the supernova settles onto the cobalt-decay tail (Fig. 2.13). The main difference between the P and L subclasses is during the plateau phase; in this phase, the P supernovae exhibit little-to-no drop in brightness, while the other subclass shows a steadily declining light curve. Anderson et al. (2014) showed that the distinction between the two classes is not clear, as the distribution of light curve shapes is rather continuous. The cause of this variation is still debated, with possible explanations ranging from increased CSM interaction (Gutiérrez et al., 2014) to lower-mass hydrogen envelopes for the IIL class (Nomoto et al., 1995).

Figure 2.14 shows the spectral evolution of a SN IIP, SN 2017eaw. As the figure shows, the spectra can be characterized as hot black-bodies, with broad features of various lines, among of which those of hydrogen are the most prominent. In a broad sense, the observed continuum of the supernova probes the optically thick regions, as it is formed by the deeper layers of the atmosphere, while the superimposed line features are created in the optically thinner outer layers above the photosphere (Sim, 2017; Vogl, 2020). Owing to the expansion of the ejecta, these lines will take the form of thousands of km/s wide P-Cygni features, which always consist of a blue-shifted absorption and a redshifted emission component. The unique shape of these line features is always related to the presence of outflows. The absorption component characteristic to this

[10] Owing to the fact that the opacity changes sharply due to the drop in the ionization. Before this phase, the photosphere position was mainly set by the change in the temperature. However, once the plateau phase, and hence the recombination temperature is reached, the effect of ionization change will take over.

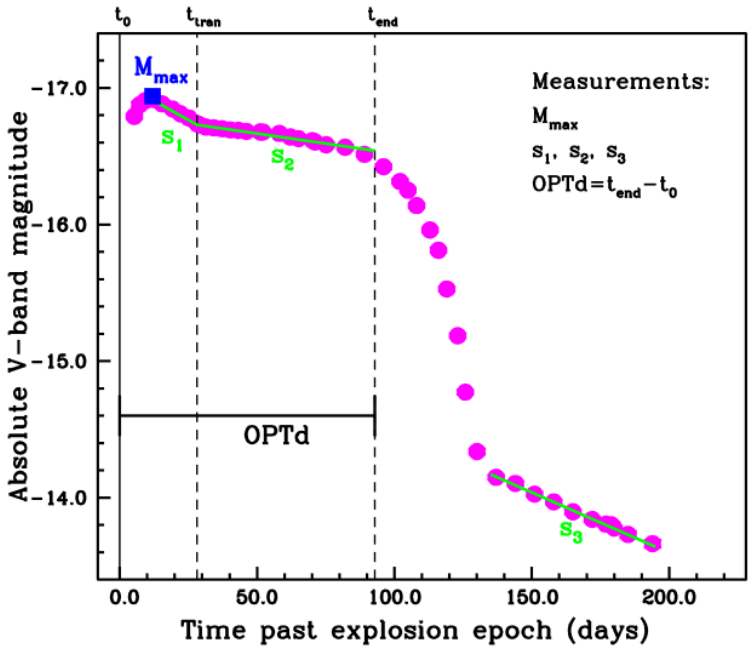

Figure 2.13: Light curve of SN IIP/L as plotted by Anderson et al. (2014). The different *s* parameters correspond to the three phases described in the main text of the post-peak evolution: the short decline, the plateau phase, and the cobalt-decay tail.

feature is caused by material situated between the observer and the photosphere. In this region, photons emitted from the photosphere can be scattered out of the line-of-sight, resulting in a deficit of photons compared to the continuum. Since the material is moving towards the observer, this depletion appears blue-shifted compared to the rest wavelength of the line. The evolution of these features is driven mostly by the changes in the excitation and ionization of the spectral forming region (Dessart & Hillier, 2011; Dessart et al., 2013), which are set by the temperature evolution rather than changes in the chemical composition. The chemical abundances of the outer hydrogen envelope of the supernova are determined by the red giant progenitor star itself, and the different elements are present homogeneously due to the convective mixing in the envelope (Davis et al., 2019).

Vogl (2020) gives an overview of the evolution of SNe II spectra: during the first days of the evolution, the spectra can be characterized as a hot (> 15000 K) black-body with wide line features (~ 10000 km/s) of hydrogen and helium superimposed. At this phase, the density distribution of the ejecta is very steep (see, for example, the modelling of SN 2006bp by Dessart et al. 2008), which represents a rapid drop in density above the photosphere that strongly suppresses line formation. As the supernova evolves, it cools, and the density profile flattens as the photosphere recedes deeper into the hydrogen envelope. In parallel, the various lines corresponding to other elements emerge from the continuum, along with the other, in particular the Balmer lines, strengthening

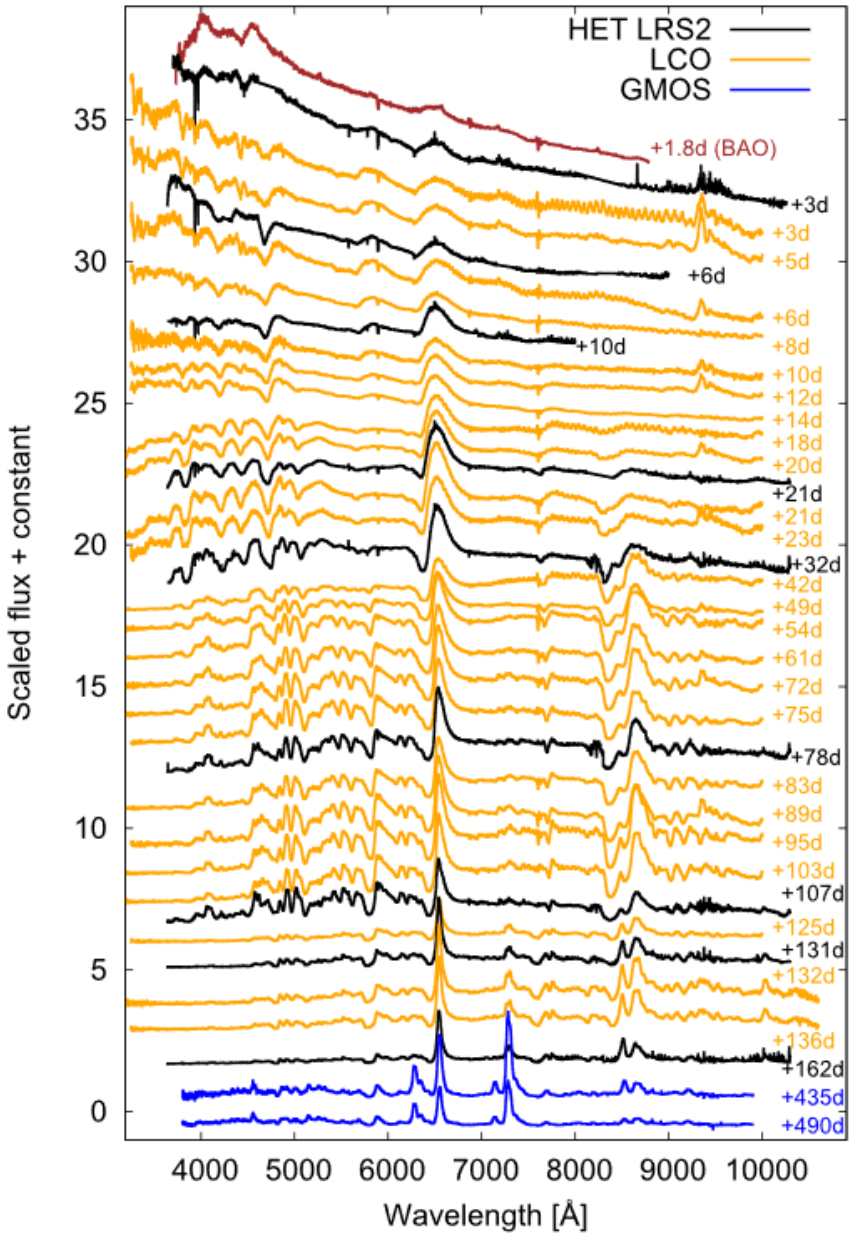

Figure 2.14: Spectral evolution of an SN IIP, SN 2017eaw from Szalai et al. (2019). The observations cover the evolution of the supernova through its photospheric phase until the nebular phase, and they show the emergence and disappearance of various line features. The different colours correspond to observations taken with various instruments.

significantly. In the following days, more and more lines of low-ionization species emerge, causing a gradual line blanketing at lower wavelengths and creating the Ca II triplet at redder wavelengths (~ 8500 Å). One month after the explosion the rapid cooling of the photosphere ceased, and the temperature settled onto the recombination temperature of hydrogen. As mentioned earlier, the spectral evolution slows down significantly at this point, with only the already existing emission lines strengthening until the end of the plateau phase. It is worth mentioning that while the overall picture is the same, the exact timespan of the changes depends a lot on the progenitor, with its mass likely being one of the key parameters (Martinez et al., 2022). This effect is also demonstrated well by the low-luminosity objects, which reach the plateau phase much faster than other SNe II (Pastorello et al., 2004; Spiro et al., 2014).

Using SNe II for distance measurements is not a newly founded technique, as the principles of the method were laid down decades ago by Kirshner & Kwan (1974). The so-called Expanding Photosphere Method is a technique that attempts to follow the gradual expansion of the supernova, measuring its photospheric temperatures and velocities, which can constrain the flux and physical size of the emitting region, ultimately constraining the luminosity. This method is a reformulation of the Baade-Wesselink technique that uses radial velocity measurements of pulsating stars to measure their luminosities (Baade, 1926; Wesselink, 1946b). This method has already been used to estimate distances in the past, yielding varying degrees of success (Schmidt et al., 1992; Dessart & Hillier, 2005; Jones et al., 2009).

The basic principle of this technique is to assume that the source of the black-body-like emission is a spherically symmetric, sharply defined photosphere, which is fairly justified for SNe II. The main requirement of the method is the ability to determine the $f_\lambda^{\rm ph}$ emitted flux at the photosphere; a problem for which the solution may be fitting black-body model SEDs to the photometric colours (Kirshner & Kwan, 1974), or performing proper radiative transfer modelling for each spectrum (Dessart et al., 2008). However, as described in Eastman et al. (1996), this black-body radiation is diluted due to electron scattering. Owing to this, to describe the supernova spectra using B_λ^T black-body models, one has to include the so-called dilution factors ξ, as first proposed by Hershkowitz et al. (1986). These, however, have to be estimated based on radiative transfer models first. In one setting of EPM, one may infer the physical flux emerging from the supernova using these tabulated values, with the dilution factor being picked based on the approximated temperature (by fitting a black body to the observations, for example). Alternatively, one may estimate the flux and other physical parameters through radiative transfer modelling straightaway, which sets the basis for the tailored EPM method (with the radiative transfer models "tailoring" the distance estimation). However, running the required radiative transfer models increases the time necessary to infer the physical parameters due to model complexity, with multiple orders of magnitude (Dessart & Hillier, 2006). Whichever path one may take, having an accurate way of estimating the physical flux allows for the estimation of the distance D through the observed angular diameter Θ according to

$$\Theta = \frac{R_{\rm ph}}{D} = \sqrt{\frac{f_\lambda^{\rm obs,\ dered}}{f_\lambda^{\rm ph}}} \tag{2.5}$$

where $R_{\rm ph}$ denotes the radius of the photosphere and $f_\lambda^{\rm obs,\ dered}$ the observed and dereddened flux. Here $f_\lambda^{\rm ph}$ may be a model that is based on a black-body (ξB_λ^T) or a radiative transfer simulation. Assuming that the supernova expands homologously, the radius can be determined by measuring the photospheric expansion velocity $v_{\rm ph}$ and the age $(t - t_0)$ of the supernova with t_0 denoting the epoch of explosion (Eastman et al., 1996):

$$R_{\rm ph} = v_{\rm ph}(t - t_0) \tag{2.6}$$

The photospheric velocity of the supernova can be determined based on the P Cygni line features, either by measuring their blueshift velocities (e.g. Hamuy 2001) or by performing the full radiative transfer modelling of the spectra (Dessart & Hillier, 2006; Dessart et al., 2008). Given this parameter, one may estimate the distance by reorganizing the above equations:

$$D = \frac{v_{\rm ph}(t - t_0)}{\Theta}. \tag{2.7}$$

The advantage of EPM is also its own bottleneck. Although the method is based on theory and does not require external calibrations from other methods, the accurate estimation of physical parameters is computationally intensive. To achieve the desired precision, it is necessary to perform the EPM measurements on radiative transfer models to estimate physical parameters self-consistently, as opposed to modelling the spectra with blackbodies, then measuring line velocities (Dessart & Hillier, 2005). In the latter, the choice of dilution factors has for long been a source of biases in the distances as shown by Jones et al. (2009) (Fig. 2.15). Moreover, without radiative transfer modelling, it is also difficult to estimate the correct photospheric velocity based on the P Cygni profiles; as shown by Dessart & Hillier (2005) as well, the absorption velocity depends significantly on the line optical depth, hence, different lines track the photospheric velocity differently. These two factors significantly limited the accuracy of EPM distances in the past.

Even though EPM has been used for decades, the effects that may cause biases in the method have not been investigated meticulously yet. One systematic that may arise for the SNe II-based method is the non-sphericity of the supernova photoshere, which is a basic assumption of EPM. This can be probed through polarimetric observations, which are useful tools for tracking the asymmetries of supernovae (Shapiro & Sutherland, 1982). In the electron scattering process, the emission from the supernova becomes linearly polarized perpendicularly to its post-scattering angle. Given a fully spherical emitting surface, the polarization of photons scattering from different parts of the atmosphere cancel each other in an integrated observation; hence, when one may track asphericities by detecting the residual part of this linearly polarized emission (Wang & Wheeler, 2008; Bose et al., 2016). Multiple studies showed that this residual polarization

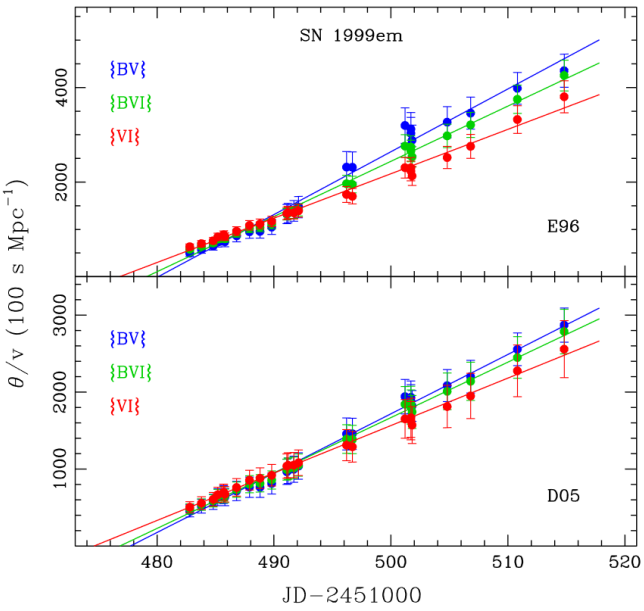

Figure 2.15: EPM analysis of SN 1999em from Jones et al. (2009). The top panel shows the EPM obtained with the dilution factors of Eastman et al. (1996), while the bottom panel shows the same for the factors of Dessart & Hillier (2005). As shown, the choice of which photometric band fluxes are taken into account as a reference (different coloured curves) and which dilution factors are assumed significantly affect the obtained fits.

is very small, typically $\sim 0.1\%$ in the early photospheric phase (Bose et al., 2016; Nagao et al., 2023, 2024), which later in the plateau phase can potentially climb to 1% in rare cases. Nevertheless, even a 1% fraction of linear polarization only corresponds to $\sim 20\%$ asphericities (Leonard et al., 2001), thus SNe II can be considered spherical for distance estimation.

The list of additional systematics is currently far from being complete. Given the complexity of the method, multiple steps may warrant deeper investigations with a focus on systematic effects; on the observational side, it is crucial to assess the uncertainties that may arise due to incorrectly estimated time of explosion or wrongly calibrated spectra. From a modelling perspective, time-dependent ionization and excitation effects may cause biases for the distance estimation: as time progresses, these time-dependent terms become more and more significant (Dessart et al., 2008; Dessart & Hillier, 2011). Most modelling applications neglect these terms given the otherwise computationally intensive solutions, hence, their precision decreases for later epochs. Additionally, biases can also arise based on the input parameters, such as the chosen density profiles, which can be simple power laws (Eastman et al., 1996) ranging to models that are motivated by stellar evolution (Utrobin, 2007; Utrobin & Chugai, 2009). Finally, the presence of CSM interaction introduces a difficulty for the modelling, as it can significantly increase the luminosity of the supernova by reprocessing a fraction of the kinetic energy of the

ejecta into radiation as it rams into the circumstellar medium (Dessart & Hillier, 2022), while also modifying line profiles (Gutiérrez et al., 2017). The existence of potential limiting factors warrants more in-depth investigations into SNe II.

2.5 Intercomparability and the need for further studies

Owing to the inconsistency between the various distance measures, mainly between TRGB and Cepheids (Freedman, 2021; Riess et al., 2022), the direct cross-checks between the different techniques are becoming increasingly essential. Such cross-checks can assess whether the calibrations of the various estimators yield consistent results and, hence, solidify the near-Universe results in the context of the Hubble tension.

Recently, multiple endeavours have been performed towards this end, cross-comparing multiple methods in the same host galaxy: both Breuval et al. (2023b) and Lee et al. (2022) estimated the distance of M33 based on Cepheids, TRGB and JAGB. These works together showed that one may not have to make it all the way to the Hubble constant to find hints of inconsistencies between the different distance estimation techniques: as shown in Fig. 2.16 from Breuval et al. (2023b), the very recent Cepheid distance estimates are not consistent with each other within $1-2\sigma$ uncertainties; and even this does not necessarily point towards tensions, such inconsistencies raise the suspicion towards potential biases still present in at least one of the methods, calling for additional studies. On the other hand, similar comparisons were done recently in multiple galaxies between TRGB and Cepheids, as summarized by Anand et al. (2024), showing overall agreement but also highlighting potential offsets on the scale of ~ 0.1 magnitudes. This warrants further investigations, which are being carried out through *HST* and *JWST* observations. For the complete set of details, see the proposals of Freedman et al. (2021), Jang (2023) and Breuval et al. (2023a).

For SNe II, such comparative studies are more limited; for example, Leonard et al. (2003) estimated and compared the Cepheid distance of the host directly to the EPM distance of 1999em, while Szalai et al. (2019) applied the EPM to 2017eaw then compared the distance to the TRGB and secondary distance measures of the host. However, it is important to point out that these measurements are based on the classical EPM approach, employing dilution factors, which are known to be a source of limitation. Comparisons with radiative transfer-based supernova distances were only carried out for a few objects up until now, namely SN 1999em and SN 2005cs by Baron et al. (2004); Dessart & Hillier (2006); Dessart et al. (2008); Vogl et al. (2020). For supernovae, studies are focusing more on internal consistency studies, namely investigating whether any differences in the observing conditions or physical parameters of the supernova drive offsets in the estimations, such as presented in Vinkó et al. (2012), Szalai et al. (2019), Scolnic et al. (2020), Graham et al. (2022), Barna et al. (2023) or Ward et al. (2023), which studies can be used for empirically identifying systematics. Some studies, such as Barna et al. (2023), showed well that even for SNe Ia, different analysis variants used on the same objects yield varying levels of agreement between the supernovae. Given there

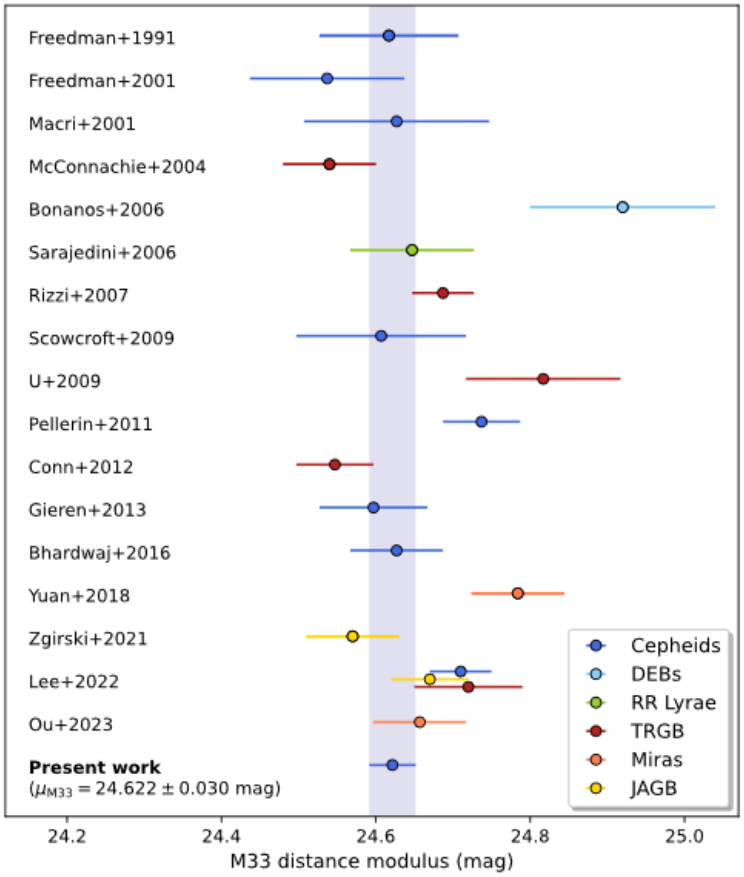

Figure 2.16: Comparison of the distance estimates for M 33 compiled by Breuval et al. (2023b). There is a significant scatter among the distances estimated through different means which was decreased over time, but it is still significant compared to the claimed precisions. The explanations might be hidden sources of uncertainties and underestimated errorbars, or systematic errors due to different choices in the various analyses.

are multiple methods used for distance estimation by the community, performing such internal comparative studies is crucial.

In the above sections, we highlighted the different ways to estimate distances in the near-Universe, along with the possible systematics that have been investigated already. The current scatter in the Hubble constant estimates calls for further comparative studies between the different methods and additional investigations of possible biases. In this thesis, our goal is to contribute to the question of the Hubble tension and the apparent discrepancy between near-Universe estimators by uncovering a limitation for Cepheids and by establishing the use of SNe II in precision distances estimations through two empirical tests.

Part II

Sibling supernovae

Summary

Recent advancements in modelling Type II supernovae showed they are promising distance estimators and can provide an independent path to the Hubble constant. Before one such estimation, however, one has to make sure the inferred uncertainties are realistic and correct. A unique way to perform such a test for SNe II is through sibling supernovae or SNe II pairs, that exploded in the same galaxy. These objects offer excellent potential for assessing the internal consistency of the modelling, owing to a significant a priori knowledge: regardless of how the individual supernovae evolve, or how they are observed, their modelling should yield the same distance in the end.

To test this, we gathered the data of four supernova pairs in the literature, which exploded in M 61 (SN 2008in and SN 2020jfo), NGC 772 (SN 2003hl and SN 2003iq), NGC 922 (SN 2002gw and SN 2008ho) and NGC 6946 (SN 2004et and SN 2017eaw). The results of this research were published in Csörnyei et al., A&A, Vol. 672, A129, 2023, and are reproduced below under the terms of the Creative Commons BY 4.0 license. We applied the methodology of Vogl et al. (2020) to estimate the physical parameter evolution and the distance to each supernova similarly to the work of Dessart et al. (2008) in a Bayesian analysis. To investigate the consistency for each pair, we applied the Bayes factor technique similar to Wang et al. (2016), which showed remarkable agreement for the pairs. Moreover, we were also able to provide a precise distance estimate for each host galaxy down to a few per cent uncertainty. This proves the internal consistency of the distance estimation method, emphasizing the potential of SNe II distance measurements.

In a future follow-up study, it will be possible to assess how the individual systematic effects (such as host metallicity, explosion energy, CSM interaction and reddening) can degrade the internal consistency of the method without the need to compare SNe II to external methods. This makes sibling supernovae a particularly advantageous testing ground for adH0cc and other SN II cosmological studies.

Own contributions I acted as the main driver of the project, taking a significant part in all aspects tied to carrying out the research and publishing it in a journal. I compiled the list of sibling supernovae and curated and recalibrated the data. I carried out the modelling, distance estimations and Bayes-factor-based statistical test following the procedure outlined in the main text. I am the main author of the manuscript, wrote most of its text and I created all the plots and figures. The research was fully performed during my PhD.

Consistency of Type II supernova distances

G. Csörnyei, R. I. Anderson, C. Vogl, S. Taubenberger, S. Blondin, B. Leibundgut, W. Hillebrandt

Abstract

Context: Type II supernovae offer a direct way of estimating distances via the expanding photosphere method, which is independent of the cosmic distance ladder. A Gaussian process-based method was recently introduced, allowing for a fast and precise modelling of spectral time series and placing accurate and computationally cheap Type II-based absolute distance determinations within reach.

Aims: The goal of this work is to assess the internal consistency of this new modelling technique coupled with the distance estimation in an empirical way, using the spectral time series of supernova siblings, that is, supernovae that exploded in the same host galaxy.

Methods: We used a recently developed spectral emulator code, trained on TARDIS radiative transfer models that is capable of a fast maximum-likelihood parameter estimation and spectral fitting. After calculating the relevant physical parameters of supernovae, we applied the expanding photosphere method to estimate their distances. Finally, we tested the consistency of the obtained values by applying the formalism of Bayes factors.

Results: The distances to four different host galaxies were estimated based on two supernovae in each. The distance estimates are not only consistent within the errors for each of the supernova sibling pairs, but in the case of two hosts, they are precise to better than 5%. The analysis also showed that the main limiting factor of this estimation is the number and quality of spectra available for the individual objects, rather than the physical differences of the siblings.

Conclusions: Even though the literature data we used was not tailored to the requirements of our analysis, the agreement of the final estimates shows that the method is robust and is capable of inferring both precise and consistent distances. By using high-quality spectral time series, this method can provide precise distance estimates independent of the distance ladder, which are of high value for cosmology.

3 Introduction

Sibling supernovae are transients that exploded in the same host galaxy. As they are located at essentially the same distance from us, they allow us to test distance estimation methods and investigate their systematics empirically. Such consistency checks were recently carried out in the literature for pairs of Type Ia supernovae (see e.g. Burns et al. 2020; Scolnic et al. 2020) as well as for a pair of a Type Ia and a Type IIP supernova (Graham et al., 2022), yielding good matches. However, no similar tests have yet been conducted on Type II supernovae specifically.

In the past, Type II supernova siblings have been analysed with different goals. For example, Poznanski et al. (2009) used such siblings to check the colour term in their standardizable candle model under the assumption that they share the same distance. More recently, Vinkó et al. (2012) and Szalai et al. (2019) used a Type IIP-IIb and a IIP-IIP pair respectively to constrain the distances to their hosts better than with a single transient. In contrast, here we perform the first dedicated distance consistency check for Type IIP supernova siblings.

Type II supernovae (SNe II) correspond to the final gravitational collapse of massive ($\geq 8M_{\odot}$), red or blue supergiant stars, which is supported by pre-explosion images (Smartt, 2009) and theoretical models (Tinyanont et al., 2022). These supernovae are historically subdivided into two main classes, Type IIP (plateau) and Type IIL (linear), based on their light curves (e.g. Patat et al. 1994). However, there are several indications that these objects can be rather explained as a continuous distribution, as opposed to distinct classes (Anderson et al., 2014; Sanders et al., 2015; Galbany et al., 2016; Morozova et al., 2017; Pessi et al., 2019).

Due to their high intrinsic luminosity and the fact that these supernovae are the most frequent stellar explosions in the Universe (Li et al., 2011), Type II SNe make for excellent distance indicators. To date, mainly two methods have been used to estimate the distances to Type II SNe: the expanding photosphere method (EPM, Kirshner & Kwan 1974), which is a geometric technique relating the photospheric radius of the SN to its angular size, and the standardised candle method (SCM, Hamuy & Pinto 2002), which is based on an empirical relation between the photospheric expansion velocity and the plateau luminosity of the supernovae. However, only the EPM provides a distance estimation that does not require any external calibration, as opposed to the SCM and other distance ladder formalism methods. It is independent of any other distance measurements and hence of the cosmic distance ladder. Owing to these advantages, it has already been applied to various sets of SNe to derive the Hubble constant (see e.g. Schmidt et al. 1992). The classical EPM analysis is, however, prone to several uncertainties as, for example, shown by Jones et al. (2009): the results can be subject to systematic differences depending on which atmospheric model – and thus, which di-

lution factors are assumed (e.g. Eastman et al. 1996 or Dessart & Hillier 2005) – or which photometric passband set is used for the photometry. To avoid such issues, as pointed out by Dessart & Hillier (2005), it is necessary to carry out the EPM based on the radiative transfer-based modelling of the spectra and estimate the input parameters through these models. We call this augmented version the tailored-EPM analysis, which bears more similarities to the Spectral-fitting Expanding Atmosphere Method (SEAM) introduced by Baron et al. (2004). This step not only allows for a more precise estimation of physical parameters but also avoids the detour of choosing the dilution factors for the EPM.

Although the number of available spectroscopic observations has grown significantly over the past years, the spectral modelling remains a time-consuming and laborious process. To change this situation, Vogl et al. (2020) developed an emulator based on spectra calculated with the TARDIS radiative transfer code (Kerzendorf & Sim, 2014), which allows for a maximum likelihood parameter estimation and modelling of the spectral time series several orders of magnitude faster than the conventional methods. To showcase the code, Vogl et al. (2020) performed the tailored-EPM analysis for SNe 1999em and 2005cs, showing that a few per cent precision in the derived distance can be achieved.

Here, we attempt to further test the method and investigate its internal consistency empirically by applying it to sibling supernovae. In their case, the maximum possible separation between the siblings is set by the line-of-sight extension of the thick disk of their host galaxies. For face-on galaxies (such as all the hosts in our sample), this is at most about 10 kpc (Gilmore & Reid, 1983). At a distance of $\sim$6 Mpc, for the closest host galaxy in our sample, this corresponds only to a maximum relative error of 0.2%. Hence, the EPM should yield the same distance for the sibling pairs within the uncertainties. As a result, siblings provide a simple empirical way to assess the consistency and robustness of the algorithm: they allow us to test whether we find the same distances for the pairs even though the underlying conditions vary (such as the metallicity, the mass of the progenitor, the amount of ejecta-CSM interaction, the reddening, etc.), as well as the overall data quality and the level of calibration. Such distance comparisons also allow us to assess whether the inferred uncertainties are reasonable.

The paper is structured as follows. In Sect. 4, we give a brief overview of the data collected for this study. Sect. 5 describes the calibration steps we applied to the data to achieve a similar level of calibration for all objects, then provides the background of the emulator-based modelling and gives an outline of the distance estimation. Sect. 6 shows the results of the modelling for the individual host galaxies, while Sect. 7 discusses these results and details the consistency check of the method. In Sect. 8 we present our summary and conclusions.

4 Data

To obtain a set of objects compatible with the goals of this study, we filtered the catalogue of known supernovae through the Open Supernova Catalog[1] (OSC, Guillochon et al. 2017). In addition to looking for supernovae that exploded in the same host, we set further constraints on the individual objects to make sure that our method could be applied to them: the objects should have at least one observation in their early photospheric phase (more precisely, in the epoch range of 10 to 35 days with respect to the time of explosion; see Sect. 5.2) to be compatible with our radiative-transfer modelling, a well-covered light curve during these epochs (optimally, in multiple bands for calibration purposes; see Sect. 5.1), and a well-constrained time of explosion from either non-detections or from fitting of the rise of the light curve.

By filtering the catalogue, we found that SN IIP pairs in four host galaxies met all the conditions that we described above: NGC 772, NGC 922, NGC 4303 (M 61), and NGC 6946 (Fig. 4.1). To retrieve the data for the supernovae in these hosts, we made use of the OSC and WISeREP[2] (Yaron & Gal-Yam, 2012). The properties of the final dataset are summarised in Table 4.1.

Host	z_{helio}	$E(B-V)_{\mathrm{MW}}$	SN	N_{spec}	N_{phot} (bands)	References
M61	0.00522	0.0193	2008in	6	22 (BVRI)	Nakano et al. (2008); de Jaeger et al. (2019)
			2020jfo	7	21 (*gri*)	Schulze et al. (2020); Sollerman et al. (2021)
NGC 772	0.00825	0.0623	2003hl	1	36 (BVRI)	Moore et al. (2003); Faran et al. (2014)
			2003iq	4	44 (BVRI)	Llapasset et al. (2003); Faran et al. (2014)
NGC 922	0.01028	0.0163	2002gw	3	34 (BVI)	Monard (2002); Galbany et al. (2016)
			2008ho	2	11 (BV)	Pignata et al. (2008); Anderson et al. 2023
NGC 6946	0.00013	0.2967	2004et	6	40 (BVRI)	Zwitter et al. (2004); Faran et al. (2014)
			2017eaw	8	96 (BVRI)	Wiggins (2017); Szalai et al. (2019)

Table 4.1: Summary table of the compiled SN sample, along with important properties of the host, namely, its heliocentric redshift (as adopted from the OSC) and reddening caused by the dust in the Milky Way (Schlafly & Finkbeiner, 2011). References are provided for the discovery and photometry of the objects; for details on the spectroscopy, see Sect. 6.

[1] https://sne.space/
[2] https://www.wiserep.org/
[3] https://www.sdss3.org/index.php
[4] https://archive.eso.org/dss/dss
[5] https://outerspace.stsci.edu/display/PANSTARRS/

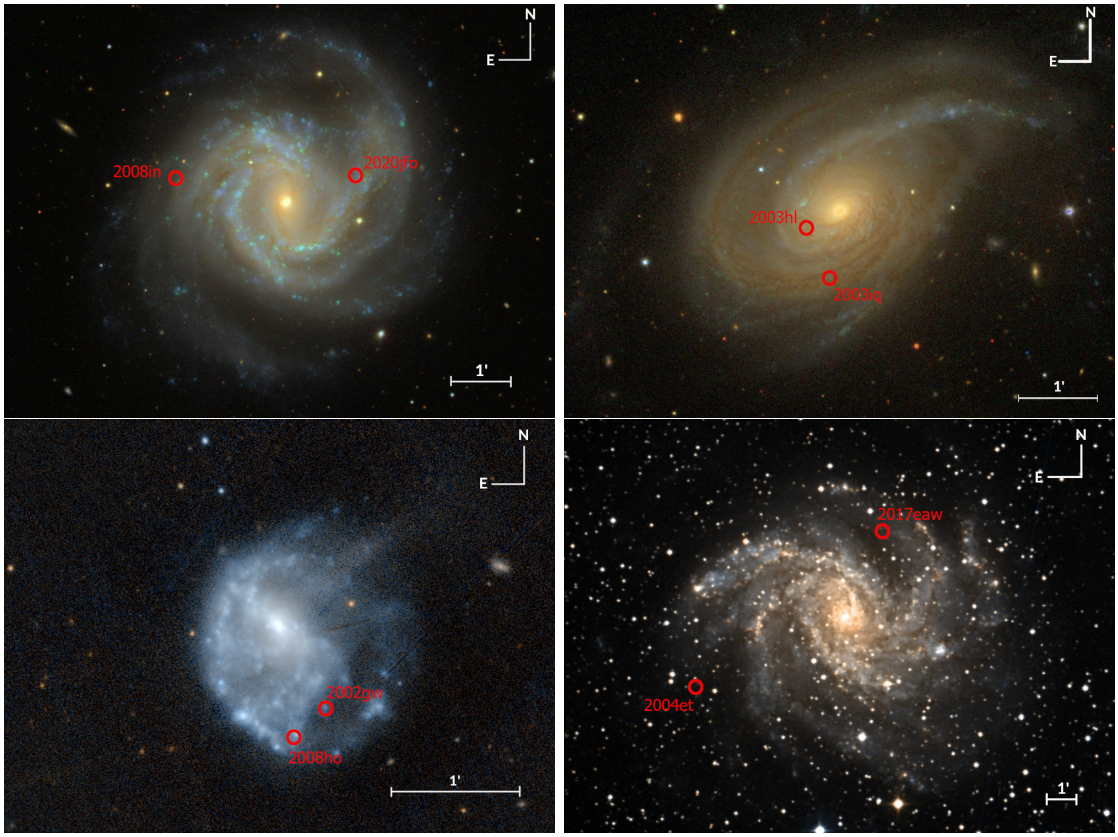

Figure 4.1: Images of the sample host galaxies. **Top left:** SDSS DR9[3]image of M61, along with the positions of SN 2008in and 2020jfo. **Top right:** SDSS DR9 image of NGC 772, along with the positions of 2003iq and 2003hl. **Bottom left:** PanSTARRS DR1[4]image of NGC 922, along with the positions of 2002gw and 2008ho. **Bottom right:** DSS[5]image of NGC 6946, along with the positions of 2004et and 2017eaw.

5 Methods

5.1 EPM and spectral modelling inputs

Before we could fit the spectral time series and perform the EPM analysis, we needed to obtain the necessary input data: an estimate of the time of explosion, t_0, photometry interpolated to the spectral epochs, and flux-calibrated spectra. We describe how we inferred t_0 from a parametric fit in Sect. 5.1.1. Section 5.1.2 explains the Gaussian process (GP) interpolation of the light curves, and Sect. 5.1.3 details how we used the interpolated magnitudes to recalibrate the spectra.

5.1.1 Time of explosion

The time of explosion is a crucial parameter in the EPM. It sets the size of the photosphere and, thus, the model luminosity. Any error in t_0 causes an error in the distance. In cases where the distance to a supernova is estimated using a single epoch, the uncertainty in the time of the explosion, t_0, translates directly into the distance uncertainty:

$$\frac{\Delta D}{D} \approx \sqrt{\left(\frac{\Delta t_0}{t - t_0}\right)^2 + \left(\frac{\Delta(\Theta/v)}{\Theta/v}\right)^2}, \tag{5.1}$$

based on linear relative error propagation, in accordance with the equations shown in Sect. 5.3. The parameters with the Δ denote the uncertainty of the given values. Assuming a 10% error on the Θ/v measurement for a single spectrum at the epoch of 20 days, a t_0 uncertainty of ± 2 days would yield $\sim 14\%$ error on the final distance, which is too large for our purposes.

Analyzing multiple spectral epochs helps in limiting the final uncertainties of the fit parameters, partially owing to the additional constraining effect exerted on t_0 by the EPM regression. For example, having four high-quality observations in the epoch range of 10 to 25 days, along with the above t_0 uncertainty of 2 days, would yield an EPM distance error of about $\sim 11\%$. While the improvement in precision is significant compared to the above case, bringing it to the required levels would require a factor of a few more spectral epochs, which is rarely available. This demonstrates that even with a sufficiently large number of observations, it is crucial to obtain a well-constrained prior estimate on t_0 for the distance determination.

We can use the constraints on t_0 from the early light curve to significantly reduce these uncertainties. Also, if the time of explosion is known to a high level of precision (to an uncertainty of less than a day ideally) and independently of the EPM analysis, even a single spectral epoch is enough to obtain a meaningful distance. Observationally, the

common approach for estimating the time of explosion has been to take the midpoint between the first detection and last non-detection (e.g. Gutiérrez et al. 2017). This is not accurate enough for our analysis. The method does not take into account the depth of the non-detections in comparison to the first detection; this can bias the estimated time of explosion and, thus, the distance. Also, the approach neglects the information from data on the rise of the light curve.

To minimise these possible biases and improve the precision, we estimated the time of explosion for each SN through the fitting of their early light curves (the initial plateau, i.e. the first $10-40$ days, depending on the individual SNe). Following Ofek et al. (2014) and Rubin et al. (2016), we fit the flux f in band W with the following:

$$f_W(t) = f_{m,W}\left[1 - \exp\left(-\frac{t - t_0}{t_{e,W}}\right)\right], \tag{5.2}$$

where t is the time, t_0 is the time of explosion, $f_{m,w}$ is the peak flux, and $t_{e,W}$ is the characteristic rise time in the particular band. Whenever the data allowed, we carried out this fitting for multiple photometric bands simultaneously to increase the accuracy of the method. In this joint fit, each of the different bands had its own $f_{m,W}$ and $t_{e,W}$ values, but the fits were connected through the global t_0 value, which was the same for all bands. To improve the fitting, we introduced two additional constraints: (i) we took the depth of the non-detections into account by placing a constraint stating that the model flux should not exceed the limiting flux (but the light curves were allowed to extend to times before the non-detection), and (ii) we required that the characteristic time scale, t_e, for the light curve rise increases with wavelength for a given supernova, as it was found previously (see, e.g. González-Gaitán et al., 2015). In this way, even the t_e values, which otherwise correspond to their own band, were constrained globally in the joint fit.

To fit the model to the set of light curves in different bands simultaneously, we applied the `UltraNest`[1] package (Buchner, 2021), which allows for Bayesian inference on complex, arbitrarily defined likelihoods and derives the necessary posterior probability distributions based on the nested sampling Monte Carlo algorithm MLFriends (Buchner, 2016, 2019). We assumed a flat prior for each of the input parameters and used a Gaussian likelihood for the parameter inference. To account for a possible underestimation of the photometric errors, which can influence the inferred parameters, we extended the likelihood with an additional term corresponding to the error inflation as described in Hogg et al. (2010). Using this procedure, we obtained a t_0 posterior distribution for each supernova. We then used the maximum of this distribution as our single "best estimate" value for t_0 to set the phase of the spectral observations for the fitting. The full distribution is used as a prior for the EPM analysis, as described in Sect. 5.3. This unique approach for obtaining t_0 in parallel to the EPM significantly enhances the precision of the distance measurements, as will be shown in Sect. 6.

[1] `https://johannesbuchner.github.io/UltraNest/`

5.1.2 Interpolated photometry

The epochs of spectral observations are not necessarily covered by individual photometric datapoints. To obtain photometry at all phases, we fit the light curves using GPs by applying the `george`[2] python package (Ambikasaran et al., 2015). In brief, GPs present a useful way to interpolate the light curves by providing a non-parametric way of fitting, while taking into account the uncertainties of the datapoints. Following several works that already used GPs for the modelling of supernova light curves (Inserra et al., 2018; Yao et al., 2020; Kangas et al., 2022), we adopted covariance functions from the Matérn family for our calculations (Rasmussen & Williams, 2006). We chose a smoothness parameter of 3/2 for our analysis. We attempted to keep the length scale of the best-fit GP curve high enough to retain its robustness against the scatter present in the datapoints. To achieve this, we omitted the rise of the light curve and the drop from the plateau from the fits. Figure A.4 shows the interpolated light curves and Table A.2 lists the magnitudes at the spectral epochs. The interpolated magnitudes are direct inputs for the EPM, as described in Sect. 5.3.

5.1.3 Flux-calibrated spectra

A reliable flux calibration is crucial for the spectral modelling and the determination of the host extinction. We therefore applied a linear flux correction to avoid possible biases in the analysis. This correction was based on the photometry: for every epoch, we calculated a set of synthetic magnitudes using the transmission curves from Bessell & Murphy (2012) (for $BVRI$ magnitudes) or Dekany et al. (2020) (in case of ZTF photometry), and we then compared these values to the corresponding interpolated magnitudes. The correction curve was then calculated by fitting the linear trend present in the ratios of synthetic and interpolated fluxes against the effective wavelengths of the passbands. Finally, the spectra were multiplied with the obtained correction trends. In some cases, additional more complex flux calibration steps were required and these are described separately for each individual supernovae.

5.2 Spectral modelling

To fit the individual spectra, we applied the methodology introduced by Vogl et al. (2020). The fitting method is based on a spectral emulator that predicts synthetic spectra for a set of supernova parameters. The training set of synthetic spectra was calculated with a modified version of the Monte Carlo radiative transfer code TARDIS (Kerzendorf & Sim, 2014; Vogl et al., 2019), which is described in detail in Vogl et al. (2020). To allow for a fast and reliable interpolation of model spectra for a given set of physical parameters, along with correct absolute magnitudes, an emulator was built on this training set with the following procedure. First, the dimensionality of the spectra was greatly reduced by the use of principal component analysis (PCA) then GPs were trained on the physical input parameters (photospheric temperature and velocity, $T_{\rm ph}$ and $v_{\rm ph}$, metallicity Z,

[2] https://george.readthedocs.io/en/latest/

	$v_{\rm ph}$ [km s^{-1}]	$T_{\rm ph}$ [K]	Z [$Z_\odot$]	$t_{\rm exp}$ [days]	n	NLTE	
			$t_{\rm exp}$ < 16 days			**H**	**He**
Min	4500	7200	0.1	6.0	9	✓	✓
Max	12000	16000	3.0	16.0	26		
			$t_{\rm exp}$ > 16 days			**H**	**He**
Min	3600	5800	0.1	6.5	6	✓	✗
Max	10700	10000	3.0	40.0	16		

Table 5.1: Parameter range covered by the extended spectral emulator. Depending on the spectral epoch, one of these two simulation sets was chosen for building the emulator.

time since explosion $t_{\rm exp}$, and the exponent of the density profile $n = -{\rm d}\ln\rho/{\rm d}\ln r$) to interpolate spectra and to predict absolute magnitudes. As described in Vogl et al. (2020), the emulator predicts spectra that in almost all cases match the simulations with a precision of better than 99%, as measured by the mean fractional error. The original version of the emulator covered the early photospheric phase, from 6.5 to 22.5 days after the explosion (Vogl et al., 2020). This was extended towards later epochs up until 38 days, and additional high-temperature models with an NLTE (non-local thermal equilibrium) treatment of He were also added (Vogl, 2020; Vasylyev et al., 2022; Vogl, 2024). The 38-day upper end is set by the modelling limitations, since after this epoch, time-dependent effects in the excitation and ionization balance tend to become important.[3] The physical range covered by the emulator is summarised in Table 5.1.

To infer the physical parameters, we used a Gaussian likelihood:

$$\ln p(f_\lambda^{\rm obs}|\theta_{\rm SN}, E(B-V)) = -\frac{1}{2}(R^{\rm T}C^{-1}R + \ln\det C + N\ln 2\pi), \tag{5.3}$$

where,

$$R = f_\lambda^{\rm obs} - f_\lambda(\theta_{\rm SN}, E(B-V)), \tag{5.4}$$

where $\theta_{\rm SN} = (v_{\rm ph}, T_{\rm ph}, Z, t_{\rm exp}, n)$ denotes the set of physical parameters, $f_\lambda^{\rm obs}$ and f_λ denote the observed and the reddened emulated spectra, respectively, N is the number of spectral bins and C is the bin-to-bin covariance matrix (see e.g. Czekala et al. 2015). The matrix C is important for the inference. It should account for uncertainties in the data and the model, and capture the correlations of these uncertainties across wavelength; otherwise, we would significantly underestimate the parameter uncertainties (see, Czekala et al., 2015). Constructing a matrix with these properties is a challenging, unsolved problem.

[3] The choice of 38 days is arbitrary to a certain degree and arguments can be made for lower and higher values for the cutoff: time-dependent effects already play a minor role at earlier epochs, while single snapshot models are probably still accurate enough for slightly later epochs. Modelling such late epochs is more complex and time intensive, henceforth the emulator is limited to earlier times, where models can be calculated in single snapshot simulations.

We thus used a simple diagonal matrix with constant values as in Vogl et al. (2020). Since we cannot infer reasonable uncertainties under these circumstances, we performed only maximum likelihood estimation for the parameters. Throughout the fitting, the t epoch of each spectrum was fixed. We treated the reddening towards the supernova separately from the other physical parameters: instead of directly including it in the likelihood function, we set up a grid of reddened spectra corresponding to various $E(B-V)$ values and then evaluated the likelihood for each separately. Apart from reducing computational time, this allowed us to quantify the uncertainties caused by the reddening using the treatment described below. We applied the reddening correction according to the Cardelli et al. (1989) law with $R_V = 3.1$. For the lower limit of the $E(B-V)$ grid, we always assumed the Galactic colour excess towards the supernova, which was determined based on the Schlafly & Finkbeiner (2011) dust maps. The best-fit $E(B-V)$ was chosen as the average of the $E(B-V)$ values that resulted in the lowest χ^2 for the individual spectra.

Apart from calculating the best-fit physical parameters, we also evaluated the angular diameter values for every $E(B-V)$ gridpoint to allow for the distance uncertainties resulting from the unknown amount of host reddening to be quantified, as described in the next section.

5.3 Distance determination

To infer the distances, D, for the supernovae, we used a variant of the tailored-EPM method (Dessart & Hillier, 2006; Dessart et al., 2008; Vogl et al., 2020). As a first step, the photospheric angular diameter of the supernova ($\Theta = R_{\rm ph}/D$, where $R_{\rm ph}$ denotes the radius of the photosphere) had to be inferred for each of the spectral epochs. The predicted apparent magnitude for a passband S depends on Θ as follows:

$$\begin{aligned} m_S &= M_S^{\rm ph}(\Sigma^*) - 5\log(\Theta) + A_S \\ M_S^{\rm ph} &= M_S + 5\log\frac{R_{\rm ph}}{10\ {\rm pc}}, \end{aligned} \tag{5.5}$$

Here, Σ^* denotes the set of physical parameters corresponding to the best fit, $M_S^{\rm ph}$ is the absolute magnitude predicted by the radiative transfer model at the position of the photosphere, and A_S denotes the broadband dust extinction in the bandpass; M_S denotes the absolute magnitude as defined by the distance modulus formula. The absolute magnitudes are transformed with above formula so that the variations in the size will have no effect. With this definition, we determined the best-fitting angular diameter Θ^* by minimising the square difference between the observed $m_S^{\rm obs}$ and model magnitudes:

$$\Theta^* = \arg\min_{\Theta} \sum_{\rm S} \left(m_{\rm S} - m_{\rm S}^{\rm obs}\right)^2. \tag{5.6}$$

Finally, assuming homologous expansion $R_{\rm ph} = v_{\rm ph}t$ (which is well motivated by observations and models for normal SNe IIP; see e.g. Woosley 1988; Dessart & Hillier 2005), we determined the distance to the supernova and its time of explosion through a Bayesian linear fit to the ratios of the angular diameters and the photospheric velocities ($\Theta/v_{\rm ph}$) against time, t. In the fit, we assumed Gaussian uncertainties for $\Theta/v_{\rm ph}$ of 10% of the measured values for a given colour excess, as in Dessart & Hillier (2006); Dessart et al. (2008); Vogl et al. (2020). We used a flat prior for the distance, whereas for the time of explosion, we used a normalised histogram of the t_0 posterior from the early light curve fit as the prior. However, instead of applying the standard χ^2-based likelihood, we used a different approach to account for the correlated errors caused by the reddening.

This is important since the reddening can affect the final EPM distance, as $E(B-V)$ influences the Θ measurements through the de-reddening of the observed magnitudes and changes in the best-fit parameters, such as the photospheric temperature. Hence, the uncertainty of the reddening introduces a correlated error to the final $\Theta/v_{\rm ph}$ measurements, which transitions over to the distance obtained from the EPM fit. Depending on the exact model, higher extinction usually leads to shorter inferred distances. To take this into account, we extended the likelihood with the uncertainty of the reddening by applying kernel density estimation.

Kernel density estimation (KDE) is an effective tool for approximating the underlying probability density distribution of an observable using only a number of realizations. We use the `scipy` KDE implementation assuming Gaussian kernels (Virtanen et al., 2020) to estimate an underlying distribution for the reddening values obtained from the individual spectral fits. The distributions calculated by KDE depend on the bandwidth of the individual Gaussian kernels. We set the bandwidth to a constant value of 0.025. This choice was based on empirical comparison with Silverman's rule (Silverman, 1986), which is regularly used for KDE: for multiple epochs, the bandwidth estimate obtained using Silverman's rule is in agreement with our preset value, thus, the resulting distributions match in the two cases. However, Silverman's rule cannot be used for a single epoch or when a sole value of $E(B-V)$ is favoured by all fits; in these cases, our bandwidth choice still provided a realistic KDE. Finally, we set the lower limit of the estimated distribution to the Galactic reddening based on the Schlafly & Finkbeiner (2011) map, to exclude non-physical cases. One of the obtained KDE distributions can be seen in Fig. 5.1.

To incorporate the correlated uncertainty in the fit, we first drew a large number of reddening samples using the obtained KDE. Then, a respective sample of $\Theta/v_{\rm ph}$ values was generated based on the $\Theta/v_{\rm ph} - E(B-V)$ linear interpolation and by adding a random offset to each value assuming 10% uncertainty. This sample not only contained the $\Theta/v_{\rm ph}$ values for the relevant reddening values only, but it also carried information about the correlated errors present in them. To represent these distributions and set up the final EPM regression, we applied a multi-dimensional Gaussian KDE on the set of $\Theta/v_{\rm ph}$ values and then used the corresponding probability density function as the likelihood for the fitting. We then evaluated this likelihood using `UltraNest`: at each step, the sampler drew an assumed distance and time of explosion value, for which the model $(\Theta/v_{\rm ph})^*$ were calculated and then the log probability density function was

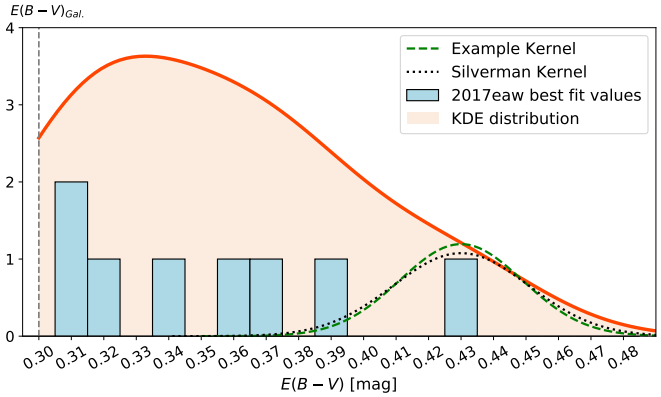

Figure 5.1: Distribution of best-fitting reddening estimates for all the epochs of SN 2017eaw (blue bars) and the constructed KDE distribution (background shape). Dashed grey line at $E(B-V) = 0.3$ mag denotes the Galactic reddening towards NGC 6946 based on the Schlafly & Finkbeiner (2011) dust map, which sets the lower limit for the KDE. The green and grey curves show the Gaussian kernels for a single observation obtained by our setting and Silverman's rule, respectively. A normalisation procedure was applied to the KDE histogram to obtain a better comparison. For more details on this supernova, see Sect. 6.4.

evaluated. As a result, we obtained a posterior distribution for the distance that includes the correlated error introduced by the uncertainty in the reddening.

6 Results

In this section, we present the distances obtained for the individual host galaxies based on their two sibling supernovae.

6.1 M 61

The spiral galaxy M61 (NGC 4303, Fig. 4.1) hosted two Type II supernovae, SN 2008in and 2020jfo. This pair of transients has not been investigated together in the literature yet, since the second supernova occurred only recently.

The first supernova, SN 2008in was discovered on JD 2454827.29 by Nakano et al. (2008). As M61 was monitored by the Robotic Optical Transient Search Experiment (ROTSE) starting from the week before the discovery (Roy et al., 2011), the fitting of the early light curve allowed for the estimation of the time of explosion independent of the EPM, from which we obtained $t_0 = \text{JD } 2454824.51^{+0.19}_{-0.14}$ (Fig. 6.1). This supernova was found to belong to the peculiar, subluminous group of SNe IIP (Roy et al., 2011). The spectral sequence for our analysis consisted of spectra obtained by Roy et al. (2011) complemented with more recently published spectra from Hicken et al. (2017).

SN 2020jfo was discovered on JD 2458975.70 by the Zwicky Transient Facility (ZTF, Schulze et al. 2020). Owing to the relatively short cadence of observations of ZTF (Bellm et al., 2019), the time of explosion, t_0, is not only constrained by a non-detection 4 days pre-discovery, but the supernova was discovered on the rise; hence, it was possible to estimate t_0 precisely by the fitting of the early light curve (Fig. 6.1). We obtained a time of explosion of $t_0 = \text{JD } 2458975.37^{+0.10}_{-0.10}$. The spectral time series of this object was presented by Sollerman et al. (2021) and Teja et al. (2022). For our study, we used seven early time spectra ($t < 20$ days).

The spectral time series and the emulator fits are shown in Fig. 6.2. For the calculation of the best-fitting models the telluric regions (as marked on the figure) were masked. After fitting, we performed the EPM analysis on both supernovae (Fig. 6.3). The light curve fits used for the flux calibration of the spectra are displayed in Appendix 8, while the best-fit parameters are listed in Table 13.3. The estimated distances to the supernovae are $D = 15.06 \pm 0.71$ Mpc and $D = 14.95 \pm 0.78$ Mpc for SN 2008in and SN 2020jfo, respectively. The classical EPM analysis of SN 2008in was conducted previously by Bose & Kumar (2014), yielding a distance of $D = 14.51 \pm 1.38$ Mpc, which is consistent with our current estimate. No prior distance measurements of SN 2020jfo had been carried out. Although the calibration quality varied significantly from epoch to epoch (since multiple instruments were used for both spectral sequences), the obtained distances are consistent within the uncertainties and agree within 1%.

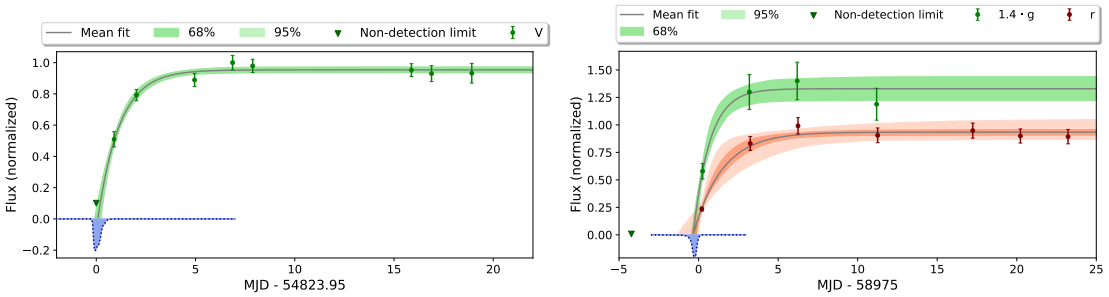

Figure 6.1: Exponential fit on the ROTSE light curve of SN 2008in (**left**) and the ZTF early light curves of SN 2020jfo (**right**). The blue shaded areas shows the obtained t_0 posteriors. The black curves show the mean fit, namely, the fit that results by taking the mean of the posterior distributions. In case of SN 2020jfo, the g-band light curve was further rescaled after the normalization to improve clarity on the figure. The shaded regions denote the 68% and 95% confidence intervals.

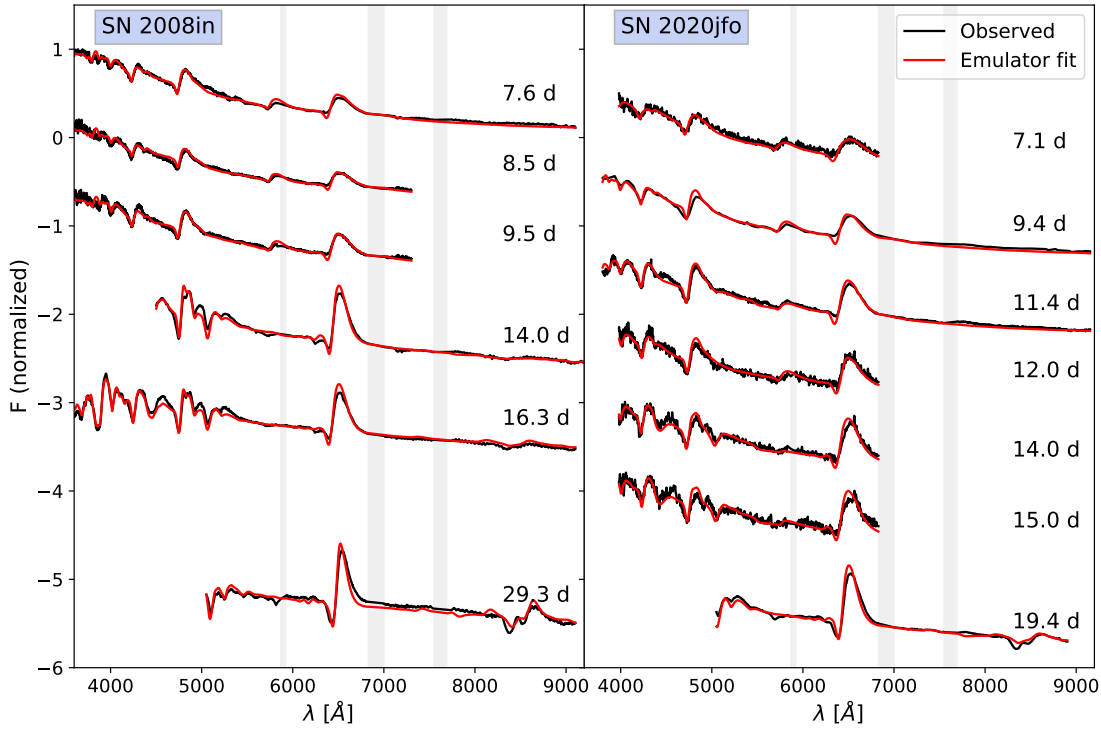

Figure 6.2: Spectral time series of SNe 2008in (Roy et al., 2011; Hicken et al., 2017) and 2020jfo (Sollerman et al., 2021), along with our fits. The grey-shaded areas denote telluric regions.

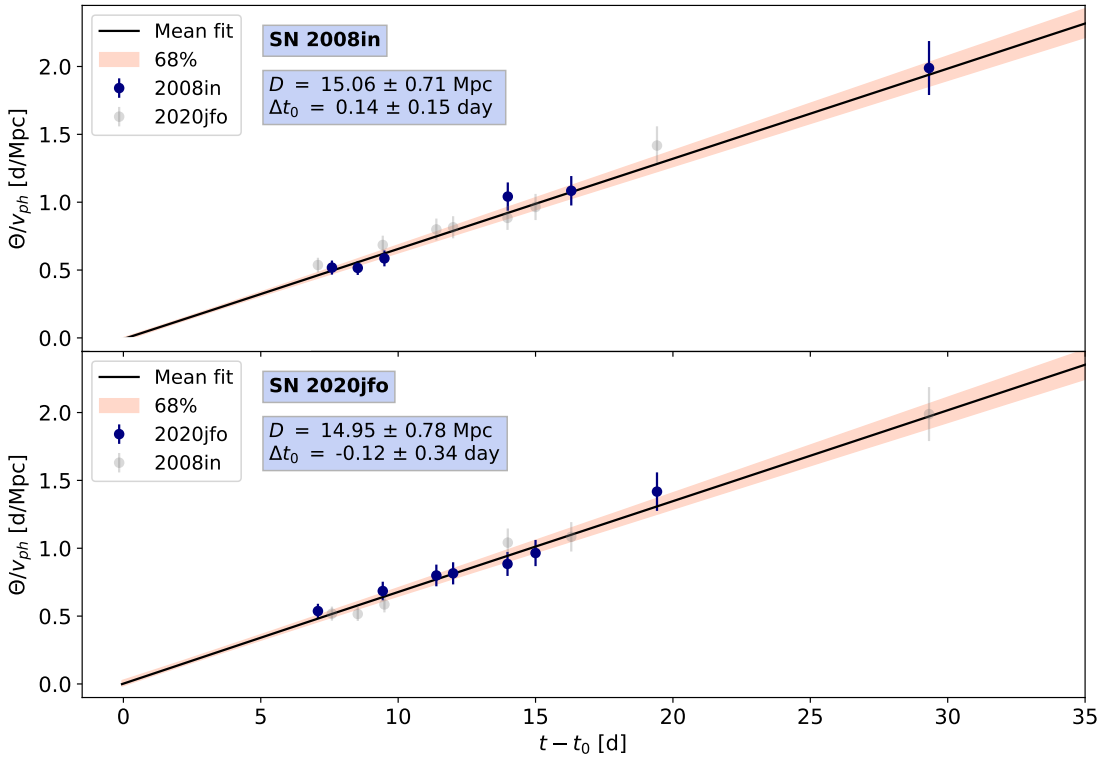

Figure 6.3: Evolution of Θ/v_{ph} for SNe 2008in (**top** panel) and 2020jfo (**bottom** panel). The derived distance, D, and the final time of explosion estimate (with respect to the initial light curve fit-based value), Δt_0, are displayed in the top left corner of each panel. The shaded region shows the 68% confidence interval of the fit. The displayed uncertainties denote the 1σ errors on Θ/v_{ph}.

6.2 NGC 772

The spiral galaxy NGC 772 (Fig. 4.1) is unique in the sense that it not only had been host to two Type II supernovae, but both objects were also observable simultaneously, as they exploded within one and a half months of one another. Both supernovae were followed up by the Carnegie Type II Supernova Program (CATS) and their spectral sequences were previously analysed by Jones et al. (2009).

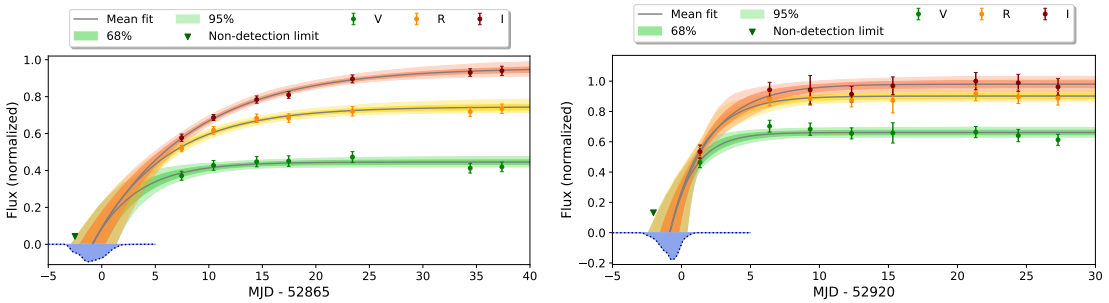

Figure 6.4: Early light curve fits of SN 2003hl (**left**) and SN 2003iq (**right**), along with the determined time of explosion posteriors (blue shaded regions).

The first supernova, SN 2003hl, was discovered on JD 2452872.0 by Moore et al. (2003). By applying the method described in Sect. 5.1 on the early light curve, along with the unfiltered pre-discovery KAIT (Katzman Automatic Imaging Telescope, Filippenko et al. 2001) non-detection on JD 2452863.0, we estimated the time of explosion to be JD $2452864.62^{+1.18}_{-1.15}$ (Fig. 6.4). We assigned the KAIT non-detection to the V-band, given that the colour of the supernova is close to zero owing to the combined effect of the very blue spectral energy distribution in such early phases and the reddening, which places the effective wavelength close to the V-band even for a red-sensitive CCD. Only one spectrum was obtained for this supernova in the temporal range covered by our emulator. Nevertheless, using the time of explosion, we could still derive an approximate EPM distance.

The second supernova, SN 2003iq was discovered by Llapasset et al. (2003) on JD 2452921.5 during the photometric follow-up observations of SN 2003hl. Owing to the monitoring of the host, a pre-discovery image was taken on JD 2452918.5 by Llapasset et al. (2003) shortly before the first detection, which already constrained the explosion date of SN 2003iq to a range of 3 days. By fitting the early light curve, we estimated its time of explosion to be JD $2452919.71^{+0.59}_{-0.65}$ (Fig. 6.4). Apart from the more precisely known t_0, this supernova has a more thorough spectral record during the photospheric phase than its sibling, as four spectra were acquired during its early evolution.

The fitted spectral time series of the supernovae are displayed in Fig. 6.5. The EPM regression derived from the obtained physical parameters is shown in Fig. 6.6. We obtain $D = 33.95 \pm 4.49$ Mpc and 26.02 ± 1.85 Mpc for the distance of NGC 772 from SN 2003hl and SN 2003iq, respectively. Although we could use only one spectrum for SN 2003hl

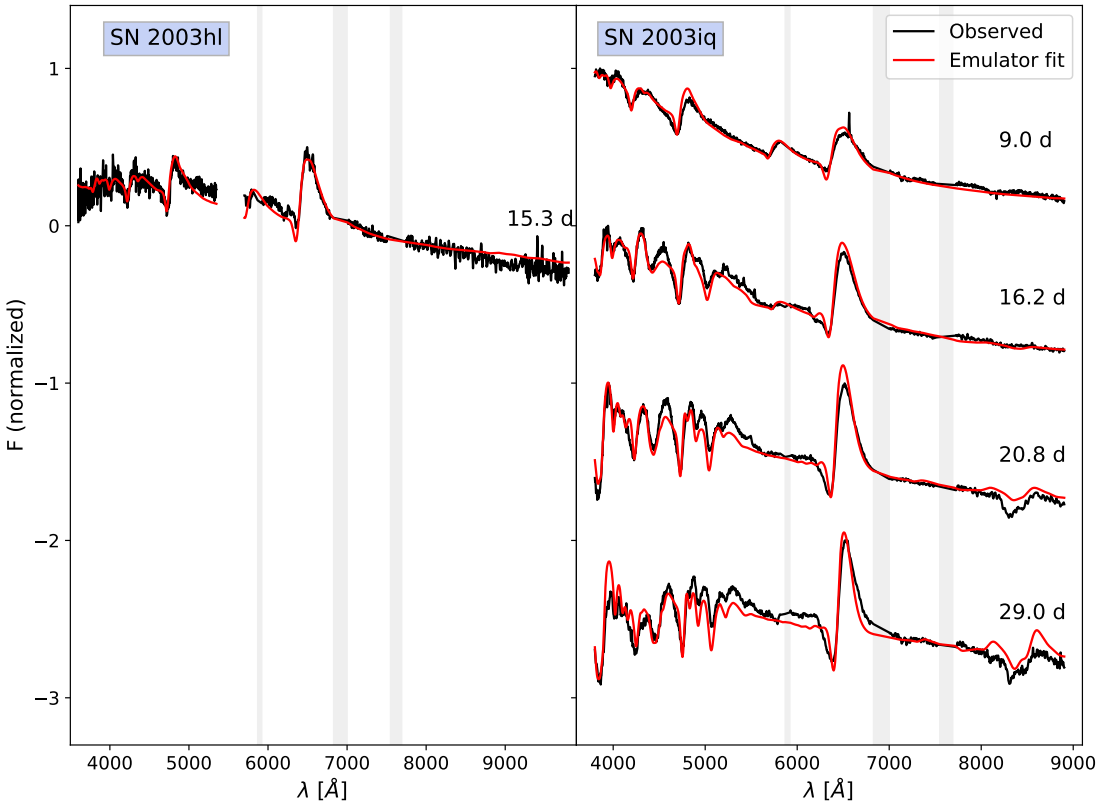

Figure 6.5: Spectral time series of SNe 2003hl and 2003iq, along with their fits. The grey-shaded areas denote telluric regions.

and, hence, the resulting distance estimate is fairly uncertain, both the final result and the $\Theta/v_{\rm ph}$ value around 15 days show a broad consistency with those of SN 2003iq.

By comparing our results with the classical EPM carried out by Jones et al. (2009), we find significant differences for SN 2003hl and SN 2003iq as well, both for the Eastman et al. (1996) and Dessart & Hillier (2005) correction factors: in the case of 2003hl, our distance is larger than the two Jones et al. (2009) estimates ($D = 17.7 \pm 2.1$ Mpc and $D = 30.3 \pm 6.3$ Mpc for the different correction factors respectively), while for SN 2003iq our distance is shorter than the previous estimates ($D = 36.0 \pm 5.6$ Mpc and $D = 53.3 \pm 17.1$ Mpc, Jones et al. 2009). However, the differences between the estimates can be explained by the significantly higher colour excess we obtained for SN 2003iq (with our best estimate being $E(B-V) = 0.14$ mag) and by the fact that we could not make use of more than one spectrum for SN 2003hl, due to the limitations in our modelling approach. On the other hand, by comparing our estimates with previous SCM distances, we find our solution for SN 2003iq is consistent with the previous result of Poznanski et al. (2009) ($D = 26.6 \pm 1.25$ Mpc), while our distance for SN 2003hl is not in tension with the SCM estimate of Olivares E. et al. (2010) ($D = 25.6 \pm 3.30$ Mpc).

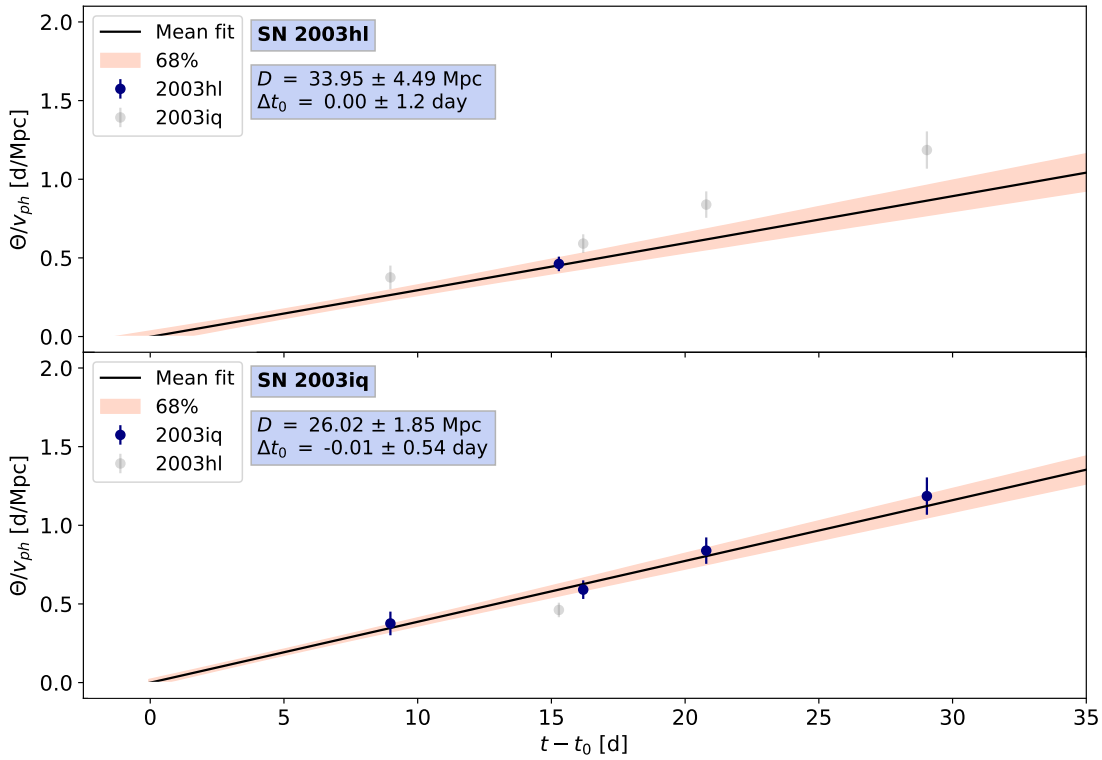

Figure 6.6: Evolution of $\Theta/v_{\rm ph}$ for SNe 2003hl (**top** panel) and 2003iq (**bottom** panel).

6.3 NGC 922

The peculiar SBcd type galaxy NGC 922 (Fig. 4.1) hosted two Type II supernovae six years apart: SN 2002gw and SN 2008ho. First, SN 2002gw was discovered on JD 2452560.8 (Monard, 2002). Although the latest non-detection occurred too far from the discovery to be useful for constraining the explosion date, the fitting of the early light curve (including the unfiltered CCD observations obtained by Itagaki et al. 2002 and Monard 2002) gave an estimate of JD $2452556.58^{+0.97}_{-1.40}$ (Fig. 6.7), which is consistent with the value obtained through performing the EPM regression in Jones et al. (2009). In total, three optical spectra were acquired for this supernova by the CATS program (Hamuy et al., 2006) in the epoch range that could be used for our EPM analysis.

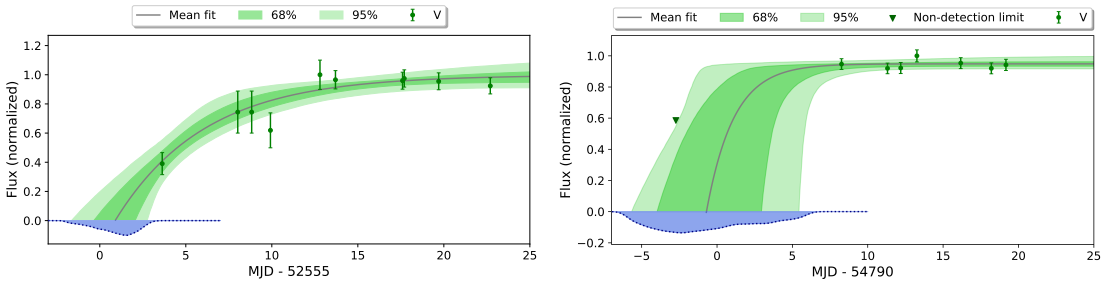

Figure 6.7: Early light curve fits of SN 2002gw (**left**) and SN 2008ho (**right**), along with the determined time of explosion posteriors (blue shaded regions).

The second supernova, SN 2008ho, was discovered on JD 2454796.61 by Pignata et al. (2008). The last pre-discovery non-detection occurred on JD 2454787.77, which provides a weak constraint on the time of explosion: we found $t_0 = \text{JD } 2454789.63^{+3.63}_{-2.54}$ from the light curve fit (Fig. 6.7). In total, two spectra were obtained for this supernova through the Carnegie Supernova Project (Hamuy et al., 2006). The spectra were recalibrated using the BV observations obtained through the CSP project (Anderson et al. 2023, private communication). For the EPM, we made use of the BV photometry from the same campaign.

The fitted spectral sequences of SN 2002gw and SN 2008ho are shown in Fig. 6.8. From the EPM regression we obtained a distance for SN 2008ho of $D = 40.02 \pm 5.07$ Mpc (Fig. 6.9). On the other hand, we found $D = 43.46 \pm 3.77$ Mpc for BV bands only and $D = 43.85 \pm 3.78$ Mpc for the full BVI set for SN 2002gw (see Fig. 6.10 for the comparison). Our distance estimates for SN 2002gw fall between the values derived by Jones et al. (2009) for the different dilution factors ($D = 37.4 \pm 4.9$ Mpc and $D = 63.9 \pm 17.0$ Mpc) and agree well with the previous SCM ($D = 48.1 \pm 6.2$ Mpc, Olivares E. et al. 2010) and photospheric magnitude method estimates ($D = 45.10 \pm 3.11$ Mpc, Rodríguez et al. 2014). Although the difference is only $\sim 1\%$, we used the BV instead of the BVI distance for SN 2002gw for the plots and the distance consistency check (Sect. 7) to make the analysis of the siblings as similar as possible. We suspect that the majority of the offset between the distances of the two SNe can be attributed

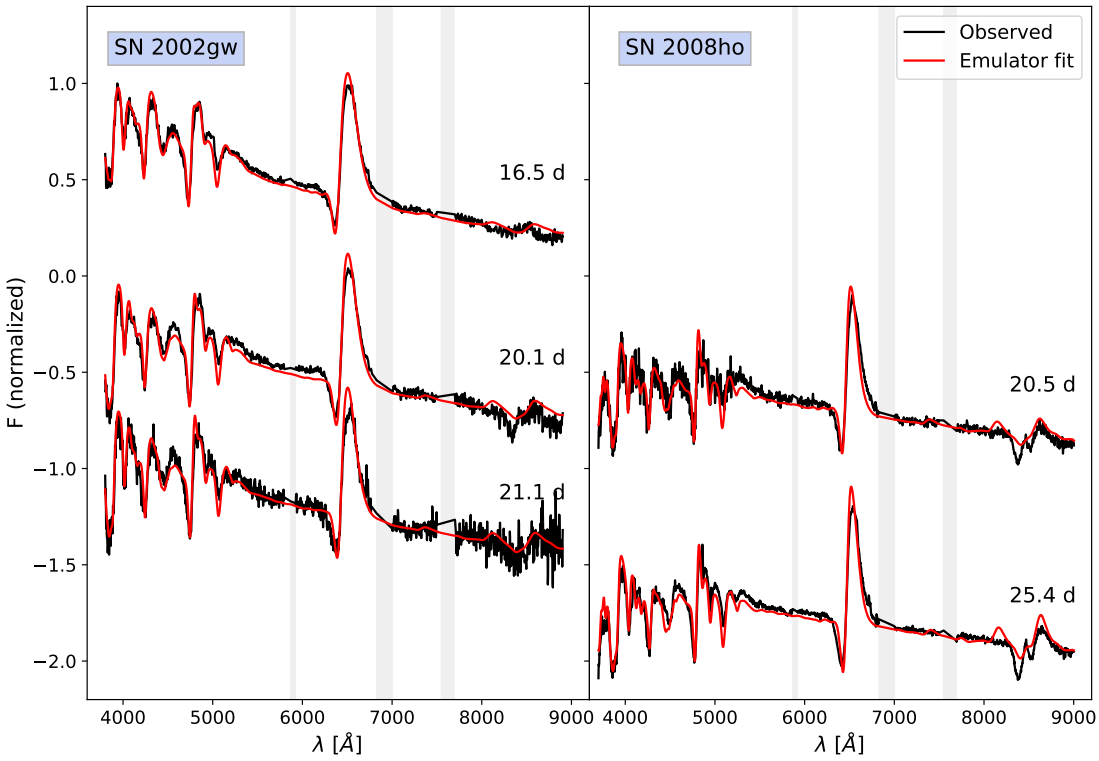

Figure 6.8: Spectral time series of SNe 2002gw and 2008ho, along with their fits. Grey-shaded areas denote telluric regions.

to the relatively large uncertainties on the times of explosion. Nevertheless, the two distances are fully consistent within 1σ.

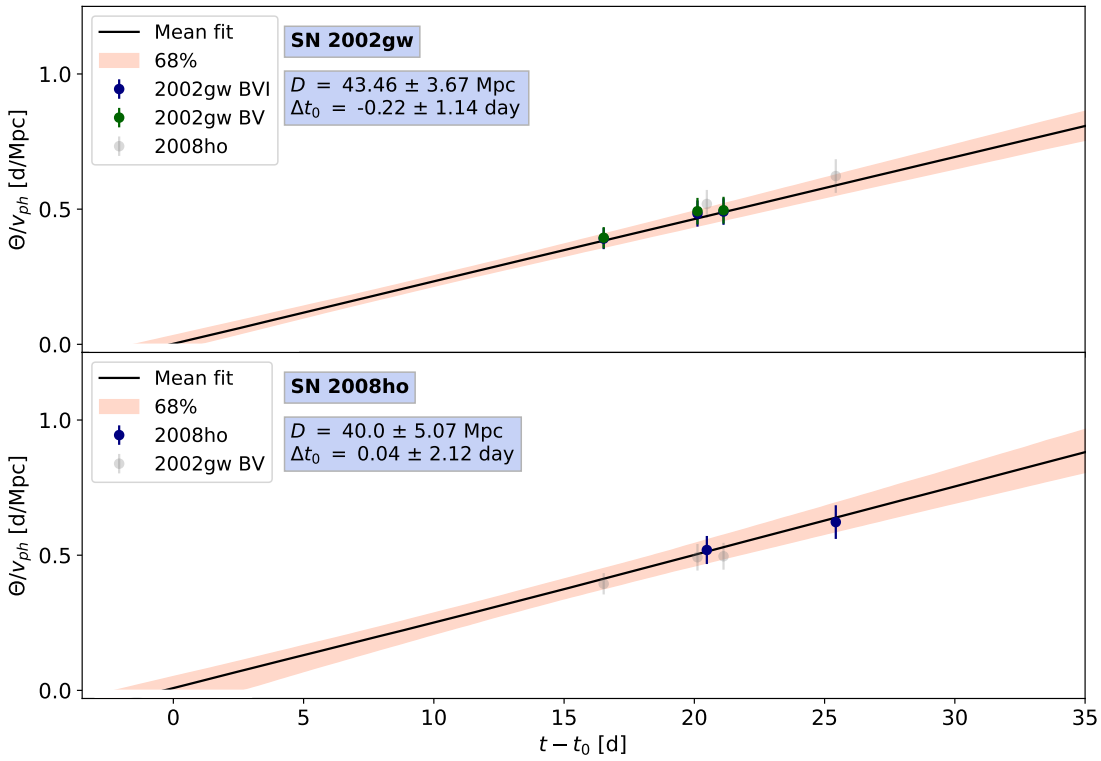

Figure 6.9: Evolution of $\Theta/v_{\rm ph}$ for SNe 2002gw (**top** panel) and 2008ho (**bottom** panel).

6.4 NGC 6946

NGC 6946 (Fig. 4.1) is a bright face-on SABcd type galaxy, which produced several Type II supernovae: SNe 1948B, 1980K, 2002hh, 2004et, and 2017eaw. Due to its proximity, the distance of this galaxy could be estimated through the tip of the red giant branch (TRGB) method (Anand et al., 2018) and the planetary nebulae luminosity function (PNLF) relation (Herrmann et al., 2008). Three of the aforementioned supernovae (SNe 2002hh, 2004et and 2017eaw) were observed spectroscopically during the early photospheric phase, which makes it possible to measure their distances through the tailored-EPM. However, only SNe 2004et and 2017eaw were optimal for our purposes: even though the spectral time series and the photometric coverage would have allowed the analysis of SN 2002hh, it was found that this supernova exhibited a very strong, two-component reddening (one component arising from the joint effect of the interstellar dust in the host and the Milky Way, the other from large quantities of local dust, see Barlow et al. 2005, Pozzo et al. 2006 and Welch et al. 2007). With the currently available data and methodology, it is not possible to obtain an accurate extinction correction. Considering the very high reddening, any error in our extinction correction would significantly impact the inferred distance. Hence, we chose to exclude SN 2002hh from the analysis.

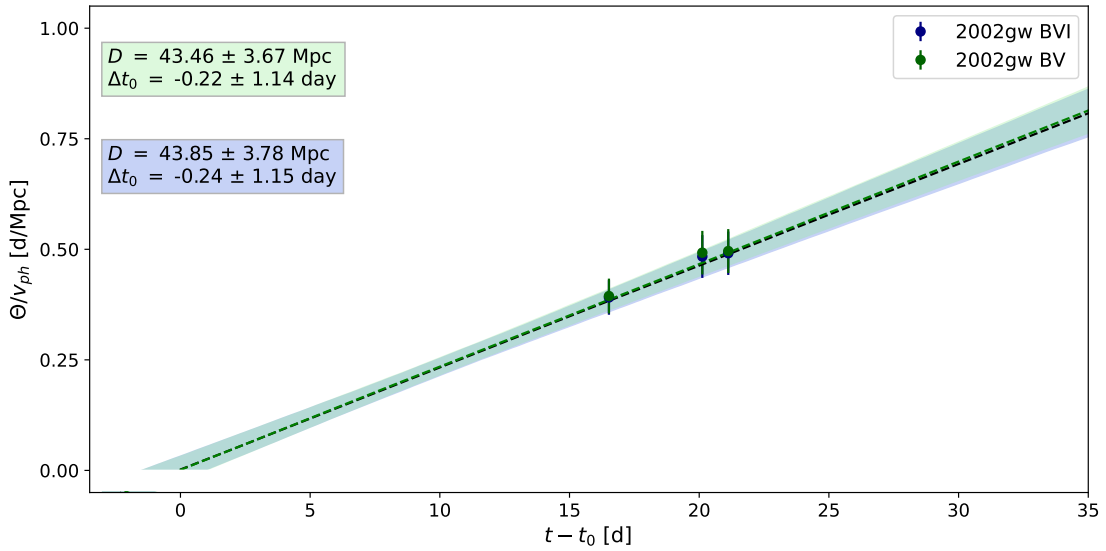

Figure 6.10: EPM regression performed for SN 2002gw on the $\Theta/v_{\rm ph}$ values calculated using the BV (green) and BVI (blue) bandpass sets.

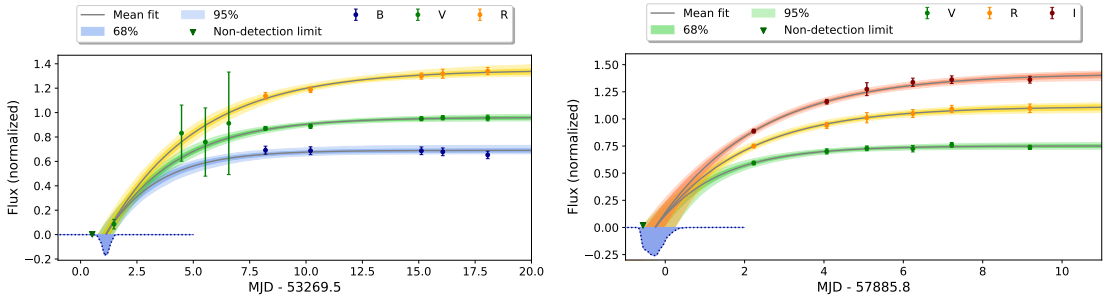

Figure 6.11: Exponential fit on the early light curves of SN 2004et (**left**) and SN 2017eaw (**right**), along with the determined time of explosion posteriors (blue shaded regions).

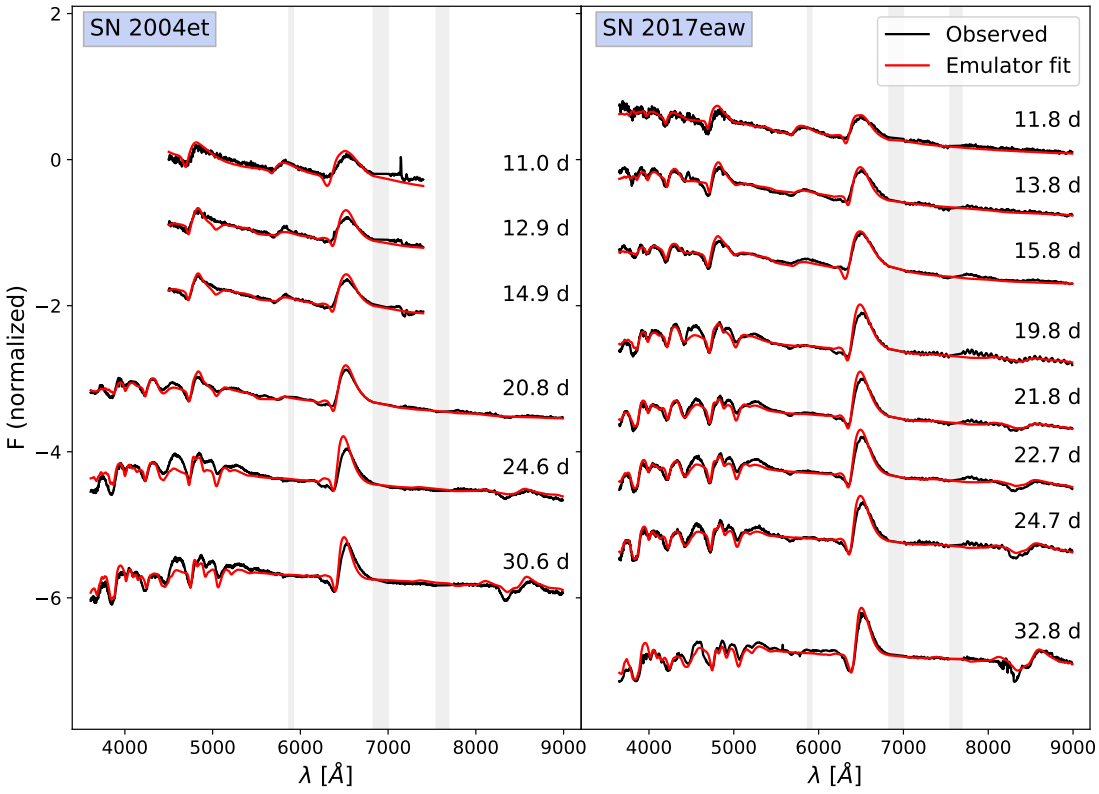

Figure 6.12: Spectral time series of SNe 2004et and 2017eaw, along with their fits.

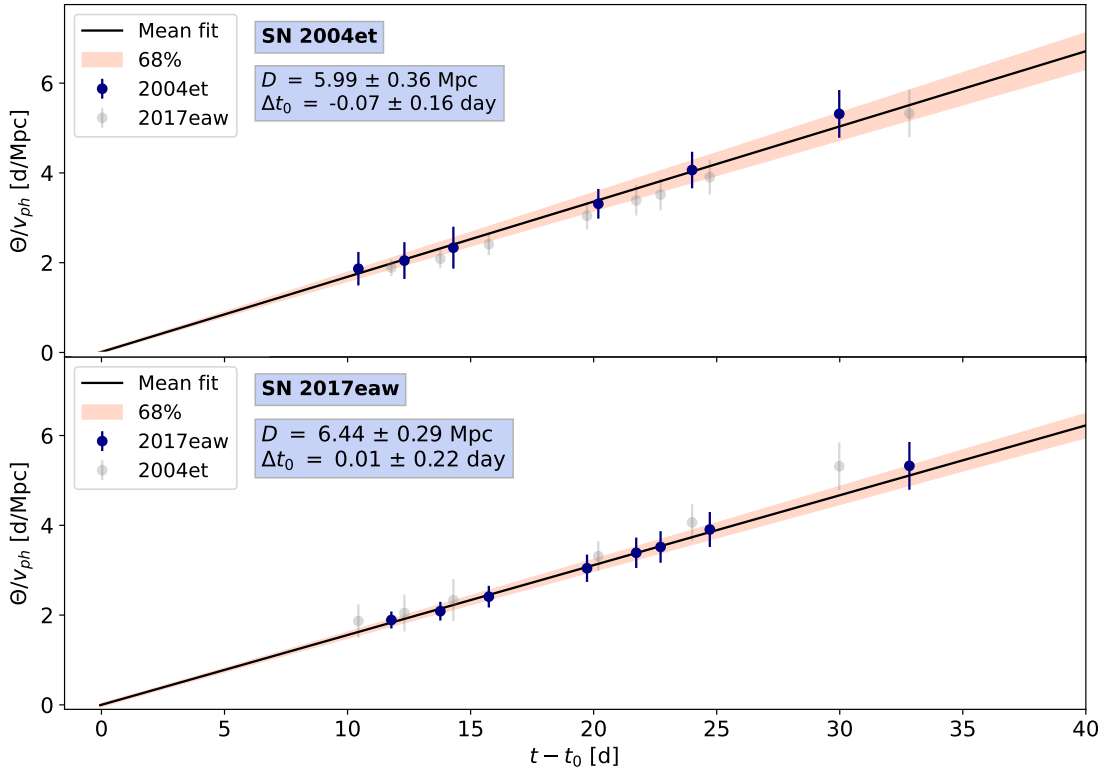

Figure 6.13: Evolution of $\Theta/v_{\rm ph}$ for SNe 2004et (**top** panel) and 2017eaw (**bottom** panel).

SN 2004et was discovered on JD 2453273 by Zwitter et al. (2004), and extensively followed up on by the 2-m Himalayan Chandra Telescope (HCT) of the Indian Astronomical Observatory (IAO) and the 3-m Shane telescope at the Lick Observatory. The resulting spectral times series have been previously studied by Sahu et al. (2006). However, the spectra taken with the HCT were subject to calibration issues, which could not be corrected with our standard linear flux re-calibration. Since these issues can influence the fitting significantly, we attempted to correct them empirically, using spectra taken with the Keck and Lick telescopes. This procedure is detailed in Appendix 8. We completed this spectral time series with three additional early-time spectra obtained at the David Dunlap Observatory (Takáts & Vinkó, 2012, courtesy of József Vinkó). However, since these spectra covered only a very narrow wavelength range, we could not apply the re-calibration procedure from Sect. 5.1.3. The pre-discovery non-detection of the supernova and the subsequent early photometry from Li et al. (2004) has allowed for an accurate determination of the time of explosion through the fitting of the early light curve (Fig. 6.11), which yielded $t_0 = \text{JD } 2453271.19^{+0.16}_{-0.17}$. Along with the tight constraints on the time of explosion, the six spectra obtained in the first month after explosion also allowed for a precise EPM analysis.

SN 2017eaw was discovered by Wiggins (2017) on JD 2457885.78, and then extensively followed up on with spectroscopic observations at the Las Cumbres Observatory 1 m

Host	SN	D [Mpc]	t_0 (MJD)	$E(B-V)$ [mag]
M61	2008in	15.06(0.71)	54824.15(0.15)	0.06(0.03)
	2020jfo	14.95(0.78)	58975.08(0.34)	0.07(0.04)
NGC 722	2003hl	33.95(4.49)	52864.26(1.20)	0.31*
	2003iq	26.02(1.85)	52919.20(0.54)	0.15(0.05)
NGC 922	2002gw	43.46(3.67)	52555.84(1.15)	0.12(0.03)
	2008ho	40.02(5.07)	54789.17(2.12)	0.21*
NGC 6946	2004et	5.99(0.36)	53270.62(0.16)	0.38(0.10)
	2017eaw	6.44(0.29)	57885.52(0.22)	0.35(0.04)

Table 6.1: Summary table of the EPM results. t_0 denotes the time of explosion as obtained by the EPM regression. The $E(B-V)$ values listed here are those determined by the spectral fitting. The values in brackets denote the uncertainties of the given quantities. In the starred (*) cases we either had only one spectrum to fit or both spectra yielded the same reddening value, which did not allow us to give a reasonable empirical uncertainty.

Galaxy	SN 1	$D_{SN\,1}$	SN 2	$D_{SN\,2}$	Bayes factor	Prior
NGC 772	2003hl	33.95 ± 4.49 Mpc	2003iq	26.02 ± 1.85 Mpc	0.890	13.44 – 53.77 Mpc
NGC 922	2002gw	43.46 ± 3.67 Mpc	2008ho	40.02 ± 5.07 Mpc	3.448	21.29 – 85.16 Mpc
NGC 4303	2008in	15.06 ± 0.71 Mpc	2020jfo	14.95 ± 0.78 Mpc	7.944	7.31 – 29.25 Mpc
NGC 6946	2004et	5.99 ± 0.36 Mpc	2017eaw	6.44 ± 0.29 Mpc	4.272	2.77 – 11.09 Mpc

Table 6.2: Bayes factors for the comparisons of the distance posteriors of the various SN pairs.

telescope and at the McDonald Observatory with the Low-Resolution Spectrograph 2 mounted on the 10 m Hobby–Eberly Telescope. The observations are described in Szalai et al. (2019). The supernova was discovered early, on the rise, and a non-detection is also available from a pre-discovery observation of the host, which yielded a time of explosion of $t_0 = \text{JD } 2457886.01^{+0.25}_{-0.20}$. In terms of spectroscopy, this supernova had the best-sampled and most homogenous spectral sequence in our sample, resulting in eight well-calibrated spectra.

The calibrated and fitted spectral sequences are shown in Fig. 6.12. For SN 2004et, the EPM regression yielded a distance of $D = 5.99 \pm 0.36$ Mpc, while for SN 2017eaw the resulting value was $D = 6.44 \pm 0.29$ Mpc (Fig. 6.13). The distance for SN 2004et is 20% higher than the classical EPM value inferred by Takáts & Vinkó (2012) and Szalai et al. (2019), while for SN 2017eaw the value we obtained is about 5-20% lower than the value from Szalai et al. (2019) (depending on the assumed reddening and the chosen epoch range of spectra of the reference work, see Szalai et al. 2019 for details). We note that our distance estimates are in much better agreement with one another, which highlights the advantage of the tailored-EPM over the classical EPM approach. The distances are also consistent with the various independent distances obtained for NGC 6946: apart from the previous EPM-based values, our estimates are in agreement with SCM distances of Poznanski et al. (2009) and de Jaeger et al. (2017) (both of which yielded $D = 6.69 \pm 0.30$ Mpc for SN 2004et) and the PNLF distance (Herrmann et al. 2008, $D = 6.1 \pm 0.6$ Mpc),

but is slightly lower than the latest TRGB estimate ($D = 6.95 \pm 0.20$ Mpc, Anand et al. 2021, from the Extragalactic Distance Database[1]).

[1] https://edd.ifa.hawaii.edu/

7 Discussion

As shown in the previous sections, the fitting procedure not only yields distances with a claimed uncertainty of ∼10% or better (Table 6.1), it does so by requiring only a limited amount of modelling choices. Due to various uncertainties in the observations and the modelling, these distances can be slightly different for the supernova siblings. The main question, in this case, is whether the estimated distances of the siblings are consistent with one another. Assuming an average galaxy, a reliable upper limit for the thickness of the disc is 10 kpc, while the width of the disc is on the order of 100 kpc (Gilmore & Reid, 1983; Zanisi et al., 2020). Consequently, in an ideal case, assuming face-on galaxies, the distances inferred for the supernova siblings should match to an uncertainty of ±0.01 Mpc, which corresponds to only ∼ 0.2% even for the most nearby pair. For more inclined galaxies, the uncertainties can be one order of magnitude larger; however, since the closest hosts we investigated are very likely to be low-inclination galaxies (M 61 and NGC 6946) and the ones farther away are not viewed edge-on either (NGC 722 and NGC 922), the offset between the siblings should remain sub-1% relative to the distance of the galaxy. Hence, the distance estimation to siblings provides an empirical test to assess the effect of these uncertainties and systematics (e.g. the CSM interaction, or data calibration issues, among others). It allows us to test whether our results are not only precise but accurate as well.

To test the consistency of the obtained distances, we performed a Bayesian model comparison. We adopted the methodology used by Wong et al. (2020b) for assessing whether pairs of strongly lensed quasars favour a single global set of cosmological parameters or individual cosmologies for each lens that are inconsistent with one another. We applied this method to the distance estimates of the siblings: thus, we asked the question of whether the measured distance posteriors of a pair have more likely been generated from a single underlying distance, $D^{\rm gal}$, or from two distinct distances, $D^{\rm ind,1}$ and $D^{\rm ind,2}$ (and would thus prove inconsistent). The probability ratio of the two scenarios is called the Bayes factor and can be calculated as:

$$F_{ij} = \frac{P(\mathbf{d_i}, \mathbf{d_j}|D^{\rm gal})}{P(\mathbf{d_i}|D^{\rm ind,i})P(\mathbf{d_j}|D^{\rm ind,j})} = \frac{\int_{D_1}^{D_2} \mathbf{d_i}\mathbf{d_j}P(D)dD}{\int_{D_1}^{D_2} \mathbf{d_i}P(D)dD \int_{D_1}^{D_2} \mathbf{d_j}P(D)dD}, \tag{7.1}$$

where $\mathbf{d_i}$ and $\mathbf{d_j}$ denote the distance posteriors of the individual supernovae in each pair. We chose a uniform prior $P(D)$ around the average distance of the host (based on previous measurements, as quoted on NASA/IPAC Extragalactic Database, NED[1]), ranging from half to twice that distance. The quoted Bayes factors can thus be understood as lower limits since they scale linearly with the width of the distance prior. If the obtained

[1] https://ned.ipac.caltech.edu/

Bayes factor exceeds unity, this can be interpreted as a sign of consistency between the two posterior distributions in accordance with the table of Kass & Raftery (1995). The higher the F value, the stronger the consistency between the siblings.

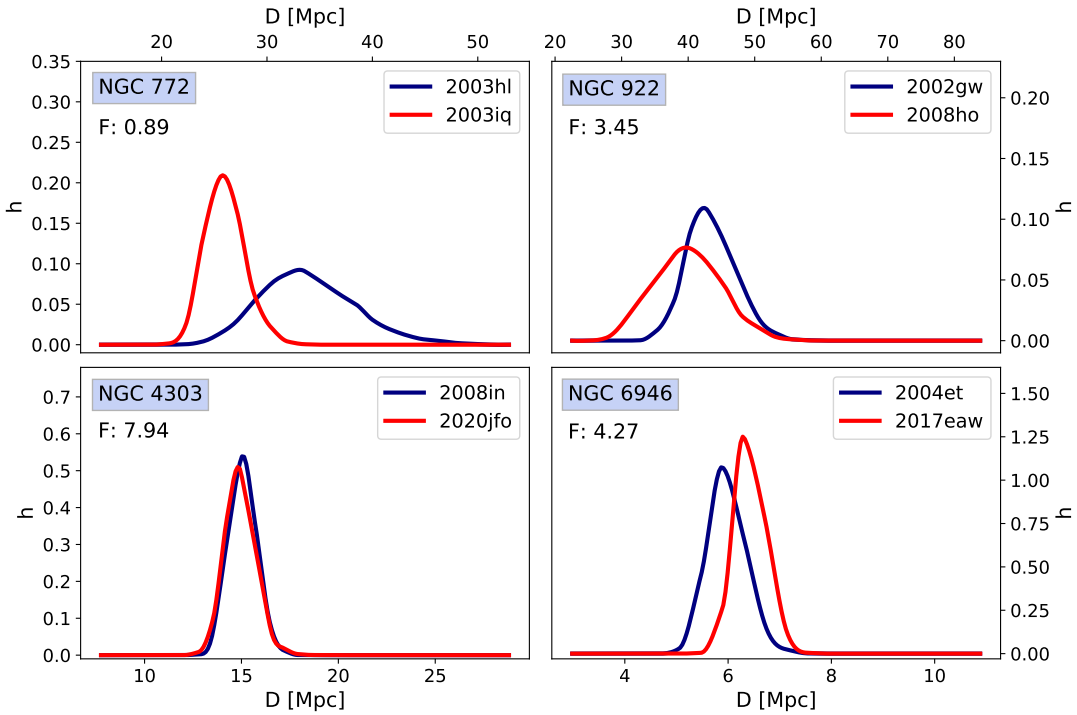

Figure 7.1: Distance posteriors obtained from the EPM analysis of the supernovae for the various host galaxies. The calculated Bayes factors are displayed in the top-left corners of the panels.

The distance posteriors from the EPM analysis are shown in Fig. 7.1, while the obtained Bayes factors are listed in Table 6.2. The consistency of the distance posteriors for the various supernovae is good, with Bayes factors being close to or over 5 for two cases, showing remarkable agreement. In the case of NGC 772 and NGC 922 the values of the Bayes factors are lower, which might be attributed to the lack of a well-sampled spectral sequence for SN 2003hl and the lack of well-constrained explosion date for SNe 2002gw and 2008ho. However, the remaining cases show that the fitting method and the analysis result in distances that are not only consistent for supernovae in the same host but are also precise to a degree of a few percent. The analysis also showed that some of the greatest limiting factors of the method are: an insufficient amount of spectra, poor quality and calibration-level of the obtained spectral times series, and weak constraints on the time of explosion. If all the conditions for the above were met, the EPM analysis would be able to yield highly precise and consistent values for the supernova pairs, as in the case of SNe 2004et and 2017eaw or in the case of SNe 2008in and 2020jfo.

We offer the caveat that some of our results may be influenced by the choice of $R_V = 3.1$. If the true R_V is different, this could, in principle, cause notable offsets between the

sibling distances, provided that the differential reddening between the objects is non-negligible and the measurement uncertainties are low enough. In our sample, however, the pairs with the most significant differential reddening had also the largest uncertainty on their distance and vice versa. Hence, it is currently not possible to estimate the scale of this effect on the basis of our four sibling pairs.

8 Summary

In this work, we investigated the consistency of the EPM distances of sibling Type II SNe, calculated based on the spectral fitting method introduced by Vogl et al. (2020). According to our analysis, the method not only yields precise results with an estimated individual distance uncertainty that is better than ∼10%, despite using literature data from a wide range of sources, but the resulting distances are consistent for SNe that are within the same host galaxy. The degree of consistency depends on how well the supernovae were observed, with the worst results occurring when the quality of the data barely allows for the EPM analysis, while the best consistency is achieved when both supernovae are similarly well observed and have a good constraint on the time of explosion. In the cases of M61 and NGC 6946, highly consistent distances are derived with mismatches of less than 5%.

The high level of consistency between siblings also shows that if there are any other systematics present between the various SNe, they are likely subdominant compared to the effect of observation quality. Such systematics may include different reddening, CSM interaction, explosion energetics, and metallicities. Checking for the effect and scale of such systematics will require a larger set of siblings with data quality that matches that of the siblings of M 61 or NGC 6946.

Apart from checking for the internal consistency of the method, we obtained precise distances for the four investigated host galaxies, even though we used literature data with a highly varying level of calibration. Furthermore, the tailored-EPM provides absolute distances is physics-based and is affected by different systematics than the other existing distance estimation techniques; thus, it can be utilised completely independently of them. These properties and the presented analysis in this paper demonstrate the potential of the tailored-EPM to provide not only precise distances but a precise Hubble parameter as well. Such an analysis is currently being conducted on high-quality spectral time series obtained for SNe II in the Hubble Flow by the `adH0cc` collaboration (accurate determination of H0 with core-collapse supernovae[1]), which will provide important clues to the Hubble tension.

[1] https://adh0cc.github.io/

Acknowledgements

We especially thank J. Anderson, M. Stritzinger and the CSP collaboration for providing us pre-published data, which helped us to improve our analysis. The research was completed with the extensive use of Python, along with the `numpy` (Harris et al., 2020), `scipy` (Virtanen et al., 2020) and `astropy` (Astropy Collaboration et al., 2018) modules. This research made use of TARDIS, a community-developed software package for spectral synthesis in supernovae (Kerzendorf & Sim, 2014; Kerzendorf et al., 2022). The development of TARDIS received support from the Google Summer of Code initiative and from ESA's Summer of Code in Space program. TARDIS makes extensive use of Astropy and PyNE. Based on observations obtained with the Samuel Oschin 48-inch Telescope at the Palomar Observatory as part of the Zwicky Transient Facility project. ZTF is supported by the National Science Foundation under Grant No. AST-1440341 and a collaboration including Caltech, IPAC, the Weizmann Institute for Science, the Oskar Klein Center at Stockholm University, the University of Maryland, the University of Washington, Deutsches Elektronen-Synchrotron and Humboldt University, Los Alamos National Laboratories, the TANGO Consortium of Taiwan, the University of Wisconsin at Milwaukee, and Lawrence Berkeley National Laboratories. Operations are conducted by COO, IPAC, and UW. This project utilises data obtained by the Robotic Optical Transient Search Experiment. ROTSE is a collaboration of Lawrence Livermore National Lab, Los Alamos National Lab, and the University of Michigan (`www.umich.edu/~rotse`). CV and WH were supported for part of this work by the Excellence Cluster ORIGINS, which is funded by the Deutsche Forschungsgemeinschaft (DFG, German Research Foundation) under Germany's Excellence Strategy-EXC-2094-390783311. The work of AH was supported by the Deutsche Forschungsgemeinschaft (DFG, German Research Foundation) – Project-ID 138713538 – SFB 881 ("The Milky Way System", subproject A10). AH acknowledges support by the Klaus Tschira Foundation. AH is a Fellow of the International Max Planck Research School for Astronomy and Cosmic Physics at the University of Heidelberg (IMPRS-HD). This work was supported by the 'Programme National de Physique Stellaire' (PNPS) of CNRS/INSU co-funded by CEA and CNES. SB acknowledges support from the ESO Scientific Visitor Programme in Garching. AF acknowledges support by the European Research Council (ERC) under the European Union's Horizon 2020 research and innovation program (ERC Advanced Grant KILONOVA No. 885281). ST has received funding from the European Research Council (ERC) under the European Union's Horizon 2020 research and innovation program (LENSNOVA: grant agreement No 771776).

Appendix

Correction of the SN 2004et HCT spectra

By comparing the spectra of SN 2004et taken at the HCT and Lick Observatory at similar epochs, we found that the former show a significant flux deficit in the wavelength range covered mainly by the Bessell V and R bands, as shown in the Fig. A.1. This trend could not be corrected by a linear flux correction based on the photometry.

To fix this issue, we took the ratios of the uncorrected HCT and the re-calibrated Keck and Lick spectra taken at close epochs (which otherwise are too old for the emulator-based fitting, see top panel of Fig. A.2), then averaged the obtained trend, assuming that it is the same for every HCT spectrum, and fitted it using Generalized Additive Models (GAMs, Hastie & Tibshirani 1990, by applying the `pyGAM` package from Python, Servén et al. 2018), as shown in the bottom panel of Fig. A.2. We then applied the fitted trend on all the HCT spectra by dividing them with this calibration curve (assuming this calibration trend remains the same regardless of epoch). With this empirical correction, we obtained the HCT spectral sequence shown in Fig. A.3, which we passed to the regular relative flux calibration routines described in Sect. 5.1.

Model parameters

In Table A.1, we show the physical parameters obtained for the various supernovae using the emulator.

Light curve fits

In Table A.2 we list the interpolated magnitudes required for the angular diameter calculations, while Fig. A.4 shows the individual light curve fits.

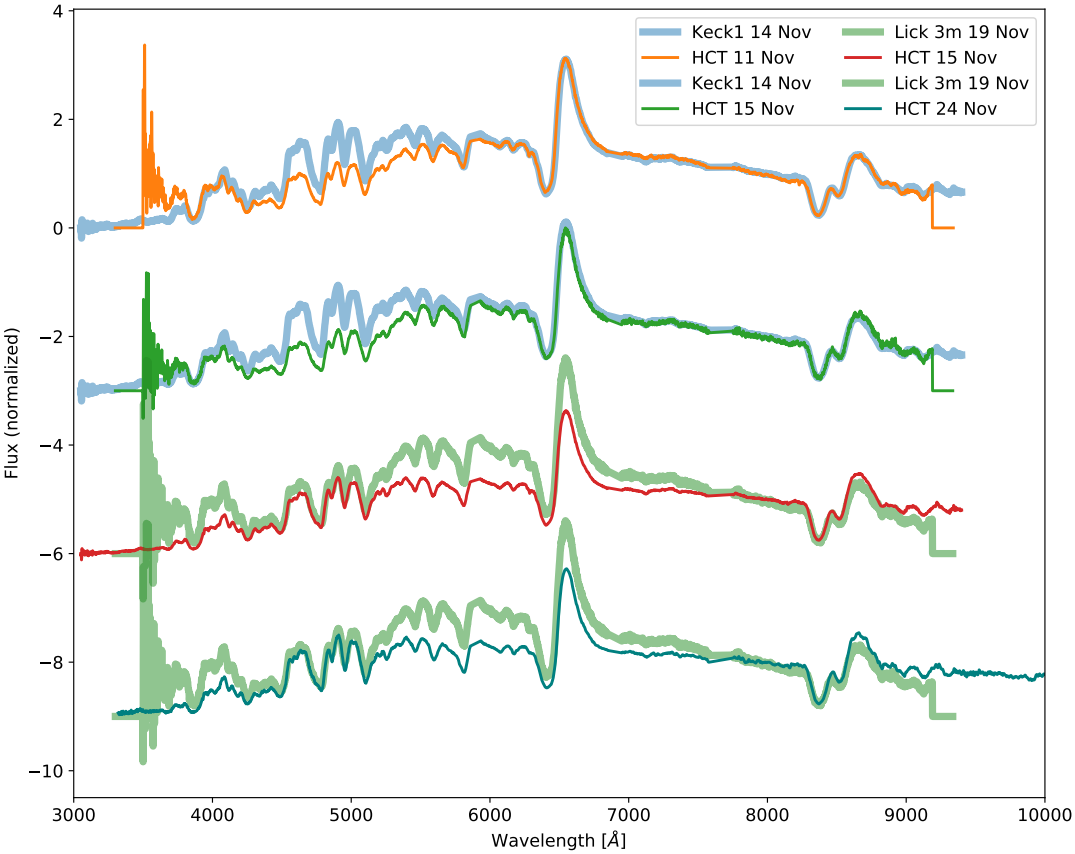

Figure A.1: Comparison of the spectra of SN 2004et taken at the HCT and the Lick observatory. The discrepancy between the two spectral sets below the 7000 $\AA$ is clear.

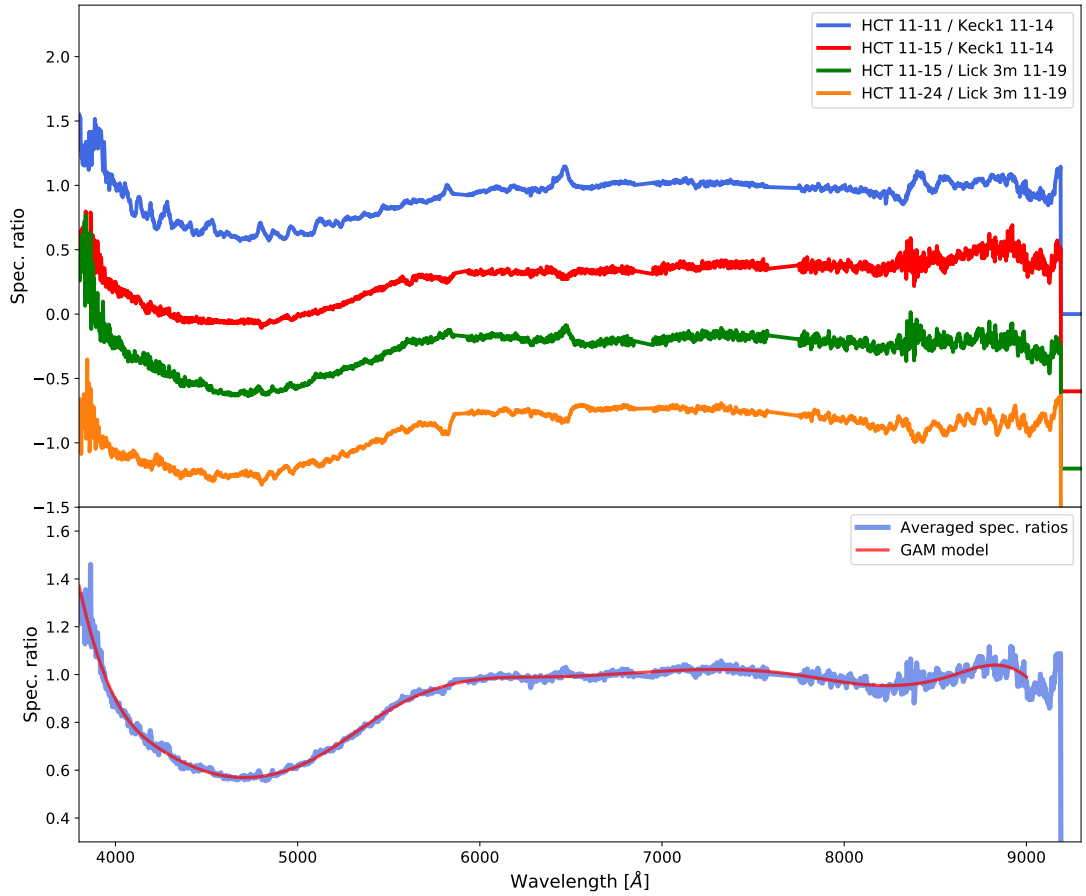

Figure A.2: Differences between the HCT and Lick observatory spectra shown in A.1. **Top panel**: Ratios of selected HCT and Keck/Lick spectra that are close in time. **Bottom panel**: Average curve calculated from the four individual ones on the top panel, along with its GAM fit.

Epoch [d]	$T_{\rm ph}$ [K]	$v_{\rm ph}$ [km/s]	n	Θ [10^8 km / Mpc]	$\Theta/v_{\rm ph}$ [d / Mpc]
M61 – NGC 4303					
2008in					
7.59	11955	8019	11.30	3.617	0.517
8.53	11081	7656	11.70	3.402	0.515
9.50	10542	7547	10.93	3.834	0.586
13.99	6948	6094	11.62	5.484	1.042
16.30	6570	6324	10.92	5.924	1.084
29.32	5962	3988	7.70	6.853	1.989
2020jfo					
7.08	10665	10518.75	9.76	4.675	0.537
9.44	10176	8898.72	9.68	5.136	0.685
11.39	8984	8606.20	9.08	5.936	0.799
12.00	9552	8071.05	9.02	5.638	0.815
13.98	8215	8450	9.86	6.420	0.884
15.00	8156	7786	9.37	6.448	0.965
19.42	6563	6519	10.50	7.984	1.417
NGC 772					
2003hl					
15.28	10425	9049	10.15	3.610	0.462
2003iq					
8.98	10196	10557	11.58	3.429	0.376
16.19	8111	8935	10.38	4.561	0.591
20.79	6571	7629	11.01	5.530	0.839
29.04	5950	5904	8.76	6.048	1.186
NGC 922					
2002gw					
16.52	6861	7396	9.47	2.501	0.391
20.12	6229	6464	8.21	2.723	0.484
21.12	6221	6304	9.13	2.677	0.491
2008ho					
20.48	6242	5053	9.53	2.404	0.551
25.43	5946	4423	8.00	2.607	0.682
NGC 6946					
2004et					
10.44	10377	12401	11.06	19.818	1.866
12.31	10308	11562	10.36	20.626	2.047
14.30	10181	10604	9.68	21.557	2.334
20.19	8505	8185	12.95	22.185	3.312
24.00	7386	7708	13.25	26.994	4.064
29.98	6294	6436	14.90	30.373	5.315
2017eaw					
11.78	9764	10388	14.69	16.971	1.891
13.77	9450	10170	12.14	18.339	2.087
15.74	8373	9975	11.18	20.771	2.410
19.73	7199	8987	11.91	23.629	3.043
21.73	6764	8569	11.88	25.082	3.388
22.72	6550	8451	11.81	25.686	3.518
24.72	6318	7866	11.46	26.551	3.907
32.83	5946	6247	8.16	28.740	5.325

Table A.1: Inferred physical parameters for the various supernovae. $T_{\rm ph}$ and $v_{\rm ph}$ denote the photospheric temperature and velocity, respectively, n is the density exponent, and Θ is the estimated angular diameter of the supernovae.

Epoch [d]	B	V	R	I	g	r
M61 – NGC 4303						
			2008in			
7.59	15.17(.02)	15.11(.01)	15.01(.01)	14.87(.02)	—	—
8.53	15.21(.02)	15.12(.01)	15.02(.01)	14.87(.02)	—	—
9.50	15.22(.02)	15.12(.01)	15.02(.01)	14.87(.02)	—	—
13.99	15.27(.02)	15.14(.01)	15.03(.01)	14.87(.02)	—	—
16.30	15.30(.02)	15.15(.01)	15.03(.01)	14.87(.02)	—	—
29.32	15.44(.02)	15.19(.01)	15.05(.01)	14.86(.02)	—	—
			2020jfo			
7.08	—	—	—	—	14.54(.02)	14.48(.02)
9.44	—	—	—	—	14.59(.01)	14.50(.02)
11.39	—	—	—	—	14.61(.01)	14.50(.02)
12.00	—	—	—	—	14.67(.01)	14.51(.01)
13.98	—	—	—	—	14.69(.01)	14.52(.01)
15.00	—	—	—	—	14.82(.01)	14.54(.01)
19.42	—	—	—	—	14.82(.01)	14.54(.01)
NGC 772						
			2003hl			
15.28	16.93(.02)	16.46(.01)	16.04(.02)	15.87(.01)	—	—
			2003iq			
8.98	15.76(.02)	15.75(.01)	15.42(.01)	15.33(.02)	—	—
16.19	15.97(.02)	15.72(.01)	15.42(.01)	15.33(.01)	—	—
20.79	16.17(.02)	15.74(.01)	15.38(.01)	15.30(.01)	—	—
29.04	16.57(.02)	15.82(.01)	15.43(.01)	15.33(.01)	—	—
NGC 922						
			2002gw			
16.52	17.66(.02)	17.32(.01)	—	16.87(.01)	—	—
20.12	17.80(.01)	17.35(.01)	—	16.84(.01)	—	—
21.12	17.83(.02)	17.36(.01)	—	16.83(.01)	—	—
			2008ho			
20.48	18.51(.01)	18.00(.01)	—	—	—	—
25.43	18.68(.01)	18.02(.01)	—	—	—	—
NGC 6946						
			2004et			
10.44	12.91(.02)	12.63(.01)	12.29(.01)	12.03(.02)	—	—
12.31	12.96(.02)	12.65(.01)	12.29(.01)	12.03(.02)	—	—
14.30	13.00(.02)	12.66(.01)	12.30(.01)	12.02(.01)	—	—
20.19	13.13(.02)	12.70(.01)	12.31(.01)	12.02(.01)	—	—
24.00	13.27(.02)	12.73(.01)	12.32(.01)	12.01(.01)	—	—
29.98	13.58(.02)	12.78(.01)	12.34(.01)	12.00(.01)	—	—
			2017eaw			
11.78	13.24(.01)	12.87(.01)	12.45(.01)	12.21(.01)	—	—
13.77	13.30(.01)	12.90(.01)	12.46(.01)	12.23(.01)	—	—
15.74	13.37(.01)	12.92(.01)	12.48(.01)	12.25(.01)	—	—
19.73	13.51(.01)	12.95(.01)	12.49(.01)	12.26(.01)	—	—
21.73	13.60(.01)	12.97(.01)	12.49(.01)	12.26(.01)	—	—
22.72	13.64(.01)	12.98(.01)	12.49(.01)	12.26(.01)	—	—
24.72	13.73(.01)	12.99(.01)	12.50(.01)	12.27(.01)	—	—
32.83	14.08(.01)	13.10(.01)	12.57(.01)	12.28(.01)	—	—

Table A.2: Interpolated magnitudes for the various supernovae. The values in the brackets denote the uncertainties of the estimates.

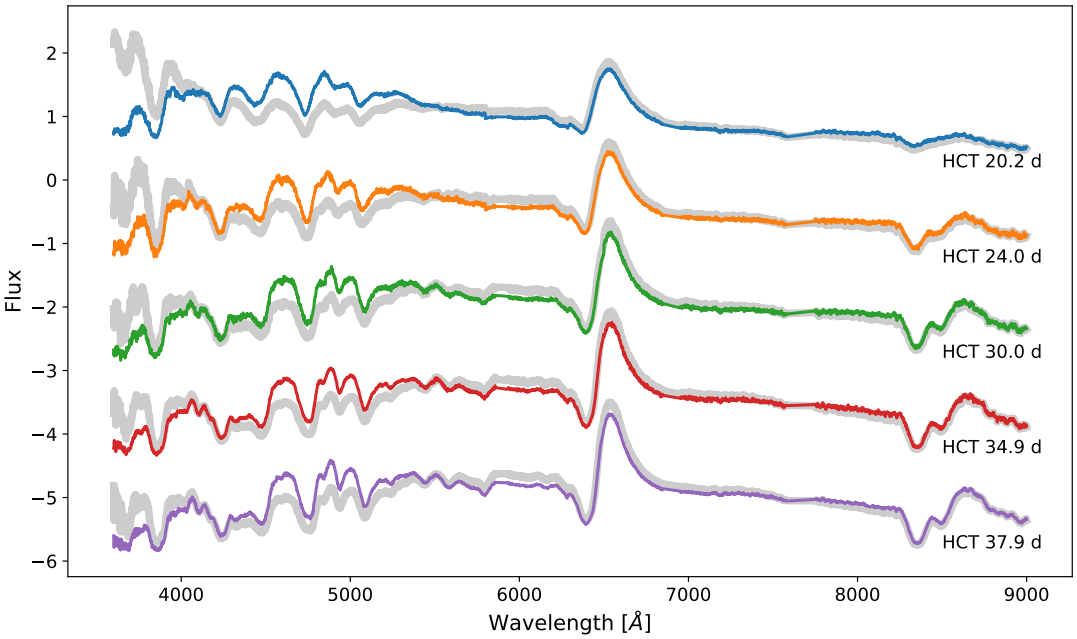

Figure A.3: Spectral sequence of SN 2004et obtained by HCT. Grey curves show the uncorrected spectra, while the coloured ones show those for which we applied the non-linear correction derived from the Keck/Lick spectra.

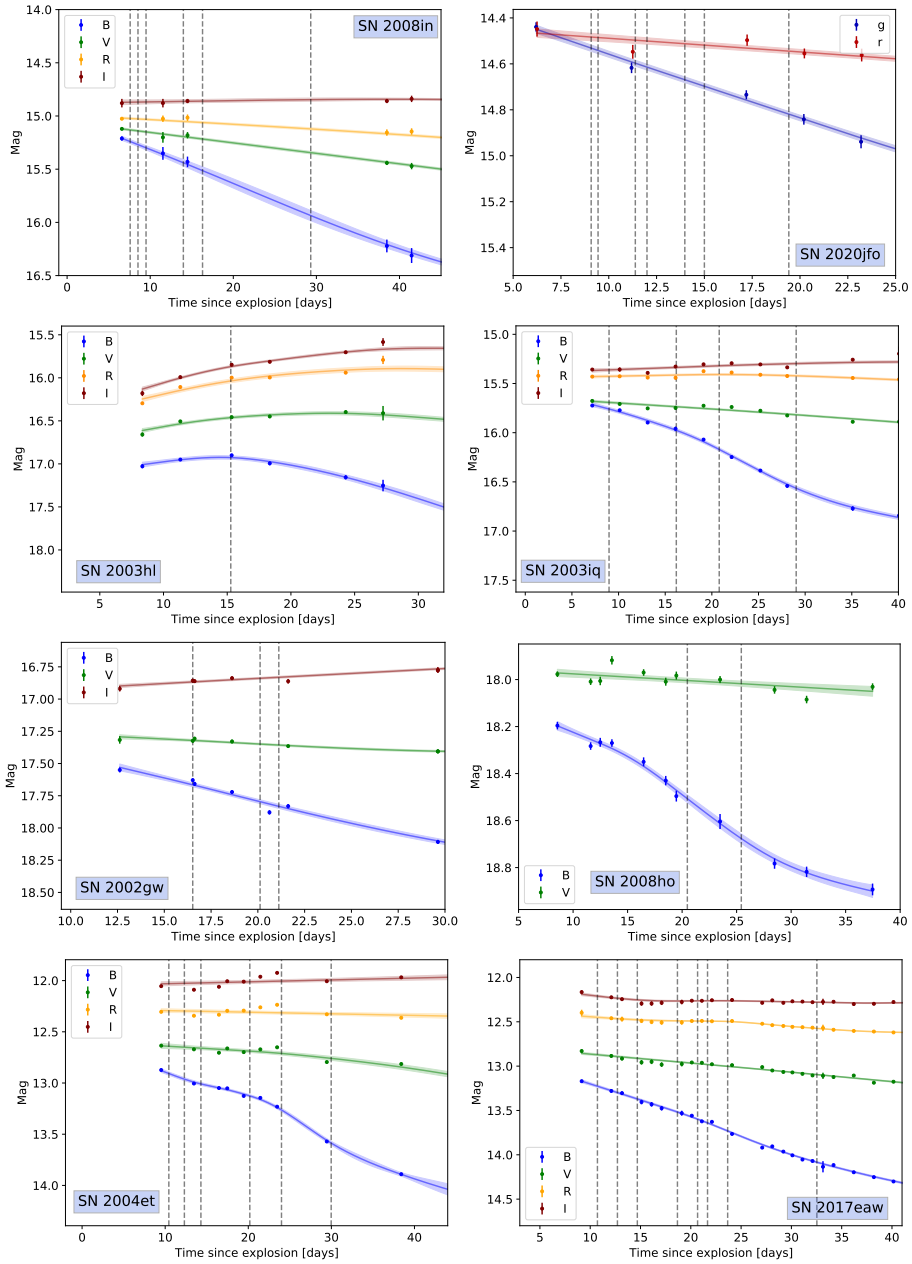

Figure A.4: Interpolated light curves of the individual supernovae. The vertical grey lines show the epochs of spectral observations.

Part III

Direct comparison of independent distance scales

Summary

Even though there are multiple distance indicators that overlap in the covered range of distances (such as Cepheids, TRGB or SBF), in the past, they were predominantly compared to one another through the estimated Hubble constant. The underlying cause was that the number of galaxies for which measurements of both techniques existed was low, with dedicated studies lacking in number to sufficiently answer the question of inconsistencies between them. However, comparing different techniques through Hubble constants is difficult due to the large number of subsequent calibration steps and the possible systematics involved.

On the other hand, recent years brought a change with a growing number of *HST* and *JWST* proposals aimed at directly cross-checking different distance indicators, along with additional publications on this subject. For the establishment of SN II distances for cosmology, it is crucial to perform a low-level cross-check between it and other primary distance indicators; not to calibrate, but to identify whether there are inherent differences between the results that may raise the question of biases. However, for SNe II, performing such a cross-check is difficult due to the number of host galaxies with known distances being limited.

To solve the issue, we performed SN II and Cepheid-based distance measurements of the Whirlpool galaxy M 51 independently of each other and compared the resulting estimates to literature TRGB distances. This analysis was published in Csörnyei et al. A&A, Vol. 678, A44, 2023, and is reproduced below under the Creative Commons BY 4.0 license. For estimating the supernova distance, we performed the EPM analysis of SN 2005cs similarly as done in Vogl et al. (2020), while for the Cepheid distance, we made use of the stellar catalogue published by Conroy et al. (2018) and analyzed it in line with the Riess et al. (2022) methodology. Both resulting distances are precise down to $\sim 3-4\%$, agree well within uncertainties, and we obtained a rich catalogue of M 51 Cepheids as well. We found significant disagreement between our distance estimates and the TRGB, which likely caused biases in previous astrophysical studies that required an assumed distance to M 51. This project showed the potential of SNe II acting as the decisive factor in the case of misalignment between Cepheids and TRGB, and it also showed how direct cross-comparison of multiple distance scales can help identify biases in various estimates. Such comparisons will help us assess the significance of the Hubble tension by resolving the near-Universe inconsistencies mainly between the TRGB and Cepheids and ensuring that all systematic effects are brought under control for all these techniques.

Own contributions I acted as the main driver of the project, taking a significant part in all aspects tied to carrying out the research and publishing it in a journal. I performed the necessary filterings of the stellar catalogue and the Cepheid selection. I carried out the modelling of the supernova and the Cepheid P-L relation, along with the distance estimations. I am the main author of the manuscript, writing the majority of it, and I created all the plots and figures. The research was fully performed during my PhD.

Reeling in the Whirlpool galaxy: Distance to M 51 clarified through Cepheids and the type IIP supernova 2005cs

G. Csörnyei, R. I. Anderson, C. Vogl, S. Taubenberger, S. Blondin, B. Leibundgut, W. Hillebrandt

Abstract

Contetxt: The distance to the Whirlpool galaxy, M 51, is still debated, even though the galaxy has been studied in great detail. Current estimates range from 6.02 to 9.09 Mpc, and different methods yield discrepant results. No Cepheid distance has been published for M 51 to date.

Aims: We aim to estimate a more reliable distance to M 51 through two independent methods: Cepheid variables and their period-luminosity relation, and an augmented version of the expanding photosphere method (EPM) on the type IIP supernova SN 2005cs, which exploded in this galaxy.

Methods: For the Cepheid variables, we analysed a recently published *Hubble Space Telescope* catalogue of stars in M 51. By applying filtering based on the light curve and colour-magnitude diagram, we selected a high-quality sample of M 51 Cepheids to estimate the distance through the period-luminosity relation. For SN 2005cs, an emulator-based spectral fitting technique was applied, which allows for the fast and reliable estimation of the physical parameters of the supernova atmosphere. We augmented the established framework of EPM with these spectral models to obtain a precise distance to M 51.

Results: The two resulting distance estimates are $D_{\rm Cep} = 7.59 \pm 0.30$ Mpc and $D_{\rm 2005cs} = 7.34 \pm 0.39$ Mpc using the Cepheid period-luminosity relation and the spectral modelling of SN 2005cs, respectively. This is the first published Cepheid distance for this galaxy. The obtained values are precise to 4-5% and are fully consistent within 1σ uncertainties. Because these two estimates are completely independent, they can be combined for an even more precise estimate, which yields $D_{\rm M\ 51} = 7.50 \pm 0.24$ Mpc (3.2% uncertainty).

Conclusions: Our distance estimates agree with most of the results obtained previously for M 51, but they are more precise than the earlier counterparts. However, they are significantly lower than the TRGB estimates, which are often adopted for the distance to this galaxy. The results highlight the importance of direct cross-checks between independent distance estimates so that systematic uncertainties can be quantified. Because of the large discrepancy, this finding can also affect distance-sensitive studies and their discussion for objects within M 51, as well as the estimation of the Hubble constant through the type IIP standardizable candle method, for which SN 2005cs is a calibrator object.

9 Introduction

The Whirlpool galaxy (or Messier 51, M 51) is one of the best-known extragalactic objects in the sky for professional and amateur astronomers. Despite its proximity and many observations conducted by generations of astronomers, the distance to M 51 remains uncertain compared to other well-studied galaxies, with little agreement between the various methods (see e.g. McQuinn et al. 2016). This uncertainty is a limiting factor for studies that use the distance as an input, such as spatially resolved or luminosity-dependent analyses, for instance in the context of star formation (Heyer et al. 2022), X-ray pulsar brightness (Rodríguez Castillo et al., 2020), or the kinematics of the interstellar medium (Pineda et al., 2020). Moreover, the distance uncertainty for M 51 also affects the extragalactic distance scale because M 51 is one of the few calibrator hosts for the type II supernova standardizable candle method (SCM) through the underluminous type IIP supernova SN 2005cs (de Jaeger et al., 2022).

In recent years, a multitude of methods has been used to constrain the distance to M 51, which yielded results in a wide range of values: the Tully-Fisher method (Tully & Fisher 1977; resulting in distances in the range of 4.9–12.2 Mpc; e.g. Tutui & Sofue 1997), the expanding photosphere method (EPM; Kirshner & Kwan 1974) applied to type II supernovae (6.02–8.40 Mpc; e.g. Takáts & Vinkó 2006; Vinkó et al. 2012), the planetary nebula luminosity function (PNLF; Jacoby 1989; 7.62–8.4 Mpc; Ciardullo et al. (2002); Feldmeier et al. (1997)), the surface brightness fluctuation (SBF; Tonry & Schneider (1988); 7.31–7.83 Mpc; e.g. Tonry et al. 2001; Ciardullo et al. 2002), and the tip of the red giant branch (TRGB; Lee et al. 1993; 8.58–9.09 Mpc; Tikhonov et al. 2015; McQuinn et al. 2016), which is most frequently quoted as the distance to M 51 (as discussed in Sect. 14). For a more complete review of these distances and their determination, we refer to McQuinn et al. (2016). Interestingly, no Cepheid distance has been determined for this galaxy to date, despite the large number of observations obtained by the *Hubble Space Telescope* (*HST*) in the past decades, for example, based on several supernovae (the type Ic SN 1994I, the low-luminosity type IIP SN 2005cs, and the type IIb SN 2011dh) or with the aim of studying stellar variability (Conroy et al., 2018). In this work, we attempt to obtain a distance to M 51 using two independent techniques: based on Cepheid variables (which is the first dedicated Cepheid study for M 51), and by applying an augmented version of EPM on SN 2005cs.

Cepheids are well-known pulsating variable stars providing one of the most robust and simple distance estimation methods through the Leavitt period-luminosity relation (Leavitt & Pickering, 1912), which made these stars the backbone of extragalactic distance measurements and Hubble constant estimations (e.g. Riess et al. 2019, 2022, see Sect. 11.1). On the other hand, type II supernovae also provide a well-established way to determine distances through the EPM (Kirshner & Kwan, 1974). This technique

provides an independent distance estimation that can be used for galaxies even in the Hubble flow (see Sect. 11.2). As opposed to the Cepheid method, which was not applied to M 51 before, the EPM has been used multiple times in the literature on SN 2005cs to constrain the distance of this galaxy (Takáts & Vinkó, 2006; Dessart et al., 2008; Vinkó et al., 2012; Bose & Kumar, 2014). However, as we further describe in Sect. 11.2, the method has recently undergone several improvements that increased its accuracy (Vogl et al., 2020). Hence, pairing and comparing the results of this augmented EPM with the first Cepheid-based measurement for M 51 offers an excellent way to narrow down the distance to this galaxy, and it provides two independent distance estimates that can serve to understand the respective systematic uncertainties.

This paper is structured as follows: in Sect. 10 we review the data we adopted for our analysis. In Sect. 11 we introduce and provide a brief outline for the different techniques. In Sect. 12 and Sect. 13 we present the individual steps of the analysis for the Cepheids and SN 2005cs. In Sect. 14 we then discuss these results and summarise our findings.

10 Data

To obtain a Cepheid distance to M 51, we made use of the catalogue and data presented in Conroy et al. (2018) (hereafter C18), which were derived based on 34 epochs taken between October 2016 and September 2017 by the *Hubble Space Telescope* (*HST*) during Cycle 24, using the Advanced Camera for Surveys (*ACS*). The photometric data published in C18 were derived using the DOLPHOT software package (Dolphin, 2000). Although this is a different software from the one that is regularly used for the reduction in Cepheid distance studies (namely DAOPHOT; e.g. Riess et al. 2022), the steps taken for the brightness and error budget estimation (e.g. the point-spread-function (PSF) model estimation or the artificial star tests) match the procedure described in the latest Cepheid works (e.g. Yuan et al. 2022). The applied photometric techniques were also tested before in the context of the Panchromatic Hubble Andromeda Treasury (PHAT) survey (Dalcanton et al., 2012), which showed its high quality. A recent work has also investigated the consistency of the different reduction methods (DAOPHOT and DOLPHOT), finding good agreement (Jang, 2023). To ensure the precision of the reduction, C18 adopted the parameter settings from Dalcanton et al. (2012) (e.g. the aperture size, the detection threshold, and the maximum step size for positional iteration; for the complete list, see Table 4 in Dalcanton et al. 2012).

The final C18 catalogue consists of F606W and F814W observations at up to 34 epochs for $\sim$ 72000 stars. In addition to presenting the photometry, C18 carried out a Lomb-Scargle method-based analysis for the observations (Lomb, 1976; Scargle, 1982) with the goal of studying long-term stellar variability in M 51. This analysis showed a period-luminosity relation that indicated that numerous Cepheids were also observed and that the data can be used to determine the distance to M 51. We emphasise that the number of available epochs in this catalogue is significantly higher than what is usually available for extragalactic Cepheids. This makes C18 an exceptionally rich dataset.

To derive the supernova distance, we applied an augmented version of EPM to the data of SN 2005cs. SN 2005cs is a type IIP supernova (SN IIP). It was discovered on 2005 June 28 by Kloehr et al. (2005). It was followed thoroughly both photometrically and spectroscopically (e.g. by Pastorello et al. 2006, 2009). We adopted the photometric data obtained by the Katzman Automatic Imaging Telescope (KAIT; Filippenko et al. 2001) owing to its good coverage and quality, along with early photometric observations from amateur astronomers as collected by Pastorello et al. (2009). We included spectroscopic observations from multiple sources that were taken in the epoch range required for our EPM approach, as described in Sect. 11.2: one spectrum from the Shane telescope[1] using

[1]Shane is the 3m Donald Shane Telescope, Lick Observatory, California (US)

KAST[2], additional three spectra from the Ekar telescope[3] obtained using the AFOSC spectrograph[4], one spectrum from the Swift satellite[5], one spectrum obtained by TNG[6] DOLORES[7], and finally, one spectrum obtained by the P200 telescope[8] using DBSP[9]. For more details on the data, we refer to Pastorello et al. (2009).

[2]Kast spectrograph
[3]Ekar is the 1.82m Copernico Telescope, INAF, Osservatorio di Asiago, Mt Ekar, Asiago (Italy)
[4]Asiago Faint Object Spectrograph and Camera
[5]Neil Gehrels Swift Observatory, NASA
[6]TNG is the 3.5m Telescopio Nazionale Galileo, Fundacións Galileo Galilei, INAF, Fundación Canaria, La Palma (Canary Islands, Spain)
[7]Device Optimized for the LOw RESolution
[8]P200 is the Palomar 200-inch Hale Telescope, Palomar Observatory, Caltech, Palomar Mountain, California (US)
[9]Double Spectrograph

11 Methods

In this section, we discuss the methods we used to infer the distance to M 51. It is important to note that the methods are completely independent of one another; in particular, the supernova-based method requires no input or calibration from other techniques and acts as a primary distance estimator.

11.1 Cepheid period-luminosity relation

The Cepheid period-luminosity relation (P-L relation hereafter; Leavitt & Pickering 1912) is the well-known correlation between the pulsation period and the luminosity of Cepheids. It has been used to determine extragalactic distances for more than a century (Hertzsprung, 1913). These distances provide the backbone of precise distance estimations today (Riess et al., 2022). The physical background of this relation and its general usage has been described in detail multiple times in the literature (see e.g. Sandage & Tammann 1968; Madore & Freedman 1991; Freedman et al. 2001; Hoffmann et al. 2016). Although easily applicable because only the brightness and pulsation period of Cepheids need to be measured, a significant limitation of the method is the effect of reddening, which increases the scatter in the P-L diagrams. To remedy this, observations are usually taken in at least two separate filters, which are then used to calculate reddening-free magnitudes through the so-called Wesenheit function (Madore, 1982),

$$W_{VI} = m_I - R_{I,V-I}(m_V - m_I), \tag{11.1}$$

where m_V and m_I denote the $V-$ and $I-$band magnitudes, while $R_{I,V-I} = A_I/E(V-I)$ denotes the total-to-selective extinction ratio. The Wesenheit function provides the greatest increase in quality when near-infrared observations are available. These observations are intrinsically less sensitive to the reddening, and make the Wesenheit magnitudes more robust against an incorrectly assumed reddening law. Nevertheless, even the optical two-band Wesenheit indices reduce the effect of reddening significantly. For our work, we employed two Wesenheit functions for the specific *HST* $F555W$, $F606W$, and $F814W$ bands,

$$W_{F555W,F814W} = F814W - 1.261 \cdot (F555W - F814W) \tag{11.2}$$

and

$$W_{F606W,F814W} = F814W - 1.757 \cdot (F606W - F814W), \tag{11.3}$$

where the total-to-selective extinction ratios were calculated for $R_V = 3.3$ assuming a Fitzpatrick (1999) reddening law and a typical Cepheid SED following Anderson (2022).

For our analysis, we chose NGC 4258 as the anchor galaxy. Its distance is known to a high precision on a geometric basis (based on a maser; Reid et al. 2019), and it hosts several Cepheids (Yuan et al., 2022). The choice of NGC 4258 was also motivated by the fact that it was observed under similar conditions as M 51: the galaxies are at approximately the same distance and were observed by *HST* with *ACS*, although using slightly mismatched filters. Hence their direct comparison allows a differential distance estimation. Since NGC 4258 was observed in $F555W$ and $F814W$, but not in $F606W$ (which was available for M 51 instead of $F555W$), we only had to characterise the PL-relation in $W_{F555W,F814W}$ (after the relevant magnitudes were converted for the M 51 sample; see Sec. 12.2). Consequently, the observed M 51 $F606W$ magnitudes and the corresponding Wesenheit function were only used directly for sample selection, as described in Sec. 12.

For the distance estimation, following Riess et al. (2022), the P-L relation for M 51 can be written as

$$[W_{F555W,F814W}]_i = \alpha \cdot (\log P_i - 1) + \beta + \mu_{0,M51} + \gamma \cdot [\mathrm{O/H}]_i, \tag{11.4}$$

where i indexes the individual Cepheids in the sample, $W_{F555W,F814W}$ denotes the Wesenheit magnitude, $[\mathrm{O/H}]_i$ is the metallicity with the usual $[\mathrm{O/H}] = 12+\log(\mathrm{O/H})$ definition, P is the period of the Cepheids, and the parameters α, β, and γ define the empirical relation. The parameters α and β can be determined by fitting the P-L relation of the anchor galaxy, NGC 4258, by adopting its distance modulus ($\mu_{0,NGC4258} = 29.397 \pm 0.032$ mag; Reid et al. 2019). For γ, we adopted the value of $\gamma = -0.201 \pm 0.071$ mag/dex, corresponding to the F555W and F814W filter set from Breuval et al. (2022). This value is slightly different from but also consistent with the factor used by Riess et al. (2022), $Z_W = -0.251 \pm 0.05$, which is applicable for the W_H Wesenheit magnitudes. However, given the 0.4 dex average metallicity difference between M 51 and NGC 4258 (Zaritsky et al., 1994; Yuan et al., 2022), this difference between Z_W and γ would only lead to a very small distance offset of 1%. Therefore, the exact choice of the metallicity factor does not affect the final estimate strongly.

11.2 Tailored EPM

To estimate the distance to M 51 based on SN 2005cs, we applied a variant of the tailored expanding photosphere method (tailored EPM hereafter; Dessart & Hillier 2006; Dessart et al. 2008; Vogl et al. 2020). The method itself is an augmented version of the classic EPM, which is a geometric technique relating the photospheric radius of a supernova to its angular diameter (Kirshner & Kwan, 1974). Although straightforward, the classical method is prone to several systematics and uncertainties (Jones et al., 2009). As pointed out by Dessart & Hillier (2005), these uncertainties can only be reliably suppressed when the relevant physical parameters for the EPM analysis are estimated through the complete radiative transfer-based modelling of the supernova spectra (which is referred to as tailoring the EPM estimation). We call this augmented version the tailored-EPM

analysis, which bears many similarities to the spectral fitting expanding atmosphere method (SEAM) introduced by Baron et al. (2004).

For the required spectral modelling of the supernova, we made use of the spectral emulator developed by Vogl et al. (2020), which is based on radiative transfer models calculated with a modified and type II supernova-specific version of TARDIS (Kerzendorf & Sim, 2014; Vogl et al., 2019). The emulator not only significantly reduces the time required for the spectral fitting, but also yields precise estimates of the physical parameters based on maximum likelihood estimation. The background of this spectral fitting method has been thoroughly described in Vogl et al. (2020), while its application and the required calibration steps were summarised in Csörnyei et al. (2023). It has been showcased in Vogl et al. (2020) and Vasylyev et al. (2022), and was also shown to provide internally consistent results for sibling supernovae (i.e. supernovae that exploded in the same galaxy, Csörnyei et al. 2023). For our work, we reapplied the steps detailed in these articles, but we summarise them for completeness in Sect. 13.

For the distance measurement, the photospheric angular diameter of the supernova first has to be estimated for each spectral epoch ($\Theta = R_{\rm ph}/D$, where $R_{\rm ph}$ denotes the radius of the photosphere, and D is the distance measured in Mpc). This estimation was made by minimizing the difference between measured and model apparent magnitudes ($m^{\rm obs}$ and m, respectively) at the given epoch, using Θ as argument,

$$\Theta^* = \arg\min_{\Theta} \sum_{\rm S} \left(m_{\rm S} - m_{\rm S}^{\rm obs} \right)^2 , \tag{11.5}$$

for all available photometric bands S. To estimate the model apparent magnitudes for each of these bands, the distance modulus formula has to be employed, and the distance has to be replaced by the angular diameter as follows:

$$\begin{aligned} m_S - M_S &= -5 + 5\log(D) + A_S \\ m_S &= M_S - 5 + 5\log\frac{R_{\rm ph}(\Sigma^*)}{\Theta(\Sigma^*)} + A_S \\ m_S &= M_S^{\rm ph}(\Sigma^*) - 5\log[\Theta(\Sigma^*)] + A_S . \end{aligned} \tag{11.6}$$

with

$$M_S^{\rm ph}(\Sigma^*) = M_S + 5\log\frac{R_{\rm ph}(\Sigma^*)}{10\ {\rm pc}}$$

Here, Σ^* denotes the set of physical parameters corresponding to the best fit, $M_S^{\rm ph}$ is the absolute magnitude predicted by the radiative transfer model at the position of the photosphere, and A_S denotes the broadband dust extinction in the bandpass. It is important to note that the distance D is the only free parameter that is not directly determined by the spectral fits. With this definition, the best-fitting angular diameter Θ^* can be determined for each of the relevant spectral epochs.

Finally, when the ejecta is assumed to be in homologous expansion ($R_{\rm ph} = v_{\rm ph}t$), the distance to the supernova and its time of explosion can be estimated through a Bayesian

linear fit to the ratios of the angular diameters and the photospheric velocities ($\Theta/v_{\rm ph}$) versus time t. In the fit, we assumed Gaussian uncertainties for $\Theta/v_{\rm ph}$ of 10% of the measured values for a given colour excess, following Dessart & Hillier (2006), Dessart et al. (2008), and Vogl et al. (2020). We set a flat prior for the distance, and for the time of explosion, we used the normalised histogram of the t_0 posterior from a fit to the early light curve as the prior (following Csörnyei et al. 2023). However, instead of applying the standard χ^2 based likelihood for the EPM, we used the modified fitting approach from Csörnyei et al. (2023) to take the correlated errors caused by the reddening into account. Essentially, we evaluated the EPM on multiple reddening values with this approach. The values were drawn from the distribution of the single epoch best-fit $E(B-V)$ estimates (see Sect. 13.4 about how these values are obtained). This approach in the end yields a more realistic uncertainty on the EPM distance.

12 Cepheids

In order to obtain a proper understanding of the data presented in C18 and to ensure the good quality of the Cepheid sample, we first reanalysed the catalogue starting from the light curves. This in turn allowed us to filter the dataset in multiple steps instead of applying cuts in the colour-magnitude diagram alone.

12.1 Filtering and sample selection

12.1.1 Period filtering

As a first quality estimation for the sample stars, we inspected the robustness of their period, if any, for the entire C18 catalogue. For this step, we compared the periods from C18 obtained with the Lomb-Scargle method in the $F606W$ and $F814W$ filters with one another and with the equivalent values we obtained using discrete Fourier transformation (DFT; Deeming 1975), for which we employed `Period04` (Lenz & Breger, 2005). Because the period should be independent of the chosen bandpass or analysis method, it can be used for an initial quality estimation. If any of the four obtained values deviated by more than 1% from the rest, we removed the corresponding star from the sample. Furthermore, additional outliers were removed based on the length of the calculated periods. Even though the C18 sample is extremely rich compared to other extragalactic light-curve samples, it is still reasonably sparse; one datapoint was taken every 10 days on average. This places a limit on the maximal non-aliased frequency that can be estimated using C18 (Nyquist, 1928; Eyer & Bartholdi, 1999). We thus calculated the Nyquist period for each of the remaining sources ($P_{Nyq.} \approx 5 - 10$ days) and kept only those for which the estimated period was longer. This single step reduced the sample size from ∼72000 to merely 950. Fig. 12.1 shows the period-Wesenheit plot for the sample after the period filtering. The plotted Wesenheit values were calculated based on Eq. 11.3, using the C18 catalogue magnitudes.

12.1.2 Filtering the light-curve shapes

After removing non-periodic stars from the catalogue, we attempted to limit our sample further based on their light curves to ensure that only Cepheids or variables with sinusoidal light curves were carried forward. The main reason for this filtering is that light curves more reliably determine the variable type than the colour and brightness. In addition to not being sensitive to reddening, this filtering also removed non-Cepheid stars that seem to scatter into the instability strip region due to reddening or blending. Because most of the sample stars were observed at 34 epochs, which is significantly

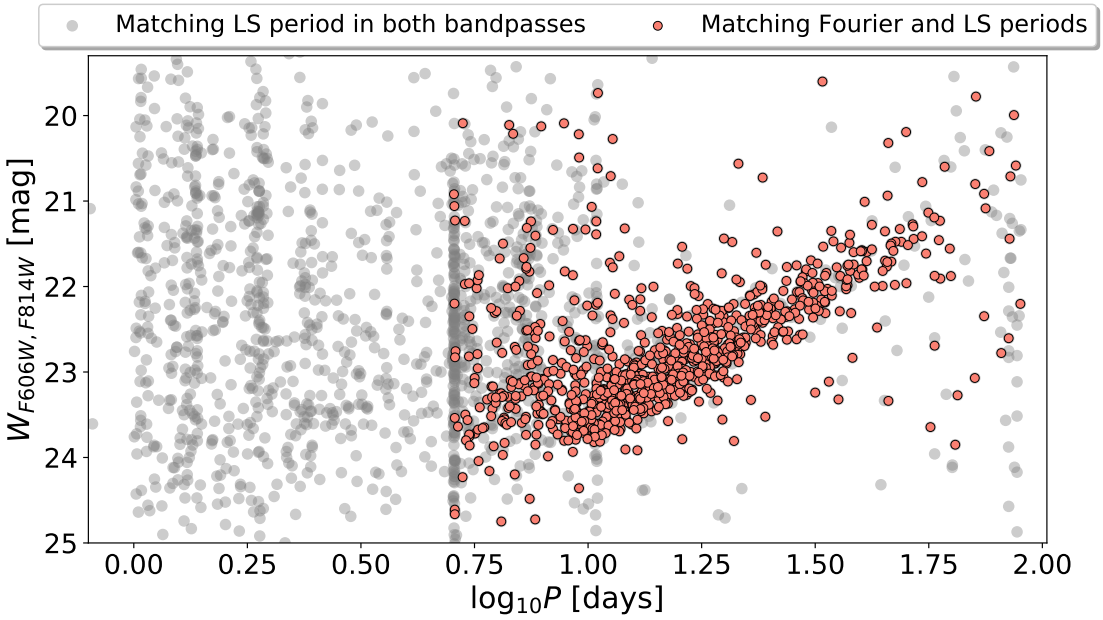

Figure 12.1: Catalogue P-L relation after the filtering based on the Lomb-Scargle (LS) and Fourier periods and the Nyquist frequency. The Wesenheit indices were calculated based on the catalogue magnitudes. The grey dots show the stars for which the LS period matched in the F606W and F814W bands, and the red dots show the stars for which the LS and Fourier periods matched for all filters.

more than what is available for Cepheids in other galaxies, we were able to perform a more detailed light-curve shape analysis. Instead of inspecting the light curves visually and selecting the Cepheid stars by hand, we applied an automated and reproducible light-curve filtering technique.

We chose to build this step on principal component analysis (PCA; Pearson 1901). The PCA is a commonly used tool for reducing the dimensionality of data, hence allowing for a fast and cheap classification and comparison of dataset elements (see e.g. Dobos et al. 2012; Bhardwaj et al. 2016; Seli et al. 2022). As a reference sample, we adopted the Cepheid set from Yoachim et al. (2009), who applied a PCA to obtain a reliable template set of Cepheid light curves. This set consists of Milky Way and LMC V - and I -band light curves that were covered well enough in phase to allow a detailed analysis of the light-curve shapes. Because the Yoachim et al. (2009) sample of Cepheids was measured in the Bessell system Bessell (1979), we converted the M 51 measurements from the *ACS* system before the light-curve fitting based on the relations described in Sirianni et al. (2005).

To apply the PCA, we first fit the light curves in the Yoachim et al. (2009) and in the M 51 C18 sample. For this purpose, we applied generalised additive models (GAMs; Hastie & Tibshirani 1990). GAMs are smooth semi-parametric models in the form of a sum of penalised B-splines, which allow modelling non-linear relations with suitable

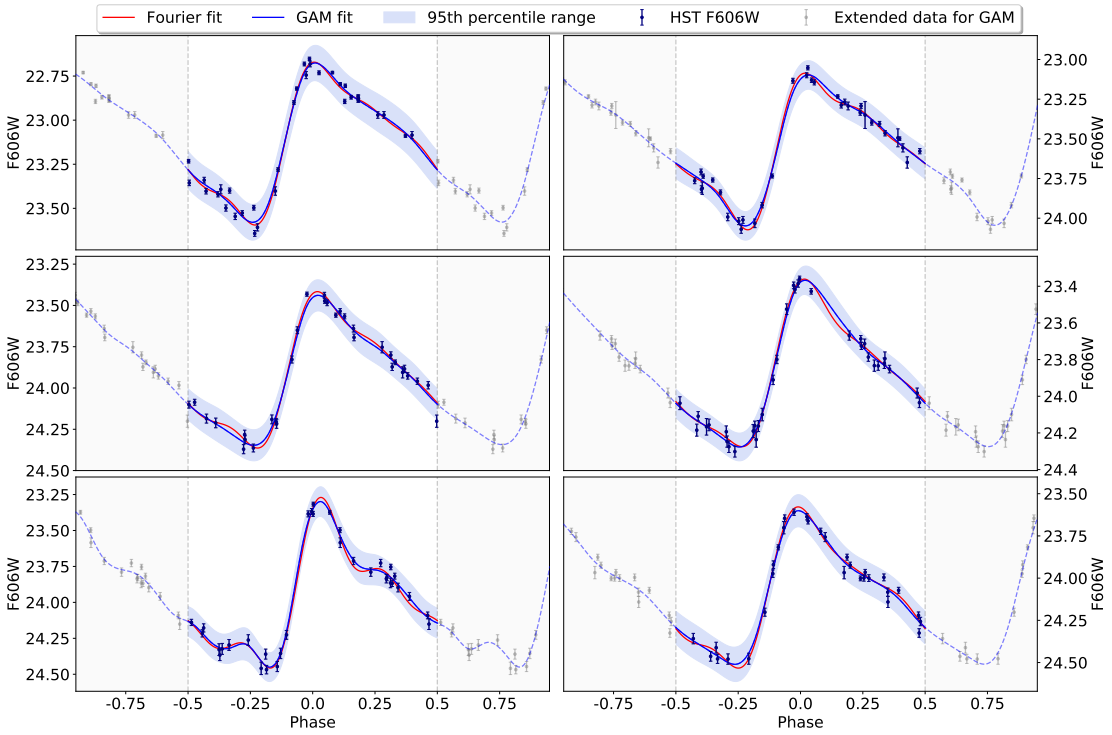

Figure 12.2: Example of GAM and Fourier fits for a handful M 51 Cepheids. The blue shaded region shows the 95th percentile range of the GAM fits. The plots show that the two models agree perfectly within these uncertainty limits. The grey shaded region shows the extension region for the GAM fitting, which was used to enhance the stability of the phase curve fits towards the edges of the region of interest (close to the phases -0.5 and 0.5).

flexibility. The method itself is similar to a Gaussian process fitting that uses splines as the kernel function. This allows a non-parametric, smooth, yet robust fitting method that takes the data uncertainties into account. To implement this method, we made use of the Python package `pyGAM` (Servén et al., 2018). While the Fourier method would also perform perfectly for Cepheid light curves, it may not handle other types of variables, such as eclipsing binaries, with similar precision. Furthermore, the number of the Fourier components has to be varied from one star to the next in order to avoid overfitting. This can lead to biases when all the light-curve models of different complexities are inspected together, however. Here, GAM models provide a viable alternative because they yield smooth light-curve models whose complexity is automatically set by the data quality. This property makes the technique favourable for generic light curves.

To fit the light curves using GAMs, we first calculated their phase curves using the C18 periods. A comparison of the GAM and DFT fitting is shown in Fig. 12.2 for a selected few M 51 Cepheids. The two models agree well for good-quality time series. In worse cases, however, in the presence of outliers or larger uncertainties, the naive Fourier method performs worse and increases the model complexity (i.e. overfits the data), as

shown in Fig. B.1. However, the GAM model remains smooth and avoids overfitting. It therefore allows for reliable filterings in more uncertain cases as well.

This light-curve fitting was carried out for the reference and M 51 sample stars. After this step, each of the light curves was rephased, so that their maximum brightness would fall on the same phase value. We then performed the PCA on the reference sample, obtaining the average curve and the eigenvectors required later on. These vectors are shown in Fig. 12.3. For our analysis, we used only the first five eigenvectors obtained by the PCA, as they contained >95% of the variance. This is similar to the choice made by Yoachim et al. (2009), who retained only the first four principal components (although they only aimed to explain ≥90% of the variation).

The basis was then used to expand the M 51 model phase curves (after applying the same phase normalisation), yielding their expansion coefficients. These expansion coefficients were then used to filter out non-Cepheid variables of the sample. To do this, we set up a grid in the field of expansion coefficients and counted the number of stars that fell in the individual grid elements (i.e. we set up a multi-dimensional histogram for the coefficients). Then, we removed every star for which the expansion coefficients fell in bins that were not covered by the reference sample stars. This approach is similar to defining a convex hull for the reference sample and using this to remove unfit elements with a lower resolution. This step ensured that only Cepheid-like or sinusoidal light curves remained in the sample.

12.1.3 Filtering the colour-magnitude diagram

As a final step of filtering, we removed stars from the sample whose colours were too blue for Cepheids or that were significantly redder than the instability strip (IS). The position of the bluer stars on the colour-magnitude diagram (CMD) cannot be explained by extinction; hence, these stars are either non-Cepheid variables or Cepheids that are strongly blended with clusters (Anderson & Riess, 2018). On the other hand, the stars on the redder end can be significantly reddened Cepheids. While the use of the Wesenheit system solves most of the errors tied to the reddening, removing these highly reddened stars will reduce our exposure to the limitations of the Wesenheit relation, resulting in a smaller scatter in the P-L relation. To this end, we constructed the cumulative density function (CDF) of the CMD by moving a dividing line along the colour axis. The slope of this dividing line was adopted from Riess et al. (2019) to ensure that it matches the instability strip.

To derive the CDF, we counted the stars left of this dividing line on the CMD, while moving it from bluer colours towards the redder ones. For the bluer edge of the instability strip, we assumed that there is a given offset value for this line at which all stars left of it are outliers, while those to its right are likely Cepheids (see the right plot of Fig. 12.4). To determine this right offset value, we calculated the first derivative of the CDF. We expect this derivative to initially be flat as long as the dividing line is left of the instability strip on the CMD. In this case, it only moves over a few stars at each step. However, when it enters the instability strip, the number of stars over which the line moves each step would drastically increase. This shows up in the derivative curve as an upturn.

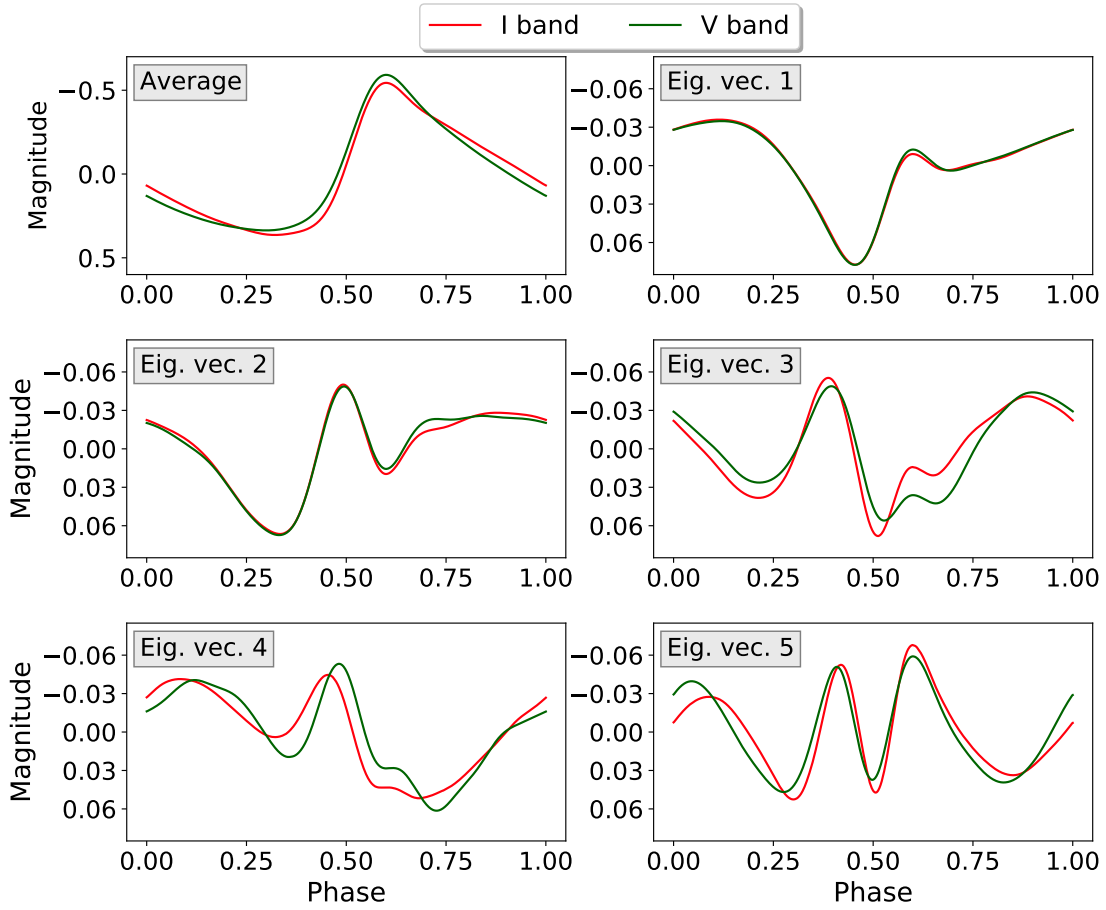

Figure 12.3: Basis vectors obtained from the PCA applied to the model light curves of the reference sample. The green curves show the Bessell V-band vectors, and the red curves show the I-band vectors.

Hence, the best position for the dividing line can be set by this upturn. Choosing the offset value corresponding to it will ensure that the filter does not enter the instability strip and thus does not remove bona fide Cepheids while removing as many outliers as possible. A similar scenario was followed at the red edge of the instability strip. Instead of searching for the rise in the CDF derivative, however, we here attempted to determine the offset where it levelled off. This procedure is shown in Fig 12.4, in which the red lines mark the filter. The best-fit offset value was found to be -0.45 for the blue edge and 0.55 for the red edge in this setup. The plot shows that the resulting Cepheid set aligns well with the reddened theoretical instability strip edges of Anderson et al. (2016) (Galactic reddening is applied), and the outliers are properly removed.

The three filters yielded a sample of M 51 variables that are most likely Cepheids in an almost completely automated manner. In total, the entire catalogue of variable stars was narrowed down from $\sim$ 72000 stars from all types to 638 Cepheids. Table 12.1

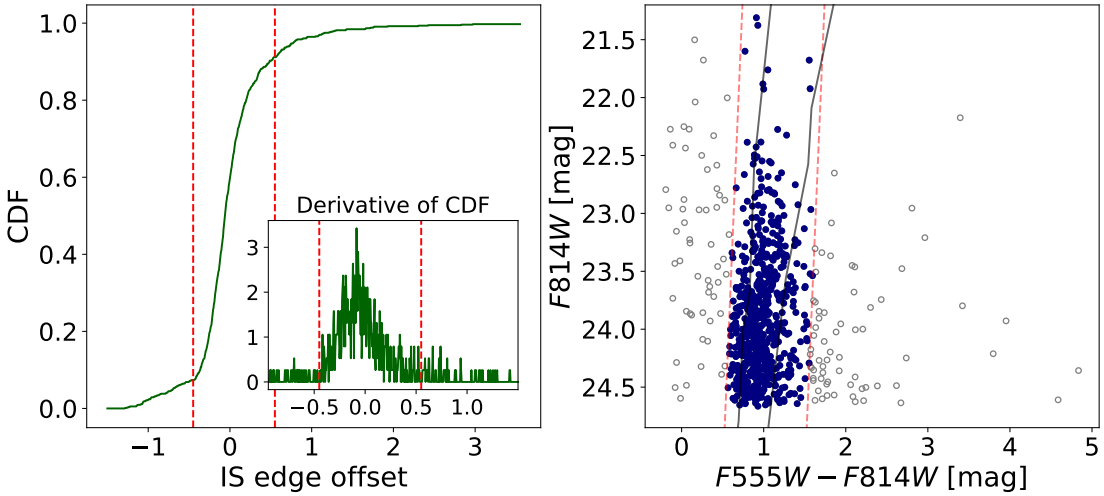

Figure 12.4: Filtering of the sample stars based on the CMD. (**Left:**) CDF of the CMD parametrised by the offset of the adopted IS slope. The inset shows the derivative of the CDF in the range of interest. The dashed red lines show the limits at which the CDF values start to either increase significantly or level off, i.e. the positions of the edges of the M 51 IS. (**Right:**) CMD of the M 51 sample, with the IS edge derived based on the CDF (red line). The grey points show the stars that were flagged as outliers. The grey curves show the theoretical instability strip edges from Anderson et al. (2016) reddened by the Galactic colour excess of 0.03 mag for comparison.

shows the change in the number of sample stars after the individual filters. As a final step, we used the GAM models to recalculate the flux-averaged magnitudes for each of the Cepheids. The magnitude uncertainties were also re-evaluated based on the GAM light-curve fit confidence intervals. The final sample of Cepheids and the corresponding period-luminosity plot are shown in Fig. 12.5. The plot shows that numerous Cepheids are available for the distance determination, and although the majority of the stars are fundamental-mode Cepheids, the overtone branch is also populated and clearly distinguishable. The positions of the Cepheids in the final sample within M 51 are shown in Fig. 12.6. The final list of M 51 Cepheids is given in Tab. B.1 in the appendix.

Filtering step	# of sample stars
-	72623
Period matching	950
Light curve filtering	759
Instability strip cut	638

Table 12.1: Changes in the Cepheid sample size after the individual filtering steps.

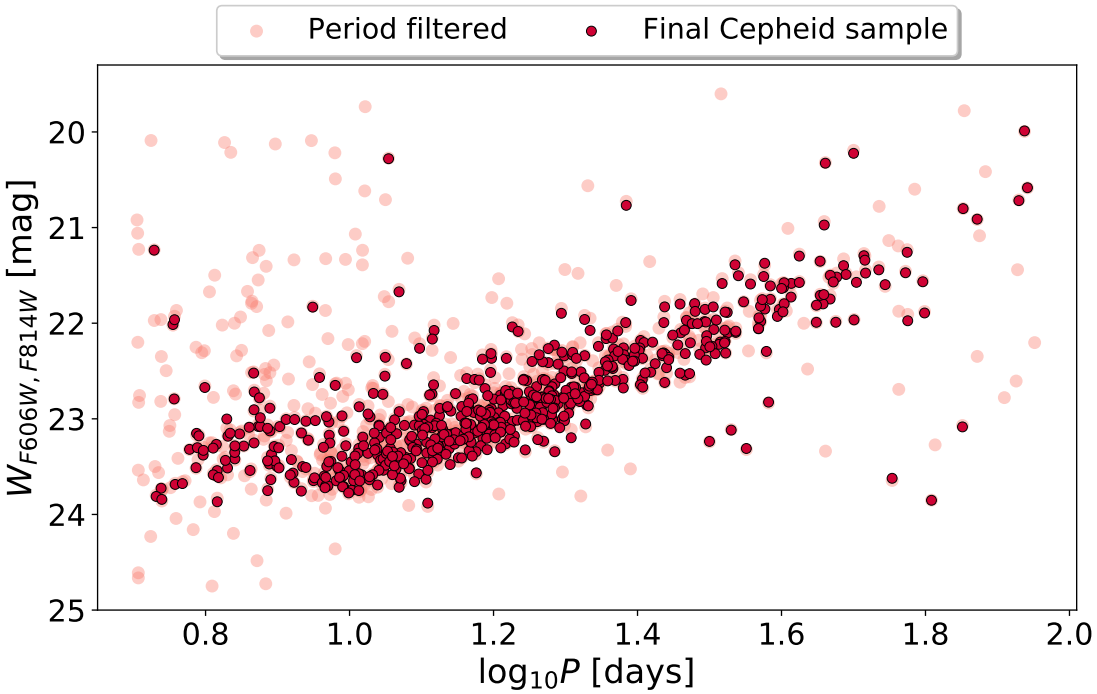

Figure 12.5: Final set of M 51 Cepheids and their period-luminosity relation. The grey dots show the resulting sample after the first filtering step, and the red points correspond to the final M51 Cepheid set after the selection for light-curve shape and CMD.

12.2 $F606W$ - $F555W$ magnitude conversion

To determine the distance modulus relative to NGC 4258, the $F606W$ observations for the M 51 sample required conversion into $F555W$. To carry this out, we made use of the spectral library of ATLAS9 stellar atmosphere models (Castelli & Kurucz, 2003) that is accessible through `pysynphot` (STScI Development Team, 2013). After limiting the models to the temperature range of Cepheids (5000 K $< T_{\rm eff} <$ 6500 K), we calculated the synthetic $F555W - F814W$ and $F606W - F814W$ colours. Then, by fitting the relation between the colours using a second-order polynomial, we inferred the $F555W$ brightnesses for the M 51 sample. We note that we carried out the conversion into each of the individual measurement epochs instead of just the Cepheid average magnitudes. The conversion curve and its fit are displayed in Fig. 12.7. The obtained transformation equation is

$$F606W - F555W = -0.129 \cdot C^2 - 0.436 \cdot C - 0.183, \tag{12.1}$$

where C denotes the original colour, $F606W - F814W$, with the sample mean subtracted from it (to minimise the fitting and conversion uncertainties). Because our model grid only extended down until 5000 K in temperature, the synthetic data do not cover all

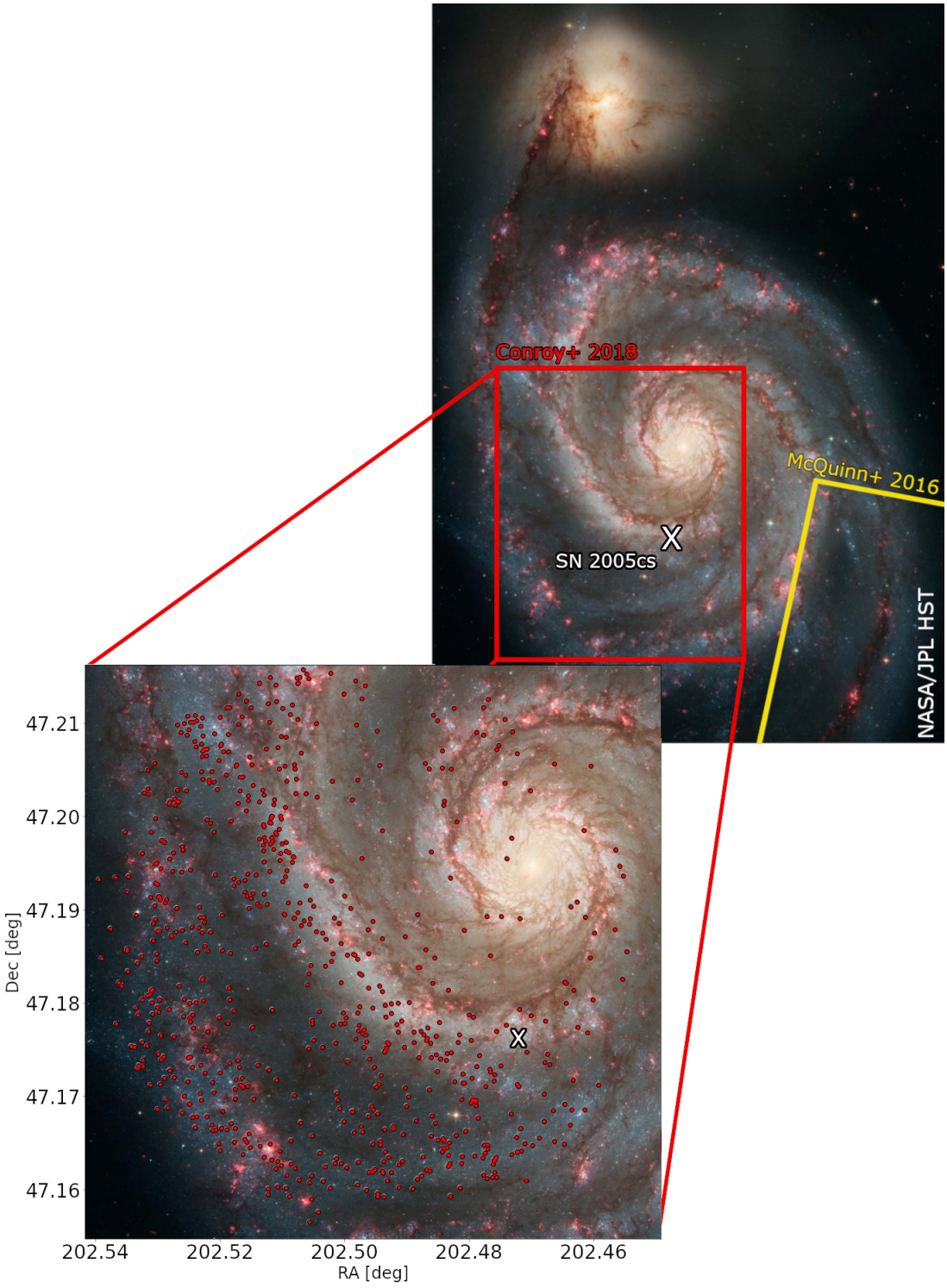

Figure 12.6: Positions of the final sample of Cepheids within M 51. The background image was taken by the *Hubble Space Telescope*. The red box indicates the field observed by C18. The yellow shape shows the position and orientation of the M 51 field used for the TRGB by McQuinn et al. (2016). The white cross denotes the position of SN 2005cs.

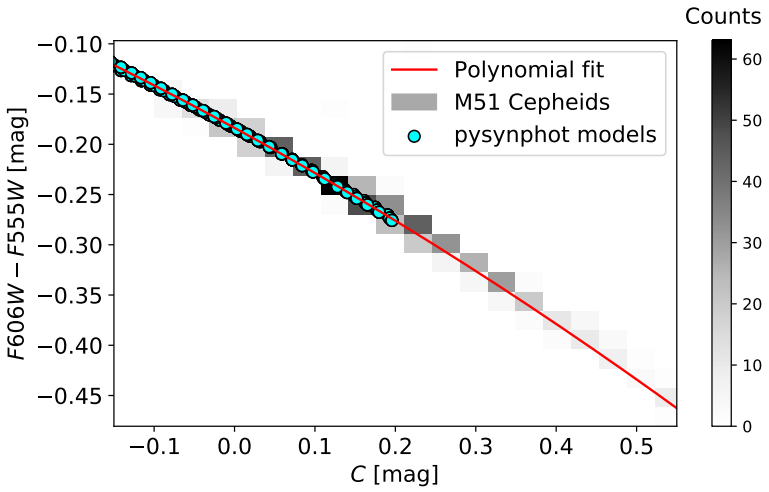

Figure 12.7: Synthetic `pysynphot` *HST* colours and the fitted trend that was subsequently used for the transformation. C denotes the $F606W - F814W$ colour, offset by the sample average. The grey shaded background shows the distribution of the M 51 Cepheid average colours after applying conversion and refitting the light curves.

colours seen in the catalogue (as some stars scatter up to redder colours due to the reddening). Nevertheless, even for the redder stars, we extrapolated an F555W magnitude using the given transformation curve. From here on, we only used the converted $F555W$ along with the original $F814W$ values for the analysis. Throughout the conversion, no reddening corrections were applied, even though this is known to impose an additional small uncertainty (because the models and the colour conversion assume an extinction-free scenario). On the one hand, constraining this uncertainty properly is hard because it requires knowledge of the internal (within M 51) reddening on a Cepheid-to-Cepheid basis. On the other hand, the good match found between the sample and the slightly reddened theoretical instability strip boundaries (Fig. 12.4) shows that the majority of the sample is not affected by strong extinction. Assuming a systematic reddening towards the M 51 Cepheids of $E(B-V) = 0.03$ mag (which is similar to the value found by our analysis of SN 2005cs; see Sect. 13) would only result in a minor $F606W - F555W$ colour difference (smaller than ~ 0.01 mag), which is negligible compared to the other systematics affecting our results. Hence, we chose to neglect this term (especially because the highly reddened stars were already clipped using the instability strip boundary estimation presented in Sect. 12.1.3).

12.3 Fitting the period-luminosity relation

In order to measure the distance to M 51 based on the newly found Cepheids, we chose NGC 4258 as the anchor galaxy. It is the only maser host with observed Cepheid variables. We adopted a distance of $D = 7.576 \pm 0.082$ Mpc for NGC 4258 following Reid et al. (2019) (which corresponds to a distance modulus of $\mu = 29.397 \pm 0.032$ mag).

The observed set of Cepheids in NGC 4258, their brightnesses in the HST bands, and their metallicities were adopted from Yuan et al. (2022). The data published in that paper were also obtained using *ACS*, hence no additional zero-point corrections were necessary. To estimate the reference P-L relation fit parameters that were later used for the distance estimation of M 51, we fit Eq. 11.4 to the NGC 4258 data set. To fit the model, we made use of the `UltraNest`[1] package (Buchner, 2021), which allows for Bayesian inference on complex, arbitrarily defined likelihoods based on the nested-sampling Monte Carlo algorithm MLFriends (Buchner, 2016, 2019). This allowed us to modify the likelihood. As pointed out for example by Breuval et al. (2022), due to the finite width of the instability strip, the Cepheids exhibit a non-negligible scatter around the true period-luminosity relation, which has to be included in the model. This intrinsic scatter is further enhanced by the photometric uncertainties. To include it, we extended the χ^2 likelihood according to Hogg et al. (2010) and applied it in the form

$$\ln p(W_{VI}|\Omega) = -\frac{1}{2}\sum_i \left(\frac{W_{VI,i} - m_{\mathrm{model},i})^2}{\sigma_i^2} + \ln 2\pi\sigma_i^2 \right), \tag{12.2}$$

where W_{VI} denotes the observed $W_{F555W,F814W}$ Wesenheit magnitudes, Ω is the set of fit parameters (slope α and offset β of the linear fit), m_{model} are the model Wesenheit magnitudes as obtained from the P-L relation, and σ^2 is the extended uncertainty, defined as the quadrature sum of the measurement uncertainty and the photometric scatter $\sigma_i^2 = \sigma^2_{\mathrm{measurement},i} + \sigma^2_{\mathrm{photometric}}$. We note that $\sigma^2_{\mathrm{photometric}}$ is defined as a constant for all sample points. It has two components: the unaccounted-for uncertainties, such as the reddening or crowding effects, and the non-negligible width of the instability strip (the intrinsic scatter). For the fitting, we assumed flat priors for all parameters. The resulting maximum a posteriori (MAP) fit along with the derived parameters is shown in Fig. 12.8.

To estimate the distance of M 51, we applied the result obtained for NGC 4258 by fitting Eq. 11.4: We fixed the slope of the P-L relation to the slope obtained from the reference fit and measured its offset relative to that of the anchor galaxy. We determined the metallicity of each M 51 Cepheid based on its position within the host and by adopting the metallicity gradient obtained by Zaritsky et al. (1994). According to this, the metallicity of M 51 is 0.4 dex higher on average than that of the anchor galaxy. To determine the distance of M 51 using only NGC 4258 as anchor, we measured the M 51 metallicities relative to those of the NGC 4258 Cepheids. It was therefore not necessary to assume a reference solar value.

Several overtone Cepheids are present in the M 51 set. They can also be used to determine the distance. However, making use of them requires the application of a few changes compared to the regular P-L analysis. We therefore conducted two versions of the Cepheid-based distance estimation to M51: one version without and one version with overtone Cepheids.

[1] https://johannesbuchner.github.io/UltraNest/

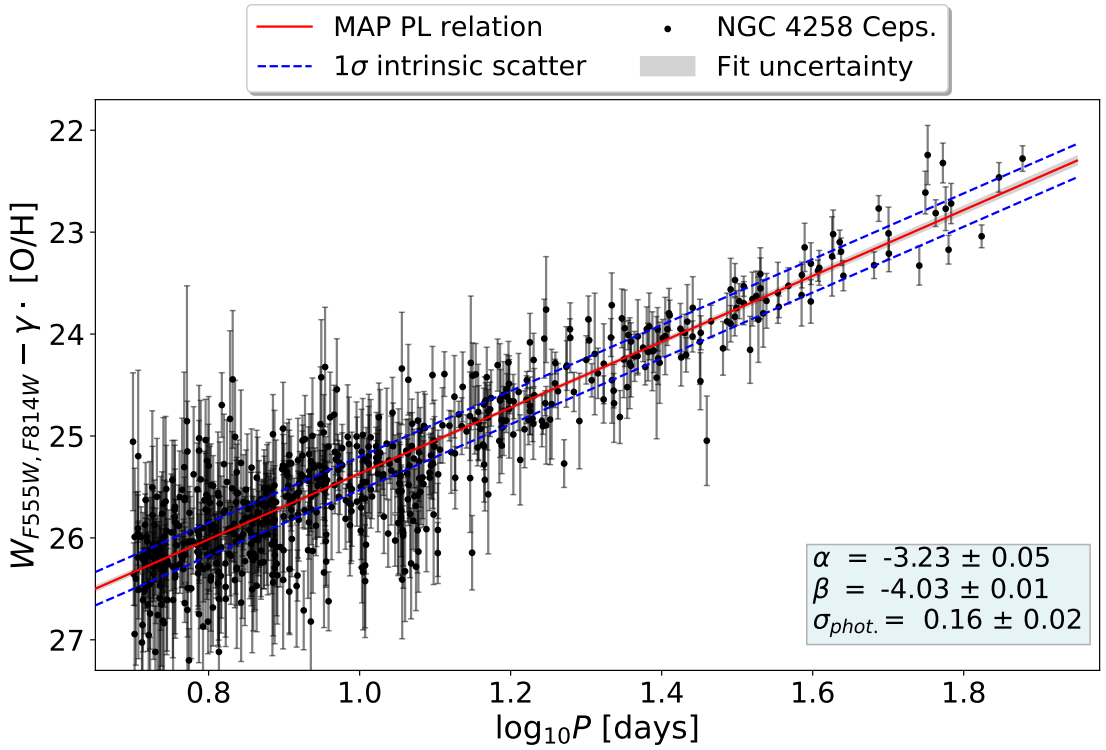

Figure 12.8: Period-luminosity relation fit to the NGC 4258 anchor data. The red line shows the MAP fit, while the dashed lines denote the range of intrinsic scatter, which is due to observational constraints and the finite width of the instability strip. For simplicity and to reduce scatter, we marginalised over the metallicity values for this plot.

12.3.1 Fit of the fundamental mode alone

In the version with the fundamental mode alone, we applied a period cut of 10 days to separate the fundamental-mode Cepheids from their overtone counterparts. The period limit for this cut was motivated by the photometric incompleteness because fundamental-mode Cepheids with shorter periods were too faint and were absent from our sample. Hence, the majority of the removed stars were overtone Cepheids. To fit the P-L relation to the filtered dataset, we applied the outlier-rejection method presented in Kodric et al. (2015, 2018). This method works iteratively, and it is based on the median absolute deviation (MAD) of the data points.

Throughout this iterative procedure, the MAD of the dataset is calculated at each step, and then the data point with the greatest deviation is discarded as long as it is at least κ times away from the model value (where κ is a tuning parameter). After this, the MAD is recalculated, and the rejection criterion is re-evaluated. For our work, we adopted $\kappa = 4$, in line with the discussion in Kodric et al. (2015). The advantage of the method is that it removes the outliers one by one, which is not only controllable, but is also governed by the statistics of the residuals. No arbitrary cuts therefore have to be made.

The obtained fit for the P-L relation of the M 51 Cepheids in this setup is displayed in Fig. 12.9. To fit the M 51 sample, we recalculated the fit parameters for the anchor galaxy NGC 4258 using only the $P > 10$ day period range to obtain an unbiased estimate on the slope (although the resulting anchor slope and offset after the step-by-step outlier removal and fitting matched the original values to better than 1%). In this way, we calculated a distance modulus of $\mu_{M51} = 29.40 + 0.09$ mag and a distance estimate of $D = 7.59 \pm 0.30$ Mpc for M 51.

It is worth comparing the fitted observed scatter values: We obtained $\sigma_{\text{phot., M51}} = 0.20$ mag for M 51 and $\sigma_{\text{phot., N4258}} = 0.16$ mag for NGC 4258. A similar result of $\sigma_{\text{phot., M101}} = 0.21$ mag can be obtained for M 101 based on the data from Hoffmann et al. (2016). It is important to note that for the comparison NGC 4258 and M 101 values we also used F160W data, which generally reduce the scatter of the Wesenheit magnitudes. The similarity of these values shows the precision of the C18 data and the high quality of the Cepheid sample well.

12.3.2 Fundamental mode and first overtone fit

To investigate how the overtone Cepheids change the distance estimate, we attempted to fit the sample without removing the overtone variables. For this estimation, we assumed that the P-L relation slopes of the fundamental mode and overtone Cepheids were the same and that they matched the slopes of the NGC 4258 Cepheid P-L relation. This assumption is supported by an earlier study on LMC Cepheids, which showed that the difference between the slopes of the fundamental mode and first overtone Cepheid P-L relations is minimal (~ 0.12 mag dex^{-1}; see Table 2 in Soszyński et al. 2015). However, it is not known exactly how much brighter the overtone Cepheids should be in the chosen Wesenheit system. For example, Soszyński et al. (2015) found a ~ 0.5 mag offset between

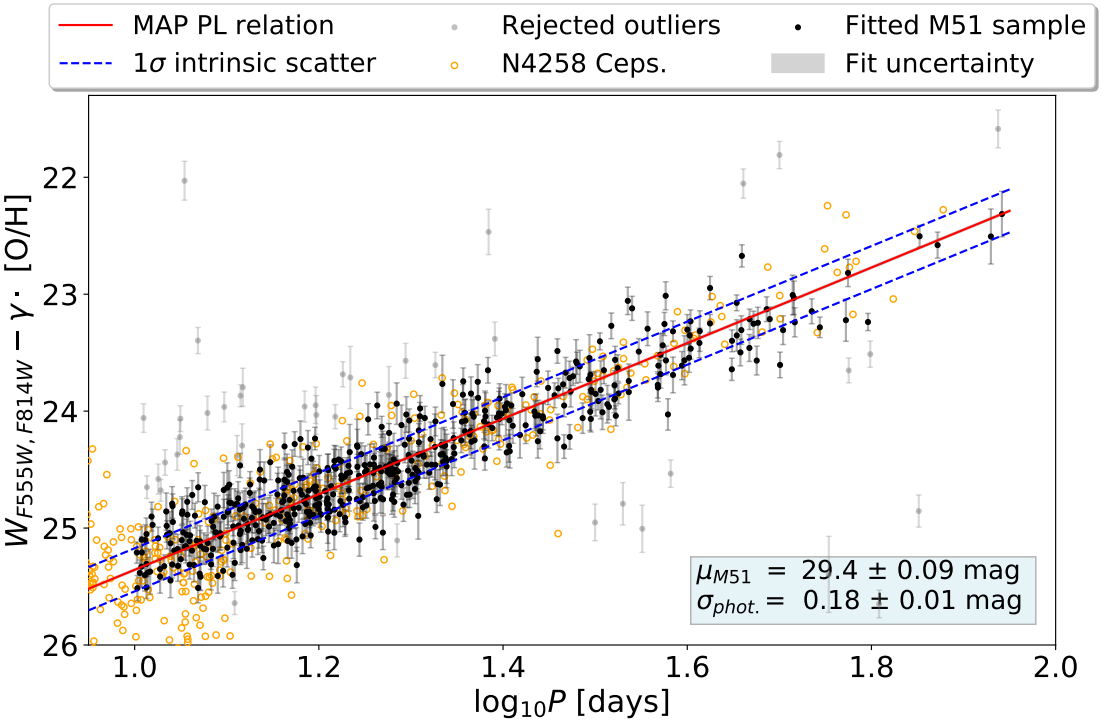

Figure 12.9: Fitting the P-L relation of the fundamental-mode Cepheids in M 51 above the period limit of $P > 10$ days. The open yellow circles show the NGC 4258 Cepheids for reference, and the faint grey points denote the stars that were rejected by the outlier-detection method. The red line corresponds to the MAP estimate, i.e. the most likely fit. The displayed distance uncertainty includes the systematic terms (namely the uncertainty in the metallicity correction and the reference NGC 4258 P-L relation).

the P-L relations. However, because (a) they used a different Wesenheit system and (b) this offset is not expected to be exactly the same in LMC and M 51, this only allows an approximate estimate for the value in our case. Although the overtone Cepheids can in principle be distinguished from the fundamental mode ones based on light curves, due to their low number they were not separated by the PCA. The analysis of the Fourier components did not separate these two subtypes either because the photometric errors on these Cepheids are relatively high. We thus attempted to separate these two types statistically based on their period-magnitude values.

To do this, we introduced two criteria during the fit. First, we assumed that all stars with $P > 10$ days were fundamental mode Cepheids because overtone Cepheids of this period are unlikely (Baranowski et al., 2009). For the second criterion, we introduced an offset parameter Δ, which measured the magnitude difference between the fundamental mode and overtone P-L relations. Throughout the fitting, each star below the period limit that was at least $1/2 \cdot \Delta$ magnitudes brighter than the fundamental mode P-L relation was assigned to the overtone class. Otherwise, it stayed among the fundamental

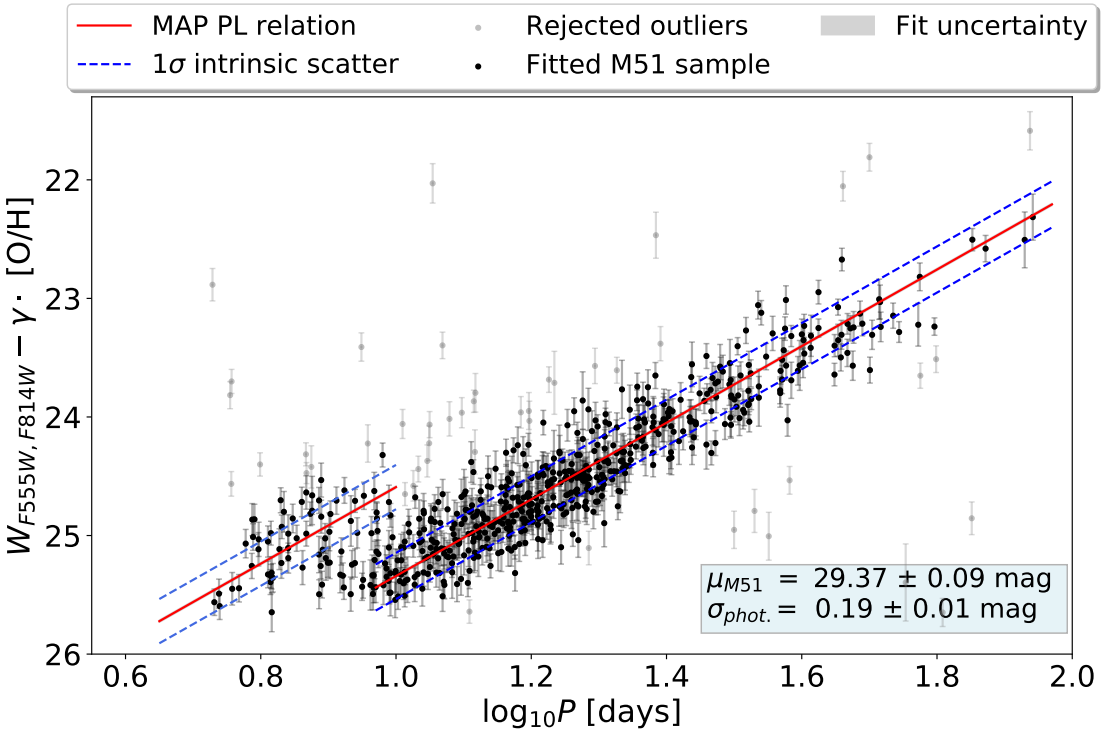

Figure 12.10: Simultaneous fitting of the fundamental mode and overtone P-L relation for the M 51 Cepheid sample. For this run, an offset of 0.75 magnitudes was assumed between the two modes. The red line corresponds to the MAP estimate. The light grey points denote the data points that were rejected by the outlier detection method, and the solid points show the points that were used to fit the relation. As before, the displayed distance uncertainty includes the aforementioned systematic terms.

mode variables. In this way, we were able to fit the P-L relation of both modes simultaneously. This ad hoc classification was revised every time a new Δ value was chosen. However, because a Bayesian fitting of this model turned out to be infeasible (due to the simultaneous incorporation of the intrinsic scatter and the offset of overtone Cepheids), we chose not to fit but to marginalise over this offset.

To marginalise, we set up multiple fits assuming different values from a reasonable offset range of [0.45, 0.95] mag. We ran the fitting for all these multiple setups (one of which is shown in Fig. 12.10), including the previously described outlier rejection, yielding a distance posterior each. Then, we combined these distributions to obtain a marginalised posterior, which included the uncertainty in the offset of the fundamental mode – overtone P-L relations.

Fig. 12.11 shows the combined posterior. By averaging over the combined posterior and then propagating the P-L relation fitting and distance modulus uncertainties valid for NGC 4258, we calculated a value of $\mu_{M51} = 29.37 \pm 0.09$ mag (a relative distance

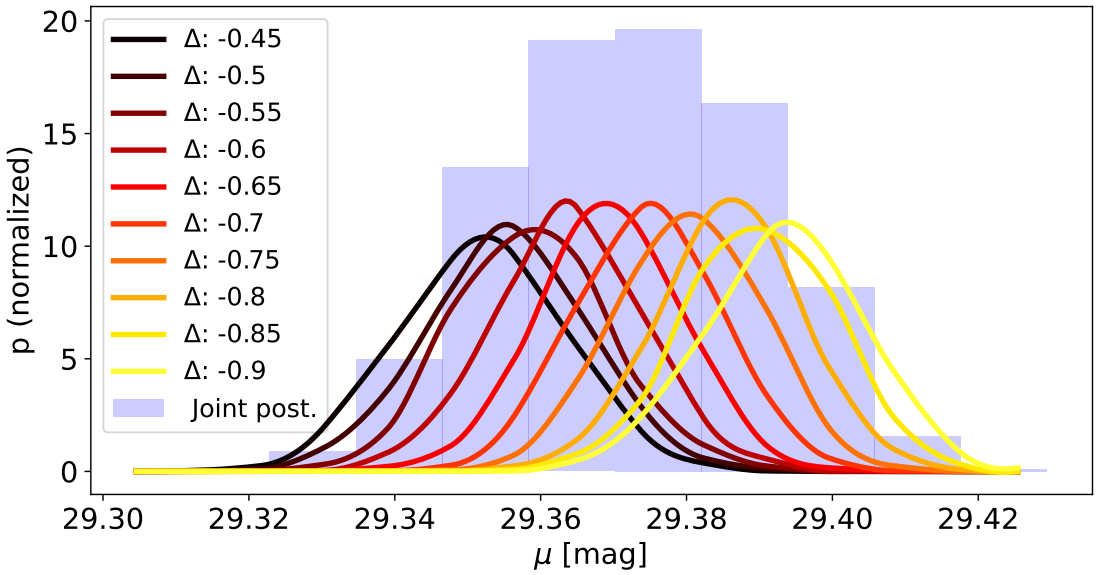

Figure 12.11: Individual distance posteriors obtained for different offset values Δ (solid curves) and the combined posterior (histogram in the background).

modulus of $\mu_{M51} - \mu_{N4258} = 0.03 \pm 0.09$ mag), which corresponds to a distance estimate of $D = 7.49 \pm 0.30$ Mpc for M 51. This estimate is consistent with the distance calculated based on the fundamental mode Cepheids alone.

To cross-check the precision of our NGC 4258-based calibration, we also carried out the distance measurement using Milky Way open cluster Cepheids as an anchor. To do this, we used the recent work of Cruz Reyes & Anderson (2023), in which the period-luminosity relation of Milky Way Cepheids was refined. To perform the calibration, we estimated the α and β fit parameters using equations 26 and 27 presented in Cruz Reyes & Anderson (2023) and based on the pivot wavelengths of the relevant F555W and F814W bands[2]. The resulting calibration parameters read $\alpha = -3.471$ and $\beta = -5.998$ (the latter of which contains the metallicity term, $\gamma \cdot [\mathrm{O/H}]_{\mathrm{MW,Cep}} \sim -1.76$). To account for the metallicity difference, we measured the [O/H] values relative to that of the Milky Way Cepheid sample when fitting Eq. 11.4. By carrying out the same distance measurement procedure as above, we arrived at distances of $\mu = 29.45 \pm 0.12$ mag and $\mu = 29.43 \pm 0.12$ mag for the versions with the fundamental mode alone and the fundamental mode plus first overtone, respectively, which perfectly agree with the results obtained previously. This validates our NGC 4258-based calibration well.

[2] http://svo2.cab.inta-csic.es/svo/theory/fps3/

13 SN 2005cs

SN 2005cs is one of the best-known SNe IIP in the literature, mostly because it belongs to the subclass of peculiar underluminous objects (Pastorello et al., 2009; Kozyreva et al., 2022). Because the host is a target that is frequently observed by amateur astronomers, several non-detections were available before its explosion, the latest one just a day before the first detection. The photometric and spectroscopic observations of this supernova are extensively described in Pastorello et al. (2009). The data we adopted and used for this supernova are summarised in Sect. 10. The time series of this supernova was analysed several times with the purpose of obtaining a distance to it based on the standardizable candle method (Hamuy, 2005) and the expanding photosphere method (Takáts & Vinkó, 2006; Dessart et al., 2008; Vinkó et al., 2012; Takáts & Vinkó, 2012). The latest independent EPM analysis by Vinkó et al. (2012) yielded a distance of 8.4±0.7 Mpc based on photospheric velocity measurements using model spectra generated by SYNOW (Parrent et al., 2010).

We repeated the analysis based on tailored EPM of SN 2005cs using the spectral emulator introduced in Vogl et al. (2020). The main goal of reanalysing the data of SN 2005cs was twofold: On the one hand, we aimed to investigate how the improvements of the spectral fitting method affect the outcome of the analysis, and on the other hand, we wished to compare this updated result to the independently obtained Cepheid distance. We stress that we did not aim to calibrate the SN II method based on this Cepheid distance because the EPM does not require any such calibration. We instead performed a single-object consistency test for the two methods. The EPM we used was already applied before on SN 2005cs in Vogl et al. (2020). We here discuss the extended version of this analysis (which includes a more complete constraint for the time of explosion, the calibration of spectra to contemporaneous photometry, and the more advanced treatment of reddening in the EPM regression). These improvements have been discussed in detail in Csörnyei et al. (2023).

13.1 Time of explosion

Estimating a high-quality distance to a supernova based on the expanding photosphere method requires precise knowledge of the time of explosion. This parameter is often determined as the mid-point between the first detection and the last non-detection, with an assumed uncertainty of half of the time elapsed between the two. However, this does not make use of all available information, such as the rise of the light curve. When this is taken into account, the EPM results can be improved by constraining the time of explosion with higher precision. Henceforth, we determined the time of explosion based

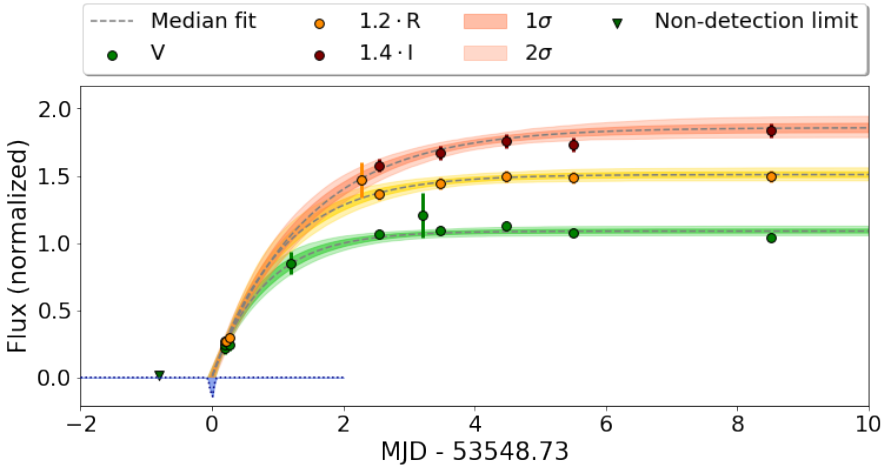

Figure 13.1: Exponential fit to the light curves of SN 2005cs, including the amateur observations. The shaded regions denote the 68% and 95% confidence intervals.

on fitting the early light curve by an inverse exponential following the reasoning of Ofek et al. (2014) and Rubin et al. (2016). We fitted the flux f in band W with a model

$$f_W(t) = f_{m,W}\left[1 - \exp\left(-\frac{t - t_0}{t_{e,W}}\right)\right], \tag{13.1}$$

where t is the time, t_0 is the time of explosion, $f_{m,w}$ is the peak flux, and $t_{e,W}$ is the characteristic rise time in the particular band. We carried out this fitting for multiple photometric bands simultaneously to increase the accuracy of the method. Similarly, as in Csörnyei et al. (2023), t_0 was treated as a global parameter for the fitting (i.e. it was the same for all bands), while each of the different bands had their own $f_{m,W}$ and $t_{e,W}$ parameters. We imposed the additional constraint on the joint fit that the characteristic rise time should increase with wavelength as seen in well-observed SNe before (see e.g. González-Gaitán et al., 2015).

Because SN 2005cs was observed very early on owing to the regular amateur observations of M 51 (see Pastorello et al. 2009 for a list of these observations, some of which are very well described [1]), the time of explosion can be very tightly constrained through the exponential fitting. The fitting that included the amateur data yielded a precise t_0 estimate of JD $2453549.23^{+0.03}_{-0.03}$ (see Fig. 13.1). This estimate was then used as an independent prior for the EPM regression.

13.2 Interpolated light curves

To measure the distance to SN 2005cs, we require knowledge of the absolute and observed magnitudes at matching epochs, which are then compared through Eq. 11.5 and Eq. 11.6. Determining the former requires the modelling of spectral observations, but photometry

[1] https://birtwhistle.org.uk/GallerySN2005cs.htm

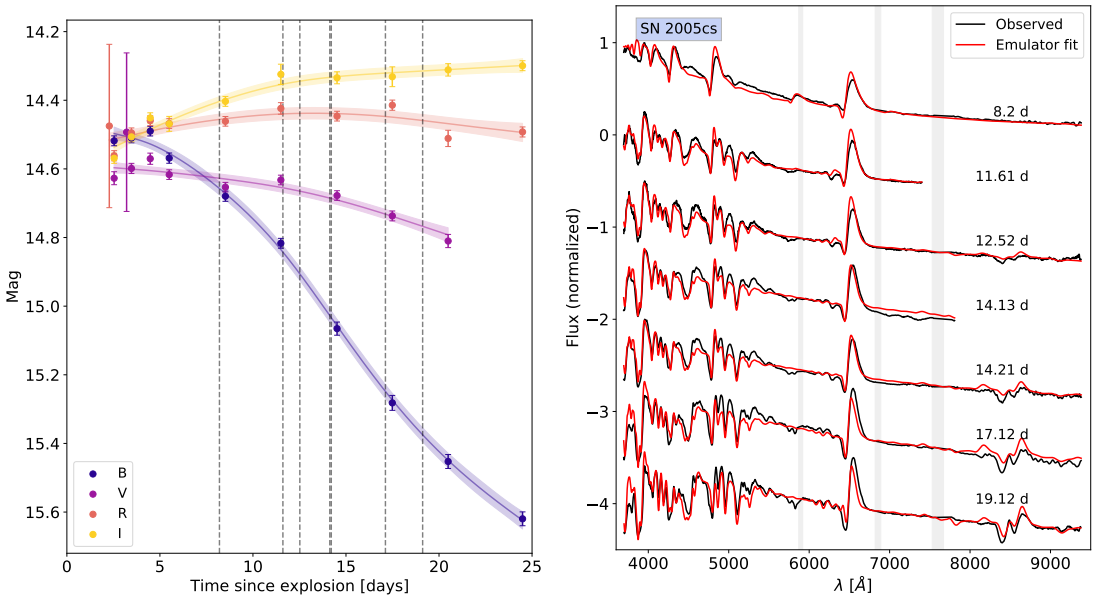

Figure 13.2: Results of modelling the photometric and spectral time series of SN 2005cs. **Left:** Gaussian process light-curve fits for 2005cs in the various bands. The dashed grey lines denote the epochs at which a spectrum was taken that was included in our sample. The epochs were measured with respect to MJD 53548.73. **Right:** The spectra and their emulator fits for the various epochs for an assumed reddening of $E(B-V) = 0.03$ mag. The grey bands indicate the telluric regions and the sodium band that were masked for the fitting.

is rarely available simultaneously with spectral epochs. We calculated the observed magnitudes at these epochs by reconstructing the light curves using Gaussian processes (GPs). For the implementation, we used the `george`[2] Python package (Ambikasaran et al., 2015). GPs present an excellent way to interpolate light curves because they provide a non-parametric way of fitting while taking into account the uncertainties in the data. As a result, we obtained smooth and continuous light-curve fits (see Fig. 13.2) that were used to estimate the brightness in the spectral epochs. The interpolated magnitudes are listed in Table 13.1.

13.3 Flux calibration of the spectra

Determining the absolute magnitudes for EPM requires estimating the physical parameters of the supernova, which are best determined through spectral fitting. Because the emulator-based modelling and hence the tailored-EPM analysis requires well-calibrated spectral time series (which is also a requirement for the precise determination of the extinction), the individual spectra had to be recalibrated first based on the photometry. We calculated the relevant set of synthetic magnitudes using the response curves from

[2] https://george.readthedocs.io/en/latest/

Epoch [d]	B	V	R	I
8.20	14.65	14.62	14.45	14.40
11.61	14.84	14.65	14.43	14.35
12.52	14.94	14.67	14.43	14.33
14.13	15.02	14.68	14.43	14.33
14.21	15.03	14.68	14.43	14.33
17.12	15.24	14.73	14.44	14.32
19.12	15.37	14.76	14.46	14.31

Table 13.1: Interpolated magnitudes for SN 2005cs. The epochs are measured with respect to the estimated time of explosion MJD 53548.73

.

Bessell & Murphy (2012) and compared them to the corresponding interpolated magnitudes. To correct for flux calibration differences that can be approximated as linear in wavelength, we fitted the first-order trend present in the pairwise ratios of synthetic and interpolated magnitudes against the effective wavelengths of the passbands (including uncertainty inflation following the description of Hogg et al. 2010). We then corrected the spectra for this trend.

13.4 Spectral modelling and tailored EPM

To fit the individual recalibrated spectra, we applied the method from Vogl et al. (2020) and passed the spectral time series to the emulator. This emulator allows for a fast and reliable interpolation of simulated spectra for a given set of physical parameters. The parameter space of the training sets we used for the emulator is summarised in Table 13.2. These training sets are identical to those used in Csörnyei et al. (2023). Similarly to that work, the choice of the training set used for the emulator was based on the epoch of the spectrum: normally, the first set would be used for spectra younger than 16 days, and the second set for older ones. However, because the evolution of SN 2005cs is accelerated, the training set designed for modelling primarily older spectra had to be employed already at an epoch of 10 days.

The epoch t of each spectrum was fixed. While the physical parameters were directly estimated by the emulator, we treated the reddening separately: as in Csörnyei et al. (2023), we set up a grid of possible $E(B-V)$ values and performed the maximum likelihood fitting for each of them by reddening the synthetic spectra with the given value. For the lower limit of the $E(B-V)$ grid, we assumed the Galactic colour excess towards the supernova, which was determined based on the dust map of Schlafly & Finkbeiner (2011). The best-fit $E(B-V)$ was then chosen as the average of the $E(B-V)$ values that resulted in the lowest χ^2 for the individual spectra.

Because SN 2005cs was a low-luminosity supernova, its spectral evolution was accelerated compared to that of other normal type IIP supernovae (Pastorello et al., 2009). It reached the limits of the emulator faster because of this and because the temperatures

	$v_{\rm ph}$ [km s^{-1}]	$T_{\rm ph}$ [K]	Z [$Z_\odot$]	$t_{\rm exp}$ [days]	n	NLTE	
		$t_{\rm exp}$ < 10 days				**H**	**He**
Min	4500	7200	0.1	2.0	9	✓	✓
Max	12000	16000	3.0	16.0	26	✓	✓
		$t_{\rm exp}$ > 10 days				**H**	**He**
Min	3600	5800	0.1	6.5	6	✓	✗
Max	10700	10000	3.0	40.0	16	✓	✗

Table 13.2: Parameter range covered by the extended spectral emulator. The individual columns show the various physical parameters: $v_{\rm ph}$ and $T_{\rm ph}$ denote the photospheric velocity and temperature, Z is the metallicity, $t_{\rm exp}$ is the time since explosion, and n is the exponent of the power-law density profile. The last columns show whether a non-local thermal equilibrium treatment was also included for H and He. The two table sections correspond to the two training sets as described in the main text.

were lower. We were therefore only able to use spectra from the first 20 days for the tailored EPM. The recalibrated spectral sequence of SN 2005cs and the corresponding models for the best-fit reddening are shown in Fig. 13.2. The best-fit parameters for the individual epochs are summarised in Table 13.3, along with the previous results from Vogl et al. (2020). The fits favoured minimum reddening, and we therefore adopted the reddening of $E(B-V) = 0.03$ mag obtained by Schlafly & Finkbeiner (2011) towards M 51. This is similar to the estimate that can be obtained from the NaID features seen in the spectra of the sibling supernova, SN 2011dh (Vinkó et al., 2012), hence it is unlikely that the foreground extinction towards M 51 is higher. Moreover, our best-fit extinction estimate is consistent with the value found by previous studies of the spectra of SN 2005cs (Baron et al., 2007; Dessart et al., 2008).

In general, we find that the obtained Θ/v estimates agree well with the previous values of Dessart et al. (2008). We note that Dessart et al. (2008) modelled two earlier epochs of SN 2005cs as well (at epochs of 4 and 5 days), but they pointed out that the emission line profiles could not be adequately reproduced. When we modelled these epochs, we encountered similar issues and found the estimated physical parameters to be unreliable. Due to these shortcomings, we decided not to include these epochs in the analysis.

As a final step of the distance determination, we performed the EPM analysis of SN 2005cs by fitting a linear function to the $\Theta/v_{ph}(t)$ values using `UltraNest`. We performed two fits with different priors on the time of explosion. For the first version, we picked a uniform prior in the range of [−1.3,2.5] days around the assumed t_0 value that was set by the last non-detection (0.5 day before the non-detection, to remain conservative) and the first KAIT detection. For the second fit, we set the prior based on the fit shown in Fig. 13.1. For both fits, the prior on the distance was set to be flat. To include the systematic uncertainties caused by the reddening in the final error estimate, we applied the treatment described in Csörnyei et al. (2023) for both versions.

Epoch [d]	$T_{\rm ph}$ [K]	$v_{\rm ph}$ [$\frac{\rm km}{\rm s}$]	n	Θ [10^8 $\frac{\rm km}{\rm Mpc}$]	$\frac{\Theta}{v}$ [$\frac{\rm d}{\rm Mpc}$]
8.20	9364	5620	9.80	5.107	1.052
11.61	7106	4816	11.16	6.617	1.590
12.52	6815	4509	11.60	6.821	1.736
14.13	6176	4354	13.72	7.553	2.008
14.21	6279	4223	13.47	7.435	2.038
17.12	6001	3993	14.13	7.650	2.218
19.12	5998	3694	13.63	7.819	2.450

Epoch	$T_{\rm C20}$ [K]	$v_{\rm C20}$ [$\frac{\rm km}{\rm s}$]	$\rm n_{C20}$	$\frac{\Theta}{v}_{\rm C20}$ [$\frac{\rm d}{\rm Mpc}$]
8.20	-	-	-	-
11.61	7003	4766	12.2	1.69
12.52	6799	4502	11.8	1.90
14.13	-	-	-	-
14.21	6720	4086	10.9	2.12
17.12	6457	4499	12.3	2.01
19.12	6349	3721	12.4	2.44

Table 13.3: Inferred physical parameters for SN 2005cs. The Θ values were calculated for the BVI bandpass combination. The values with the C20 subscript refer to the values found by Vogl et al. (2020) using an earlier version of the emulator. The epochs are measured with respect to the estimated time of explosion MJD 53548.73.

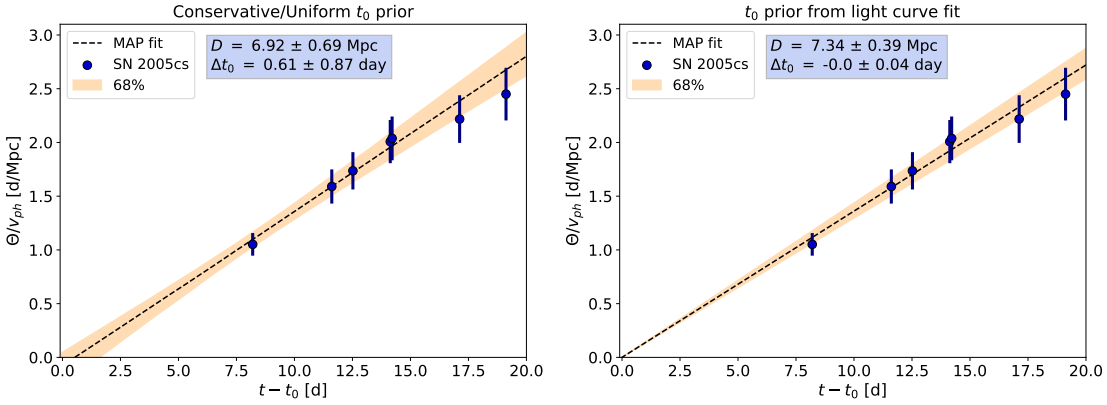

Figure 13.3: EPM regression obtained for SN 2005cs in the two versions (the **left** plot shows the more conservative approach, where we adopted a flat prior for t_0, and the **right** plot shows the fit for the t_0 prior that is informed by the light curve). The x -axis shows the time elapsed since the explosion epoch t_0, MJD 53548.73, for both plots. The points show the evolution of $\Theta/v_{\rm ph}$ for this supernova as inferred from spectral fitting. The shaded region shows the uncertainty of the fit.

The results of the two EPM regressions are shown in Fig. 13.3. In the more conservative case, we obtain a distance of $D = 6.92 \pm 0.69$ Mpc when the amateur observations are not taken into account. This corresponds to $\mu = 29.20 \pm 0.20$ mag. When we tighten the t_0 prior used for the EPM regression based on the light curve, the final fit yields a distance of $D = 7.34 \pm 0.39$ Mpc (i.e. $\mu = 29.33 \pm 0.11$ mag). We point out that the resulting t_0 estimate of the conservative version is in tension with the amateur photometric data because SN 2005cs was already visible in images taken earlier. Hence, we strongly favour the approach that uses the early light-curve fit. We also note that including the tighter constraints reduces the EPM distance uncertainties by almost a factor of two. This highlights the importance of having an informed prior on the time of explosion for a precise distance estimate.

14 Discussion

We measured two independent distances for M 51: $D = 7.59 \pm 0.30$ Mpc based on Cepheid variables and the period-luminosity relation (by including fundamental mode Cepheids alone, otherwise, this modifies to $D = 7.49 \pm 0.30$ Mpc when using both fundamental mode and first overtone Cepheids and applying the alternative fitting), and $D = 7.34 \pm 0.39$ Mpc based on the updated EPM modelling of SN 2005cs ($D = 6.92 \pm 0.69$ Mpc in the case of the more conservative approach). This consistency highlights the precision of the tailored EPM along with its robustness, and it strengthens the Cepheid distance as well. Because the estimates based on Cepheids and SN 2005cs are completely independent, their average can be taken to obtain a higher-precision distance. When the distance based on the fundamental mode Cepheid alone is combined with the favoured SN 2005cs estimate, the resulting value is $D = 7.50 \pm 0.24$ Mpc. This estimate is precise to 3.2%, which is remarkable for an extragalactic distance. As we expand on below, this distance is more than 10% lower than the estimates used previously for this galaxy.

It is important to note for the Cepheid distances that we did not consider the effects of the stellar association bias in our analysis (i.e. Cepheids may be blended with their birth clusters, which would cause a bias in the estimated brightness). The effect of this bias on the estimated distances was investigated by Anderson & Riess (2018) and will be further inspected by Spetsieri et al. (2023, in prep.). Based on their results, accounting for the bias can have sub-percent effects on the Cepheid brightnesses, and it might increase the inferred distance by the same amount (on the scale of 10^{-3} mag, as noted in Anderson & Riess 2018). We note that if we accounted for this bias, our Cepheid distance would match the supernova-based result slightly less well, but they would still remain fully consistent.

Fig. 14.1 shows the comparison of our distances with other previous distance estimates. Because we estimated the first Cepheid-based distance to M 51, there are no other results of the same method to which we can compare our value. By comparing our SN 2005cs distance to the other SN II-based distances, we find that it is lower but not inconsistent with the previous EPM and global fitting estimates of Vogl et al. (2020) and Pejcha & Prieto (2015) ($D = 7.80 \pm 0.43$ and $D = 7.80 \pm 0.37$, respectively). Most of the difference between our results and theirs can be attributed to the different choices of the explosion time. Compared to the work presented in Vogl et al. (2020), we applied a linear flux correction to the spectra, estimated the time of explosion based on light-curve fits, used an extended set of model spectra for the emulator, and calculated the distance based on a different set of observed spectra. The tentative consistency of our EPM distance with this previous estimate shows that the uncertainties are realistic, that is, the estimator is robust, despite the multiple changes made in the analysis. On the other hand, our EPM distance estimate disagrees with that calculated by Dessart et al. (2008). We found

μ [mag]	D [Mpc]	Method	Data
		This work	
$\mathbf{29.40 \pm 0.09}$	$\mathbf{7.59 \pm 0.30}$	Fund. mode P-L	Conroy et al. (2018)
$\mathbf{29.37 \pm 0.09}$	$\mathbf{7.49 \pm 0.30}$	Fund. + Overtone P-L	Conroy et al. (2018)
$\mathbf{29.20 \pm 0.20}$	$\mathbf{6.92 \pm 0.69}$	SN 2005cs EPM flat t_0	2005cs
$\mathbf{29.33 \pm 0.11}$	$\mathbf{7.34 \pm 0.39}$	SN 2005cs EPM LC t_0	2005cs
μ [mag]	D [Mpc]	Reference	Data
		Tip of the Red Giant Branch (TRGB)	
29.67 ± 0.09	8.58 ± 0.36	McQuinn et al. (2017)	McQuinn et al. (2016)
29.78 ± 0.13	9.05 ± 0.54	Tikhonov et al. (2015)	archival HST
29.79 ± 0.14	9.09 ± 0.59	Tikhonov et al. (2015)	archival HST
29.74 ± 0.14	8.88 ± 0.57	Tikhonov et al. (2015)	archival HST
		SN optical	
29.46 ± 0.12	7.80 ± 0.43	Vogl et al. (2020)	2005cs
29.46 ± 0.11	7.80 ± 0.40	Pejcha & Prieto (2015)	2005cs
29.77 ± 0.08	8.99 ± 0.33	Rodríguez et al. (2014)	2005cs
29.63 ± 0.05	8.43 ± 0.19	Rodríguez et al. (2014)	2005cs
29.51 ± 0.14	7.97 ± 0.51	Bose & Kumar (2014)	2005cs
29.37 ± 0.04	7.49 ± 0.14	Bose & Kumar (2014)	2005cs
28.96 ± 0.17	6.20 ± 0.48	Bose & Kumar (2014)	2005cs
28.91 ± 0.05	6.06 ± 0.14	Bose & Kumar (2014)	2005cs
29.62 ± 0.05	8.40 ± 0.19	Vinkó et al. (2012)	2005cs, 2011dh
29.67 ± 0.05	8.60 ± 0.20	Takáts & Vinkó (2012)	2005cs
29.38 ± 0.06	7.50 ± 0.21	Takáts & Vinkó (2012)	2005cs
29.61 ± 0.21	8.35 ± 0.81	Poznanski et al. (2009)	2005cs
29.75 ± 0.12	8.90 ± 0.49	Dessart et al. (2008)	2005cs
29.75 ± 0.16	8.90 ± 0.66	Dessart et al. (2008)	2005cs
29.50 ± 0.18	7.90 ± 0.66	Baron et al. (2007)	2005cs
29.40 ± 0.29	7.59 ± 1.01	Takáts & Vinkó (2006)	2005cs
29.02 ± 0.44	6.36 ± 1.29	Takáts & Vinkó (2006)	2005cs
29.60 ± 0.30	8.32 ± 1.14	Richmond et al. (1996)	1994I
28.90 ± 0.69	6.02 ± 1.91	Baron et al. (1996)	1994I
29.20 ± 0.30	6.29 ± 0.96	Iwamoto et al. (1994)	1994I
		Planetary Nebula Luminosity Function (PNLF)	
29.41 ± 0.12	7.62 ± 0.42	Ciardullo et al. (2002)	Feldmeier et al. (1997)
29.52 ± 0.12	8.02 ± 0.44	Ferrarese et al. (2000)	Feldmeier et al. (1997)
29.62 ± 0.15	8.40 ± 0.58	Feldmeier et al. (1997)	Feldmeier et al. (1997)
		Surface Brightness Fluctuations (SBF)	
29.32 ± 0.14	7.31 ± 0.47	Tully et al. (2013)	Tonry et al. (2001)
29.38 ± 0.27	7.52 ± 0.93	Ciardullo et al. (2002)	Tonry et al. (2001)
29.42 ± 0.27	7.66 ± 0.95	Tonry et al. (2001)	Tonry et al. (2001)
29.47 ± 0.28	7.83 ± 1.01	Ferrarese et al. (2000)	Tonry et al. (2001)
29.59 ± 0.15	8.28 ± 0.57	Richmond et al. (1996)	Richmond et al. (1996)

Table 14.1: Previous distance measurements for M 51 from the literature, along with the new estimates. The list contains the data plotted in Fig. 14.1. The Data column shows the source of the data that were used for the analysis, except for supernovae, in which case, the individual objects are listed. For a more complete list of distances and a review of each method, we refer to Table 2 in McQuinn et al. (2016).

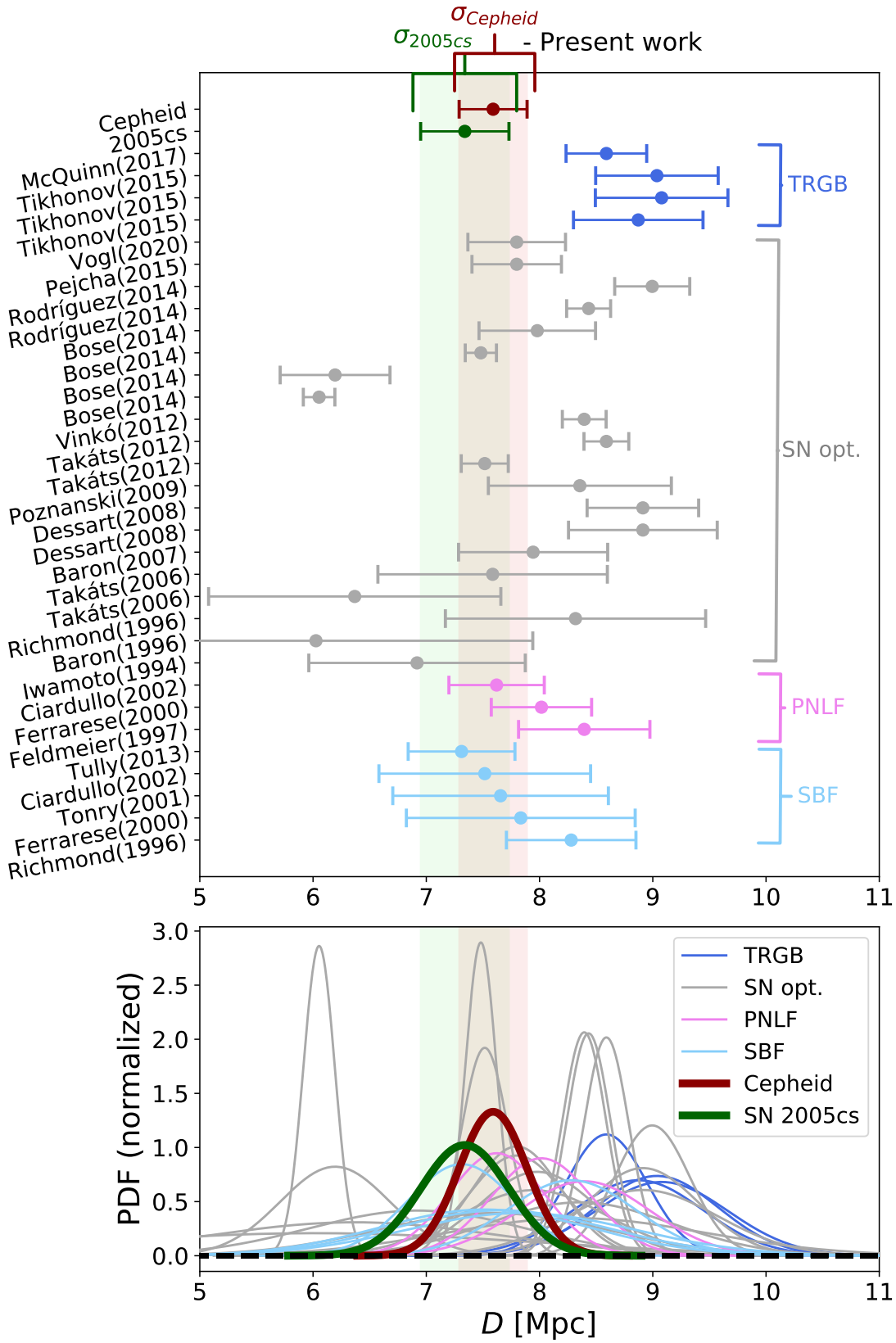

Figure 14.1: Comparison of the various distance estimates. **Top:** Individual distance estimates from multiple publications making use of the SBF, the TRGB, or optical supernova observations. The coloured regions in the background show the 1σ ranges of the estimates presented in this paper. **Bottom:** Individual distance probability distributions assuming Gaussian uncertainties.

that a significant portion of the mismatch can be explained by the 2.1-day difference in the adopted time of explosion. We note that the t_0 estimate of Dessart et al. (2008), which is purely based on the EPM regression, is in tension with the last photometric non-detection of SN 2005cs. If we accounted for this time difference by fixing the time of explosion to the value obtained by Dessart et al. (2008), the two results would be consistent.

The most relevant feature in Fig. 14.1 is the fact that the two distances obtained by us disagree by 2σ at least with the TRGB values, even with the most recently obtained value from McQuinn et al. (2017) ($D = 8.58 \pm 0.44$ Mpc, updated from McQuinn et al. 2016 to include systematic uncertainties). The difference between the distance estimates can be even more than 10%, inducing a $\sim 0.2 - 0.4$ mag difference in the absolute magnitudes ($15 - 30\%$ difference in flux). Since TRGB distances were used widely as a benchmark for studies that considered the absolute luminosities of objects within M 51 (e.g. supergiant (Jencson et al., 2022) or pulsar studies Brightman et al. (2022)), this difference in distance or luminosity affects the astrophysical results. It also causes a non-negligible change in the SNe IIP standardizable candle method as well, which uses SN 2005cs as a calibrator (de Jaeger et al., 2022). When the TRGB value is used, this object falls slightly away from the rest of the sample in terms of the calibrated absolute magnitude (see Fig. 1 of de Jaeger et al. 2022). The newly estimated Cepheid distance, however, would place SN 2005cs closer to the rest of the sample, which in turn would revise the calibration parameters as well.

An explanation for this offset between the TRGB and the Cepheid (or the EPM-based) distance eludes us. It cannot be ruled out that the offset is due to inherent systematic differences: for example, Anand et al. (2022) found an offset between the TRGB and the maser distance of NGC 4258, our anchor. However, the scale of this offset was only a few percent, hence it cannot explain the entirety of the difference we found. There were also indications of offsets between Cepheid and TRGB distances, and consequently, of the inferred Hubble constants, namely that the TRGB value of Freedman (2021) (69.8 ± 2.2 km s^{-1}) was found to be significantly different from the SH0ES estimate (73.04 ± 1.04 km s^{-1}, Riess et al. 2022). The question whether there truly is a systematic difference may be solved by acquiring a large enough sample of galaxies where both methods to be used for a precision distance estimation (see the *HST* proposal of Jang et al. 2022).

Another explanation for the offset may be that previous TRGB results overestimated the distance of M 51. As discussed by Jang et al. (2021), Freedman (2021), Anderson (2022), and Madore et al. (2023), the choice of the field (e.g. if it is too close to the disk of the galaxy) can influence the analysis through the internal reddening of the host, or through blending. Moreover, Wu et al. (2022) and Scolnic et al. (2023) have shown that the apparent magnitude of the TRGB feature depends on the contrast between RGB and AGB stars near the tip. This may be important for the McQuinn et al. (2016) TRGB value because the field chosen for analysis lies close to or partially even on top of a spiral arm of M 51. This means that the field is far more crowded and reddened and has a higher contribution from AGB stars than in usual TRGB analyses. This effect was discussed by Anderson et al. (2023) as well. They noted that disk fields could sample a different population of stars than those used to calibrate the TRGB method, and they

showed that different groups of stars can exhibit the TRGB at systematically different luminosities. On the other hand, Tikhonov et al. (2015) calculated a distance that was consistent with the estimate of McQuinn et al. (2016), even though the underlying field was farther away from M 51 (but Tikhonov et al. 2015 used one of the earlier versions of the TRGB method).

The method for determining the tip of the red giant branch on the CMD has been shown to influence the measurement, as shown by Wu et al. (2022). Curiously, most of the inconsistency between our distances and the TRGB can be remedied when the absolute magnitude of the tip is assumed to be dimmer. Recent analyses (e.g. Jang et al. 2021; Anand et al. 2022) assumed an absolute magnitude of about $M_{\mathrm{F814W}} = -4.06$ mag (similarly to McQuinn et al. 2016). However, assuming a value of $M_{\mathrm{F814W}} = -3.94$ mag, which is perfectly within the range of absolute magnitudes found by Rizzi et al. (2007), would lead to a TRGB distance estimate of $\mu = 29.55$ mag. This is also supported by the recent analysis of Anderson et al. (2023), who found a similarly fainter calibration magnitude for the TRGB method. This would be consistent with our estimates within 2σ. As noted by Rizzi et al. (2007), the TRGB absolute magnitude weakly correlates with the metallicity even in the I band, which could explain the distance offsets, given the supersolar value for M 51.

It is worth noting that despite the large offsets between our estimates and the TRGB value, the Cepheid and EPM distances are consistent with results of secondary distance indicators, such as PNLF (7.62 ± 0.42 Mpc, Ciardullo et al. 2002) and SBF (7.31 ± 0.47 Mpc, Tully et al. 2013). These methods were calibrated based on Cepheids, and a good agreement is therefore expected (nevertheless, it is important that our estimates are independent of these because M 51 had no published Cepheid distance before our analysis, and the supernova distance requires no calibration). Based on these results and the good agreement among all independent indicators except for the TRGB, we find it more likely that M 51 is located closer to us than previously assumed.

15 Conclusions

The distance to M 51 was measured using two independent approaches: the well-established P-L relation method of Cepheid variable stars, yielding a distance of $D = 7.59 \pm 0.30$ Mpc ($D = 7.49 \pm 0.30$ Mpc when both fundamental mode and overtone Cepheids are used), and by applying the tailored expanding photosphere method on SN 2005cs, resulting in $D = 7.34 \pm 0.39$ Mpc ($D = 6.92 \pm 0.69$ without using light curve information to estimate the explosion time). Combinination of these two independent estimates yields a distance of $D_{\mathrm{M}\,51} = 7.50 \pm 0.24$ Mpc for M 51. The consistency of the obtained values demonstrates the potential of SN IIP-based distances well: Even though the analysis does not rely on any calibration with other distance estimation methods, it produced a distance that is not only comparable in precision but also agrees with the result based on the Cepheid P-L relation. A similar consistency was achieved between our results and some other secondary distance indicators, such as surface brightness fluctuations or the planetary nebula luminosity function.

Both of our estimates disagree with the previously obtained TRGB values. It is unclear whether this inconsistency is an inherent difference between the various methods, even though former studies did not show systematic offsets of such magnitudes. Understanding this offset is important from the point of view of luminosity-critical studies: Because the difference between the newly obtained distances and the latest TRGB value is as large as 10%, the choice of the distance measure can significantly affect the astrophysical conclusions for objects within M 51.

This work also demonstrates that the improvements in the spectral modelling have placed non-computation intensive and accurate type IIP supernova distances well within reach. By obtaining spectral time series that are well suited for this type of analysis, these supernovae might be used to estimate distances that are well within the Hubble flow independently of the distance ladder. Data like this have been obtained by the Nearby Supernova Factory and the adh0cc collaborations, with the ultimate goal of inferring the local Universe Hubble constant through tailored EPM.

Acknowledgements

The authors thank the anonymous referee for the constructive comments and remarks that helped improve the paper. We also thank Jason Spyromilio for the comments he provided while writing the manuscript, and Zoi Spetsieri for carrying out a check on stellar association bias for the Cepheid sample. The research was completed with the extensive use of Python, along with the `numpy` (Harris et al., 2020), `scipy` (Virtanen et al., 2020) and `astropy` (Astropy Collaboration et al., 2018) modules. This research made use of TARDIS, a community-developed software package for spectral synthesis in supernovae (Kerzendorf & Sim, 2014; Kerzendorf et al., 2022). The development of TARDIS received support from the Google Summer of Code initiative and from ESA's Summer of Code in Space program. TARDIS makes extensive use of Astropy and PyNE. CV and WH were supported for part of this work by the Excellence Cluster ORIGINS, which is funded by the Deutsche Forschungsgemeinschaft (DFG, German Research Foundation) under Germany's Excellence Strategy-EXC-2094-390783311. RIA acknowledges support from the European Research Council (ERC) under the European Union's Horizon 2020 research and innovation programme (Grant Agreement No. 947660). RIA further acknowledges funding by the Swiss National Science Foundation through an Eccellenza Professorial Fellowship (award PCEFP2_194638). ST acknowledges funding from the European Research Council (ERC) under the European Union's Horizon 2020 research and innovation program (LENSNOVA: grant agreement No 771776). SB acknowledges support from the Alexander von Humboldt foundation and thanks Sherry Suyu and her group at the Technische Universität München (TUM) for their hospitality. This work was supported by the 'Programme National de Physique Stellaire' (PNPS) of CNRS/INSU co-funded by CEA and CNES. The data underlying this work is publicly available (via Wiserep for the Pastorello et al. 2009 data, and via CDS for the Conroy et al. 2018 catalogue). The data produced in this work, such as the final M 51 Cepheid catalogue and the flux calibrated spectral time series of SN 2005cs is available at the GitHub page of the author [1]. The Cepheid catalogue shown in Table B.1 is available in electronic form at the CDS via anonymous ftp to cdsarc.cds.unistra.fr (130.79.128.5) or via `https://cdsarc.cds.unistra.fr/cgi-bin/qcat?J/A+A/`.

[1] `https://github.com/Csogeza/M51`

Appendix

Examples for differences between the Fourier method and GAM

Fig. B.1 shows examples of light curves for which the Fourier and GAM fits yielded significantly different results. In these cases, the naive Fourier method overfits the data. This can be avoided by limiting the number of Fourier terms used for the fitting for each object individually. However, the GAM method performs well in these cases and results in smooth light curves that can still be compared reasonably well to the rest of the sample. Even though the uncertainties are high, these variable stars were still included for the further filtering steps because of the smooth GAM fits, whereas the Fourier method would have removed them using our approach.

Cepheid catalogue

In Tab B.1 we show the list of Cepheids that were found by our filtering. This list is complete, that is, even the stars that were flagged as outliers by the σ clipping method are included. For the full table including photometric errors, we refer to the online version of the article. This table includes all variables that remained in the sample after removing the stars with a bluer colour than the instability strip. The σ clip column shows the variables that were not classified as outliers by the σ clipping algorithm we applied (denoted with the plus). For the full table, we refer to the online appendix of the article or the alternative sources described at the end of the acknowledgements section. The metallicities are measured according to the Zaritsky et al. (1994) scale.

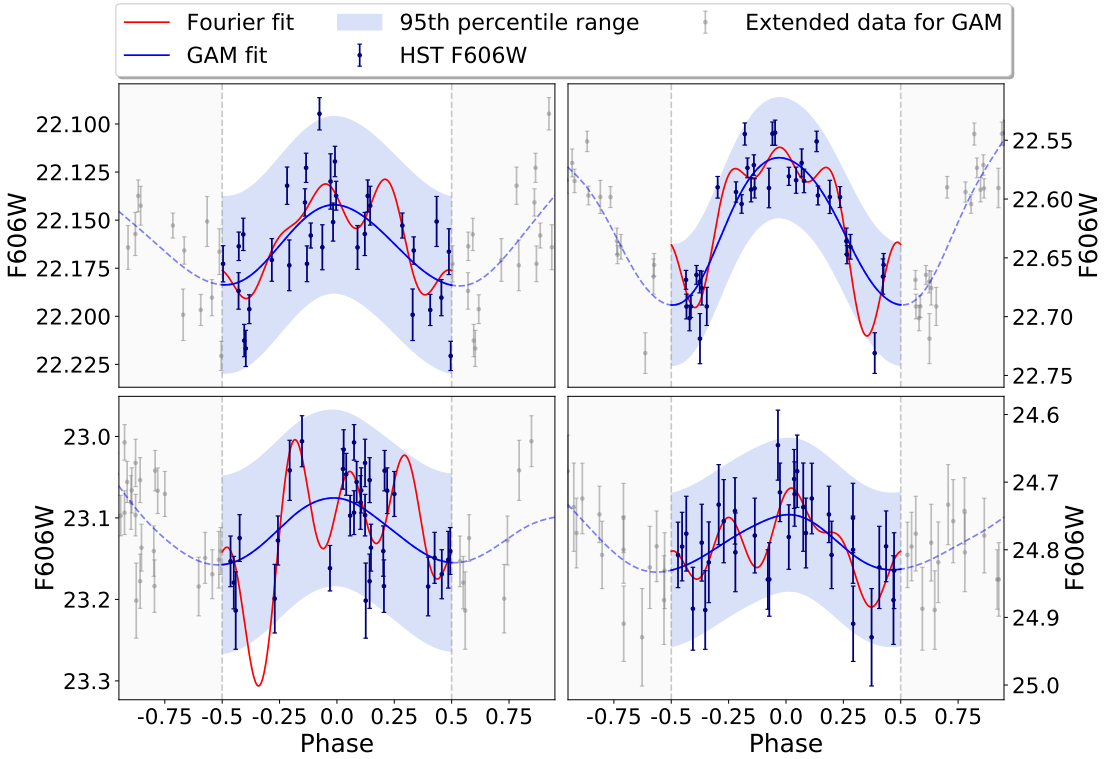

Figure B.1: Example light-curve fits for which the Fourier and the GAM method yield different results.

RAJ2000 [deg]	DEJ2000 [deg]	P [days]	F555W [mag]	F606W [mag]	F814W [mag]	$W_{F555W,F814W}$ [mag]	[O/H] [dex]	σ-clip
202.467	47.178	86.59	23.231	22.765	21.676	19.716	9.303	
202.471	47.189	87.42	22.811	22.520	21.760	20.435	9.346	+
202.531	47.202	24.22	22.872	22.601	21.882	20.633	9.120	
202.497	47.203	50.13	23.488	23.020	21.923	19.949	9.253	
202.522	47.207	71.16	22.926	22.651	21.926	20.664	9.153	+
202.480	47.187	45.63	23.445	23.114	22.275	20.799	9.318	+
202.476	47.212	74.44	23.603	23.235	22.324	20.711	9.297	+
202.494	47.205	52.08	23.184	22.972	22.385	21.378	9.265	+
202.515	47.201	48.55	23.334	23.090	22.426	21.281	9.186	+
202.516	47.171	51.81	23.350	23.087	22.384	21.165	9.160	+
...	...	...	...	...	...	...	...	...

Table B.1: List of the Cepheid variables found in our analysis.

Part IV

Uncovering limitation for Cepheid distances

Summary

Cepheids, being the oldest extragalactic distance estimators, have been investigated for systematics multiple times. One of the issues that were recurrently re-analysed is the issue of binarity; given that about $40-45\%$ of Cepheids occur in binary systems (Neilson et al., 2015), it is crucial to investigate if the presence of a companion star affects the period-luminosity relation fits significantly. One aspect that may cause biases is the orbital motion of the Cepheid, which can alter the measured parallax values, leading to a distance bias for those objects (Groenewegen, 2018).

To detect companions around Cepheids efficiently, one may investigate the changes in their pulsation periods, as they can bear the marks of binarity. For this, one has to calculate the light curve $O-C$ diagram (Sterken, 2005) for each sample star. This technique provides a framework for the efficient comparison of observations and predictions, allowing us to test for, among other effects, the binary nature of the Cepheids. In our work, published in Csörnyei et al., MNRAS, Vol. 511, Issue 2, 2125−2146, 2022, which is reproduced below with permission from MNRAS, we presented the $O-C$ diagrams of 148 Galactic Cepheid variables, covering up to a century of photometric observations for each star, hence providing the most precise period-change values to date. We found indications of binary nature for multiple Cepheids and investigated the light-time effect for one particular object. Apart from presenting a catalogue of period change rates, we also brought attention to a systematic effect that was not considered before for these variables: in our sample, all long-period ($P > 20$ days) Cepheids and a significant fraction of the shorter-period sample showed signs of period-fluctuations, or the random-walk of the period, beyond the steady evolution. The importance of this effect lies in the fact that its strength scales with the period length; as Percy et al. (1997) showed for Mira variables, the fluctuations cause bigger and bigger uncertainties as one looks at the longer period members of the sample. According to our analysis, this can account for $\sim 1\%$ period uncertainty for a 100-day period Cepheid. While this may not cause a significant issue for current-day studies, as the effect of fluctuations averages out for shorter period variables, it can cause noticeable uncertainties when only the bright, long-period stars are utilized for distance estimation. Moreover, this poses an upper limit for the precision with the current methodology, as the fluctuations can only be reliably separated from the period values through a meticulous $O-C$ analysis. This warrants further studies into the pulsation and fluctuations of Cepheids.

Own contributions I acted as the main driver of the project, taking part in the observations, leading the analysis, and summarizing the results. I gathered the data for each of the variables, and I calculated all the $O-C$ diagrams. I performed the analysis of the data, both for the individual and collective analysis, along with the statistical tests. I am the leading author of the article, I have written a significant part of the content in the manuscript, and I have created the figures. I carried out part of this work during my BSc and MSc programmes, namely the data gathering and $O-C$ calculation of multiple sample stars, but the research of the full sample, along with the collective analysis was conducted during my PhD. The manuscript was entirely written up during my PhD.

Study of changes in the pulsation period of 148 Galactic Cepheid variables

G. Csörnyei, L. Szabados, L. Molnár, B. Cseh, N. Egei, Cs. Kalup, V. Kecskeméthy, R. Könyves-Tóth, K. Sárneczky, R. Szakáts

Abstract

Investigating period changes of classical Cepheids through the framework of O-C diagrams provides a unique insight to the evolution and nature of these variable stars. In this work, the new or extended $O-C$ diagrams for 148 Galactic classical Cepheids are presented. By correlating the calculated period change rates with the *Gaia* EDR3 colours, we obtain observational indications for the non-negligible dependence of the period change rate on the horizontal position within the instability strip. We find period fluctuations in 59 Cepheids with a confidence level of 99%, which are distributed uniformly over the inspected period range. Correlating the fluctuation amplitude with the pulsation period yields a clear dependence, similar to the one valid for longer period pulsating variable stars. The non-negligible amount of Cepheids showing changes in their $O-C$ diagrams that are not or not only of evolutionary origin points toward the need for further studies for the complete understanding of these effects. One such peculiar behaviour is the large amplitude period fluctuation in short period Cepheids, which occurs in a significant fraction of the investigated stars. The period dependence of the fluctuation strength and its minimum at the bump Cepheid region suggests a stability enhancing mechanism for this period range, which agrees with current pulsation models.

16 Introduction

The classical Cepheid variable stars (hereafter Cepheids) are objects of fundamental importance for both stellar astrophysics and extragalactic distance determination. These variables represent a brief phase in the post-main-sequence evolution of intermediate-mass ($4 - 12$ $M_{\odot}$) central helium burning stars, which populate the classical instability strip in the Hertzsprung–Russell diagram (HRD). Their importance lies in the periodic variability of these objects: the characteristic feature of their pulsation, the period, allows for the calibration of the cosmic distance ladder and an independent estimation of the Hubble constant via the famous period-luminosity (PL) relation (Freedman et al., 2001; Riess et al., 2019) or its reddening free formulation (Wesenheit function). Measuring the exact value of the period and the rate of its change can also give implications on the physical parameters of these stars and their evolution using pulsation (Bono et al., 1999; Marconi et al., 2010) and evolutionary models that take into account various recently discovered effects, e.g. realistic core overshooting and meridional mixing from rapid rotation (Maeder & Meynet, 2001; Anderson et al., 2014). It has been shown that, apart from the pulsation period, which is obviously the most crucial property for these variables, light curve parameters (amplitude, skewness and acuteness) can play an important role in the estimation of physical properties (Bellinger et al., 2020), however, the role of period changes on the precision of these estimations has not been investigated. Since Cepheids in different locations within the instability strip exhibit different period change rates, these values can be used to infer the probable value of physical properties of the stars, as well (Turner et al., 2006).

The pulsation period of Cepheids can change for multiple reasons. In most cases, the physical process behind these changes is stellar evolution, i.e. the movement of the Cepheid on the HRD. This trajectory through the instability strip is associated with changes in the physical properties, which in turn change the period of pulsation: if the star evolves towards the cool edge of the instability strip, the period increases, while it decreases when evolving towards the hot edge. Superimposed on the curve corresponding to stellar evolution, low-frequency quasi-cyclic period variations can also appear, e.g., in the case of S Vul (Mahmoud & Szabados, 1980), several long-period Cepheids in the LMC (Rodríguez-Segovia et al., 2021) or for many Cepheids mentioned in this article. These variations are due to period and phase fluctuations accumulating in time and building up a phase-lag that will appear as a change in the pulsation period (Balázs-Detre & Detre, 1965). The timescale of these fluctuations varies within a wide range, from decades to even centuries. Due to these variations, period determination using $O - C$ diagrams can become uncertain, thus other methods might be necessary for this purpose when the baseline of the $O - C$ diagrams is not long enough to reliably separate the signals originating from the evolution and the fluctuations (Lombard &

Koen, 1993). In most of the cases, long term photometry allows for the reliable separation of the stellar evolution from the fluctuations on the $O-C$ diagram. However, in some cases, as for BY Cas and DX Gem, the time span covered by observations and the timescale of fluctuations are comparable, which can even lead to the misidentification of the Cepheid's crossing number, as it was shown by Berdnikov (2019a). Although now there are photometric data from long enough timescales for the effects of evolution and fluctuations to be separated reliably for bright Cepheids, fluctuations can still prove a problem for the period change determination of fainter Cepheids that are observed less regularly. Physical processes behind such fluctuations could be either short-term variations in the atmospheric structure (Deasy & Wayman, 1985), or minor changes in helium abundance gradients in upper layers of Cepheids (Cox, 1998). The century long temporal coverage of light curves not only allows the investigation of period changes through the simple methodology of $O-C$ diagrams (Sterken, 2005), but it can give us an unprecedented insight into the nature of these fluctuations as well, which facilitates the refinement of current pulsation models.

Apart from the evolutionary changes and the random fluctuations of the pulsation period, binarity of the Cepheid can also cause observable effects in the $O-C$ diagram. One of these is the light-time effect (LiTE), which arises from the orbital motion of the variable star. This effect can be easily distinguished from the evolutionary effect, since it results in a periodic feature in the $O-C$ graph. The orbital modulation can be detected in the $O-C$ diagram of binary Cepheids when the orbital period is sufficiently long, because in the case of short orbital periods the amplitude of this cyclic pattern would be too small to recognize. A very clear indication that a superimposed wavelike signal is caused by the LiTE instead of fluctuations is the stability of the signal; since the fluctuation waves are caused by accumulating random processes, the shape of the resulting quasi-cyclic signal will get distorted, however, as the LiTE is caused by a deterministic process, its shape will remain stable over time. The importance of light time effect lies in the fact that it can be used for a rough estimation of the orbital parameters. So far only a few Cepheids have been found to show LiTE (AW Per and RX Aur, Szabados 1992 and Vinkó 1993), with a few more awaiting spectroscopic confirmation.

Another effect characteristic of binary Cepheids is a phase jump or phase slip seen in the $O-C$ diagram. A phase jump in the $O-C$ diagram has a stepwise, while the phase slip has a sawtooth-like shape; in the first case the period remains the same while the phase of the pulsation suddenly changes, while in the second case, the period of pulsation changes rapidly, then returns to the previous value after a given amount of time (period jump-rejump). Such phase jumps have been found in the $O-C$ diagrams of several Cepheids (e.g. Szabados 1989). One of the most prominent examples of Cepheids exhibiting such features in their $O-C$ diagrams is Polaris (Turner et al., 2005), which displayed a parabolic $O-C$ trend corresponding to a continuously increasing period that was interrupted by a phase jump after which the period continued to increase with the previous rate, with a significant phase difference.

The idea that phase jumps appear only in the $O-C$ diagrams of binary Cepheids is based solely on empirical data. Each Cepheid showing such an effect is either a member of a known spectroscopic binary or suspected to have a companion based on indepen-

dent evidence. Moreover, no phase jump was ever detected for any well-studied single Cepheid. The size of a phase jump is usually in the order of several hundredths of the pulsation period. Unfortunately, there is no theoretical explanation for the occurrence of such phase jumps or slips. For Polaris, Turner et al. (2005) suggested the brief interruption of the Cepheid's regular evolution by a short-lived blueward evolution associated with a small change in the average radius of the star, or alternatively, by a sudden increase in the mass of the Cepheid. However, these effects appear to be too spontaneous and peculiar to explain the phase jumps generally, especially when the phase jump occurs multiple times for a given star, which was observed to occur among Cepheids. Szabados (1992) suspects that the occurrence of phase jumps is governed by the orbital motion. In this case, a possible explanation for the phase jumps could be the perturbing effect of the companion star that exerts increased influence on the upper layers of the atmosphere of the Cepheid (where the pulsation takes place) near periastron passage. The stepwise structure of the $O-C$ diagrams in the case of phase jumps contradicts current evolutionary models, which predict continuous change of pulsation period otherwise.

Even though only a few Cepheid variables were observed in the programs of the *Coriolis*, *MOST*, *Kepler* and *CoRoT* space missions, the advent of high precision space photometry brought improvements in the period change studies of these variables as well. Based on the observations of the Solar Mass Ejection Imager (SMEI) instrument onboard the *Coriolis* satellite, Spreckley & Stevens (2008) connected slow changes in the light curve of the Polaris to a quite fast evolutionary phase and by supplementing the existing $O-C$ diagram suggested that another phase jump occurred. Berdnikov & Stevens (2010) studied the period changes of short period Cepheids based on SMEI photometry and detected random fluctuations in four of the observed stars. By analysing the *MOST* observations of SZ Tau and RT Aur, Evans et al. (2015) revealed cycle-to-cycle variations that are a function of the pulsation phase. The stability of their pulsation was also investigated and, besides finding temporal variations on a scale of decades, it was pointed out that the pulsation of overtone Cepheids is more erratic than that of fundamental mode variables. In the case of the *Kepler* mission, there was only one Cepheid in the observed field, V1154 Cyg. Derekas et al. (2012, 2017) provided a detailed analysis of the data and found cycle-to-cycle fluctuations on the $O-C$ diagram, which were attributed to instabilities in the light-curve shape caused by convection and hot spots based on the suggestion of Neilson & Ignace (2014). Poretti et al. (2015) performed the fluctuation tests similar to the work by Evans et al. (2015) on the *CoRoT* data for seven Cepheids, and found small cycle-to-cycle variations. Since these space missions covered only a few Cepheids, our understanding on these small fluctuations is limited, which is expected to change through future works based on the data from the currently ongoing *TESS* project (Plachy et al., 2021).

In this work, our primary aim is to expand the collection of existing $O-C$ diagrams of known binary Cepheids by using century-long photometric observational data of these variables. To get a more complete set of diagrams, the initial set of variables was extended with stars that, to our current knowledge, do not belong to binary systems.

The structure of this paper is as follows. In Section 17 we describe the available data and the differences of our method from the standard $O-C$ method. In Section 18

we discuss the results obtained for Cepheids that exhibited some peculiarities on their $O - C$ diagrams individually. Then, in Section 19 we analyse our sample collectively, first by placing the period change rates into broader context by comparing the results with previous works, then by discussing the period fluctuations in general. Finally, in Section 20 we summarize our results and conclude the paper.

17 Data and the method of the analysis

17.1 Data and observations

To achieve the near century long coverage of the temporal behaviour of the pulsation period, we attempted to acquire all available processed photometric data for every star. The first half of the 20th century was covered by the Harvard College Observatory Plate database (DASCH project, Grindlay et al. 2012, for stars on the northern galactic hemisphere) and by the observations of the American Association of Variable Star Observers (AAVSO, Kafka 2021, for suitably bright Cepheids). The later part of the century was covered by various articles from the literature, and by the earlier works of Szabados (1989), Szabados (1991) and Berdnikov et al. (1997). The complete set of references for articles used for the individual Cepheids can be found in Table C.1. To complete this dataset with more recent observations, we used the photometric data obtained by the *Hipparcos* (Perryman et al., 1997b), the All Sky Automated Survey (ASAS, Pojmanski 2001), INTEGRAL-OMC (Winkler et al., 2003), KELT[1], ASAS-SN (Shappee et al., 2014; Kochanek et al., 2017), the Optical Gravitational Lensing Experiment (OGLE, Udalski et al. 2015), the Solar Mass Ejection Imager (SMEI, Eyles et al. 2003), as well as the Kamogata Sky Survey (Morokuma et al., 2014) projects. To supplement these data, we have monitored some Cepheids with the 60/90 cm Schmidt telescope at Piszkéstető Observatory. The photometric data acquired through this telescope can be found in Table 17.1.

17.2 Construction of the $O-C$ diagrams

We followed the changes in the pulsation period of individual Cepheids using the method of $O-C$ diagrams (Sterken, 2005). To analyse the photometric datasets of each Cepheid, we applied Discrete Fourier Transformation (DFT, Deeming 1975) on the measurements, for which we used the Period04 software (Lenz & Breger, 2005). We analysed the data from the various sources separately, to account for differences in circumstances valid for individual observational series, by keeping the frequencies and the relative phases of the harmonics fixed to a pre-calculated parameter set, which were based on the dataset with the widest coverage and most data points, while allowing the amplitudes to change during the fitting procedure.

As a first step of the analysis, every set of observations were split into smaller subsets. For each survey, depending on the temporal coverage of the data, 300-450 day long temporal bins were defined depending on the length of the pulsation period, in which

[1] https://exoplanetarchive.ipac.caltech.edu/

Cepheid	JD	V
YZ Aur	2458806.402	9.8815
YZ Aur	2458807.618	9.8637
YZ Aur	2458823.473	10.392
YZ Aur	2458824.418	10.129
YZ Aur	2458828.623	10.052
YZ Aur	2458855.319	10.683
...	...	...

Table 17.1: List of observations taken at the Piszkéstető Observatory. The brightness values are differential magnitudes except for X Lac, for which we used previously taken unpublished measurements which are not transformed to the international system. The full list of observations is available in the online supplement of the article.

each data point was moved to a new subset. The folded light curves of each previously created subset of measurements were calculated, which then were used to determine the observed (O) epoch values of the average (zero point) brightness on the brightening edge of the light curve. To determine the O values, we fitted the phase folded light curves corresponding to the different epochs with the previously calculated Fourier components representative of the data source at hand, by only allowing the mean brightness and phase offset of the model light curve to change. The O values were then simply calculated from the phase offset of the best fit model. The use of the median brightness on the ascending branch was motivated based on the Fourier fit qualities: for longer and longer pulsation periods, the complexity of the light curve increases, which in turn means that more and more Fourier components will need to be taken into account. For older, less accurate datasets the fitting of the high order components could become uncertain, which in turn could introduce a bias to the inferred $O-C$ values, when they are based on the epoch of maximum brightness. However, it was found that the rising branch itself, and the epoch of average brightness on it can be fitted with suitable accuracy even in such cases, thus providing a viable alternative for datasets with lower amount of observations. The advantage of using the epoch of average brightness over that of the maximum becomes even more important for Cepheids with pulsation periods between 8-10 days, due to the secondary maximum present on the light curve. It was also found by Derekas et al. (2012), that the most accurate $O-C$ values can be obtained through measuring the epoch of average brightness on the rising branch. The average brightness value was determined as the baseline for the sinusoidal components at the Fourier fitting of the separate datasets. By this definition the brightness value at the zero point is slightly different for various datasets as it will account for the differences between the different surveys and measurement systems, thus the resulting $O-C$ points will be comparable. Although the phase folding method inevitably decreases the resolution of the resulting $O-C$ curve, the precision of the results increases, since the error of the phase calculation will decrease significantly.

To complete the construction of the $O-C$ diagram, the errors of the individual $O-C$ differences had to be calculated. The most important factor that governs the precision of the individual $O-C$ values is the number of photometric data points used for their derivation. Since we only fit the average brightness and the phase shift of a given light curve shape, even a low number of data points is enough for the $O-C$ calculation, however to make sure that the results we obtain are meaningful, we set the lower limit on this number to 8. Another factor that needs to be taken into account when estimating the accuracy of the $O-C$ points is the phase distribution of photometric data points in each of the folded light curves. Obviously, if the phase curves created with the method explained above were well-covered, i.e. the calculated phases covered the possible range in an approximately uniform manner, then the standard least-squares method could be used to fit the known light-curve shape to the phase curve, which would allow for the straightforward calculation of the covariance matrix. However, if the phase-curves were not well covered, which occurred frequently in the case of long period variables observed in a series of short-cadence observation runs (e.g. with IOMC), then the above method could significantly underestimate the error of the $O-C$ differences. To avoid this problem, the errors have been calculated by applying bootstrapping throughout the fitting procedure; at each step 75% of the data points have been randomly selected, and fitted with the precomputed light-curve shape. This step was carried out a hundred times for each phase curve. The final uncertainty of the individual $O-C$ residuals was calculated as the square root of the sum of overall phase shift and light-curve zero point variance.

The $O-C$ derivation method inherently contains a minor bias through the use of Fourier decomposition for the fitting, as it can obviously just approximate the actual shape of the light curve, which could cause biases in cases when a dozen or more Fourier components are required for the description. Although these biases can be minimized properly by measuring the moment of the average brightness on the rising branch instead of that of the maximum, a more precise and general method could be achieved by using a non-parametric light curve fitting instead of the Fourier decomposition. Nevertheless, since we used the same amount of Fourier components for every dataset of the individual stars, these biases affect each of the reductions similarly, thus they did not lead to noticeable artefacts between the different data sources.

18 Remarks on individual Cepheids

The $O-C$ curves corresponding to evolutionary changes are usually represented as parabolic trends, which correspond to constant rate of period change (for a sample of $O-C$ diagrams showing solely the effects of stellar evolution, see Fig.18.1). There have been numerous studies from the last decades showing such behaviour (e.g. Parenago 1956, Szabados 1983, Berdnikov et al. 1997). The rate of period change depends on the position of the Cepheid within the instability strip and the crossing number, and is usually modelled by a linear function of time, which rates are well approximated by current pulsation and evolutionary models (Anderson et al., 2016).

However, there is no physical model that restricts the period change of a star to be linear, since the luminosity and the temperature themselves change in a nonlinear manner. Hence, as it has been argued by Fernie (1990b), in some cases higher order polynomial fits are necessary for certain $O-C$ diagrams, which indicate not only the change of period itself, but variations in the rate of period change as well. Such behaviour is common among Cepheids, significant deviations can be observed from parabolic fits to the $O-C$ plot in numerous cases. Determining the period change rate for a large set of Cepheids allows for the statistical study of this phenomenon, as well as giving way for the refinement of existing period-based empirical relations. However, there are quite a few classical Cepheid variables that exhibit peculiar $O-C$ diagrams, for which the statistical description is not yet available due to the small number of such objects, thus these stars have to be treated separately.

In this section we present and discuss the $O-C$ diagrams exhibiting features which could not be explained by evolutionary changes with superimposed relatively small amplitude fluctuations, such as phase jumps or slips, or large amplitude waves that partially, if not completely, obscure the effect of evolution on the diagram. In the large sample of analysed Cepheids, we found 16 of such $O-C$ diagrams, which are presented below.

18.1 Cepheids showing wavelike $O-C$ structure

Out of the 16 Cepheids that exhibit peculiar $O-C$ diagrams, we found 9 stars that show a remarkable wavelike modulation. Such wavelike signals can arise either due to the presence of a companion star through LiTE, or due to the fluctuations present in the pulsation of the Cepheid, in which case the modulation can even obscure the effect of evolution on the $O-C$ diagram. To model these wavelike signals we simultaneously fitted the underlying parabolic trend corresponding to stellar evolution and the superimposed modulation (except for UY Mon, where we could not calculate such a fit reliably, see Sec. 18.1.7). By this procedure, we fitted a single sinusoidal waveform for each Cepheid,

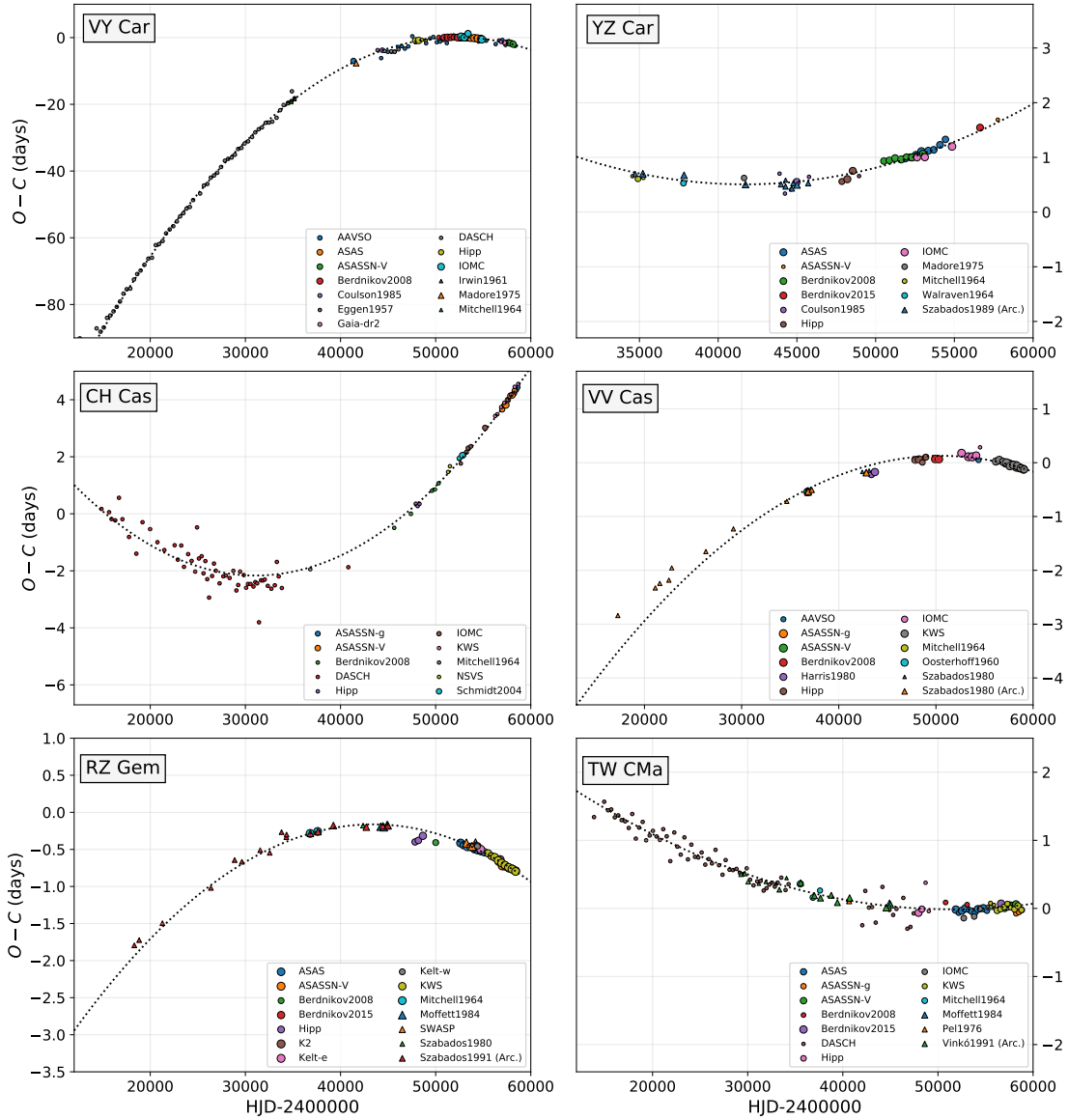

Figure 18.1: Sample Cepheids from our set showing no features apart from the evolutionary signal. The size of the datapoints indicate the inverse of the uncertainty with a non-linear scaling.

except for IR Cep, where involvement of one additional sinusoidal component is motivated based on the systematic deviations present in the residuals calculated with respect to the parabolic plus single sinusoidal model fit. In the case of the other Cepheids, we either did not find any additional signals in the residual data after fitting the parabola and the modulation, or due to the randomness and possible fluctuation origin of the modulation (as in the case of VZ CMa and DX Gem, see Sec. 18.1.2 and 18.1.6) we decided that adding further components would not change the outcome of the analysis significantly.

For these Cepheids, similarly to the other Cepheids showing evolutionary changes, we then statistically analysed the residuals calculated by various models (for the constant period, the linear period-change, and the linear period change plus sinusoidal signal cases) using F-test, in order to determine the significance of the wavelike modulation in the modelling. The final F-statistics and the associated p-values can be found in the summary table in the Appendix (Table C.2). In a later section (Sec. 19.2) we then used these solutions along with those of Cepheids showing evolutionary changes for the collective analysis.

18.1.1 RX Aurigae

RX Aur is a bright intermediate period Cepheid, whose binarity was long suspected based on the slope of its colour-colour loop and the LiTE-like nature of its $O-C$ diagram (Szabados, 1988). The total mass of the system inferred based on this diagram did not rule out the presence of a companion (Szabados, 1988), and it is further supported by the RV measurements of Gorynya et al. (1996), who marked the star as a possible binary.

By extending the $O-C$ diagram with more recent photometric measurements we confirm the LiTE explanation of the $O-C$ diagram (Fig. 18.2). The $O-C$ diagram was calculated using the following elements:

$$C_{\rm med} = 2443830.177 + 11.6241 \cdot E$$

Fitting the evolutionary trend and the superimposed modulation (Fig. 18.3) yielded an orbital period of $P_{\rm orb} = 37928 \pm 7678$ d $= 103.84 \pm 21.02$ yr and an amplitude of $A = 0.255 \pm 0.107$ d, which are approximately 1.92 and 1.15 times larger, respectively, than the previously calculated values (Szabados, 1988). Since, as seen in Fig. 18.2, the maximum of the variation in the residual terms is only covered once by our dataset, a more detailed and reliable orbital parameter determination is not yet possible, as the few data points near that extremum do not provide sufficient constraint for the fitting procedure. However, the knowledge of the orbital period and semi-major axis (amplitude) allows for the determination of the total mass of the system through the

$$\left(\frac{A}{\sin i}\right)^3 P_{\rm orb}^{-2} = M_1 + M_2 \tag{18.1}$$

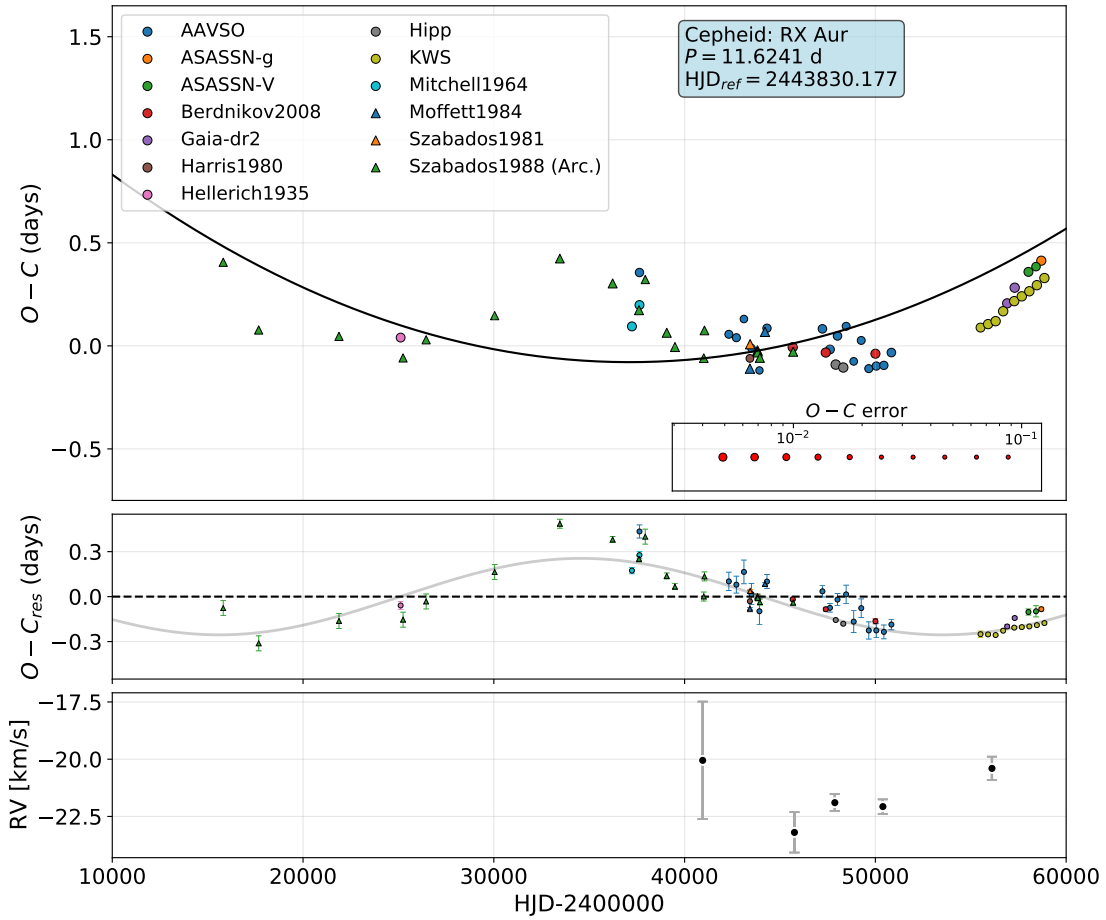

Figure 18.2: $O-C$ diagram of RX Aurigae, exhibiting a parabolic change corresponding to evolution of the Cepheid and a wavelike signature superimposed (top panel), the residual $O-C$ values with the corresponding fit (middle panel) and the available mean RV values.

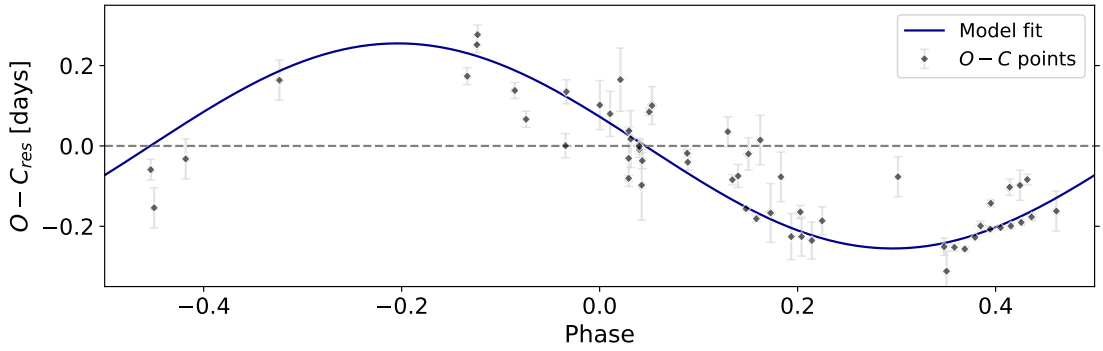

Figure 18.3: Phase diagram of the residual $O-C$ variation of RX Aur. The elements used for the calculation of the phase diagram were $T_0 = 2442312.825$ and $P = 37928.243$ d.

formula (since $A = a \sin i$, with a being the semi-major axis of the orbit), where A is measured in astronomical units, $P_{\rm orb}$ in years. The resulting parameters are as follows:

$$\begin{aligned} a \sin i &= (44.152 \pm 18.515)\ \text{AU} \\ &= (6.605 \pm 2.769) \cdot 10^9\ \text{km} \\ (M_1 + M_2) \sin^3 i &= (7.999 \pm 6.239) M_\odot. \end{aligned}$$

The resulting mass is consistent with the values inferred by Kervella et al. (2019b) with the assumption that the orbital plane is oriented along or near the line of sight ($i \gtrsim 60°$), and the obtained orbital period also falls into the range proposed by them. However, no significant signal can be extracted from the available RV data (from the measurements of Schmidt 1974, Barnes et al. 1987, Gorynya et al. 1996, Imbert 1999 and Borgniet et al. 2019) displayed in Fig. 18.2, which show a low scatter ($\sigma_{\rm RV} \sim 1.155$ km/s) and their distribution is not aligned in phase with the suspected LiTE either, hence it is not possible to reach a solid conclusion on the origin of the observed $O - C$ signal yet.

18.1.2 VZ Canis Maioris

VZ CMa is a short period Cepheid whose pulsation mode was investigated in various studies, yielding different results: Kienzle et al. (1999) classified this star as an overtone pulsator, while according to Groenewegen & Oudmaijer (2000) this Cepheid is a fundamental mode pulsator. Its multiplicity was also studied in various articles: it was first suspected by Stobie & Balona (1979) and Szabados (1993) based on its color indices and amplitude ratios respectively, then was finally confirmed spectroscopically by Szabados (1996). The $O-C$ diagram of the object was studied by Berdnikov & Pastukhova (1994), who found it to be parabolic.

By extending the previously available data with the archival measurements of Hacke & Richert (1990), and with that of modern surveys, we found that the $O - C$ diagram of VZ CMa exhibits a large amplitude wave (Fig. 18.4), which was interpreted as a parabolic pattern before, due to the lack of sufficient data. The $O - C$ diagram was calculated with the following elements:

$$C_{\rm med} = 2452663.377 + 3.126151 \cdot E$$

Fitting the parabolic trend and the wavelike signal simultaneously, we estimated the period of the modulation to be 24475 d (67.01 yr) and its peak-to-peak amplitude to be approximately 0.3 d. Although the values inferred here could indicate a LiTE origin for the signal, the unusual, non-sinusoidal shape points towards the presence of fluctuations in the pulsation. This ambiguity is not lifted by the RV datasets either, as the combined observations of Stobie & Balona (1979) and Kienzle et al. (1999) cover a much shorter timespan than the period of the signal, henceforth we cannot conclude whether this wave originates from binarity or period fluctuations.

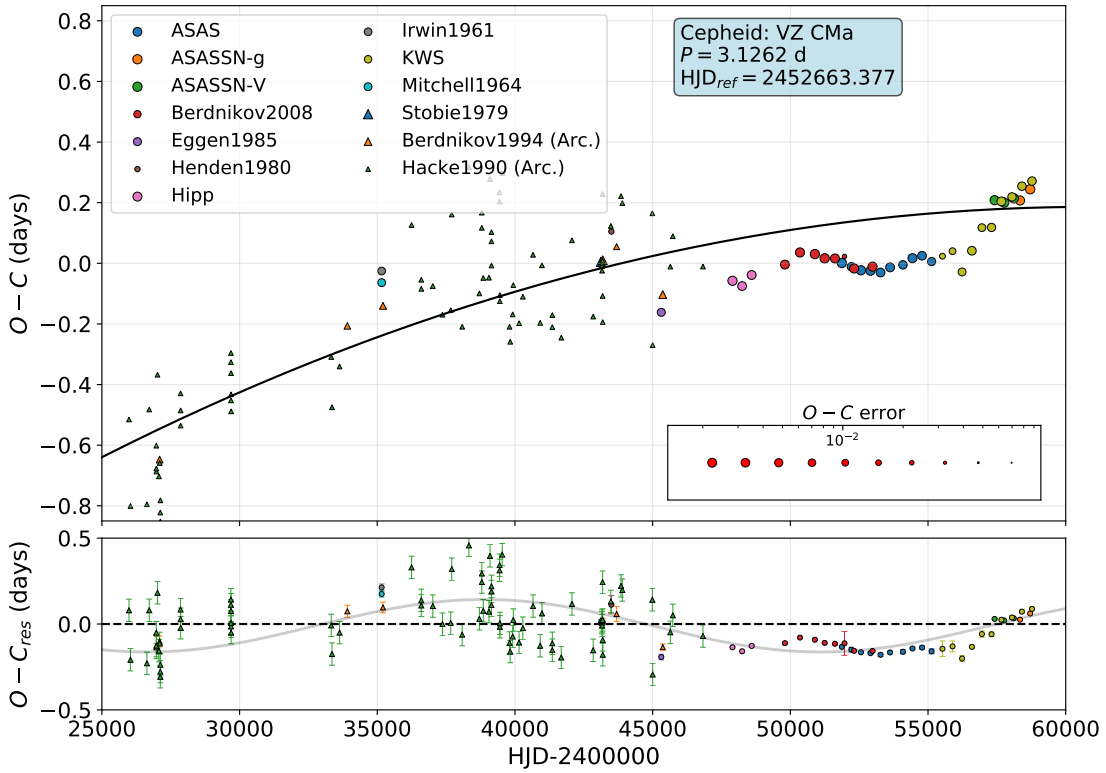

Figure 18.4: $O-C$ diagram of VZ CMa exhibiting a larger amplitude quasi-periodic signal, which could either be attributed to LiTE (which however, would not explain the systematic deviations of data points at HJD 2450000 on the lower panel) or to period fluctuations.

18.1.3 BY Cassiopeiae

BY Cas is short period Cepheid with a long history of cluster membership and binarity studies. Membership in NGC 663 was first suggested by Malik (1965), which was contradicted by the later study of Usenko & Klochkova (2015) citing large color excess, parallax and RV differences, concluding that BY Cas is a foreground star, in agreement with the result of Anderson et al. (2013) too. However, according to the latest analysis of Glushkova et al. (2015), this Cepheid shows connection not only to its nearest cluster NGC 663, but also to the clusters NGC 654, NGC 659, and the association Cas 8, too. BY Cas was also revealed to have a companion with an orbital period of ∼560 d (Gorynya et al., 1994).

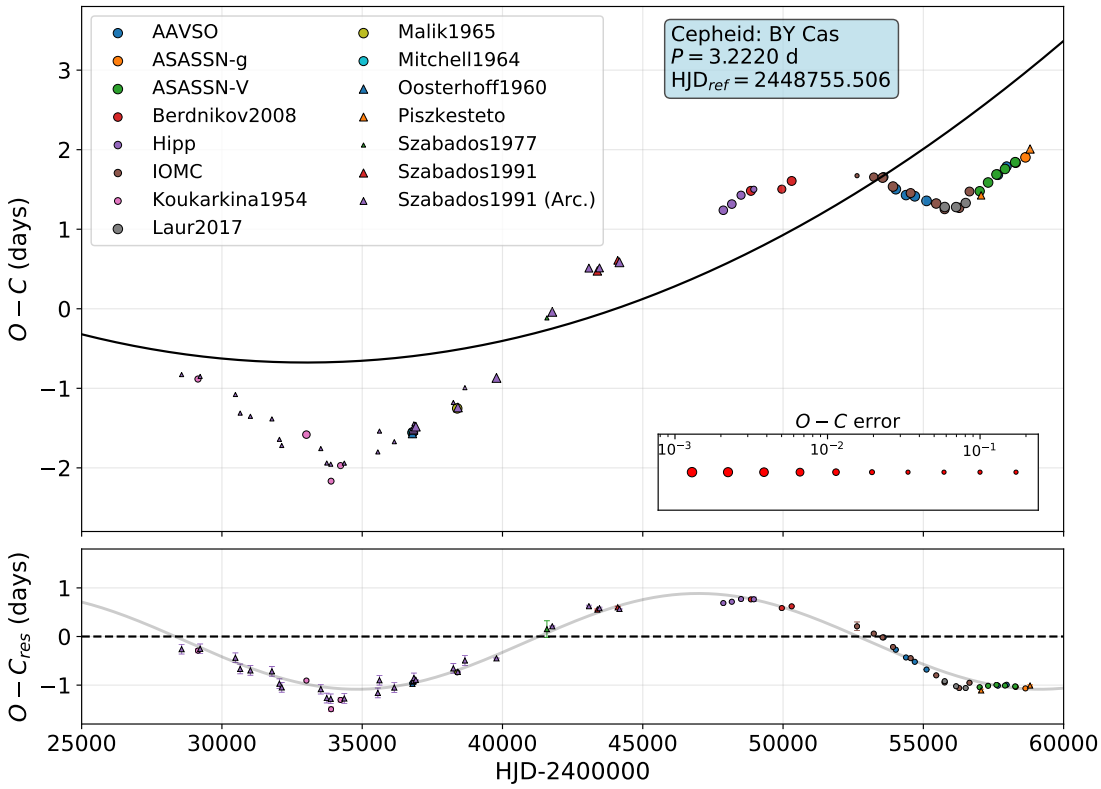

Figure 18.5: $O-C$ diagram of BY Cas, showing an evolutionary change with a large amplitude wavelike signal superimposed.

The period changes of this variable were investigated by Szabados (1991) and Berdnikov & Pastukhova (1994), and more recently by Berdnikov (2019b). The former analysis described the variations as a sequence of sudden period changes, while the latter work proposed evolutionary changes with a wavelike pattern superimposed. Our independent analysis showed that the $O-C$ diagram can indeed be explained by evolutionary changes with a wavelike signal on top of it (Fig. 18.5). The presented $O-C$ diagram was calculated with the following elements:

$$C_{\mathrm{med}} = 2448755.506 + 3.222019 \cdot E$$

Using the parabolic fit we estimated the period change rate to be 0.338 s·yr^{-1}, which is two orders of magnitude smaller than the one estimated by Berdnikov & Pastukhova (1994), and places this object in the group of third crossing Cepheids, in agreement with the findings of Berdnikov (2019b). The best explanation for the superimposed modulation is the period fluctuation, which is relatively common for these Cepheids (as shown in the later sections).

18.1.4 IR Cephei

IR Cep is a short period Cepheid which was first studied in detail by Szabados (1977), revealing strong period change. This Cepheid was found to exhibit a peculiar light curve: according to Kun & Szabados (1988), the light curve of this Cepheid rather resembles that of larger amplitude Cepheids. Thus it was suggested that IR Cep might be a classical Cepheid, but with a bright companion whose constant contribution to the emitted light reduces the observable amplitude of the variable, however, no close binary component was found by the RV analysis of Marschall et al. (1993). Kun & Szabados (1988) also suggested the possible association of this Cepheid to Cep OB2.

IR Cep turned out to be peculiar in its pulsation as well: this Cepheid was classified as a first overtone pulsator by Groenewegen & Oudmaijer (2000), but Szabó et al. (2007) showed that a first overtone classification would lead to excessive phase lag discrepancy for this star. They note however, that according to its position on the phase lag diagram it would quite naturally fit in the class of fundamental mode Cepheids.

Based on the acquired photometric measurements the corresponding $O-C$ diagram has been drawn, which covers more than a century (Fig. 18.6). The presented diagram was calculated using the following elements:

$$C_{\mathrm{med}} = 2453453.824 + 2.114088 \cdot E$$

The rate of period change is 0.042 s·yr^{-1}, while the approximate period and peak-to-peak amplitude of the seemingly periodic signal are 15150 d (41.47 yr) and 0.29 d. The origin of this wavelike signal is uncertain, as the amplitude could allow for LiTE, which is also favoured by the more stable form of the signal, however due to the short temporal coverage of the RV data obtained by Marschall et al. (1993) and Gorynya et al. (1998) this could not be confirmed spectroscopically, hence the fluctuation origin cannot be excluded either.

18.1.5 V532 Cygni

V532 Cyg is a short period Cepheid known to be a binary system member. The presence of a companion star was first suspected by Madore (1977) based on the shape of its colour-colour loop, then a similar conclusion was reached by Usenko (1990) and Szabados (1991) later on. This was later confirmed by the RV observations of Gorynya et al. (1996), finding a 388 d orbital period.

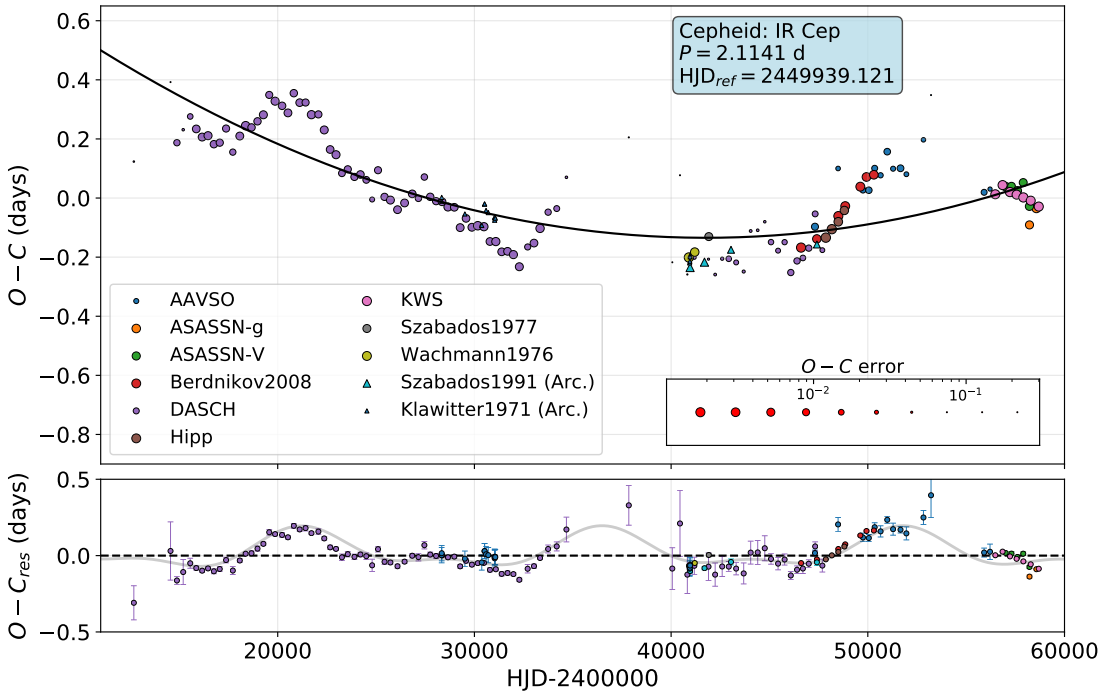

Figure 18.6: $O-C$ diagram of IR Cep (top panel). In the bottom panel the parabolic term corresponding to the evolution of the Cepheid had been subtracted. A simple Fourier fit of two harmonics can be seen plotted on the residual data points. The current amount of data points did not allow the addition of more harmonics terms, but this fit illustrates well that the shape of the residual signal remains relatively unchanged during the time interval covered by observations.

The period changes of this Cepheid were studied several times in the literature: Szabados (1977, 1991) first described the $O-C$ diagram as a sequence of period jumps, however, it was later shown that it can be described by evolutionary changes and a large wavelike signal superimposed (Berdnikov, 2019c). The latter behaviour of the $O-C$ diagram is also confirmed by our independent study, as shown in Fig. 18.7. The presented $O-C$ diagram was calculated using the following elements:

$$C_{\mathrm{med}} = 2441705.834 + 3.283536 \cdot E$$

As it is shown in the $O-C$ diagram, the period of the Cepheid is indeed decreasing due to its evolution with a rate of -0.104 s·yr^{-1}, which places it among the second crossing Cepheids. The large amplitude ($A = 0.612 \pm 0.013$ d) of the superimposed signal suggests that the fluctuation of the period is a suitable explanation.

18.1.6 DX Geminorum

DX Gem is a short period Cepheid which was for long considered one of the few first crossing Cepheids due to its large period change rate. The first period analysis on this

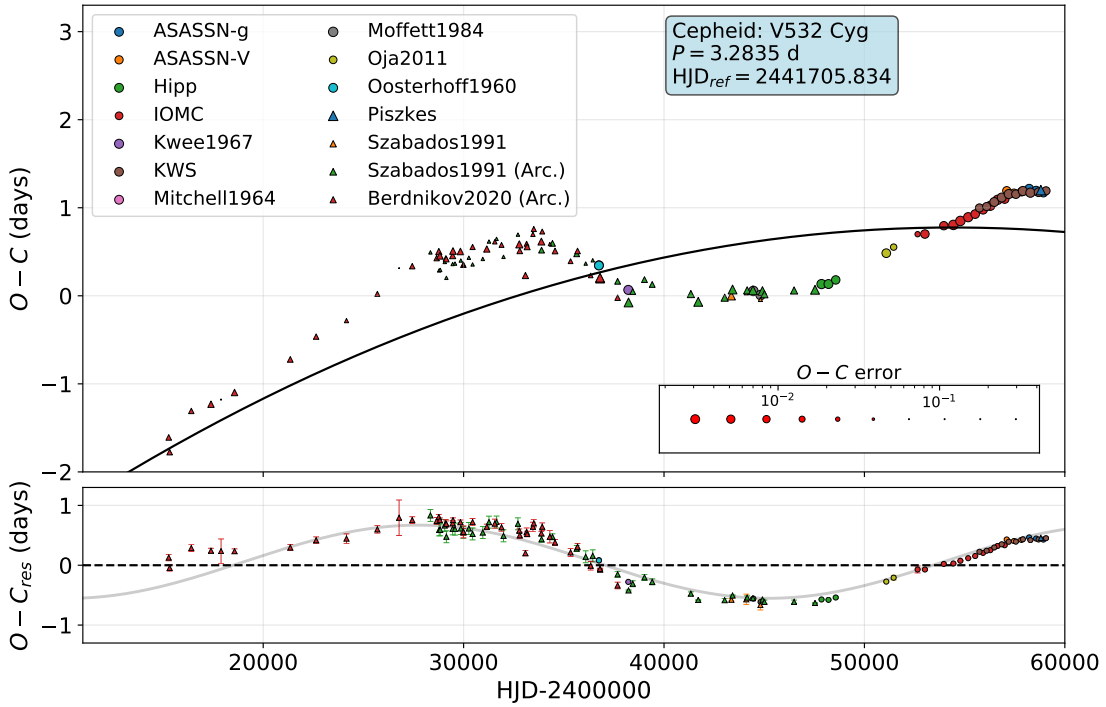

Figure 18.7: $O-C$ diagram of V532 Cyg exhibiting an evolutionary trend with large amplitude wavelike modulation superimposed.

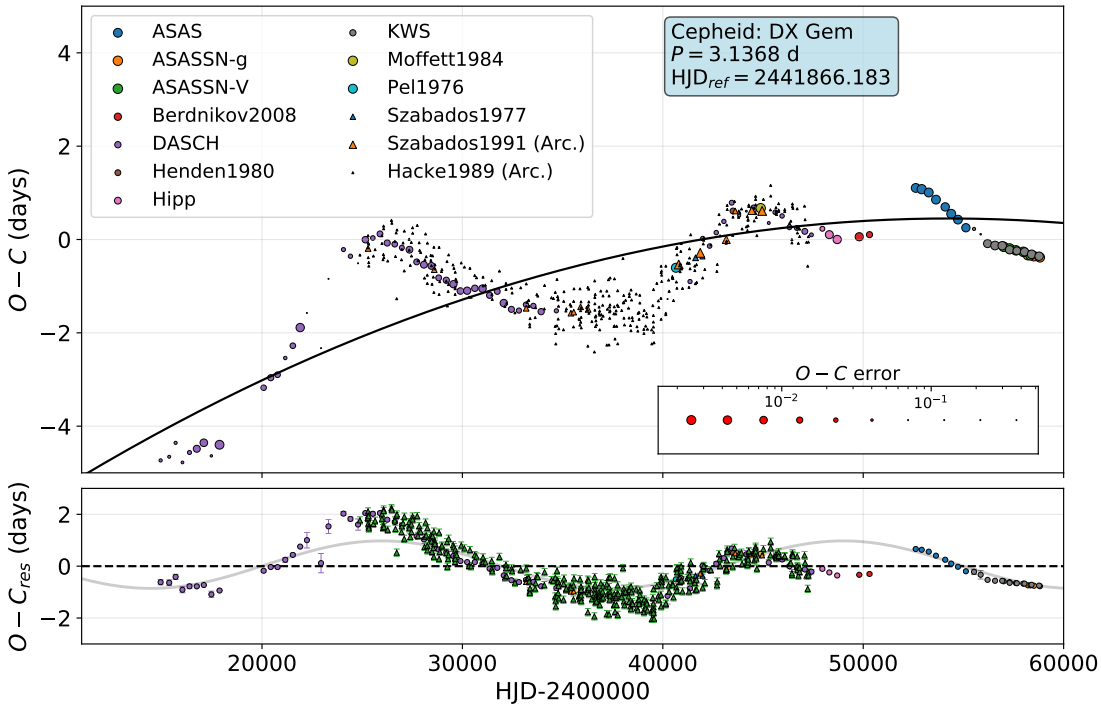

Figure 18.8: $O-C$ diagram of DX Gem (top panel). In the bottom panel the parabolic term corresponding to the evolution of the Cepheid had been subtracted. The remaining residual term exhibits a wavelike pattern, which is unstable and too large in amplitude to be connected to LiTE.

Cepheid was done by Szabados (1977, 1991), in which a series of phase jumps that appeared to be in accord with the binarity (Burki, 1985) of the object were suggested as interpretation. However, Berdnikov (2019a) showed that the $O-C$ diagram can be described by an evolutionary change with a wavelike signal superimposed.

According to our independent analysis, the $O-C$ diagram of DX Gem indeed cannot be explained by evolutionary changes alone (see Fig. 18.8). Our $O-C$ diagram was calculated using the following elements:

$$C_{\mathrm{med}} = 2441866.183 + 3.136779 \cdot E$$

From the obtained fit it is apparent that the Cepheid exhibits a shortening period with a rate of -0.186 s·yr^{-1}, hence it belongs to the class of second crossing Cepheids. The residual large amplitude modulation ($A = 0.917 \pm 0.027$ d) cannot be explained by LiTE, thus the most reasonable explanation for it is the presence of fluctuations in the period.

18.1.7 UY Monocerotis

UY Mon is a short period Cepheid that was rather neglected in the past: it was first correctly classified by Imbert (1981), as it was considered as an eclipsing binary before,

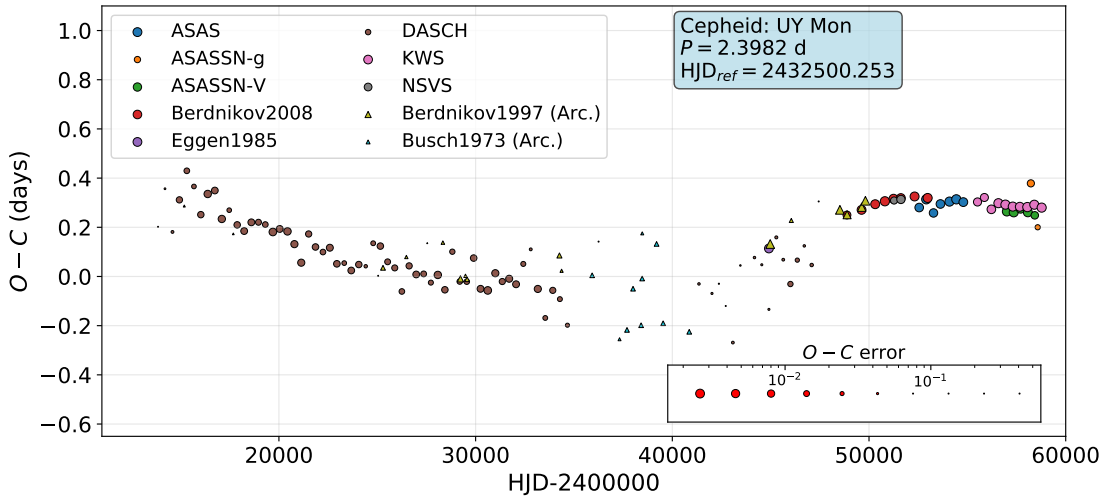

Figure 18.9: $O-C$ diagram of UY Mon exhibiting a long-term low amplitude wavelike signal, which could be a result of LiTE caused by a formerly unknown binary component in the vicinity of the Cepheid.

and it has not been studied in terms of RV data and cluster membership yet. The period changes of this Cepheid were investigated before by Berdnikov et al. (1997), who found an increasing period.

In our analysis, we extended the $O-C$ diagram compiled by Berdnikov et al. (1997) in both directions using the Harvard Observatory plate archives and more recent observations. The $O-C$ diagram was calculated using the following elements:

$$C_{\mathrm{med}} = 2432500.253 + 2.398185 \cdot E$$

According to our results, the $O-C$ diagram of UY Mon looks like a slanted sinusoidal signal, with a possible period longer than 45000d (∼120 yr). As the amplitude of this oscillation is small compared to the length of the period, the possibility of LiTE cannot be excluded. However, the time interval covered by the compiled data does not allow us to determine whether this signal is indeed periodic, thus further photometric and long-term RV observations are necessary for a firm conclusion.

18.1.8 Y Ophiuchi

Y Oph is an intermediate period Cepheid that was frequently analysed in the past. It is a known binary with an orbital period of ∼1222.5 d (Szabados, 1989): the presence of the companion was first suspected by Pel (1978) based on photometry, as Y Oph appeared too blue for its pulsation period. However, no such companion was detected from the IUE spectra (Evans, 1992) nor through NACO lucky imaging Gallenne et al. (2014). On this basis, its true nature remains elusive.

By collecting not only the more recent measurements, but the results from previous works on this Cepheid as well (Parenago, 1956; Szabados, 1989; Fernie, 1990b) we com-

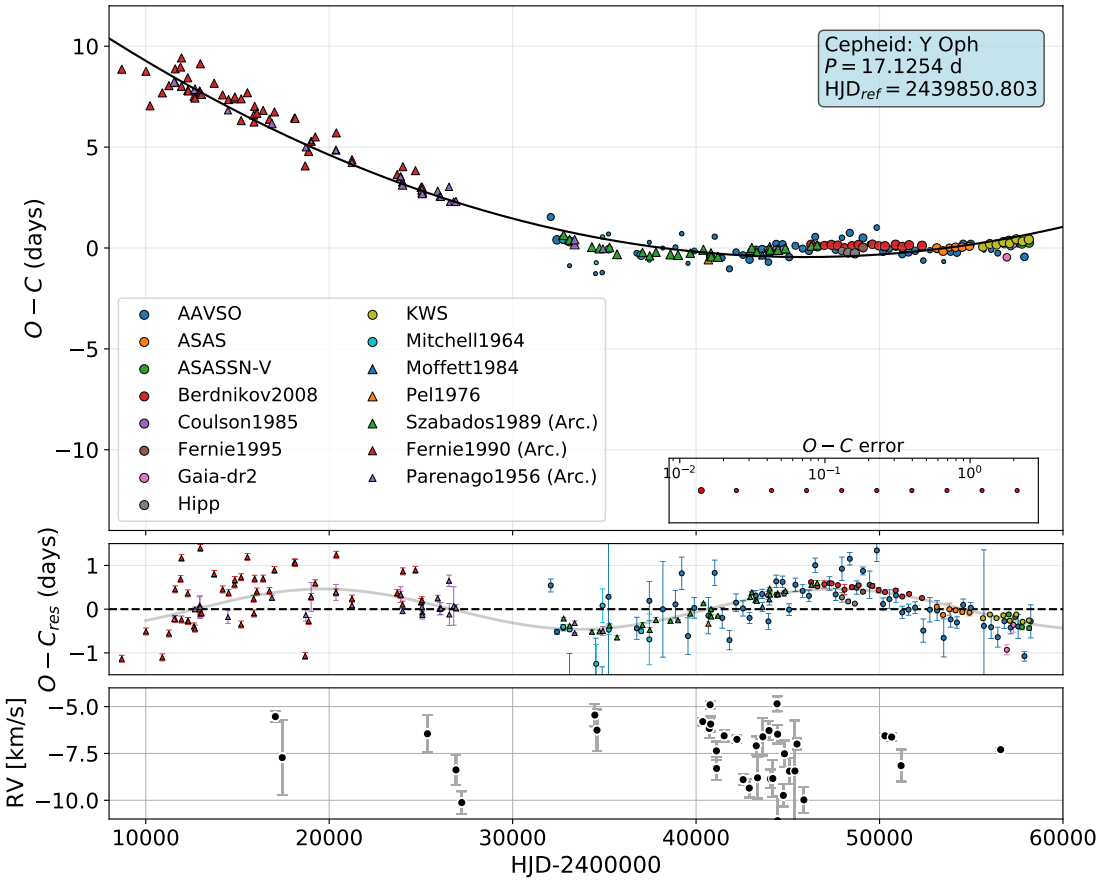

Figure 18.10: $O-C$ diagram of Y Oph exhibiting a wavelike trend corresponding to the LiTE superimposed on the secular period change of the Cepheid (top panel), the residual $O-C$ diagram obtained after subtracting the parabola (middle panel) and the available RV data points whitened for both the pulsation and the orbital motion of the Cepheid (bottom panel).

piled an $O-C$ diagram spanning almost a century (Fig. 18.10). To calculate the $O-C$ diagram, we assumed the following elements:

$$C_{\mathrm{med}} = 2439848.803 + 17.127827 \cdot E.$$

The obtained $O-C$ diagram can be described by a combination of the parabolic trend corresponding to the evolution of the Cepheid and a wavelike signal superimposed, with the period of the modulation being $P = 27948 \pm 1164$ d $= 76.52 \pm 3.19$ yr and the amplitude $A = 0.461 \pm 0.024$ d (Fig. 18.11). If we assume that this periodic variation originated from LiTE, then the obtained amplitude corresponds to a semi-major axis of $a \sin i = 79.82 \pm 4.19$ AU $= (1.194 \pm 0.063) \cdot 10^{10}$ km, which agrees well with the long period of this wave. Although the duration of the covered time interval does not allow for a detailed fit of the residual curve, the accuracy of the simple sinusoidal fit

suggests that the assumed orbit has a low inclination, which also agrees well with this period–semi-major axis pair. Since the period is much longer than the one obtained for the previously suspected companion, the light-time interpretation of the wavelike signal would suggest that a third component is present in the system of Y Oph, but no signal with such a period could be extracted from the presently available RV data (bottom panel of Fig. 18.10). Henceforth, we cannot yet confirm the presence of the third component, however, as we will show it in Sec. 19, the amplitude of the modulation we found is larger and can be considered an outlier compared to the fluctuation amplitudes of similar period Cepheids, which also favours the new companion and the LiTE explanation.

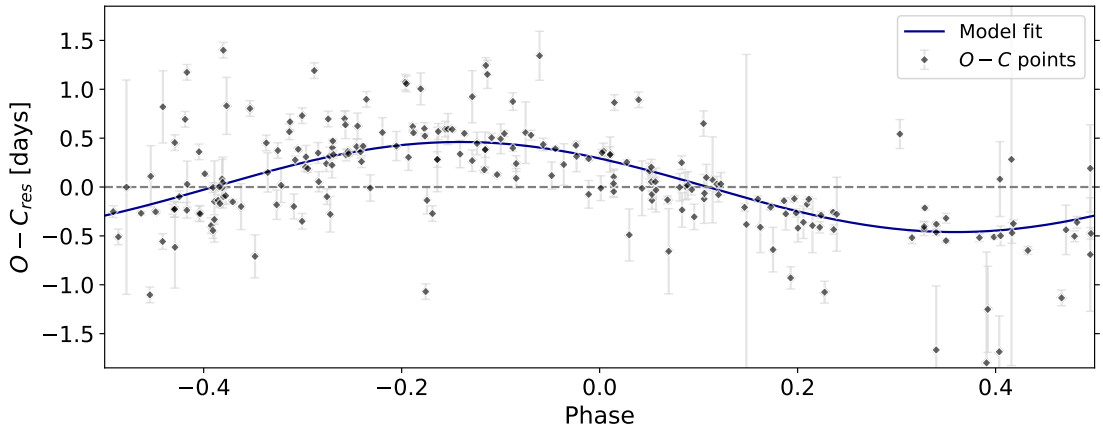

Figure 18.11: Phase diagram of the residual $O-C$ data points of Y Oph and the obtained fit. The elements used for calculating the phase diagram were $T_0 = 2451548.800$ and $P = 27948.469$ days.

18.1.9 AW Persei

AW Per is a short period Cepheid in a binary system. The binary nature of the star was discovered by Miller & Preston (1964) based on Ca II and K line measurements, with the orbit being investigated later on by Welch & Evans (1989), Vinkó (1993), and then by Evans et al. (2000). This object was also found to exhibit LiTE that could be matched to RV observations (Szabados, 1991).

To further investigate the signal created by the LiTE we extended the $O-C$ dataset of Szabados (1991) with more modern observations from various sources. The resulting $O-C$ diagram (Fig. 18.12) was calculated with the following elements:

$$C_{\mathrm{med}} = 2442708.076 + 6.463688 \cdot E.$$

Similarly to RV data, the LiTE also allows for the detailed estimation of orbital parameters. We must note however, that we did not aim to refine the set of parameters obtained by Evans et al. (2000), we only investigated this possibility for confirmation

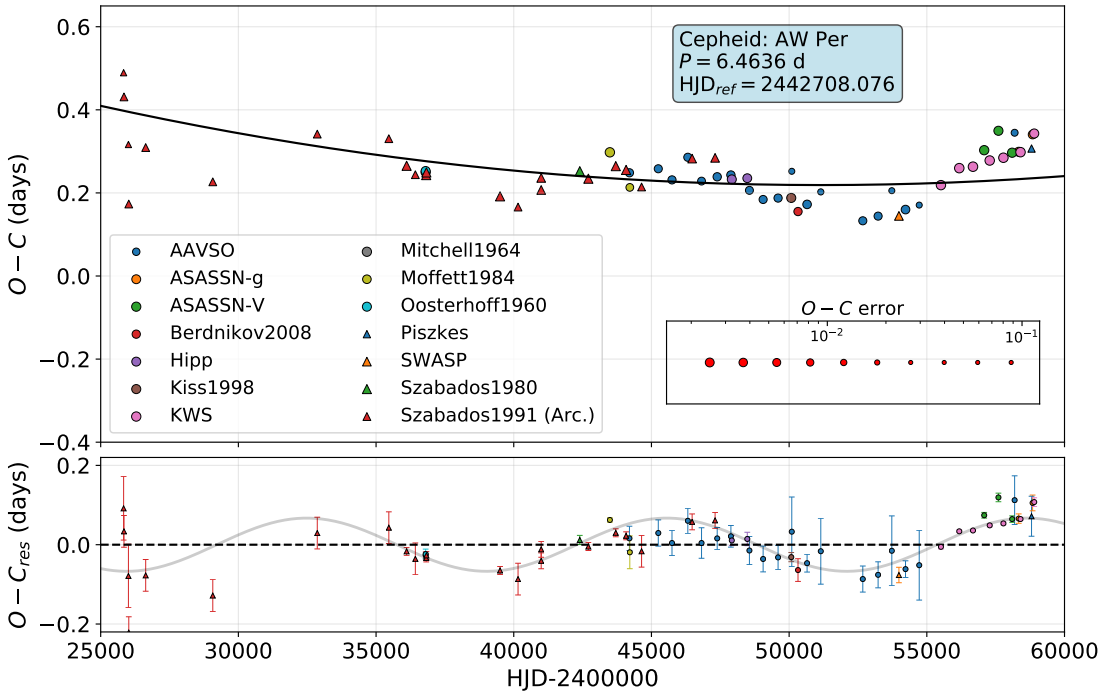

Figure 18.12: $O-C$ diagram of AW Per exhibiting a wavelike trend corresponding to the LiTE superimposed on the secular period change of the Cepheid (top panel) and the residual $O-C$ diagram obtained after subtracting the parabola (bottom panel). The fitting of this wavelike trend can be used for the determination of orbital elements as described in the text.

purposes. The $O-C$ variation due to the orbital motion can be described as

$$O-C = \frac{a\sin i}{c}(1-e^2)\left[\frac{\sin(\nu+\omega)}{1+e\cos\nu} - \frac{\sin(\nu_0+\omega)}{1+e\cos\nu_0}\right], \tag{18.2}$$

where a, e, i, and ω refer to the semi-major axis, eccentricity, inclination and longitude of periastron of the orbit of the pulsating star, respectively. In the equation, ν represents the true anomaly of the pulsator at a given time, while ν_0 denotes the true anomaly at the epoch chosen for the $O-C$ calculation. Based on Eq. 18.3 the semi-amplitude can also be defined:

$$K = \frac{a\sin i}{c}(1-e^2) \tag{18.3}$$

To fit this profile to the obtained set of $O-C$ residuals, we utilized the `RadVel` RV fitting toolkit developed by Fulton et al. (2018), which we appropriately modified using Eq. 18.3 for the fitting of $O-C$ diagrams. Using the Monte Carlo based fitting procedure of the code we obtained a fit plotted in Fig. 18.13 and for which the fitting parameters are listed in Table 18.1. As it is clearly visible from the obtained results, the precision of the $O-C$ diagram based orbital parameters is far worse than the ones obtained by Evans et al. (2000) based on higher precision RV measurements, but our results are consistent

Parameter	Credible Interval	Max. L.	Units
P	12078^{+340}_{-280}	12052	d
	$33.07^{+0.93}_{-0.77}$	32.99	yr
$T_{\rm conj}$	2422894^{+770}_{-760}	2422915	
e	$0.45^{+0.21}_{-0.2}$	0.49	
ω	$2.38^{+0.47}_{-5.1}$	2.6	rad
K	$0.051^{+0.01}_{-0.012}$	0.053	d
$a \sin i$	$1.66^{+1.14}_{-0.58} \cdot 10^9$	$1.81 \cdot 10^9$	km
	$11.08^{+7.62}_{-3.88}$	12.10	AU

Table 18.1: Orbital elements obtained by fitting the residual $O-C$ diagram of AW Per using the Monte Carlo based code. The Max. L. columns shows the maximum likelihood estimates of the given parameters.

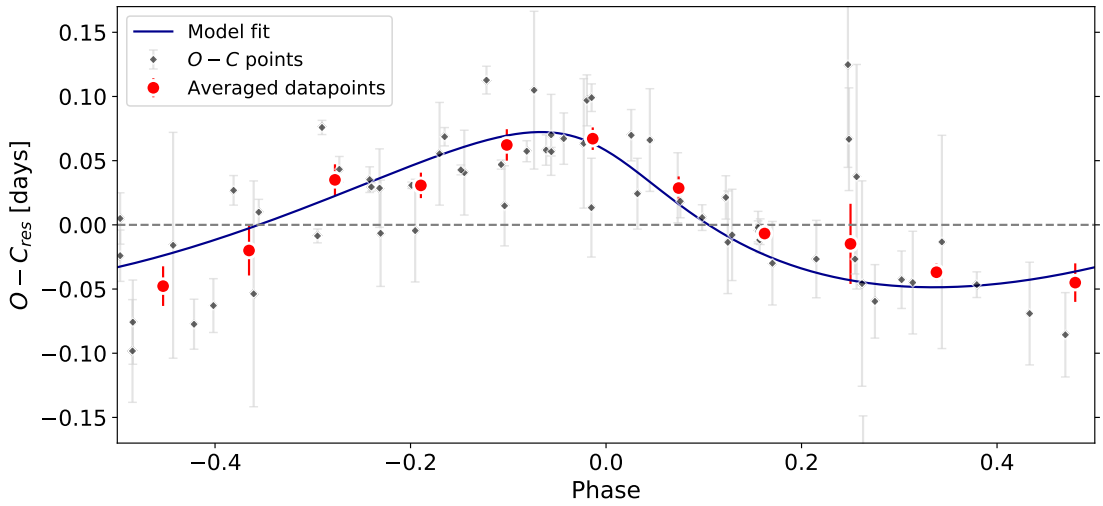

Figure 18.13: Best fit to the residual $O-C$ data of AW Per calculated by the `RadVel` software. The grey diamonds represent phase folded $O-C$ residual data, the blue curve the calculated model fit, while the red points show the binned average values of the data points. For the calculation of phases the orbital period of 12078 d has been used.

with the values obtained previously. It is worth mentioning however, that there is a significant deviation between the orbital period values, as our result for this parameter differs from the one obtained by Evans et al. (2000) ($P = 14594 \pm 324$ d) by more than 7σ. Based on the fact that our photometric dataset covers a longer timeframe than the one covered by RV observations, our result suggests that the orbital period of the binary is indeed significantly shorter than previously thought. To reach a firm conclusion, however, further photometric and spectroscopic observations are required.

18.2 Cepheids showing phase jumps/slips

Of the $O - C$ diagrams we found to be peculiar, 5 could be explained through phase jumps or slips. In case of a phase jump, the phase of the pulsation changes rapidly, while the period remains relatively the same, leading to a stepwise $O-C$ graph. In the case of a phase slip however, the period of the pulsation seems to change rapidly, just to return to the previous value after a given amount of time (period jump-rejump), resulting in a sawtooth-shaped $O - C$ diagram. Such behaviours, which cannot be explained through stellar evolution, have been empirically associated with the Cepheids being binaries, as only some of those were found to exhibit it. However, the complete explanation for this phenomenon is still elusive.

18.2.1 XZ Carinae

XZ Car is a long period Cepheid which was found to be possibly linked to various open clusters in the past: Glushkova et al. (2015) claimed a possible relation between the Cepheid and the open cluster Ruprecht 93, while Chen et al. (2015) found the membership in ASCC 64 to be more probable, based on proper motion, age, and instability-strip selection criteria, although none of these associations were marked likely by Anderson et al. (2013) earlier. Anderson et al. (2016) found the Cepheid to exhibit time dependent γ-velocity changes, indicating the binary nature of the star.

The period changes of this object were not investigated before, despite being a relatively bright star. According to our analysis, the $O - C$ diagram of XZ Car can only be explained through a phase jump, as the data points available from before HJD 2440000 show a systematic offset from the rest of the data, and no evolutionary signal was visible (Fig. 18.14). The $O - C$ diagram was calculated using the following elements:

$$C_{\mathrm{med}} = 2452624.168 + 16.652232 \cdot E$$

The phase jump occurred between HJD 2438000 and 2442000, and altered the phase of the pulsation by 0.67 d (i.e. 0.040 phase), assuming that the period was unchanged before and after the jump (Fig. 18.14). Apart from the phase jump, no other signal could be extracted that would indicate period change in the Cepheid. We note that due to the low amount of available data before the assumed occurrence of the phase jump this interpretation remains uncertain, however, if true, it could yield an additional empirical link between the presence of a companion star and the phase jump nature of the $O - C$ diagram.

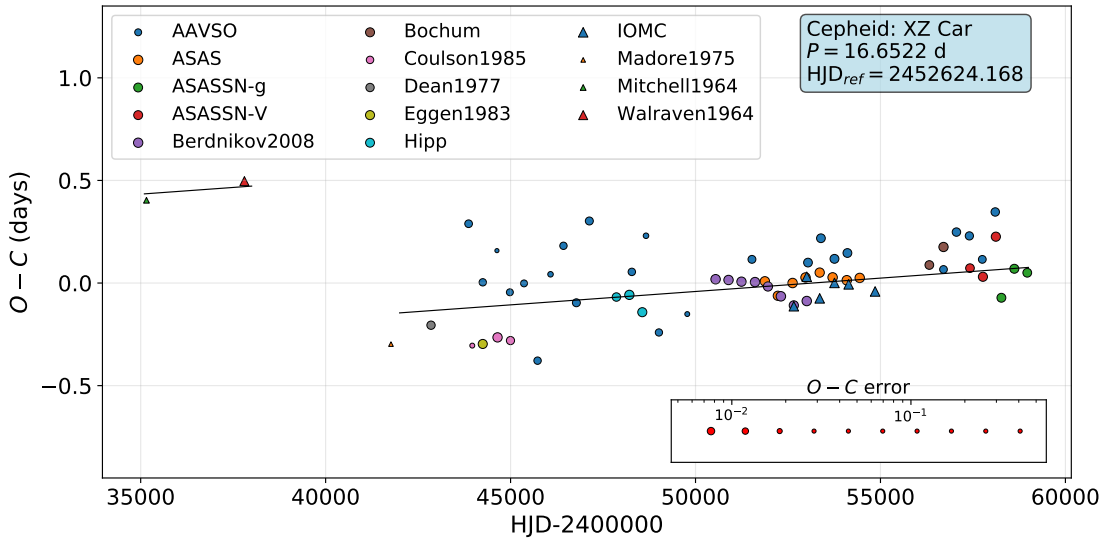

Figure 18.14: $O-C$ diagram of XZ Car exhibiting a phase jump between HJD 2438000 and 2442000, which altered the phase of the pulsation by 0.77 d.

18.2.2 UX Carinae

UX Car is a short period Cepheid, possibly linked to the open cluster IC 2581 based on its photometric and kinematic properties (Glushkova et al., 2015). However, the latest *Gaia* measurements suggest that the Cepheid is outside the cluster, with the *Gaia* EDR3 distance of the star being 1.52 kpc (Gaia Collaboration, 2016; Bailer-Jones et al., 2021), while the distance of IC 2581 being 2.45 kpc (Kaltcheva & Golev, 2012). This association was also marked unlikely by Anderson et al. (2013) previously.

This Cepheid was not investigated in terms of period changes before. Based on our studies, this variable exhibits rapid period jumps, as it can be seen in Fig. 18.15. The $O-C$ diagram was calculated using the following elements:

$$C_{\rm med} = 2453453.824 + 3.682171 \cdot E$$

As seen in the figure, the $O-C$ diagram shows a series of period jumps and rejumps, which is best explained by a series of constant period segments:

before HJD 2425000:	$P = 3.6822968 \pm 0.0000129$ d
HJD 2425000−2429000:	$P = 3.6821750 \pm 0.0000285$ d
HJD 2429000−2451000:	$P = 3.6822724 \pm 0.0000030$ d
after HJD 2451000:	$P = 3.6821861 \pm 0.0000052$ d

Since UX Car was found to be a possible binary by Kervella et al. (2019a) based on proper motion studies (although with low probability, due to the large separation), binarity could explain the shape of the $O-C$ diagram, which cannot be interpreted by evolution alone.

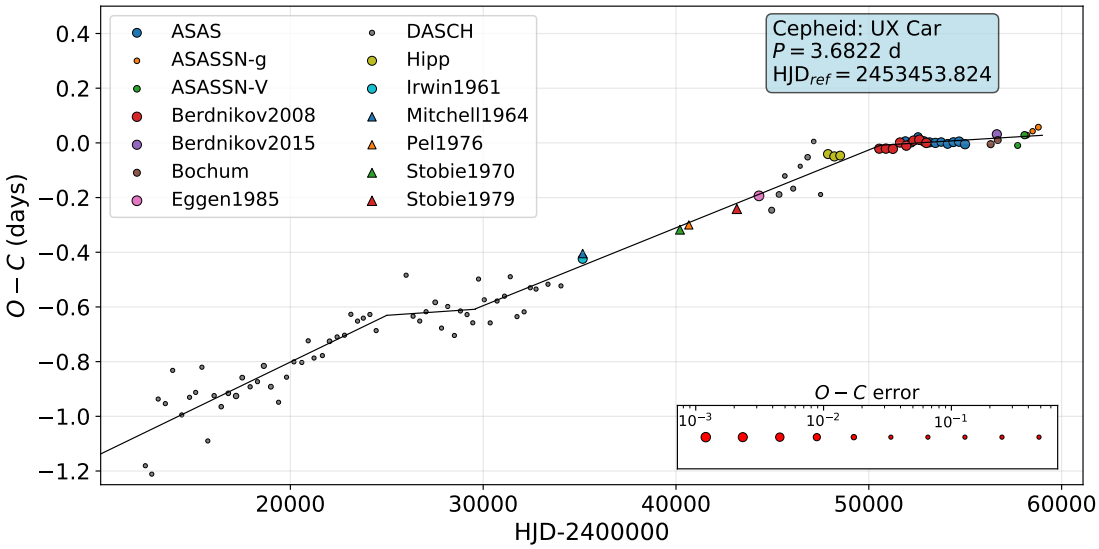

Figure 18.15: $O-C$ diagram of UX Car, interpreted as a series of period jumps. Three distinct jumps were covered by the observational data, along with the possibility of a fourth one: the first occurred at approximately HJD 2424900, while the second one at HJD 2428900, and the third at HJD 2451000. A fourth period jump could occur at HJD 2457700, but to confirm this, additional photometric observations would be necessary.

18.2.3 R Crucis

R Cru is a short period Cepheid that has been frequently studied in the past owing to its vicinity to and possible membership in the open clusters NGC 4349 (Majaess et al., 2012) or Loden 624 (Anderson et al., 2013). The membership in the former cluster was rejected by Chen et al. (2015), based on the distance difference between the cluster and the Cepheid and the fact the R Cru is brighter than the instability strip of the open cluster.

The binary nature of R Cru was first suspected by Lloyd Evans (1982) based on its γ-velocity drift, then the presence of the companion was confirmed by HST imaging (Evans et al., 2016a) and a possible X-ray emission was also identified at the position of the resolved companion (Evans et al., 2016b). This binary companion was also confirmed by Kervella et al. (2019a,b) through finding a slight offset in separation between the *HST* and *Gaia* observation epochs. They also determined the spectral type of R Cru B, which was found to be compatible with the X-ray radiation.

Despite being relatively bright, no $O-C$ diagram has been constructed yet for this Cepheid. According to our analysis, R Crucis underwent a period jump approximately at HJD 2433000 and pulsated with a modified period until approximately HJD 2446000 (Fig. 18.16):

before HJD 2432900: $P = 5.8257576 \pm 0.0000141$ d
HJD 2432900−2446100: $P = 5.8255291 \pm 0.0000109$ d
after HJD 2446100: $P = 5.8257880 \pm 0.0000061$ d

The presented $O - C$ diagram was calculated using the following elements:

$$C_{\mathrm{med}} = 2448157.512 + 5.825771 \cdot E$$

After the phase jump the period of the Cepheid returned to a value slightly longer than before, which suggests that the period of the Cepheid is increasing, however this could only be determined by observing another period jump. Nevertheless, the jump–rejump structure of the $O - C$ diagram could be linked to the presence of a companion, as evolutionary changes alone cannot explain this behaviour.

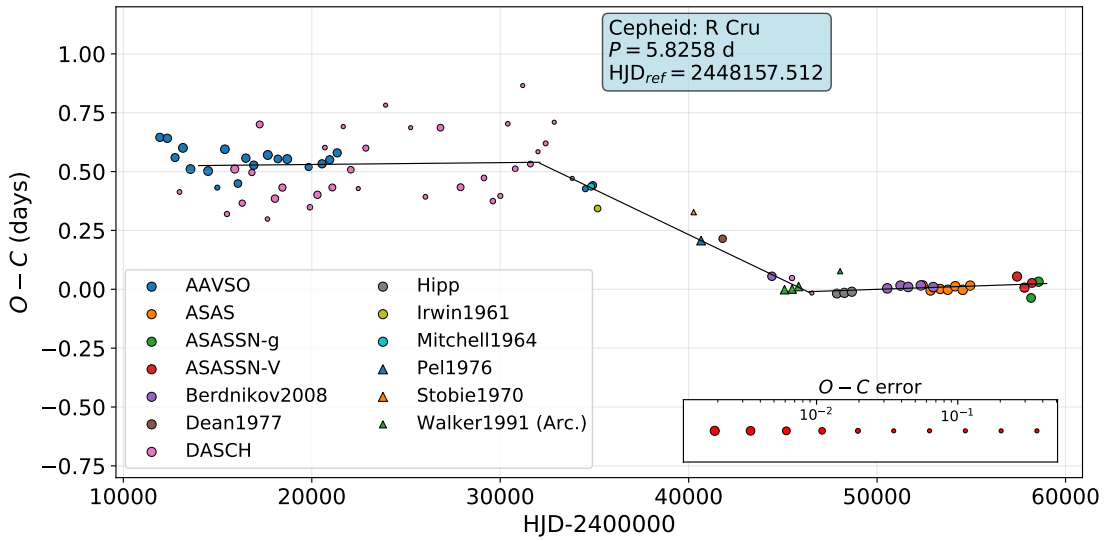

Figure 18.16: $O - C$ diagram of R Cru exhibiting a period jump at HJD 2433000, which modified the period of the Cepheid until HJD 2446000. The jump–rejump nature of the $O - C$ diagram provides another indication for the existence of the binary component.

18.2.4 DT Cygni

DT Cyg is a short period Cepheid which was frequently observed in the past decades. The $O - C$ diagram of the Cepheid constructed by Szabados (1991) showed peculiar period jump–rejump behaviour. This Cepheid was also suggested to be in a binary system, first by Leonard & Turner (1986), then by Szabados (1991) based on RV measurements, however, the orbital motion is yet to be confirmed.

By analysing the obtained $O-C$ diagram of DT Cyg we confirm the previous statement by Szabados (1991), that a second rapid period change occurred near HJD 2446000

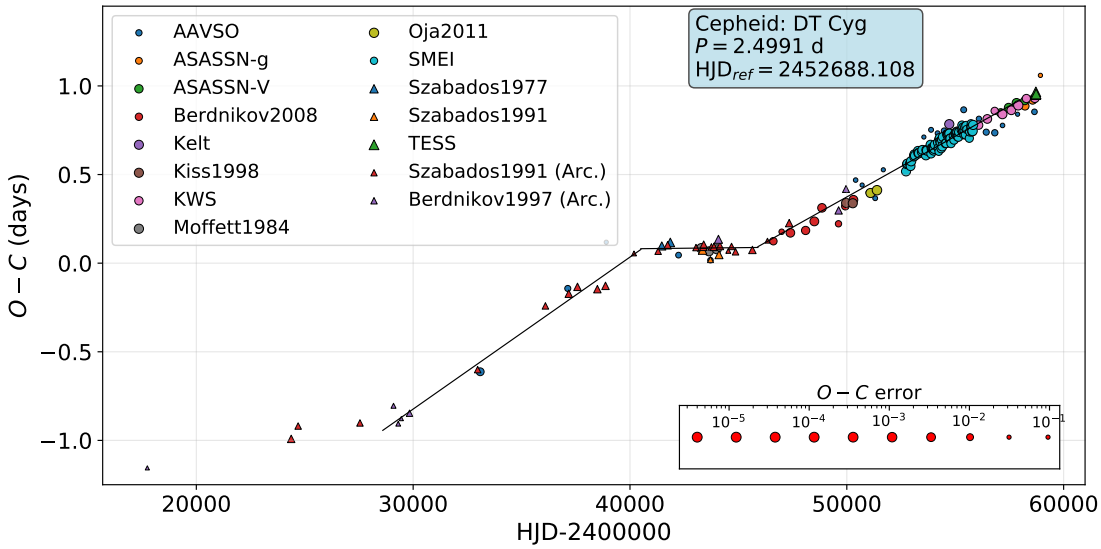

Figure 18.17: $O-C$ diagram of DT Cyg, exhibiting a clear case of period jump.

(Fig. 18.17). Our $O-C$ diagram was calculated using the following elements:

$$C_{\mathrm{med}} = 2452688.108 + 2.499063 \cdot E$$

The pulsation of DT Cyg can be characterized with the following periods:

before HJD 2441300:	$P = 2.4992250 \pm 0.0000093$ d
HJD 2441300−2445900:	$P = 2.4990380 \pm 0.0000116$ d
after HJD 2445900:	$P = 2.4992363 \pm 0.0000025$ d

It is not possible to determine how the period changed before HJD 2428600 based on the current diagram. The peculiar structure of the $O-C$ diagram could be linked to the presence of a companion, since evolutionary changes alone cannot explain it. Moreover, as it can be seen from the values above, the average pulsation period of DT Cyg became shorter after the rejump, which suggests that the star belongs to the second crossing Cepheids.

18.2.5 BN Puppis

BN Pup in an intermediate period Cepheid which was not investigated in terms of period changes before. The Cepheid was suspected to be connected to NGC 2533, but this turned out to be unlikely based on the large distance and age differences (Havlen, 1976; Anderson et al., 2013). The binary nature of the object was not investigated before, with only limited amount of RV data being available (Coulson & Caldwell, 1985; Pont et al., 1994; Storm et al., 2011).

Based on the compiled $O-C$ diagram plotted in Fig. 18.18, we have some indication that the Cepheid might have a companion. The phase jump in the case of this Cepheid

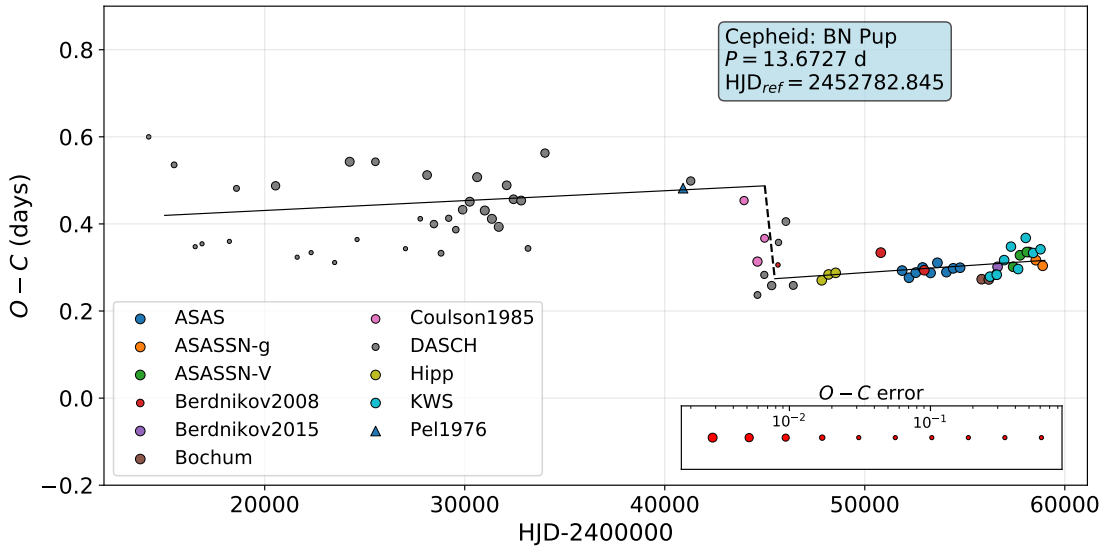

Figure 18.18: $O-C$ diagram of BN Pup, with a phase jump of 0.2 d visible at approximately HJD 2444500 which indicates binarity of the Cepheid.

is less ambiguous than in other cases since it is detected in data from a single source (DASCH photometry) and it is also supported by the precise photometric measurements of Pel (1976). The presented diagram was calculated using the following elements:

$$C_{\max} = 2452782.845 + 13.672693 \cdot E$$

The phase jump occurred at approximately HJD 2444500 and altered the phase of the pulsation with ∼0.2 d. The values of the pulsation period before and after the phase jump are in agreement within errors. To determine whether a long period signal can be extracted from the RV data, we reanalysed the measurements of Coulson & Caldwell (1985), Pont et al. (1994), and Storm et al. (2011). According to the Fourier decomposition of the signal, a period of ∼4300 d can be extracted, but the sparseness and the uncertainty of the RV data does not allow us to determine whether it is truly connected to the binary nature of the Cepheid. The phase jump exhibited by the $O-C$ diagram could suggest that BN Pup is possibly a member in a binary system, if one assumes an empirical correspondence between the two, although further RV measurements are necessary to validate this assumption.

18.3 Overtone Cepheids

The remaining two Cepheids that were found to exhibit peculiar $O-C$ diagrams show erratic or semi-erratic period changes, which, to our current best understanding, can only be explained through a set of linear segments (consecutive intervals of random, but otherwise constant-period pulsations) and is a characteristic of overtone pulsators.

During the observed timeframe, none of these Cepheids showed recurrence in the change of their pulsation period.

18.3.1 X Lacertae

X Lac is a short period Cepheid which is possibly connected to the open cluster FSR 384 (Glushkova et al., 2015) (although this association was marked as unlikely by Anderson et al. (2013) before). The period changes of this Cepheid were extensively studied by Evans et al. (2015), finding that it shows an erratic period change. Apart from the erratic period change, the low pulsation amplitude also points towards the overtone nature of the pulsation (Storm et al., 2011), which makes this object interesting, as only a few overtone pulsators are known with such a long period.

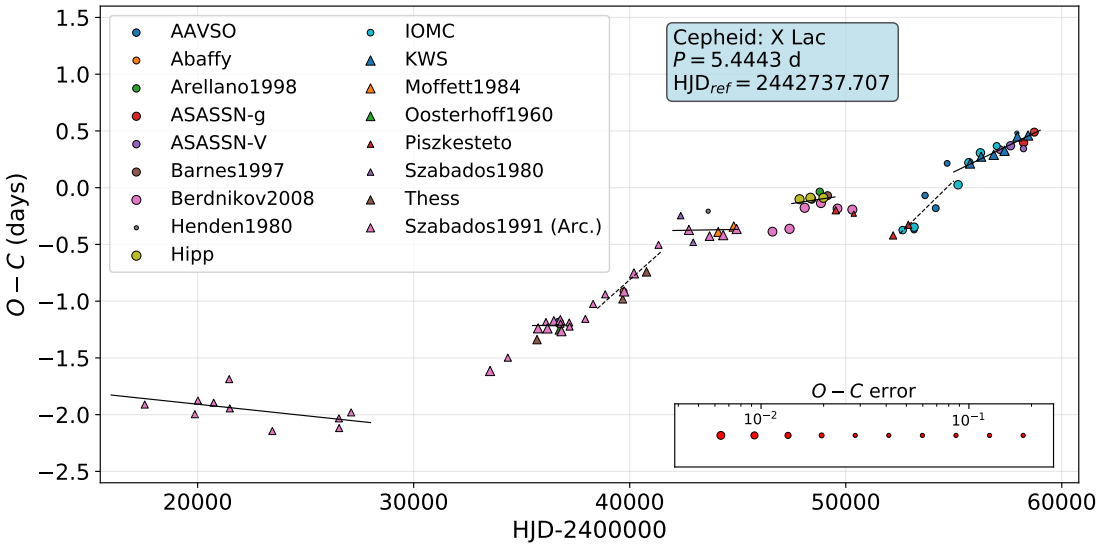

Figure 18.19: $O-C$ diagram of X Lac exhibiting an erratic behaviour which can best be described with a series of rapid period changes.

Our analysis of the available photometric data yielded very similar results to those presented by Evans et al. (2015): the resulting $O-C$ diagram is best fitted with a series of linear segments as shown in Fig. 18.19. The presented $O-C$ diagram was calculated with the following elements:

$$C_{\mathrm{med}} = 2442737.707 + 5.444322 \cdot E$$

According to our analysis, the $O-C$ diagram of X Lac can be best described with the following periods:

before HJD 2428000:	$P = 5.4442119 \pm 0.0000659$ d
HJD 2435500−2437000:	$P = 5.4445175 \pm 0.0001767$ d
HJD 2438500−2441500:	$P = 5.4456094 \pm 0.0002935$ d
HJD 2442000−2445000:	$P = 5.4443820 \pm 0.0000715$ d

HJD 2447500−2449500: $P = 5.4444422 \pm 0.0001904$ d
HJD 2452500−2455000: $P = 5.4451025 \pm 0.0003423$ d
after HJD 2455000: $P = 5.4448548 \pm 0.0000447$ d

Our analysis shows that the period change sequence of X Lac is indeed erratic throughout the observed timeframe, which supports the assumption that this Cepheid is an overtone pulsator.

18.3.2 EU Tauri

EU Tau is a short period Cepheid and an overtone pulsator (Gieren et al., 1990). The binary nature of the object was first suspected based on RV data (Gorynya et al., 1996), however a later study by Evans et al. (2015) found this unlikely. The period changes of EU Tau were investigated by Berdnikov et al. (1997) and Evans et al. (2015), finding first a linear, then erratic period change, respectively.

The obtained $O-C$ diagram (Fig. 18.20) was calculated using the following elements:

$$C_{\mathrm{med}} = 2432499.902 + 2.10241 \cdot E.$$

According to our analysis, which matches with the finding of Evans et al. (2015), the $O-C$ diagram can be best described as three constant period segments:
before HJD 2435000: $P = 2.1023336 \pm 0.0000028$ d
HJD 2437000−2451000: $P = 2.1025187 \pm 0.0000017$ d
after HJD 2452500: $P = 2.1022962 \pm 0.0000047$ d

Since the transitions between these segments were not covered by observations, their nature cannot be established. To determine whether the pulsation periods are truly erratic, or if there is any connection between them, further observations are required.

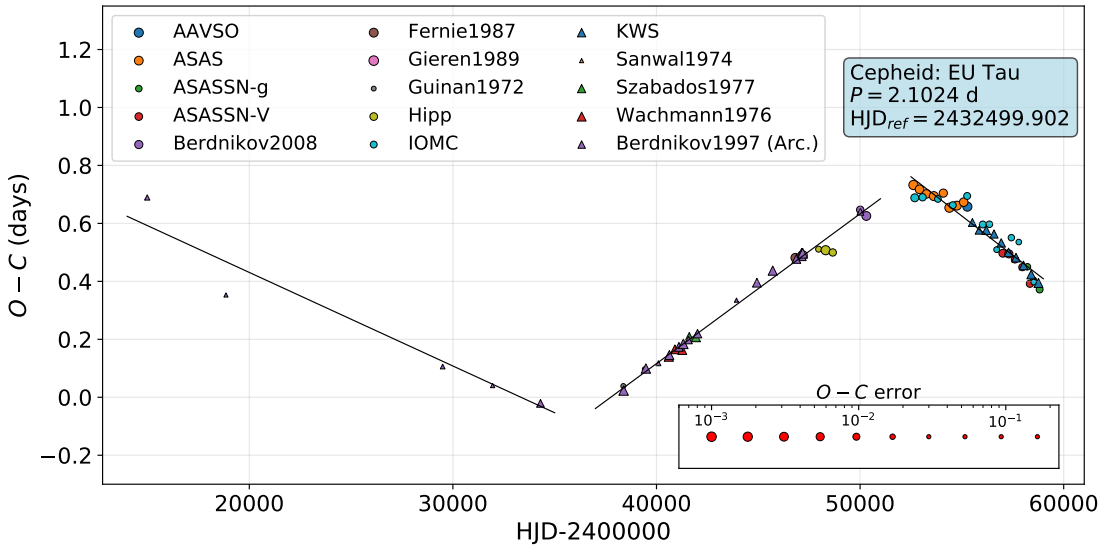

Figure 18.20: $O - C$ diagram of EU Tau, showing two rapid period changes, between which the pulsation of the star can be described with constant period values.

19 Collective analysis on period change rates and fluctuations

19.1 Colour-magnitude diagram and period change rates

Apart from the Cepheids detailed in the previous sections, we have obtained $O-C$ diagrams for 132 additional Cepheids (see Table C.1 for the complete list), which all show a parabolic shape, thus dominated by the evolution of the variable star. As a result, our Cepheid sample contains 141 stars that exhibit clear evolutionary changes in their $O-C$ diagrams, including those that were termed peculiar based on additional features in their $O-C$ diagrams in Sect 3.1.

The recent advancement in astrometry owing to the measurements of the *Gaia* space probe allows for the construction of the colour-magnitude diagram (CMD) for the current set of Cepheids with an unprecedented accuracy. Figure 19.2 shows the CMD based on the *Gaia* DR2 and *Gaia* EDR3 data (Gaia Collaboration, 2016, 2018, 2021; Lindegren et al., 2021; Riello et al., 2021) as a comparison. Since neither of the data releases contained measurements of the Galactic extinction for all the Cepheids, we applied the attenuation correction on the individual photometric measurements based on the colour-excess values listed in the DDO database of Galactic Classical Cepheids[1]. For the Cepheids which were not listed on the website, or scattered far from the rest of the variables on the CMD due to the false value of the colour excess (KL Aql, V898 Cen) we used the more recent measurements (Schmidt, 2015; Groenewegen, 2020), but in the case of V898 Cen the resulting position was still slightly different from the rest of the dataset. For the additional Cepheids that have no published colour-excess values at all (EV Cir, V5738 Sgr, GP Mus, V2744 Oph, CE Pup, DU Pyx and V520 Vel) we assumed the extinction values inferred by Anders et al. (2019). The colour excess values were then converted to the *Gaia* passband system using the scaling given in Casagrande & VandenBerg (2018).

As seen in Fig. 19.2, the data from EDR3 show a much smaller scatter and exhibit a much clearer trend for the pulsation period of the Cepheids, which demonstrates well the improvement of the *Gaia* data compared to the previous data releases. On the right panel of Fig. 19.2 we attempted to draw the limiting lines of the strip populated by the Cepheids; for the approximate alignment of these lines we omitted all Cepheids with uncertain or non-published extinction mentioned above. The resulting lines are notably not parallel, which indicates that for longer period Cepheids the possible range of colour index values is broader, which means that the instability *strip* of Cepheids could in fact

[1] http://www.astro.utoronto.ca/DDO/research/cepheids/cepheids.html

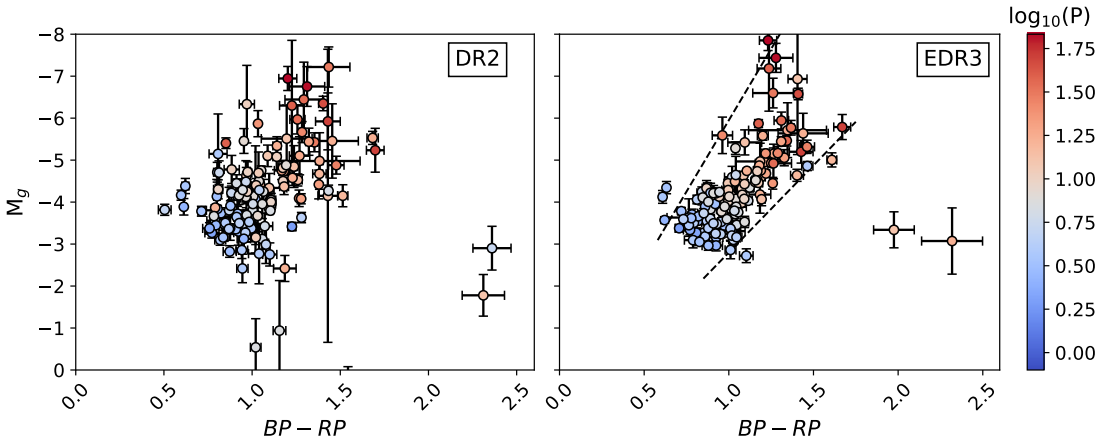

Figure 19.1: Colour-magnitude diagrams of the investigated Cepheids calculated from the *Gaia* DR2 (left) and *Gaia* EDR3 (right) datasets. The dashed lines show the assumed edges of the instability strip. The error bars show the uncertainties arising due to the parallax and the reddening errors.

be an instability *wedge*, as proposed earlier by Fernie (1990a). This also matches the results previously obtained from the observations of IUE for a smaller sample of Cepheids (Evans, 1992). To examine this possibility even further, more accurate extinction values would be required, which are planned to be published with the complete third data release of *Gaia* in 2022.

By fitting the $O - C$ diagrams of the investigated Cepheids with second order polynomials, along with a sinusoidal modulation superimposed when statistically motivated, and then applying the method described by Sterken (2005) we could determine the rates of period change for each of the variable stars. Our results and conclusions on period change rates essentially match those presented by Turner et al. (2006): the values inferred by us are well explained by the evolutionary models discussed in that work and the ratio of Cepheids showing positive and negative period changes is also identical, if one considers the possible selection effects (70% of our sample Cepheids show positive period changes, while this value was 67% in Turner et al. (2006)). The deviations from evolutionary models we find in our sample are also very similar to the previous results: several short period Cepheids exhibit a period change rate that fall between the value ranges expected for first and third crossing Cepheids, while several intermediate period Cepheids show a period change rate that is smaller than predicted by evolutionary models.

As it was discussed by Neilson et al. (2012), the inclusion of convective core overshooting and enhanced mass loss can explain these deviations. Moreover, they showed that the difference between the ratio of stars showing positive and negative period changes for observations and predictions (where the unmodified evolutionary models estimate significantly larger fraction of positive period change Cepheids, namely 85%) can also be explained through mass loss, although they note that there is currently no explana-

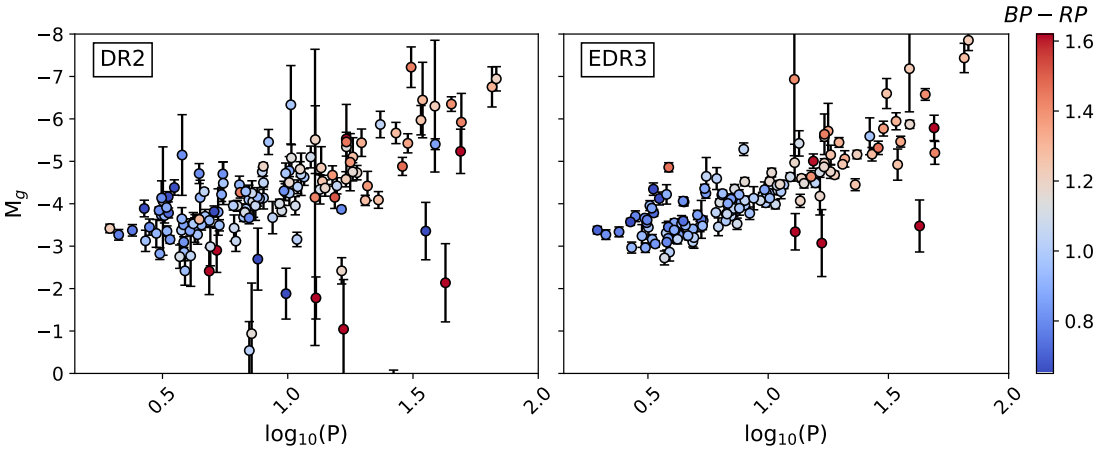

Figure 19.2: Period-luminosity relation of the investigated Cepheids, calculated from the *Gaia* DR2 (left) and *Gaia* EDR3 (right) datasets. The individual points are coloured by the dereddened *Gaia* $BP - RP$ values. The right panel demonstrates well the improvement of quality in the Cepheid distances between the two data releases.

tion for large mass loss rate they found to be required. Complementary to this work, Miller et al. (2020) investigated how rotation and convective core overshooting alter the distribution of period change rates, finding that they do not assert significant influence on then, despite being important parameters for the evolution of Cepheids.

As it was noted by Turner et al. (2006), the period change rate could be an important probe for the estimation of stellar properties. To test this observationally, we correlated the period change rates of Cepheids to their colours for a moderate range of pulsation periods (between 2 and 5 days) as seen in Fig. 19.3. The period range was chosen based on the CMD, as the relevant effect was visible primarily for short period Cepheids, while for longer periods the scatter on the CMD was too large for detecting a meaningful effect. As seen in the plot, bluer Cepheids exhibit slightly larger period change rates, which decrease toward the red edge of the instability strip. The individual points are coloured by the pulsation period length, which show no significant correlation with either the period change rate or the colour within the considered period range. This agrees well and observationally validates the statement in Turner & Berdnikov (2004), in which they note that at a given pulsation period, Cepheids at the high-temperature edge of the instability strip should exhibit larger rate of period change than those at the low-temperature edge, due to the former having larger masses.

This demonstrates that the period change rate can indeed provide a valuable observational probe for the determination of physical parameters. In addition to the pulsation period, which can be used to estimate both the "vertical" and the "horizontal" position of the Cepheid within the instability strip, and the corresponding physical parameters owing to the period-luminosity and period-colour relations (assuming an underlying mass-luminosity relation and a pulsation model, see, e.g., Beaulieu et al. 2001), the period change rate can independently probe the "horizontal" direction. Since the period

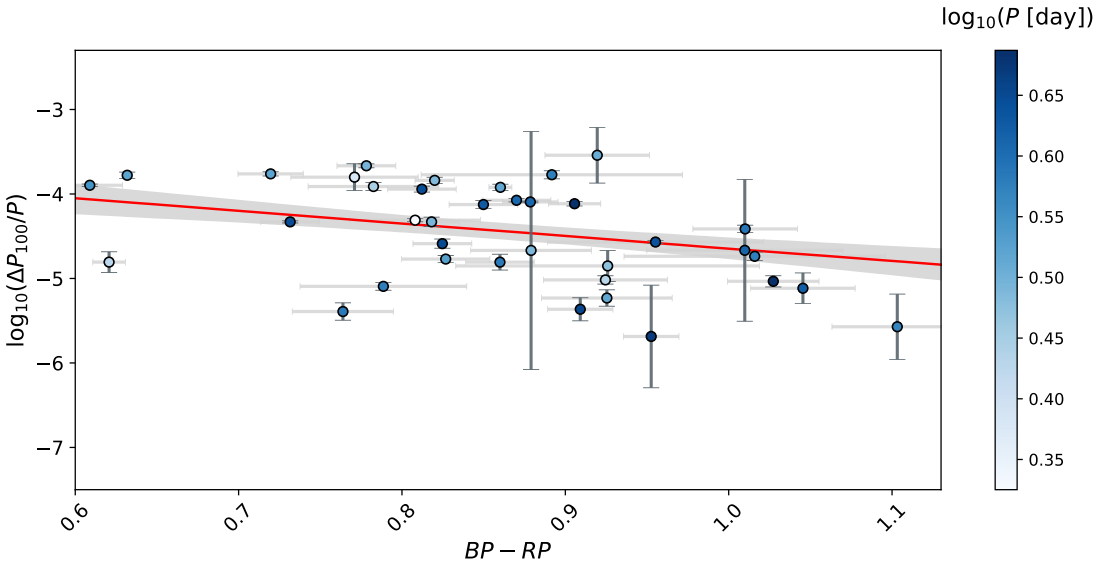

Figure 19.3: Correlation plot of the colours and period changes of short period Cepheids (pulsation period range of 2-5 days). The red line shows the best linear fit to the whole dataset, while the grey shaded area shows the 1σ quantile of the fit. Period changes decrease within errors towards the red edge of the instability strip.

and period change rate values are not tightly correlated due to the various crossing modes, mass loss, and convective core overshooting rates, this correlation is not bound to the pulsation period, which is also well shown in Fig. 19.3. Henceforth, the period change rate could be used to enhance the precision of colour and temperature estimation of Cepheids when coupled with the period values. Further investigation of this correlation is beyond the scope of this work, however we note that it would be worthwhile to analyse to what extent can it be used for the inference of physical properties. Combined with the new data from *Gaia* it could provide a simple way to constrain the effective temperature of the variables compared to the conventional spectroscopic method, yet it could prove to be more precise than the current, solely colour based empirical relations.

Owing to the long temporal coverage of the newly calculated $O-C$ diagrams one can not only calculate the period change rate, but its acceleration as well: in such cases the resulting $O-C$ diagrams systematically deviate from the parabolic fit, since their complete description would require higher-order polynomials, as it was also noted in previous works (Szabados, 1983; Fernie, 1984; Turner et al., 2006). In our sample, most of the long period Cepheids exhibit such $O-C$ diagrams (most notably, EV Aql, S Vul and SV Vul). Naturally, all Cepheids are expected to show such high order terms in their $O-C$ diagrams, but due to the short observed timeframes these terms are usually negligible for Cepheids that exhibit smaller period change rates.

To visualize this expectation we attempted to recover the higher order period change from theoretical models: by adopting the evolutionary trajectory models and instability strip edges from Georgy et al. (2013) and Anderson et al. (2016) respectively, and the

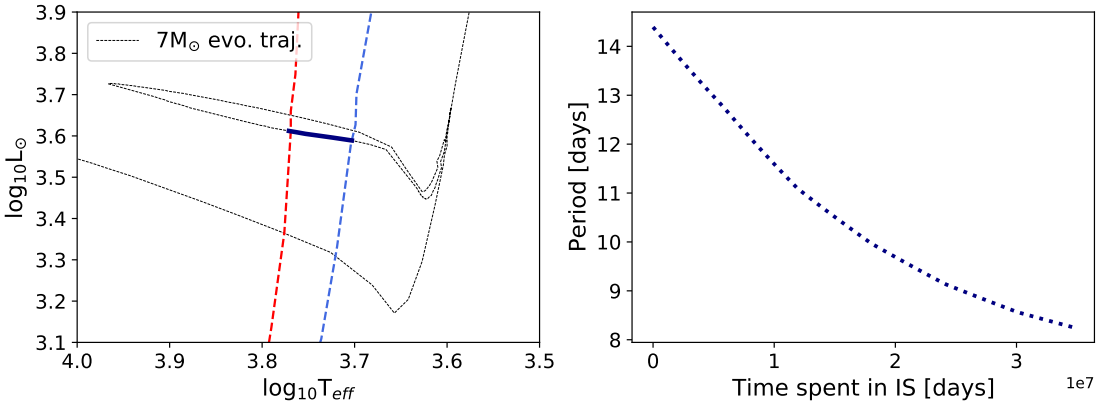

Figure 19.4: Period values estimated for the second crossing of a $7M_{\odot}$ star at different times (right panel), showing a curved evolution indicating a non-linearly changing period, with the left panel showing the corresponding evolutionary trajectory (with the important segment highlighted).

period-mass-luminosity-temperature relations of De Somma et al. (2020), we calculated how the pulsation period would change for a single star due to stellar evolution. An example of the results is shown in Fig. 19.4: the theoretical models also yield non-linearly changing period, which validates the expectation for higher order terms in the $O-C$ values. Currently, the interpretation of these higher order terms is not yet complete, but they will also yield additional valuable information about the pulsation of these stars similarly to the period change rates.

19.2 Period fluctuations

Apart from examining the overall rate of period change for the Cepheids in our sample, the $O-C$ diagrams also made it possible to investigate random fluctuations present in the pulsation. An example for such fluctuation signal can be seen in the $O-C$ diagram of SV Vul (Fig. 19.5): it shows a long-term trend corresponding to the evolution of the Cepheid and a quasi-periodic wavelike signal superimposed, with varying shape. Such wavelike signals cannot be explained by LiTE, as their amplitudes are too large compared to their period, and the shape of the waves also changes in time. The physical explanation for such modulations is that random fluctuations in the pulsation period accumulate and cause wavelike signals of varying shapes. For long, this was the only classical Cepheid for which fluctuations were detected (Turner et al., 2009). Recently, Rodríguez-Segovia et al. (2021) also found that five additional long period Cepheids in the LMC reliably show such large amplitude fluctuations, highlighting their ubiquity. It was expected that fluctuations are present in most Cepheid variables as well, but detection would require continuous space-based photometry, where consecutive epochs can be observed Turner et al. (2010). Multiple studies attempted to detect and quantify fluctuations this way, as we discussed in Sect. 16.

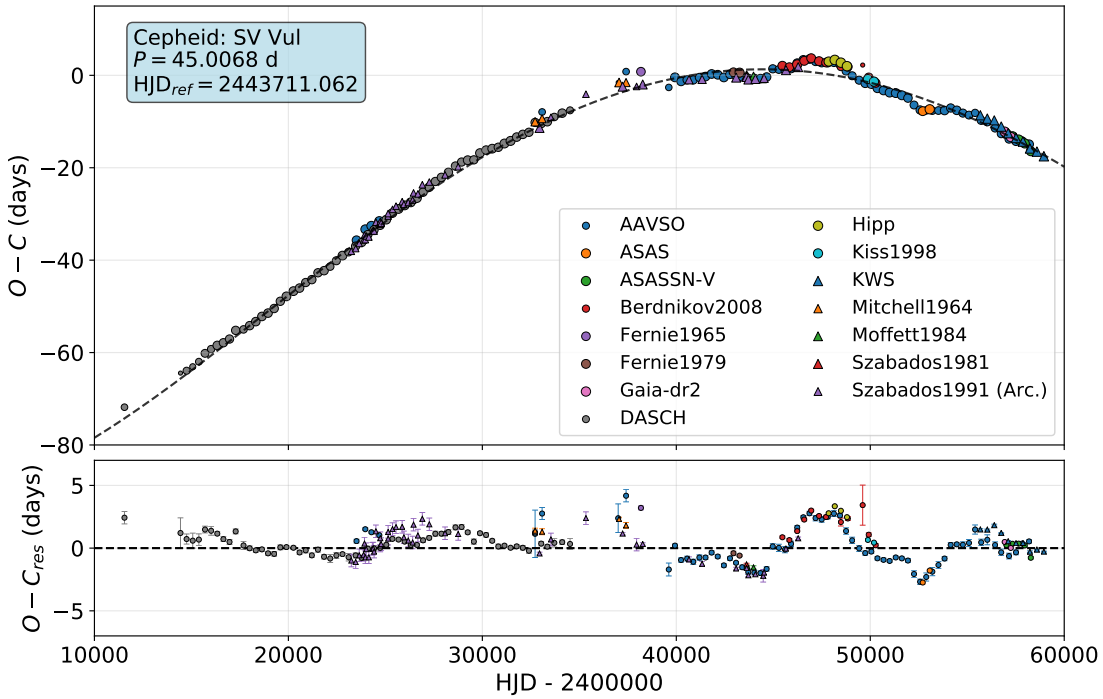

Figure 19.5: $O-C$ diagram of SV Vul (top panel), showing a long-term change corresponding to stellar evolution, with superimposed period fluctuations, and the residual $O-C$ diagram (bottom panel) after subtracting the evolutionary changes.

As we will show below, such period fluctuations are more common among Cepheids than previously thought. It has been shown that longer period variables, like RV Tauri or Mira stars, can exhibit long term quasi-periodic waves in their $O-C$ diagrams due to the period fluctuations, which becomes more prominent for longer pulsation periods (Percy et al., 1997; Percy & Colivas, 1999; Molnár et al., 2019), however, no such conclusions were drawn for classical Cepheids. In the sample of stars we investigated, we found that 51 Cepheid showed wavelike signals in the residual $O-C$ diagrams that most probably originated from fluctuations, apart from the Cepheids that were termed 'peculiar' in the previous sections. To select these Cepheids from our sample, we performed F-tests on their $O-C$ diagram fits to analyse the residuals of the models and to check whether they indicate that the use of more complex models (i.e. which also fit for an assumed wavelike modulation) are validated. We compared three different models for the test: the constant period model (linear $O-C$ diagram), the linear period change model (parabolic $O-C$ diagram) and the linear period change plus wavelike modulation (superposition of a parabolic and a sinusoidal change), in which case we simultaneously fit for both the evolutionary changes and the modulation. Table C.2 of the Appendix show the results obtained for the different model pairs. We included Cepheids in the fluctuating sample when the F-test conducted for the comparison of the parabolic and parabolic plus wave fits yielded an F-statistics larger than 10, which means that the more complex model

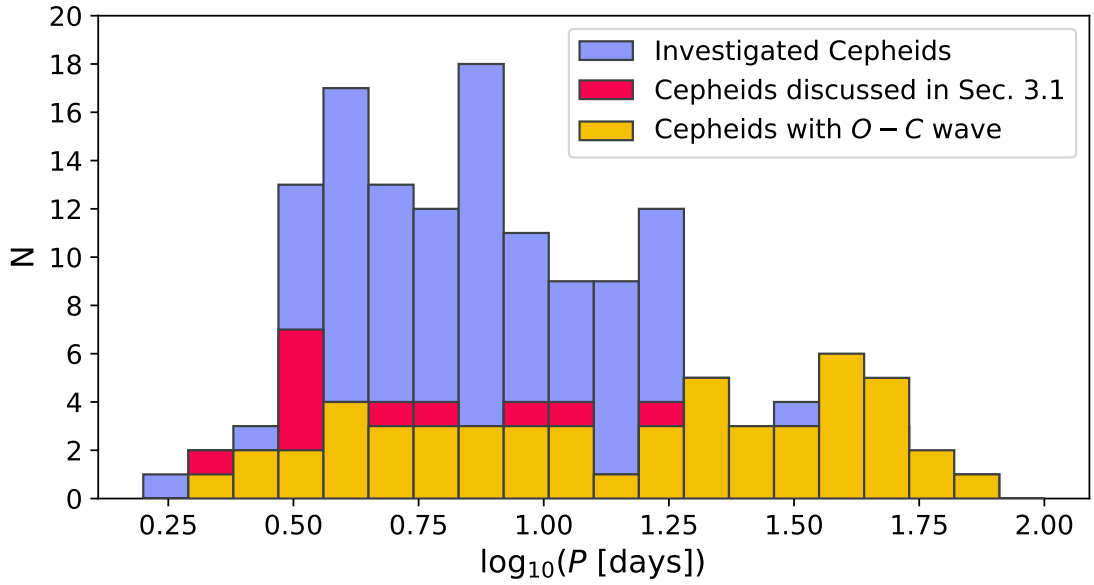

Figure 19.6: Distribution of Cepheids according to their pulsation periods. The blue histogram shows all investigated Cepheids, while the yellow ones show only those that show a wavelike signal in their $O-C$ diagram superimposed the trend corresponding to the evolution. In addition, the red histogram shows the fraction corresponding to the Cepheids termed 'peculiar' in the previous sections, while showing wavelike signals in the $O-C$ diagrams.

was favoured at a significance level of 0.99 (with the difference between the degrees of freedom of the compared models being $DF = 3$). To remove possible contaminations, or Cepheids for which the fitting code yielded erroneous results, we rejected every star where the period of the sinusoidal fit was either shorter than 3000 days (8-10 times the folding time used for the construction of the $O-C$ diagrams, to avoid sampling effects) or longer than five quarters of the observed time frame (in which case the sinusoidal waveform overfitted the parabolic change).

In Fig. 19.6 we plotted the distribution of the investigated Cepheids according to their pulsation periods along with the information about what fraction of Cepheids show fluctuations in their $O-C$ diagram. As seen on the plot, all long period ($\log_{10} P > 1.25$) Cepheids show fluctuations (with the sole exception being EZ Vel, however the temporal coverage of its photometry did not allow for a detailed fit for the $O-C$ diagram), which was expected based on the behaviour RV Tauri stars with similar periods. The ratio of stars exhibiting such modulations starts to drop for intermediate period stars and falls to a value of ∼25–40%, which remains approximately the same for shorter period Cepheids too. We suspect that at least a fraction of the stars that were not included in the fluctuating sample also show wavelike modulations of such nature as well, however their overall amplitude was lower than the scatter of the residual $O-C$ diagram, hence they remained below detectability.

It is important to note that the apparently general fact, that all longer period ($\log_{10} P > 1.25$) Cepheids exhibit period fluctuations to some extent, has not been known before, thus it can have important implications for the calibration of the distance ladder via PL relation of Cepheids. Extragalactic Cepheids are generally difficult to observe, as their light curve spans only a few hundred or a thousand days at most, with sparse sampling. Consequently, it is impossible to determine their fluctuation-free, evolution based "true period", and the resulting period value can be affected by the cumulative effect of the period fluctuations. Whereas the shorter period ($1.25 < \log_{10} P < 1.48$) population of these Cepheids exhibit only smaller fluctuations and the possible error on the inferred period values remains below a few hundredths of a day, for longer period Cepheids (e.g., for one of the longest period Cepheids in our sample, for S Vul) such fluctuations could lead to a cumulative effect that alters the inferred period by more than 0.5 day, which would then add a detectable term to the final uncertainty. While such effects might not affect the PL relationship significantly due to the use of a larger sample of stars or the inclusion of shorter period variables (for which the period determination is more accurate) as was done in Riess et al. (2019), it could severely increase the uncertainty of the results based entirely on long or ultra-long period Cepheids (e.g., Bird et al. 2009).

We also measured how the strength and size of these accumulated period fluctuations change for different pulsations periods. For this purpose, we applied the Eddington–Plakidis method (E–P method) (Eddington & Plakidis, 1929) on each Cepheid in our sample that showed signs of fluctuations. According to this method, one must whiten the calculated $O - C$ values for the effect of evolution, then take the absolute values of all delays $u(x) = |a(r + x) - a(r)|$ for each rth maximum, $a(r)$, for every possible x cycle separation in the residual dataset. According to Eddington & Plakidis (1929), if the irregular signal is present due to the fluctuation of the phase and period at the same time, then the $\langle u(x) \rangle$ means of all accumulated delays should be related to the random period fluctuation ϵ by Eq. 19.1:

$$\langle u(x) \rangle^2 = 2\alpha^2 + x\epsilon^2 \tag{19.1}$$

where α characterizes the errors in the measured times used for the $O - C$ data points.

We produced Fig. 19.8 by comparing the resulting ϵ period fluctuation parameter (obtained by fitting the E–P diagrams for $x < 100$ cycle separations) with the corresponding pulsation period, which shows that there is a significant connection between the size of fluctuations and the pulsation period.

However, the E–P method has two drawbacks which are inherent to its definition, one of which is that one has to manually set what maximal cycle separation is considered for the linear fit described above. There is no statistical background on what one should choose for the maximal cycle separation, and since Cepheids show a very large variation of such E–P diagrams, one has to set this value manually. This makes the method infeasible for large datasets, since one either has to tune this value for each star, or pick a general value, which might not be optimal for every sample member. Due to this, the resulting ϵ fluctuation parameter will also be more uncertain, and its value will be based on a modelling choice. An example for this is also shown in Fig. 19.7: as seen

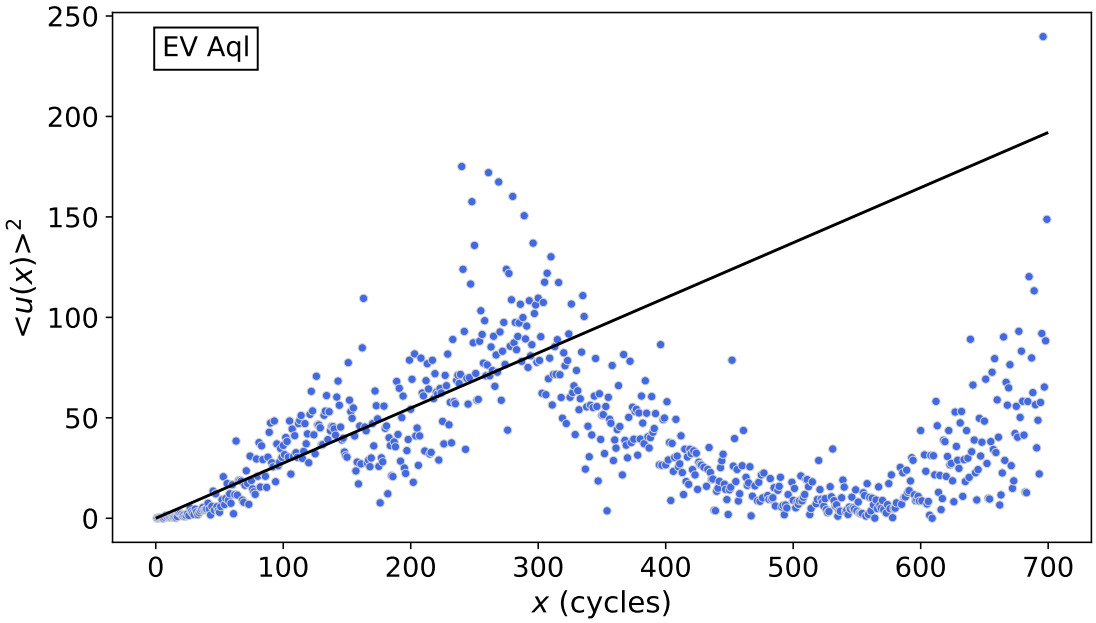

Figure 19.7: The Eddington–Plakidis diagram of EV Aql, along with the calculated fit for cycle separations $x < 100$. As the diagram shows, multiple choices are possible for this maximal value, which can influence the final result for the period fluctuation parameter.

in the figure, multiple ranges could be considered for the fitting of the diagram, which sets a range for the final fluctuation parameter values as well. Additionally, the E-P method also has the disadvantage of not being able to provide an upper limit for the fluctuation parameter, therefore if the $O - C$ diagram is dominated by uncorrelated noise, the resulting E–P diagram will show no structures, unlike in Fig. 19.7. Hence, no linear fitting can be carried out in those scenarios.

To circumvent this issue, we calculated a correlation diagram similar to Fig. 19.8 using the result of the $O - C$ diagram fits instead. For each of the Cepheids where fluctuations were found by the F-test, we simply correlated the measured amplitude of the wavelike modulation with the pulsation period of the star. Unlike in the case of the Eddington-Plakidis method, here we were able to determine a detectability limit even when the amplitude of the modulation could not be measured, i.e., when no fluctuations were found: in this case the detectability limit could still be determined as the maximal value of the Fourier spectrum calculated for the residuals after fitting and subtracting the evolutionary changes.

Through this procedure we obtained Fig. 19.9, which shows similar trends as the Eddington–Plakidis method based diagram, except for the shorter period Cepheids. As expected, the detectability limit drawn out by the non-detections increases slightly with period as the light curves of the Cepheids become more and more complex, thus more difficult to fit, but still, a reasonable amount of fluctuating Cepheids were found throughout

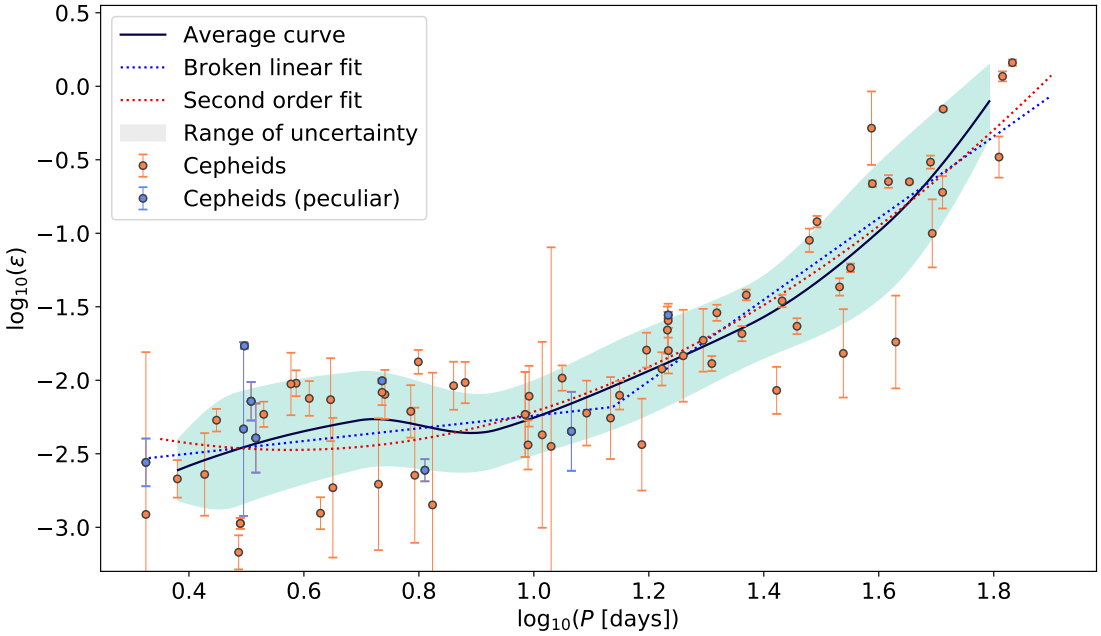

Figure 19.8: Correlation between the Eddington-Plakidis ϵ parameter calculated for cycle separations $x < 100$ and the pulsation period. The blue and red dashed curves show the two fits described in the text. The black curve shows the empirical average, while the blue region shows the empirical standard deviation around it. For the fitting of the coloured curves, the peculiar Cepheids were not taken into account.

the investigated period range, which defines the underlying trend reliably. As it is shown by the average curve in Fig. 19.9, the amplitude of the fluctuations decreases linearly against the logarithm of the period for longer period Cepheids ($\log_{10} P > 1.25$), only to reach a minimum for intermediate period Cepheids around a period of $\log_{10} P \approx 0.8$ and increases again for short period stars. We note that the Cepheids where we found no modulations, and hence are marked as non-detections on the diagram, can significantly influence the position of this minimum. However, the fact that the largest detected fluctuations in the intermediate period range stay well below the maximal ones found for both shorter and longer period Cepheids supports the notion that there is a minimum for these modulations in the period range of bump Cepheids, suggesting a quenching mechanism for these variables. Moreover, Fig. 19.9 also supports the LiTE explanation described above for the modulation found for RX Aur and Y Oph, as both stars are outliers for the trend defined by the fluctuations.

We also investigated how easing the F-test based constraints affects the results: if we lower the confidence level from 0.99 to 0.95, the F-test based procedure favours the inclusion of further 23 Cepheids into the fluctuation sample. Most of these stars fall in the period range of bump Cepheids, with the amplitudes of the wavelike signals being close or at the noise level of their $O - C$ diagrams. In case these stars are included, the fraction of Cepheids showing fluctuations jumps to a level of ∼50% instead of 25-40%,

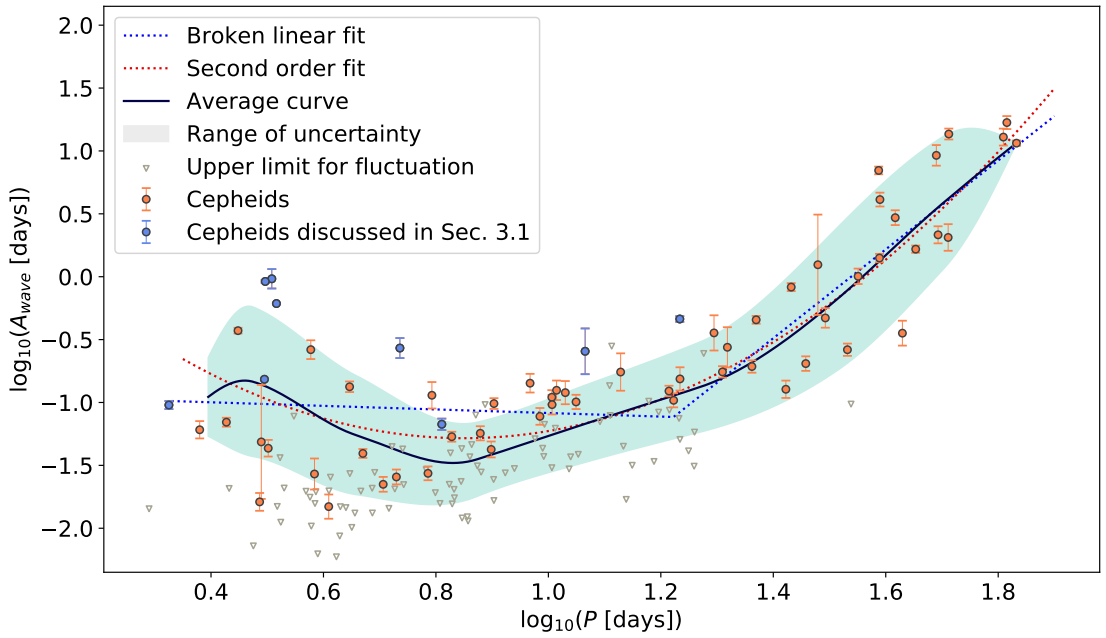

Figure 19.9: Correlation between the measured fluctuation amplitudes and the pulsation periods. The legend is the same as for Fig. 19.8. The non-detection limits calculated from the Fourier spectrum for individual Cepheids are marked with grey triangles.

and remains constant thorough the lower end of the pulsation period range, suggesting an even higher frequency for the presence of these modulations. In terms of fluctuation strength, since the fluctuation amplitudes are close to the detection limits assumed for these stars in Fig. 19.9, which were taken into account for the fitting, neither the actual position of the found fluctuation minimum, nor the general trend changes significantly if we ease the constraints.

As seen in the figures, multiple interpretations are possible: since there are two separate point clouds in the resulting plot, we can either assume that the fluctuation features observed in them are of the same origin, or of different ones.

By assuming that the fluctuations detected for short and long period Cepheids are of the same origin, the correlation plot can be fitted by a quadratic function. This fit shows that the size of fluctuations decreases from the longer periods towards shorter periods, reaching a minimum at the lower end of the period range of bump Cepheids, then growing back again for shorter period stars. This picture agrees with the presence of a quenching mechanism for bump Cepheids, and it also follows well the average curve.

If one assumes that the two parts of the fluctuation diagram are of different origins (i.e. the fluctuations are of different nature for long and short period stars), then the plot can be fitted by a broken linear curve. One wing of this broken linear curve on the Eddington-Plakidis based diagram (Fig. 19.8) shows that for long period Cepheids the fluctuations scale linearly with the pulsation period, which agrees with the findings of Percy & Colivas (1999) for longer period Mira stars, indicating that this fluctuation

effect is a similar period fluctuation in both types of variable stars. However, in this case there is no explanation for the short period wing, as this fit would suggest that fluctuations detected for shorter period Cepheids are of different origin than the former one. In the case of the amplitude-based diagram, the broken linear fit shows a similar linear trend for the longer period Cepheids. Based on these fits, the linear scaling present between the fluctuations and the period for long period Cepheids weakens considerably on intermediate and short period ranges, as the level of fluctuations seems not to change as significantly over this range.

The datapoints at short periods ($\log_{10} P < 0.8$) also show a much larger scatter around the model fits compared to other period ranges, with a clear gap in the amplitude distribution (around $\log_{10} A \approx -1.0$, where we find several Cepheids with both significantly larger and smaller fluctuations in this period range). This can indicate that there are more than one type of fluctuations present at short periods, one for normal and one for overtone Cepheids, presumably (with smaller and larger fluctuations, respectively). Their comprehensive modelling would require a more complete sample of shorter period Cepheids, but such an analysis is beyond the scope of this paper. Nevertheless, the supposed models show that either the change in the nature of fluctuation signals occurs at, or the overall strength of the fluctuations have a minimal value close to the period range of the bump Cepheids, both of which suggests that the pulsation of the bump Cepheids is subject to less such random fluctuations and provides an additional proof for the increased stability of the pulsation of these stars.

20 Summary

In this work we presented updated or completely new $O-C$ diagrams for a total of 148 Classical Cepheids. Out of these stars, four Cepheids (RX Aur, UY Mon, Y Oph, and AW Per) show signs of possible LiTE (only the case of AW Per and RX Aur has been known before). Further five Cepheids (XZ CMa, UX Car, R Cru, DT Cyg, and BN Pup) exhibit $O-C$ diagrams which either further confirm or raise the question of their binary nature. For the interesting cases of BY Cas, V532 Cyg, DX Gem and VZ CMa we found large amplitude fluctuations influencing the pulsation of the variables, while for IR Cep we found a similarly large amplitude and complex, yet stable wavelike signal superimposed on the evolutionary changes of the star, which could either be caused by fluctuations or binarity. The proper understanding of these peculiar variations would require further analysis of these stars.

By analysing the obtained set of $O-C$ diagrams showing evolutionary changes, we measured the rates of period change for the individual stars and compared these values to those given by stellar evolution models. The ratio of the number of Cepheids showing positive and negative period changes in our random sample agrees with the ratio given by models that include enhanced mass loss. By plotting the CMD of the obtained sample of Cepheids using the recently published *Gaia* EDR3 data, we could show that the rates of period change do not increase as consistently toward the cooler and brighter stars as one would expect based on the models, but the rates of period change vary systematically from the blue edge to the red edge of the instability strip. Considering this, it possibly yields an observational evidence that the rate of period change carries significant information about the physics of these variables.

After fitting and analysing the obtained $O-C$ diagrams, we found that a significant fraction of the Cepheids in our sample exhibit detectable period fluctuations in the form of quasi-periodic waves, similar to those found in the case of other, longer period pulsating stars. By measuring the strength of the fluctuations using the Eddington-Plakidis method and a model fitting based approach, we found that the period fluctuation scales linearly for longer period Cepheids (in a logarithmic sense), which is similar to the behaviour of Mira stars, while for shorter period Cepheids this scaling significantly weakens or disappears. The presence of such fluctuations and their increasing strength for long period Cepheids can have important implications for PL relation based distance determinations, as they could add an additional uncertainty term to the pulsation period, that was previously unaccounted for. Due to the detection limits set by the scatter in the data, we could only detect these fluctuations in about a third of the investigated short and intermediate period Cepheids. We showed that the explanation and analysis of the dependence of fluctuation strength on the periods of short period Cepheids depends largely on whether one or two fluctuation processes are assumed: in the first case the

fluctuation strength shows a minimum in the range of bump Cepheids, then it increases back at short periods, while in the latter case we find that the fluctuation strength depends on only weakly or is independent of the period for shorter period stars. Either way, the scatter among the fluctuation strengths increases for short period Cepheids, which suggests a non-negligible contribution from overtone Cepheids that exhibit larger fluctuation signals. Whichever interpretation is correct, the lack of strongly fluctuating bump Cepheids and the fluctuation minimum found by the joint fit in their period range suggests the increased stability of the pulsation of these stars, which is in agreement with the presence of a quenching mechanism.

Data availability

All source data used for our analysis are openly available online, except for the measurements carried out at the Piszkéstető Observatory, which are published as online material accompanying the article. The resulting $O - C$ files, from which the conclusions were drawn, are also published in the online supplement and will be accessible in an accompanying Vizier table. The data and the code used for our analysis is available on the GitHub page of the author: https://github.com/Csogeza/O-C_extract.

Acknowledgements

We thank the referee for their useful comments that helped to improve this paper. The research was completed with the extensive use of Python, along with the `numpy` (Harris et al., 2020), `scipy` (Virtanen et al., 2020) and `astropy` (Astropy Collaboration et al., 2018) modules, and with the `R` software (R Core Team, 2020). Some of the data used in the article were made available to the community through the Exoplanet Archive on behalf of the KELT project team. This research made use of NASA's Astrophysics Data System (ADS). For the data search and retrieval the authors made extensive use of the Vizier, CDS and Simbad websites of the Strasbourg astronomical Data Center (https://cds.u-strasbg.fr/). This work has made use of data from the European Space Agency (ESA) mission *Gaia* (https://www.cosmos.esa.int/gaia), processed by the *Gaia* Data Processing and Analysis Consortium (DPAC, https://www.cosmos.esa.int/web/gaia/dpac/consortium). Funding for the DPAC has been provided by national institutions, in particular the institutions participating in the *Gaia* Multilateral Agreement. We acknowledge with thanks the variable star observations from the AAVSO International Database contributed by observers worldwide and used in this research. The research leading to these results has been supported by the Hungarian National Research, Development and Innovation Office (NKFIH) grants K-129249, GINOP-2.3.2-15-2016-00003 and Élvonal KKP-137523 ('SeismoLab'), and by the Lendület LP2018-7/2021 grant of the Hungarian Academy of Sciences. Cs. K. acknowledges the support provided from the ÚNKP-20-2 and ÚNKP-21-2 New National Excellence Programs of the Ministry of Innovation and Technology from the source of the National Research, Development and Innovation Fund.

Appendix

Summary table for Cepheids showing evolutionary changes

In Table C.1 we present the period change rates calculated for the Cepheids showing evolutionary period changes along with the data from *Gaia* DR3 necessary for the CMD.

Cepheid	P [d]	$\Delta P/_{100yr}$	g	$BP-RP$	$E(B-V)$	$\log_{10}\epsilon$ [d]	π [mas]	References
U Aql	7.024	2.820e-05	9.443	1.02	0.397		0.96	1,2,3,13,53,58,60,64,75,81,A28
SZ Aql	17.141	2.267e-04	7.986	1.755	0.614		0.421	2,3,12,13,55,58,74,75,81,96,A29
TT Aql	13.755	-1.223e-05	6.945	1.744	0.4858		0.888	1,2,3,12,13,24,53,55,58,60,75,81,97,A29
EV Aql	38.671	-3.213e-03	11.191	1.931	0.705	-0.285	0.029	2,3,13,17,49,55,58,81,89,A1
FF Aql	4.471	2.582e-05	5.143	1.148	0.221	-2.731	1.81	2,3,13,53,58,60,74,75,81,85,97,98,A5
KL Aql	6.108	-3.729e-05	10.025	1.312	0.24	-2.212	0.228	2,3,13,43,53,55,58,74,79,90,A25
V336 Aql	7.304	5.232e-05	9.321	1.666	0.67		0.47	2,3,13,53,55,58,74,81,96,A25
V493 Aql	2.988	1.407e-05	10.572	1.7	0.777		0.4	2,3,13,30,53,55,58,74
V496 Aql	6.807	3.075e-05	7.351	1.438	0.442		0.944	2,3,13,53,58,74,75,81,A29
V916 Aql	13.443	1.045e-04	10.044	2.186	1.089		0.478	2,3,13,17,49,55,58,89
...	...	...	...	...	...	...	...	...

Table C.1: Summary table compiled for the Cepheids showing evolutionary changes. The ϵ parameter shown in the table corresponds to the period-fluctuation parameter of the Eddington-Plakidis method, which is summarized in Sect. 3.2. The complete table along with the list of photometry references and estimated uncertainties is available in the online supplements of the article.

Cepheid	$F_{\text{H0:lin H1:par}}$	$F_{\text{H0:lin H1:par+wave}}$	$F_{\text{H0:par H1:par+wave}}$	Amplitude [days]
U Aql	22.61	6.12	0.72	
SZ Aql	60.94	17.12	1.77	
TT Aql	6.79	10.48	11.08	
EV Aql	**91.78**	**315.39**	**205.72**	**6.997**
FF Aql	63.1	24.2	7.02	
KL Aql	**109.7**	**70.61**	**22.26**	**0.027**
V336 Aql	18.55	4.79	0.39	
V493 Aql	5.59	9.02	8.8	
V496 Aql	9.98	3.54	1.33	
V916 Aql	**158.75**	**92.54**	**23.69**	**0.175**
...	...	...	...	

Table C.2: Summary table of the F-test model comparison conducted for Cepheids showing evolutionary changes: columns 2-3 show the F-statistic and p-value for the case when we compare the residuals of the linear and parabolic fit; columns 4-5 show the results for the linear vs. parabolic plus wave model; columns 6-7 show the results for the parabolic vs. parabolic plus wave model. The last column shows the amplitude of the found wave (if the F-statistic was higher than 10 in the parabolic vs. parabolic plus wave model comparison). When fitting the parabolic plus wave model, we simultaneously optimized for both the parameters of the parabolic change and the wavelike modulation as well. To accept the parabolic plus wave model as a refinement of the simple parabolic fit, we also set the requirement that the found wave should have a period longer than 3000 days (about ten times the folding time used for the $O-C$ diagram calculations) but has to be shorter than five quarters of the timespan covered by observations (to avoid overfitting). Therefore, some of the F-test results were rejected, even though the parabolic plus wave fit seemed more optimal (for example, CH Cas, XX Cen or U Vul). We highlighted the Cepheids that match the criteria with bold fonts. The complete table is available in the online supplement of the article.

#	Reference	#	Reference	#	Reference
[1]	AAVSO (Kafka, 2021)	[48]	Harris (1980)	[95]	Szabados (1977)
[2]	ASAS (Pojmanski, 2001)	[49]	DASCH (Grindlay et al., 2012)	[96]	Szabados (1980)
[3]	ASAS-SN (Shappee et al., 2014)	[50]	Hellerich (1935)	[97]	Szabados (1981)
[4]	Abaffy (private comm.)	[51]	Henden (1980)	[98]	Szabados (1991)
[5]	Arellano Ferro (1984)	[52]	Henden (1996)	[99]	TESS (Ricker et al., 2015)
[6]	Arellano Ferro et al. (1998)	[53]	Hipparcos (Perryman et al., 1997b)	[100]	Tabur (private comm.)
[7]	Arp et al. (1959)	[54]	Hoffmeister (1960)	[101]	Bahner & Mavridis (1971)
[8]	Asarnova (1957)	[55]	IOMC (Winkler et al., 2003)	[102]	Usenko (1992)
[9]	Babel et al. (1989)	[56]	Irwin (1961)	[103]	Wachmann (1976)
[10]	Bahner et al. (1962)	[57]	Kepler K2 (Howell et al., 2014)	[104]	Walraven et al. (1958)
[11]	Barnes et al. (1987)	[58]	KWS (Morokuma et al., 2014)	[105]	Walraven et al. (1964)
[12]	Barnes et al. (1997)	[59]	KELT (Pepper et al., 2007)	[106]	Walter (1943)
[13]	Berdnikov (2008)	[60]	Kiss (1998)	[107]	Weaver et al. (1960)
[14]	Berdnikov et al. (2009)	[61]	Koukarkina (1954)	[108]	Williams (private comm.)
[15]	Berdnikov et al. (2011)	[62]	Kovacs & Szabados (1979)	[A1]	Berdnikov & Pastukhova (1994)
[16]	Berdnikov et al. (2014)	[63]	Kox (1935)	[A2]	Berdnikov & Turner (2001)
[17]	Berdnikov et al. (2015)	[64]	Krebs (1936)	[A3]	Berdnikov & Caldwell (2001)
[18]	Berdnikov et al. (2019)	[65]	Kurochkin (1954)	[A4]	Berdnikov & Turner (2004)
[19]	Bersier (2002)	[66]	Kwee (1967)	[A5]	Berdnikov et al. (2014)
[20]	Bochum (Hackstein et al., 2015)	[67]	Landolt (1971)	[A6]	Berdnikov (2019c)
[21]	Buchancowa et al. (1972)	[68]	Laur et al. (2017)	[A7]	Erleksova (1978)
[22]	Burnashev & Burnasheva (2009)	[69]	Madore (1975)	[A8]	Erleksova & Irkaev (1982)
[23]	Connolly et al. (1983)	[70]	Malik (1965)	[A9]	Fernie (1990b)
[24]	Coulson & Caldwell (1985)	[71]	Mauder & Schöffel (1968)	[A10]	Hacke (1989)
[25]	Cousins & Lagerweij (1968)	[72]	Millis (1969)	[A11]	Hacke & Richert (1990)
[26]	Cousins & Lagerweij (1971)	[73]	Mitchell et al. (1961)	[A12]	Heiser (1996)
[27]	Dean (1977)	[74]	Mitchell et al. (1964)	[A13]	Kiehl & Hopp (1977)
[28]	Dean (1981)	[75]	Moffett & Barnes (1984)	[A14]	Klawitter (1971)
[29]	Detre (1935)	[76]	NSVS (Woźniak et al., 2004)	[A15]	Mahmoud & Szabados (1980)
[30]	Diethelm & Tammann (1982)	[77]	Udalski et al. (2015)	[A16]	Meyer (2006)
[31]	Eggen (1951)	[78]	Oja (2011)	[A17]	Miller & Wachmann (1973)
[32]	Eggen et al. (1957)	[79]	Oosterhoff (1960)	[A18]	Nijland (1935)
[33]	Eggen (1983)	[80]	Parkhurst (1908)	[A19]	Oosterhoff (1935)
[34]	Eggen (1985)	[81]	Pel (1976)	[A20]	Oosterhoff (1943)
[35]	Feinstein & Muzzio (1969)	[82]	Pingsdorf (1935)	[A21]	Parenago (1956)
[36]	Fernie et al. (1965)	[83]	Present paper	[A22]	Romano (1958)
[37]	Fernie (1970)	[84]	Reed (1968)	[A23]	Strohmeier (1968)
[38]	Fernie (1979)	[85]	SMEI (Eyles et al., 2003)	[A24]	Szabados (1977)
[39]	Fernie & Garrison (1981)	[86]	SWASP (Pollacco et al., 2006)	[A25]	Szabados (1980)
[40]	Fernie et al. (1995)	[87]	Schmidt & Reiswig (1993)	[A26]	Szabados (1981)
[41]	Filatov (1957)	[88]	Schmidt et al. (1995)	[A27]	Szabados (1988)
[42]	Floria & Kukarkina (1953)	[89]	Schmidt et al. (2004)	[A28]	Szabados (1989)
[43]	Gaia DR2 (Gaia Collaboration, 2018)	[90]	Schmidt et al. (2005)	[A29]	Szabados (1991)
[44]	Gaposchkin (1958)	[91]	Shobbrook (1992)	[A30]	Szabados et al. (2013)
[45]	Gieren (1981)	[92]	Stobie (1970)	[A31]	Vinkó (1991)
[46]	Gieren (1985)	[93]	Stobie & Balona (1979)	[A32]	Walker et al. (1991)
[47]	Grayzeck (1978)	[94]	Szabados (1976)		

Table C.3: Complete list of references used for the calculation of the $O - C$ diagrams along with the abbreviations.

21 Conclusion & Outlook

The overview and results presented in this thesis showed the advancements and challenges that make current days an exciting era for distance estimations. The improvements in instrumentation and computation pushed the measurement precision far beyond previous capabilities. This not only broadened the range of possible estimation methods but also revealed possible issues with our current understanding the of Universe in the form of the Hubble tension. In this context, measuring the Hubble constant using many independent probes is critical to assess the significance of the tension. Furthermore, it is also crucial to look deeper into the physics of the different distance indicators, in order to be able to rule out possible systematics as well. While these studies on one hand ensure that the measured distances are trustworthy enough in the near-Universe to provide a solid foundation for further extragalactic research, they also add to the ever-growing list of works trying to answer whether we need physics beyond ΛCDM to explain our Universe.

Summary The goal of this thesis was to add to the ever-growing list of improvements for near-Universe distance indicators. We approached this goal from two aspects. First, we empirically tested the improved version of SN II-based distance estimation. The foundation of the technique is provided by the Expanding Photosphere method (Kirshner & Kwan, 1974). Our method is a variant of the tailored EPM method, which is an improved version of the classical technique introduced by Dessart et al. (2008). To allow for a precise distance estimation, we based our model parameter inference on TARDIS radiative transfer models (Kerzendorf & Sim, 2014; Kerzendorf et al., 2022) as described in (Vogl et al., 2019, 2020). With this, we achieve the efficient estimation of accurate physical parameters for SNe II, along with absolute distances to their host galaxies as well (as described in detail in Vogl 2020).

As a start, we showcased our results obtained for sibling supernovae, that is to say, supernovae, which exploded in the same galaxy (Part. II). These object pairs make it possible to assess the internal consistency of the fitting and distance estimation method empirically. For this work, we made use of a pair of supernovae from four different host galaxies: M 61 (SN 2008in and SN 2020jfo), NGC 772 (SN 2003hl and SN 2003iq), NGC 922 (SN 2002gw and SN 2008ho) and NGC 6946 (SN 2004et and SN 2017eaw). After computing the best fit radiative transfer models following the methodology of Vogl et al. (2020), making use of a PCA- and Gaussian Process-based spectral emulator, we compared the pairwise EPM distances using Bayes factors following the formalism outlined in Wang et al. (2016). The test showed good agreement between the pairwise distance posteriors, showing the potential of the radiative transfer-based spectral modelling and the subsequent EPM distance estimation. In our analysis, the main limiting factor was the data quality rather than the potential systematic effects hidden in the

estimator. While this result is promising for the precision of SN II distances, as these potential systematics are not significant enough to bring down their internal consistency, the current sample does not allow for a deeper view on how effects that vary from supernova to supernova, such as the scale of CSM interaction, explosion energy or reddening affect the analysis. To make such an investigation possible, more high-quality pairs are required.

As a second observational test, we performed a direct cross-comparison of the supernova distance with the Cepheid and TRGB estimate (Part III). This cross-check was not performed to calibrate the supernova method but to investigate whether the method yields distance estimates in the same ballpark as the other independent techniques. To this end, we estimated the distance to the spiral galaxy M 51 based on a supernova it hosted, SN 2005cs (Pastorello et al., 2006, 2009). To compare it to independent distance scales, we estimated a Cepheid distance to the galaxy following the SH0ES formalism (Riess et al., 2022) by making use of the Cepheid sample presented in Yuan et al. (2022) as a reference. To obtain the necessary Cepheid sample in M 51, we analyzed the rich photometric dataset presented in Conroy et al. (2018). The resulting dataset made it possible to infer a $\sim$ 3% precise Cepheid distance to M 51. We then compared our distances to the independently obtained TRGB distances of Tikhonov et al. (2015) and McQuinn et al. (2017). The comparison showed that the Cepheid and supernova distances while being in perfect agreement, are discrepant with the TRGB estimates (2σ discrepancy). According to our assessment, this offset is likely caused by issues in the calibration and field choice of the applied TRGB method. The test showed the necessity of additional direct cross-checks between different indicators. Moreover, the advantage of having three independent distance estimators was also emphasized. Similar cross-checks have already been performed in the literature by, for example, Lee et al. (2022), Breuval et al. (2023b) or Anand et al. (2024), but either for Cepheids and TRGB only or for J-AGB as a third indicator. However, the independence of the TRGB and J-AGB methods is arguable, as it is for Cepheids and Miras and other pulsators. However, using SNe II as a third independent estimator can ensure a more complete cross-check and help tip the scale when comparing Cepheids and TRGB.

In parallel to showcasing the supernova method, we also investigated the nature of the pulsation of Classical Cepheid variables, which form the core of extragalactic distance estimation to date, in Part. IV. We did this by investigating the changes in the pulsation period of these variables through the $O-C$ diagram technique, similar to Szabados (1989), Szabados (1991) and Turner et al. (2006). This technique, being among the oldest ways of analysing light curves, is based on comparing observations to a model prediction, and then analysing the residuals. Depending on the assumed prediction, this method then allows for detecting changes in light curve periodicity, which can indicate effects ranging from stellar evolution to binarity. Thanks to the efforts of the community in digitizing the measurements taken in the early parts of the past century (mainly owing to the DASCH collaboration, Grindlay et al. 2012) and the recent rich all-sky surveys (such as ASAS, Pojmanski 2001) well-covered century-long $O-C$ diagrams could be compiled for a large sample of stars. In the above work, we performed this for 149 Galactic Cepheid variables for a collective analysis. Apart from detecting signs tied to

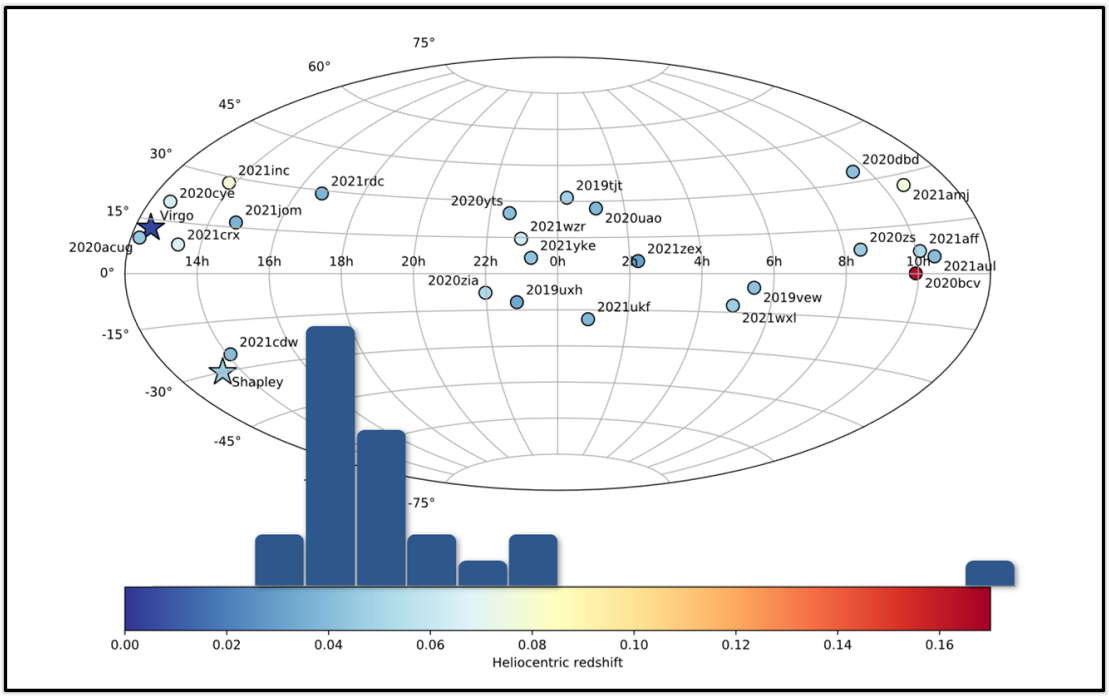

Figure 21.1: The adH0cc sample of supernovae. The top panel shows the positions of the observed supernovae in the sky, while the bottom histogram depicts their redshift distribution. This shows that the objects are sufficiently far in the Hubble flow so that the peculiar velocities do not affect the redshift significantly and that the supernovae are not all clustered in the same supercluster of galaxies, making them perfect for cosmological studies. Image courtesy of Stefan Taubenberger.

the multiplicity of the variables, we detected period fluctuations in all Cepheids above the period range of bump Cepheids, and in a significant fraction of objects below it. Such fluctuations have already been detected for variables of longer period (Percy et al., 1997), and for Cepheids as well using high-cadence photometry from Kepler (Derekas et al., 2012, 2017) and TESS (Plachy et al., 2021), but this is the first collective overview of the effect, investigating it for a statistical sample, rather than a handful of objects. Apart from showing that Cepheids are not perfect clocks, as their pulsation is affected by random fluctuations, which has implications for pulsation theory, it also highlights that treating the pulsation with pinpoint precision may bias our distance measurements.

As a whole, these results contribute significantly to our knowledge of near-Universe distance indicators and will help to alleviate the possible inconsistencies between them. This, in turn, will assist us in determining the significance of the Hubble tension in future studies.

Outlook The thesis offers multiple avenues to continue and to further connect ongoing investigations that concern the Hubble tension. The main framework that sets the scope for this project is the research carried out by the `adh0cc` (accurate determination of H_0 from core-collapse supernovae) collaboration. As its name shows, the main goal of this

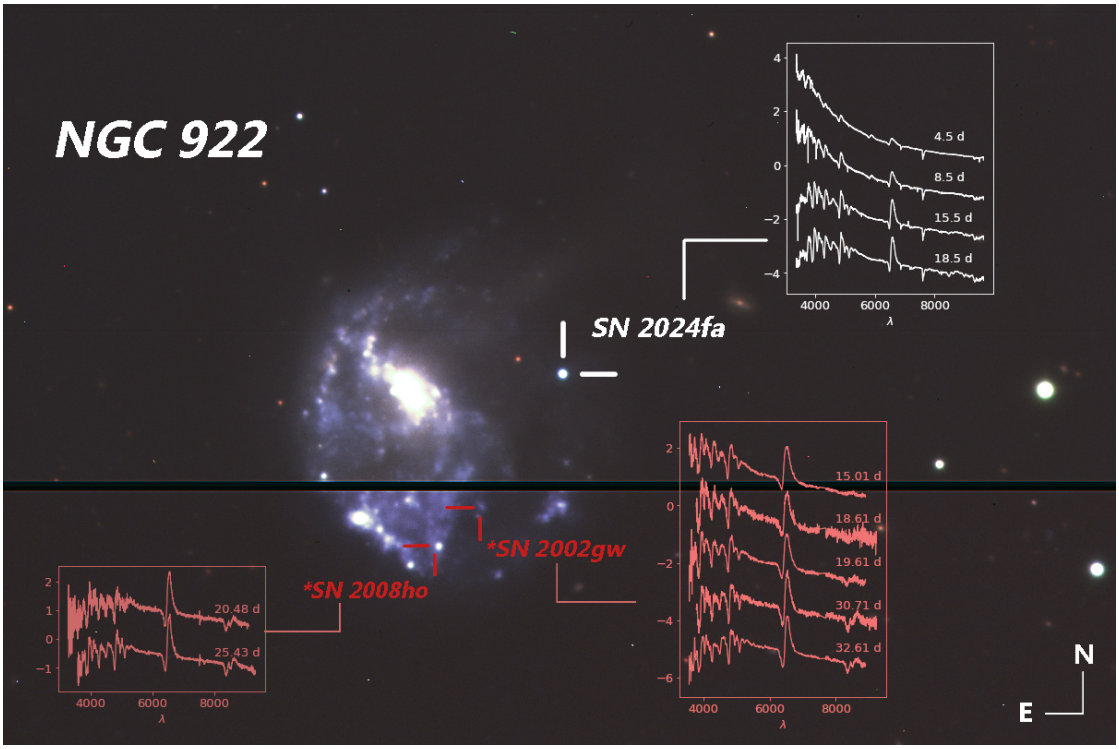

Figure 21.2: Recent observation of a new supernova sibling, SN 2024fa. The picture shows the VLT image of the host galaxy along with the positions of the new and old supernova sites. The inset plots show the spectral time series available for the individual supernovae either taken by VLT or from the literature (see Part. II).

project is to determine the Hubble constant solely based on SNe II, not by using external calibrations, but by applying spectral modelling and EPM on them, as in Vogl (2020). For this, we will utilize recent data obtained through an ESO VLT Large Programme, for which the observations have already been finished. The supernova sample that will be used for the cosmological inference, which counts 24 SNe, is visualized in Fig. 21.1. As shown, our supernova sample extends well into the Hubble flow, reducing the effect of peculiar velocities. This sample is complimented by spectrophotometric observations of an additional 21 SNe from the SNfactory supernova programme (Aldering et al., 2002) at slightly lower redshifts. Combined, these two data sets will allow for estimating a competitive and distance ladder-independent Hubble constant value.

Given the inconsistencies between some of the distance estimators in the near Universe, not only employing new distance estimators but ensuring that their predicted uncertainties are realistic, is critical. For this reason, upcoming studies will estimate the consequences of various systematic effects, such as choices on how the SN II radiative transfer models are calculated (for example, whether time-dependent effects are included or not Dessart & Hillier 2011) or the way the time of explosion is calculated, along with observational effects, such as galaxy contamination. We also aim to expand the empir-

ical studies for SNe II, mainly the sibling study, to assess which systematic effects may drive more significant offsets between distances. To this end, we have already initiated collecting data for additional SN II siblings to obtain further high-quality pairs. In our ongoing VLT Monitoring campaign, we have already observed six new SNe II which exploded in host galaxies that exhibited SNe II before; Fig. 21.2 shows one such case. This sample already doubles the currently existing sample of sibling SN II pairs and will be utilized for an elaborate study on systematics. To perform this, we will estimate the distance offsets between the sibling supernovae of each pair, then correlate these values with the differences between the reddening, scale of CSM interaction or the explosion energies of the supernovae. This sample will also allow us to test the consistency of other SN II-based methods, such as the SCM (de Jaeger et al., 2022).

In addition, it will be equally important to carry out additional comparisons between supernovae, Cepheids, TRGB and other distance indicators. The speciality of SNe II in this context is that they offer absolute distances, which may be cross-checked with independent techniques on multiple rungs of the distance ladder, including SNe Ia. Such comparisons will allow us to identify where issues lay if the distance ladder is the source of the Hubble tension. To make these studies more precise, it is essential to begin obtaining independent distances to SNe II host galaxies through Cepheids and TRGB, utilizing HST or $JWST$, to provide a low-uncertainty setting for the cross-comparisons.

Finally, the study conducted for the Cepheid variables showed that fluctuations are present even for Classical Cepheids, an effect not yet constrained in previous studies. Through simulating mock-Cepheid sets, it is possible to put an upper limit on the period uncertainties caused by the fluctuations, which would indicate the uncertainty they cause for the Hubble constant. Even though for Cepheids these period uncertainties are on the scale of less-than-percent level, it is important to note that for more evolved giants, which pulsate with longer, but less stable periods (such as Miras, OSARGs), these may be of greater importance, especially for distance estimations. To this end, further collective studies aimed at understanding the scale and nature of these fluctuations are important.

This thesis highlights that the world of distance estimations has not yet come to a halt; quite the opposite. The discovery of the expansion of the Universe and the subsequent emergence of the Hubble tension fueled more and more studies that aim to understand how we measure distances in the cosmos and utilize a wide variety of objects as standardizable candles. With the steady growth of new methods along with richer and deeper observations, it can be said without doubt that the coming decades will be an exciting time for distance estimations.

Acronyms

ΛCDM	Λ cold dark matter
ACS	Advanced Camera for Surveys
adH0cc	accurate determination of H_0 with core-collapse supernovae
AGB	Asymptotic Giant Branch
BAO	Baryonic Acoustic Oscillation
CCHP	Carnegie-Chicago Hubble Program
CMB	cosmic microwave background
CMD	colour-magnitude diagram
DFT	Discrete Fourier Transformation
GAM	generalized additive models
GP	Gaussian Process
GRB	gamma-ray burst
HCT	Himalayan Chandra Telescope
HRD	Hertzsprung–Russel Diagram
HST	Hubble Space Telescope
EPM	Expanding Photosphere Method
H_0	Hubble–Lemaître constant
LiTE	Light time effect
IAU	International Astronomical Union
IR	infrared
JAGB	J-Band AGB
JWST	James Webb Space Telescope
KAIT	Katzman Automatic Imaging Telescope
KDE	kernel-density estimate
LMC	Large Magellanic Cloud
M	Messier
MIR	mid-IR

NIR	near-IR
NGC	New General Catalogue
NLTE	non-local thermodynamic equilibrium
OGLE	Optical Gravitational Lensing Experiment
OSARG	OGLE Small Amplitude Red Giant
OSC	Open Supernova Catalogue
PCA	principal component analysis
PNLF	Planetary Nebula Luminosity Function
P-L	period-luminosity
RGB	red giant branch
ROTSE	Robotic Optical Transient Search Experiment
SBF	surface brightness fluctuations
SCM	standardizable candle method
SDSS	Sloan Digital Sky Survey
SFR	star formation rate
SMC	Small Magellanic Cloud
SH0ES	Supernovae, H_0, for the Equation of State of Dark Energy
SN	Supernova
SN Ia	Type Ia Supernova
SN II	Type II Supernova
SNFactory	Nearby Supernova Factory
TRGB	Tip of the red giant branch
VLT	Very Large Telescope
WMAP	Wilkinson Microwave Anisotropy Probe
ZTF	Zwicky Transient Facility

Acknowledgments

First and foremost, I would like to thank my supervisors, advisors and colleagues: Wolfgang Hillebrandt, Christian Vogl, Stefan Taubenberger, Bruno Leibundgut and the members of the adH0cc collaboration for creating such a kind and welcoming working group, which I could be part of during my PhD years. I would like to thank Wolfgang Hillebrandt for the opportunity to enter the exciting world of supernovae and for always being available for discussions. Throughout my PhD, Wolfgang provided great support and advice, setting up an environment that allowed me to pursue my own ideas and assisting me a great deal in all sorts of administrative matters (also, for not being angry at me for me breaking his bike). Special thanks go to Christian and Stefan for all the enticing discussions and for answering all my dumb questions, making my learning easier and bearing with my hard-headedness. They were always available for discussions, contributing countless hours outside their work-time at night to help with my projects. Beyond my direct working group, I would like to thank Richard Anderson for co-advising me on multiple Cepheid-related projects and for making it possible for me to visit Geneva. Multiple thanks go to the members of my past working group at the Konkoly Observatory, in particular, László Szabados, for helping me kick-start my career early, and for allowing me to be a long-term observatory assistant at the institute, which years I will always cherish. I would also like to especially thank Christian and Stefan for providing valuable comments and insights for this thesis and for meticulously catching my minor and not-so-minor mistakes. Special thanks go to all the colleagues and students contributing to the adH0cc collaboration, making it a truly promising project, in particular to Bruno Leibundgut, who is the PI of this collaboration. In addition, I would like to thank the IMPRS PhD representatives and students around MPA and MPE for creating such a welcoming and flourishing atmosphere for both scientific and social life, which I believe is truly unique! I would also like to acknowledge the participants of the Garching SN meeting, along with all the enticing discussions, which greatly improved my education on supernovae. Moreover, special thanks go to my family for their support and encouragement over the years that set me on the path to this PhD thesis. Finally, I would like to thank *Dulcita* for putting up with me, being there any and all the time, and making the time spent with the writing of this thesis multitudes more enjoyable. *¡Te amo!*

Bibliography

Addison, G. E., Watts, D. J., Bennett, C. L., et al. 2018, Astrophysical Journal, 853, 119

Alcock, C., Allsman, R. A., Axelrod, T. S., et al. 1995, Astronomical Journal, 109, 1653

Aldering, G., Adam, G., Antilogus, P., et al. 2002, in Society of Photo-Optical Instrumentation Engineers (SPIE) Conference Series, Vol. 4836, Survey and Other Telescope Technologies and Discoveries, ed. J. A. Tyson & S. Wolff, 61–72

Ambikasaran, S., Foreman-Mackey, D., Greengard, L., Hogg, D. W., & O'Neil, M. 2015, IEEE Transactions on Pattern Analysis and Machine Intelligence, 38, 252

Anand, G. S., Riess, A. G., Yuan, W., et al. 2024, arXiv e-prints, arXiv:2401.04776

Anand, G. S., Rizzi, L., & Tully, R. B. 2018, Astronomical Journal, 156, 105

Anand, G. S., Tully, R. B., Rizzi, L., Riess, A. G., & Yuan, W. 2021, arXiv e-prints, arXiv:2108.00007

Anand, G. S., Tully, R. B., Rizzi, L., Riess, A. G., & Yuan, W. 2022, Astrophysical Journal, 932, 15

Anders, F., Khalatyan, A., Chiappini, C., et al. 2019, Astronomy & Astrophysics, 628, A94

Anderson, J. P., González-Gaitán, S., Hamuy, M., et al. 2014, Astrophysical Journal, 786, 67

Anderson, R. I. 2019, Astronomy & Astrophysics, 631, A165

Anderson, R. I. 2022, Astronomy & Astrophysics, 658, A148

Anderson, R. I., Eyer, L., & Mowlavi, N. 2013, Monthly Notices of the Royal Astronomical Society, 434, 2238

Anderson, R. I., Koblischke, N. W., & Eyer, L. 2023, arXiv e-prints, arXiv:2303.04790

Anderson, R. I. & Riess, A. G. 2018, Astrophysical Journal, 861, 36

Anderson, R. I., Saio, H., Ekström, S., Georgy, C., & Meynet, G. 2016, Astronomy & Astrophysics, 591, A8

Arcavi, I. 2017, in Handbook of Supernovae, ed. A. W. Alsabti & P. Murdin, 239

Arellano Ferro, A. 1984, Monthly Notices of the Royal Astronomical Society, 209, 481

Arellano Ferro, A., Rojo Arellano, E., González-Bedolla, S., & Rosenzweig, P. 1998, Astrophysical Journal Supplement, 117, 167

Arp, H., Sandage, A., & Stephens, C. 1959, Astrophysical Journal, 130, 80

Asarnova, T. A. 1957, Peremennye Zvezdy, 12, 76

Astropy Collaboration, Price-Whelan, A. M., Sipőcz, B. M., et al. 2018, Astronomical Journal, 156, 123

Baade, W. 1926, Astronomische Nachrichten, 228, 359

Baade, W. 1956, Publications of the Astronomical Society of the Pacific, 68, 5

Babel, J., Burki, G., Mayor, M., Waelkens, C., & Chmielewski, Y. 1989, Astronomy & Astrophysics, 216, 125

Bahner, K., Hiltner, W. A., & Kraft, R. P. 1962, Astrophysical Journal Supplement, 6, 319

Bahner, K. & Mavridis, L. N. 1971, Ann. Fac. Tech. Univ. Thessaloniki, 5, 65

Bailer-Jones, C. A. L., Rybizki, J., Fouesneau, M., Demleitner, M., & Andrae, R. 2021, Astronomical Journal, 161, 147

Balázs-Detre, J. & Detre, L. 1965, Veroeffentlichungen der Remeis-Sternwarte zu Bamberg, 27, 184

Baranowski, R., Smolec, R., Dimitrov, W., et al. 2009, Monthly Notices of the Royal Astronomical Society, 396, 2194

Barlow, M. J., Sugerman, B. E. K., Fabbri, J., et al. 2005, Astrophysical Journal Letters, 627, L113

Barna, B., Nagy, A. P., Bora, Z., et al. 2023, Astronomy & Astrophysics, 677, A183

Barnes, T. G., I., Fernley, J. A., Frueh, M. L., et al. 1997, Publications of the Astronomical Society of the Pacific, 109, 645

Barnes, Thomas G., I., Moffett, T. J., & Slovak, M. H. 1987, Astrophysical Journal Supplement, 65, 307

Baron, E., Branch, D., & Hauschildt, P. H. 2007, Astrophysical Journal, 662, 1148

Baron, E., Hauschildt, P. H., Branch, D., Kirshner, R. P., & Filippenko, A. V. 1996, Monthly Notices of the Royal Astronomical Society, 279, 799

Baron, E., Nugent, P. E., Branch, D., & Hauschildt, P. H. 2004, Astrophysical Journal Letters, 616, L91

Beaton, R. L., Bono, G., Braga, V. F., et al. 2018, Space Science Reviews, 214, 113

Beaulieu, J. P., Buchler, J. R., & Kolláth, Z. 2001, Astronomy & Astrophysics, 373, 164

Bellinger, E. P., Kanbur, S. M., Bhardwaj, A., & Marconi, M. 2020, Monthly Notices of the Royal Astronomical Society, 491, 4752

Bellm, E. C., Kulkarni, S. R., Graham, M. J., et al. 2019, Publications of the Astronomical Society of the Pacific, 131, 018002

Berdnikov, L. N. 2008, VizieR Online Data Catalog, II/285

Berdnikov, L. N. 2019a, Astronomy Letters, 45, 435

Berdnikov, L. N. 2019b, Astronomy Letters, 45, 593

Berdnikov, L. N. 2019c, Astronomy Letters, 45, 677

Berdnikov, L. N. & Caldwell, J. A. R. 2001, Journal of Astronomical Data, 7, 3

Berdnikov, L. N., Ignatova, V. V., Pastukhova, E. N., & Turner, D. G. 1997, Astronomy Letters, 23, 177

Berdnikov, L. N., Kniazev, A., Dambis, A., & Kravtsov, V. V. 2019, Peremennye Zvezdy, 39, 2

Berdnikov, L. N., Kniazev, A. Y., Kravtsov, V. V., Pastukhova, E. N., & Turner, D. G. 2009, VizieR Online Data Catalog, J/PAZh/35/348

Berdnikov, L. N., Kniazev, A. Y., Sefako, R., et al. 2015, Astronomy Letters, 41, 23

Berdnikov, L. N., Kniazev, A. Y., Sefako, R., et al. 2011, VizieR Online Data Catalog, J/AZh/88/886

Berdnikov, L. N., Kniazev, A. Y., Sefako, R., Kravtsov, V. V., & Zhujko, S. V. 2014, Astronomy Letters, 40, 125

Berdnikov, L. N. & Pastukhova, E. N. 1994, Astronomy Letters, 20, 479

Berdnikov, L. N. & Stevens, I. R. 2010, in Variable Stars, the Galactic halo and Galaxy Formation, ed. C. Sterken, N. Samus, & L. Szabados, 207

Berdnikov, L. N. & Turner, D. G. 2001, Astronomical and Astrophysical Transactions, 19, 689

Berdnikov, L. N. & Turner, D. G. 2004, Astronomical and Astrophysical Transactions, 23, 599

Bersier, D. 2002, Astrophysical Journal Supplement, 140, 465

Bessell, M. & Murphy, S. 2012, Publications of the Astronomical Society of the Pacific, 124, 140

Bessell, M. S. 1979, Publications of the Astronomical Society of the Pacific, 91, 589

Bhardwaj, A., Kanbur, S. M., Marconi, M., et al. 2016, Monthly Notices of the Royal Astronomical Society, 466, 2805

Bildsten, L., Paxton, B., Moore, K., & Macias, P. J. 2012, Astrophysical Journal Letters, 744, L6

Bird, J. C., Stanek, K. Z., & Prieto, J. L. 2009, Astrophysical Journal, 695, 874

Blinnikov, S., Potashov, M., Baklanov, P., & Dolgov, A. 2012, Soviet Journal of Experimental and Theoretical Physics Letters, 96, 153

Boesgaard, A. M. & Steigman, G. 1985, Annual Reviews in Astronomy and Astrophysics, 23, 319

Bonanos, A. Z., Stanek, K. Z., Kudritzki, R. P., et al. 2006, Astrophysical Journal, 652, 313

Bono, G., Caputo, F., Fiorentino, G., Marconi, M., & Musella, I. 2008, Astrophysical Journal, 684, 102

Bono, G., Caputo, F., Marconi, M., & Musella, I. 2010, Astrophysical Journal, 715, 277

Bono, G., Marconi, M., & Stellingwerf, R. F. 1999, Astrophysical Journal Supplement, 122, 167

Bono, G., Marconi, M., & Stellingwerf, R. F. 2000, Astronomy & Astrophysics, 360, 245

Borgniet, S., Kervella, P., Nardetto, N., et al. 2019, Astronomy & Astrophysics, 631, A37

Bose, S. & Kumar, B. 2014, Astrophysical Journal, 782, 98

Bose, S., Kumar, B., Misra, K., et al. 2016, Monthly Notices of the Royal Astronomical Society, 455, 2712

Bresolin, F., Garnett, D. R., & Kennicutt, Robert C., J. 2004, Astrophysical Journal, 615, 228

Breuval, L., Riess, A., Anand, G. S., et al. 2023a, A 1% cross-calibration of Cepheids, TRGB, and JAGB in five nearby galaxies with HST, HST Proposal. Cycle 31, ID. #17520

Breuval, L., Riess, A. G., Kervella, P., Anderson, R. I., & Romaniello, M. 2022, Astrophysical Journal, 939, 89

Breuval, L., Riess, A. G., Macri, L. M., et al. 2023b, Astrophysical Journal, 951, 118

Brightman, M., Bachetti, M., Earnshaw, H., et al. 2022, Astrophysical Journal, 925, 18

Buchancowa, N., Wisniewski, W., & Kunchev, P. 1972, Information Bulletin on Variable Stars, 727, 1

Buchner, J. 2016, Statistics and Computing, 26, 383

Buchner, J. 2019, Publications of the Astronomical Society of the Pacific, 131, 108005

Buchner, J. 2021, The Journal of Open Source Software, 6, 3001

Burki, G. 1985, in IAU Colloq. 82: Cepheids: Theory and Observation, ed. B. F. Madore, 71

Burnashev, V. I. & Burnasheva, B. A. 2009, Bulletin Crimean Astrophysical Observatory, 105, 78

Burns, C. R., Ashall, C., Contreras, C., et al. 2020, Astrophysical Journal, 895, 118

Cardelli, J. A., Clayton, G. C., & Mathis, J. S. 1989, Astrophysical Journal, 345, 245

Casagrande, L. & VandenBerg, D. A. 2018, Monthly Notices of the Royal Astronomical Society, 479, L102

Castelli, F. & Kurucz, R. L. 2003, in Modelling of Stellar Atmospheres, ed. N. Piskunov, W. W. Weiss, & D. F. Gray, Vol. 210, A20

Catelan, M. & Smith, H. A. 2015, Pulsating Stars

Cerny, W., Freedman, W. L., Madore, B. F., et al. 2020, arXiv e-prints, arXiv:2012.09701

Cervantes-Cota, J. L., Galindo-Uribarri, S., & Smoot, G. F. 2023, Universe, 9, 501

Chen, X., de Grijs, R., & Deng, L. 2015, Monthly Notices of the Royal Astronomical Society, 446, 1268

Chiosi, C. 1998, in Stellar astrophysics for the local group: VIII Canary Islands Winter School of Astrophysics, ed. A. Aparicio, A. Herrero, & F. Sánchez, 1

Ciardullo, R., Feldmeier, J. J., Jacoby, G. H., et al. 2002, Astrophysical Journal, 577, 31

Clark, D. H. & Clark, M. D. H. 2004, Measuring the cosmos: how scientists discovered the dimensions of the universe

Connolly, L. P., Palmer, L. H., Goodrich, B. D., et al. 1983, Publications of the Astronomical Society of the Pacific, 95, 192

Conroy, C., Strader, J., van Dokkum, P., et al. 2018, Astrophysical Journal, 864, 111

Coulson, I. M. & Caldwell, J. A. R. 1985, South African Astronomical Observatory Circular, 9, 5

Cousins, A. W. J. & Lagerweij, H. C. 1968, Monthly Notes of the Astronomical Society of South Africa, 27, 138

Cousins, A. W. J. & Lagerweij, H. C. 1971, Monthly Notes of the Astronomical Society of South Africa, 30, 12

Cox, A. N. 1998, Astrophysical Journal, 496, 246

Cox, J. P. 1980, Theory of Stellar Pulsation. (PSA-2), Volume 2, Vol. 2

Cruz Reyes, M. & Anderson, R. I. 2023, Astronomy & Astrophysics, 672, A85

Csörnyei, G., Vogl, C., Taubenberger, S., et al. 2023, Astronomy & Astrophysics, 672, A129

Czekala, I., Andrews, S. M., Mandel, K. S., Hogg, D. W., & Green, G. M. 2015, Astrophysical Journal, 812, 128

Da Costa, G. S. & Armandroff, T. E. 1990, Astronomical Journal, 100, 162

Dalcanton, J. J., Williams, B. F., Lang, D., et al. 2012, Astrophysical Journal Supplement, 200, 18

Davis, M., Efstathiou, G., Frenk, C. S., & White, S. D. M. 1985, Astrophysical Journal, 292, 371

Davis, S., Hsiao, E. Y., Ashall, C., et al. 2019, Astrophysical Journal, 887, 4

de Jaeger, T., Galbany, L., Riess, A. G., et al. 2022, Monthly Notices of the Royal Astronomical Society, 514, 4620

de Jaeger, T., González-Gaitán, S., Hamuy, M., et al. 2017, Astrophysical Journal, 835, 166

de Jaeger, T., Zheng, W., Stahl, B. E., et al. 2019, Monthly Notices of the Royal Astronomical Society, 490, 2799

De Somma, G., Marconi, M., Molinaro, R., et al. 2020, Astrophysical Journal Supplement, 247, 30

De Somma, G., Marconi, M., Molinaro, R., et al. 2022, Astrophysical Journal Supplement, 262, 25

Dean, J. F. 1977, Monthly Notes of the Astronomical Society of South Africa, 36, 3

Dean, J. F. 1981, South African Astronomical Observatory Circular, 6, 10

Deasy, H. P. & Wayman, P. A. 1985, Monthly Notices of the Royal Astronomical Society, 212, 395

Deeming, T. J. 1975, Astrophysics and Space Sciences, 36, 137

Dekany, R., Smith, R. M., Riddle, R., et al. 2020, Publications of the Astronomical Society of the Pacific, 132, 038001

Derekas, A., Plachy, E., Molnár, L., et al. 2017, Monthly Notices of the Royal Astronomical Society, 464, 1553

Derekas, A., Szabó, G. M., Berdnikov, L., et al. 2012, Monthly Notices of the Royal Astronomical Society, 425, 1312

Dessart, L., Blondin, S., Brown, P. J., et al. 2008, Astrophysical Journal, 675, 644

Dessart, L., Gutiérrez, C. P., Ercolino, A., Jin, H., & Langer, N. 2024, arXiv e-prints, arXiv:2402.12977

Dessart, L. & Hillier, D. J. 2005, Astronomy & Astrophysics, 439, 671

Dessart, L. & Hillier, D. J. 2006, Astronomy & Astrophysics, 447, 691

Dessart, L. & Hillier, D. J. 2011, Monthly Notices of the Royal Astronomical Society, 410, 1739

Dessart, L. & Hillier, D. J. 2022, Astronomy & Astrophysics, 660, L9

Dessart, L., Hillier, D. J., Waldman, R., & Livne, E. 2013, Monthly Notices of the Royal Astronomical Society, 433, 1745

Detre, L. 1935, Astronomische Nachrichten, 257, 361

Di Valentino, E., Mena, O., Pan, S., et al. 2021, Classical and Quantum Gravity, 38, 153001

Diethelm, R. & Tammann, G. A. 1982, Astronomy & Astrophysics Supplement, 47, 335

Dobos, L., Csabai, I., Yip, C.-W., et al. 2012, Monthly Notices of the Royal Astronomical Society, 420, 1217

Dolphin, A. E. 2000, Publications of the Astronomical Society of the Pacific, 112, 1397

Eastman, R. G., Schmidt, B. P., & Kirshner, R. 1996, Astrophysical Journal, 466, 911

Eddington, A. S. 1918, Monthly Notices of the Royal Astronomical Society, 79, 2

Eddington, A. S. 1923, The mathematical theory of relativity

Eddington, A. S. 1930, Monthly Notices of the Royal Astronomical Society, 90, 668

Eddington, A. S. & Plakidis, S. 1929, Monthly Notices of the Royal Astronomical Society, 90, 65

Eggen, O. J. 1951, Astrophysical Journal, 113, 367

Eggen, O. J. 1983, Astronomical Journal, 88, 998

Eggen, O. J. 1985, Astronomical Journal, 90, 1297

Eggen, O. J., Gascoigne, S. C. B., & Burr, E. J. 1957, Monthly Notices of the Royal Astronomical Society, 117, 406

Einstein, A. 1908, Jahrbuch der Radioaktivität und Elektronik, 4, 411

Einstein, A. 1915, Sitzungsberichte der Königlich Preussischen Akademie der Wissenschaften, 844

Einstein, A. 1917, Sitzungsberichte der Königlich Preussischen Akademie der Wissenschaften, 142

Eisenstein, D. J. & Hu, W. 1998, Astrophysical Journal, 496, 605

Erleksova, G. E. 1978, Information Bulletin on Variable Stars, 1460, 1

Erleksova, G. E. & Irkaev, B. N. 1982, Peremennye Zvezdy, 21, 715

Evans, N. R. 1992, Astrophysical Journal, 389, 657

Evans, N. R., Bond, H. E., Schaefer, G. H., et al. 2016a, Astronomical Journal, 151, 129

Evans, N. R., Pillitteri, I., Wolk, S., et al. 2016b, Astronomical Journal, 151, 108

Evans, N. R., Szabó, R., Derekas, A., et al. 2015, Monthly Notices of the Royal Astronomical Society, 446, 4008

Evans, N. R., Vinko, J., & Wahlgren, G. M. 2000, Astronomical Journal, 120, 407

Eyer, L. & Bartholdi, P. 1999, Astronomy & Astrophysics Supplement, 135, 1

Eyles, C. J., Simnett, G. M., Cooke, M. P., et al. 2003, Solar Physics, 217, 319

Faran, T., Poznanski, D., Filippenko, A. V., et al. 2014, Monthly Notices of the Royal Astronomical Society, 442, 844

Feinstein, A. & Muzzio, J. C. 1969, Astronomy & Astrophysics, 3, 388

Feldmeier, J. J., Ciardullo, R., & Jacoby, G. H. 1997, Astrophysical Journal, 479, 231

Fernie, J. D. 1969, Publications of the Astronomical Society of the Pacific, 81, 707

Fernie, J. D. 1970, Astronomical Journal, 75, 244

Fernie, J. D. 1979, Astrophysical Journal, 231, 841

Fernie, J. D. 1984, in IAUS, Vol. 105, Observational Tests of the Stellar Evolution Theory, ed. A. Maeder & A. Renzini, 441

Fernie, J. D. 1990a, Astrophysical Journal, 354, 295

Fernie, J. D. 1990b, Publications of the Astronomical Society of the Pacific, 102, 905

Fernie, J. D., Demers, S., & Marlborough, J. M. 1965, Astronomical Journal, 70, 482

Fernie, J. D. & Garrison, R. G. 1981, Publications of the Astronomical Society of the Pacific, 93, 330

Fernie, J. D., Khoshnevissan, M. H., & Seager, S. 1995, Astronomical Journal, 110, 1326

Ferrarese, L., Mould, J. R., Kennicutt, Robert C., J., et al. 2000, Astrophysical Journal, 529, 745

Filatov, G. S. 1957, Peremennye Zvezdy, 11, 474

Filippenko, A. V., Li, W. D., Treffers, R. R., & Modjaz, M. 2001, in Astronomical Society of the Pacific Conference Series, Vol. 246, IAU Colloq. 183: Small Telescope Astronomy on Global Scales, ed. B. Paczynski, W.-P. Chen, & C. Lemme, 121

Fitzpatrick, E. L. 1999, Publications of the Astronomical Society of the Pacific, 111, 63

Floria, N. F. & Kukarkina, N. P. 1953, Trudy Gosudarstvennogo Astronomicheskogo Instituta, 23, 3

Foglizzo, T., Kazeroni, R., Guilet, J., et al. 2015, Publications of the Astronomical Society of Australia, 32, e009

Follin, B. & Knox, L. 2018, Monthly Notices of the Royal Astronomical Society, 477, 4534

Freedman, W. L. 2021, Astrophysical Journal, 919, 16

Freedman, W. L., Hughes, S. M., Madore, B. F., et al. 1994, Astrophysical Journal, 427, 628

Freedman, W. L. & Madore, B. F. 2010, Annual Reviews in Astronomy and Astrophysics, 48, 673

Freedman, W. L. & Madore, B. F. 2023, arXiv e-prints, arXiv:2308.02474

Freedman, W. L., Madore, B. F., Gibson, B. K., et al. 2001, Astrophysical Journal, 553, 47

Freedman, W. L., Madore, B. F., Hoyt, T., et al. 2020, Astrophysical Journal, 891, 57

Freedman, W. L., Madore, B. F., Hoyt, T., et al. 2021, Answering the Most Important Problem in Cosmology Today: Is the Tension in the Hubble Constant Real?, JWST Proposal. Cycle 1, ID. #1995

Frei, Z. & Patkós, A. 2005, Inflációs kozmológia (Typotex Kft)

Friedmann, A. 1922, Zeitschrift fur Physik, 10, 377

Friedmann, A. 1924, Zeitschrift fur Physik, 21, 326

Fulton, B. J., Petigura, E. A., Blunt, S., & Sinukoff, E. 2018, Publications of the Astronomical Society of the Pacific, 130, 044504

Gaia Collaboration. 2016, Astronomy and Astrophysics, 595, A1

Gaia Collaboration. 2018, Astronomy and Astrophysics, 616, A1

Gaia Collaboration. 2021, Astronomy & Astrophysics, 649, A1

Gaia Collaboration, Prusti, T., de Bruijne, J. H. J., et al. 2016, Astronomy & Astrophysics, 595, A1

Galbany, L., Hamuy, M., Phillips, M. M., et al. 2016, Astronomical Journal, 151, 33

Gallenne, A., Kervella, P., Mérand, A., et al. 2014, Astronomy & Astrophysics, 567, A60

Gaposchkin, S. 1958, Astronomical Journal, 63, 234

Gastine, T. & Dintrans, B. 2008, Astronomy & Astrophysics, 490, 743

Georgy, C., Ekström, S., Eggenberger, P., et al. 2013, Astronomy & Astrophysics, 558, A103

Ghirardini, V., Bulbul, E., Artis, E., et al. 2024, arXiv e-prints, arXiv:2402.08458

Gieren, W. 1981, Astrophysical Journal Supplement, 47, 315

Gieren, W., Storm, J., Konorski, P., et al. 2018, Astronomy & Astrophysics, 620, A99

Gieren, W. P. 1985, Astrophysical Journal, 295, 507

Gieren, W. P., Moffett, T. J., Barnes, Thomas G., I., Matthews, J. M., & Frueh, M. L. 1990, Astronomical Journal, 99, 1196

Gilbert, K. M., Kalirai, J. S., Guhathakurta, P., et al. 2014, Astrophysical Journal, 796, 76

Gilmore, G. & Reid, N. 1983, Monthly Notices of the Royal Astronomical Society, 202, 1025

Glushkova, E. V., Zabolotskikh, M. V., Rastorguev, A. S., Grudskaya, A. V., & Koposov, S. E. 2015, Baltic Astronomy, 24, 360

González-Gaitán, S., Tominaga, N., Molina, J., et al. 2015, Monthly Notices of the Royal Astronomical Society, 451, 2212

Górski, M., Pietrzyński, G., Gieren, W., et al. 2018, Astronomical Journal, 156, 278

Gorynya, N. A., Rastorguev, A. S., & Samus, N. N. 1996, Astronomy Letters, 22, 33

Gorynya, N. A., Samus, N. N., & Rastorgouev, A. S. 1994, Information Bulletin on Variable Stars, 4130, 1

Gorynya, N. A., Samus', N. N., Sachkov, M. E., et al. 1998, Astronomy Letters, 24, 815

Graham, M. L., Fremling, C., Perley, D. A., et al. 2022, Monthly Notices of the Royal Astronomical Society, 511, 241

Grayzeck, E. J. 1978, Astronomical Journal, 83, 1397

Greene, J. E., Murphy, J. D., Graves, G. J., et al. 2013, Astrophysical Journal, 776, 64

Grindlay, J., Tang, S., Los, E., & Servillat, M. 2012, in IAU Symposium, Vol. 285, New Horizons in Time Domain Astronomy, ed. E. Griffin, R. Hanisch, & R. Seaman, 29–34

Groenewegen, M. 2023, arXiv e-prints, arXiv:2307.03033

Groenewegen, M. A. T. 2018, Astronomy & Astrophysics, 619, A8

Groenewegen, M. A. T. 2020, Astronomy & Astrophysics, 635, A33

Groenewegen, M. A. T. & Oudmaijer, R. D. 2000, Astronomy & Astrophysics, 356, 849

Guillochon, J., Parrent, J., Kelley, L. Z., & Margutti, R. 2017, Astrophysical Journal, 835, 64

Gutiérrez, C. P., Anderson, J. P., Hamuy, M., et al. 2014, Astrophysical Journal Letters, 786, L15

Gutiérrez, C. P., Anderson, J. P., Hamuy, M., et al. 2017, Astrophysical Journal, 850, 90

Guy, J., Astier, P., Baumont, S., et al. 2007, Astronomy & Astrophysics, 466, 11

Habing, H. J. & Olofsson, H. 2003

Hacke, G. 1989, Zentralinstitut fuer Astrophysik Sternwarte Sonneberg Mitteilungen ueber Veraenderliche Sterne, 11, 194

Hacke, G. & Richert, M. 1990, Veroeffentlichungen der Sternwarte Sonneberg, 4, 336

Hackstein, M., Fein, C., Haas, M., et al. 2015, Astronomische Nachrichten, 336, 590

Hamuy, M. 2005, in IAU Colloq. 192: Cosmic Explosions, On the 10th Anniversary of SN1993J, ed. J.-M. Marcaide & K. W. Weiler, Vol. 99, 535

Hamuy, M., Folatelli, G., Morrell, N. I., et al. 2006, Publications of the Astronomical Society of the Pacific, 118, 2

Hamuy, M. & Pinto, P. A. 2002, Astrophysical Journal Letters, 566, L63

Hamuy, M. A. 2001, PhD thesis, The University of Arizona

Harris, C. R., Millman, K. J., van der Walt, S. J., et al. 2020, Nature, 585, 357–362

Harris, H. C. 1980, PhD thesis, Washington Univ., Seattle.

Hastie, T. & Tibshirani, R. 1990, Generalized Additive Models (Routledge)

Havlen, R. J. 1976, Astronomy & Astrophysics, 49, 307

Heiser, A. M. 1996, Publications of the Astronomical Society of the Pacific, 108, 603

Hellerich, J. 1935, Astronomische Nachrichten, 256, 221

Henden, A. A. 1980, Monthly Notices of the Royal Astronomical Society, 192, 621

Henden, A. A. 1996, Astronomical Journal, 112, 2757

Herold, L. & Ferreira, E. G. M. 2023, Physical Review D, 108, 043513

Herrmann, K. A., Ciardullo, R., Feldmeier, J. J., & Vinciguerra, M. 2008, Astrophysical Journal, 683, 630

Hershkowitz, S., Linder, E., & Wagoner, R. V. 1986, Astrophysical Journal, 301, 220

Hertzsprung, E. 1913, Astronomische Nachrichten, 196, 201

Hertzsprung, E. 1926, Bulletin of the Astronomical Institutes of the Netherlands, 3, 115

Heyer, M., Gregg, B., Calzetti, D., et al. 2022, Astrophysical Journal, 930, 170

Hicken, M., Friedman, A. S., Blondin, S., et al. 2017, Astrophysical Journal Supplement, 233, 6

Hillebrandt, W. & Niemeyer, J. C. 2000, Annual Reviews in Astronomy and Astrophysics, 38, 191

Hoffmann, S. L., Macri, L. M., Riess, A. G., et al. 2016, Astrophysical Journal, 830, 10

Hoffmann, S. L., Macri, L. M., Riess, A. G., et al. 2017, VizieR Online Data Catalog, J/ApJ/830/10

Hoffmeister, C. 1960, Veroeffentlichungen der Sternwarte Sonneberg, 4, 315

Hogg, D. W. 1999, arXiv e-prints, astro

Hogg, D. W., Bovy, J., & Lang, D. 2010, arXiv e-prints, arXiv:1008.4686

Horvath, I., Bagoly, Z., Balazs, L. G., et al. 2024, Monthly Notices of the Royal Astronomical Society, 527, 7191

Howell, S. B., Sobeck, C., Haas, M., et al. 2014, Publications of the Astronomical Society of the Pacific, 126, 398

Hoyt, T. J. 2023, Nature Astronomy, 7, 590

Hubble, E. 1929, Proceedings of the National Academy of Science, 15, 168

Hubble, E. & Humason, M. L. 1931, Astrophysical Journal, 74, 43

Hubble, E. P. 1925a, Popular Astronomy, 33, 252

Hubble, E. P. 1925b, Astrophysical Journal, 62, 409

Hubble, E. P. 1926a, Astrophysical Journal, 63, 236

Hubble, E. P. 1926b, Astrophysical Journal, 64, 321

Ibata, R. A., Lewis, G. F., McConnachie, A. W., et al. 2014, Astrophysical Journal, 780, 128

Imbert, M. 1981, Information Bulletin on Variable Stars, 1983, 1

Imbert, M. 1999, Astronomy & Astrophysics Supplement, 140, 79

Inserra, C., Smartt, S. J., Gall, E. E. E., et al. 2018, Monthly Notices of the Royal Astronomical Society, 475, 1046

Irwin, J. B. 1961, Astrophysical Journal Supplement, 6, 253

Itagaki, K., Nakano, S., Monard, L. A. G., & Africa, S. 2002, IAU Circular, 7996, 4

Iwamoto, K., Nomoto, K., Höflich, P., et al. 1994, Astrophysical Journal Letters, 437, L115

Iwanek, P., Soszyński, I., Skowron, D., et al. 2018, Acta Astronomica, 68, 213

Jacoby, G. H. 1989, Astrophysical Journal, 339, 39

Jameson, R. F. 1986, Vistas in Astronomy, 29, 17

Jang, I. S. 2023, Monthly Notices of the Royal Astronomical Society, 521, 1532

Jang, I. S., Dhawan, S., Freedman, W. L., et al. 2022, TRGB and Cepheid distance scales: is there local tension?, HST Proposal. Cycle 30, ID. #17079

Jang, I. S., Hoyt, T. J., Beaton, R. L., et al. 2021, Astrophysical Journal, 906, 125

Janka, H.-T. 2017, in Handbook of Supernovae, ed. A. W. Alsabti & P. Murdin, 1575

Jencson, J. E., Sand, D. J., Andrews, J. E., et al. 2022, Astrophysical Journal, 930, 81

Jenkins, L. F. 1952, General catalogue of trigonometric stellar parallaxes.

Jha, S., Kirshner, R. P., Challis, P., et al. 2006, Astronomical Journal, 131, 527

Jones, H. S. 1944, Nature, 153, 181

Jones, M. I., Hamuy, M., Lira, P., et al. 2009, Astrophysical Journal, 696, 1176

Kafka, S. 2021, Observations from the AAVSO International Database

Kaltcheva, N. T. & Golev, V. K. 2012, Publications of the Astronomical Society of the Pacific, 124, 128

Kangas, T., Yan, L., Schulze, S., et al. 2022, Monthly Notices of the Royal Astronomical Society, 516, 1193

Kapteyn, J. C. 1914, Astrophysical Journal, 40, 43

Kapteyn, J. C. 1918, Astrophysical Journal, 47, 104

Kapteyn, J. C. & de Sitter, W. 1909, Publications of the Kapteyn Astronomical Laboratory Groningen, 23, 1

Kass, R. E. & Raftery, A. E. 1995, Journal of the American Statistical Association, 90, 773

Kenworthy, W. D., Jones, D. O., Dai, M., et al. 2021, Astrophysical Journal, 923, 265

Kervella, P., Gallenne, A., Evans, N. R., et al. 2019a, Astronomy & Astrophysics, 623, A117

Kervella, P., Gallenne, A., Remage Evans, N., et al. 2019b, Astronomy & Astrophysics, 623, A116

Kerzendorf, W., Sim, S., Vogl, C., et al. 2022, tardis-sn/tardis: TARDIS v2022.2.27, Zenodo

Kerzendorf, W. E. & Sim, S. A. 2014, Monthly Notices of the Royal Astronomical Society, 440, 387

Kiehl, M. & Hopp, U. 1977, Information Bulletin on Variable Stars, 1329, 1

Kienzle, F., Moskalik, P., Bersier, D., & Pont, F. 1999, Astronomy & Astrophysics, 341, 818

Kirshner, R. P. 2004, Proceedings of the National Academy of Science, 101, 8

Kirshner, R. P. & Kwan, J. 1974, Astrophysical Journal, 193, 27

Kiss, L. L. 1998, Monthly Notices of the Royal Astronomical Society, 297, 825

Klawitter, P. 1971, Information Bulletin on Variable Stars, 548, 1

Kloehr, W., Muendlein, R., Li, W., Yamaoka, H., & Itagaki, K. 2005, IAU Circular, 8553, 1

Kochanek, C. S., Shappee, B. J., Stanek, K. Z., et al. 2017, Publications of the Astronomical Society of the Pacific, 129, 104502

Kodric, M., Riffeser, A., Seitz, S., et al. 2018, Astrophysical Journal, 864, 59

Kodric, M., Riffeser, A., Seitz, S., et al. 2015, Astrophysical Journal, 799, 144

Koukarkina, N. P. 1954, Peremennye Zvezdy, 10, 92

Kovacs, G. & Szabados, L. 1979, Information Bulletin on Variable Stars, 1719, 1

Kovtyukh, V., Lemasle, B., Chekhonadskikh, F., et al. 2016, Monthly Notices of the Royal Astronomical Society, 460, 2077

Kox, H. 1935, Astronomische Nachrichten, 256, 21

Kozyreva, A., Janka, H.-T., Kresse, D., Taubenberger, S., & Baklanov, P. 2022, Monthly Notices of the Royal Astronomical Society, 514, 4173

Krebs, C. 1936, Astronomische Nachrichten, 261, 109

Kumar Aluri, P., Cea, P., Chingangbam, P., et al. 2023, Classical and Quantum Gravity, 40, 094001

Kun, M. & Szabados, L. 1988, Information Bulletin on Variable Stars, 3241, 1

Kurochkin, N. E. 1954, Peremennye Zvezdy, 10, 171

Kwee, K. K. 1967, Bulletin of the Astronomical Institutes of the Netherlands, 19, 260

Landolt, A. U. 1971, Publications of the Astronomical Society of the Pacific, 83, 43

Lapi, A., Boco, L., Cueli, M. M., et al. 2023, Astrophysical Journal, 959, 83

Laur, J., Kolka, I., Eenmäe, T., Tuvikene, T., & Leedjärv, L. 2017, Astronomy & Astrophysics, 598, A108

Leavitt, H. S. 1908, Annals of Harvard College Observatory, 60, 87

Leavitt, H. S. & Pickering, E. C. 1912, Harvard College Observatory Circular, 173, 1

Lee, A. J., Rousseau-Nepton, L., Freedman, W. L., et al. 2022, Astrophysical Journal, 933, 201

Lee, M. G., Freedman, W. L., & Madore, B. F. 1993, Astrophysical Journal, 417, 553

Léget, P. F., Pruzhinskaya, M. V., Ciulli, A., et al. 2018, Astronomy & Astrophysics, 615, A162

Lemaître, G. 1927, Annales de la Société Scientifique de Bruxelles, 47, 49

Lenz, P. & Breger, M. 2005, Communications in Asteroseismology, 146, 53

Leonard, D. C., Filippenko, A. V., Ardila, D. R., & Brotherton, M. S. 2001, Astrophysical Journal, 553, 861

Leonard, D. C., Kanbur, S. M., Ngeow, C. C., & Tanvir, N. R. 2003, Astrophysical Journal, 594, 247

Leonard, P. J. T. & Turner, D. G. 1986, Journal of the Royal Astronomical Society of Canada, 80, 240

Levesque, E. M., Massey, P., Olsen, K. A. G., et al. 2005, Astrophysical Journal, 628, 973

Li, W., Filippenko, A. V., van Dyk, S. D., & Cuillandre, J. C. 2004, IAU Circular, 8414, 2

Li, W., Leaman, J., Chornock, R., et al. 2011, Monthly Notices of the Royal Astronomical Society, 412, 1441

Li, X. & Shafieloo, A. 2019, Astrophysical Journal Letters, 883, L3

Lindegren, L., Klioner, S. A., Hernández, J., et al. 2021, Astronomy & Astrophysics, 649, A2

Livio, M. & Mazzali, P. 2018, Physics Reports, 736, 1

Llapasset, J. M., Yamaoka, H., & Ayani, K. 2003, Central Bureau Electronic Telegrams, 48, 1

Lloyd Evans, T. 1982, Monthly Notices of the Royal Astronomical Society, 199, 925

Lomb, N. R. 1976, Astrophysics and Space Sciences, 39, 447

Lombard, F. & Koen, C. 1993, Monthly Notices of the Royal Astronomical Society, 263, 309

Macaulay, E., Nichol, R. C., Bacon, D., et al. 2019, Monthly Notices of the Royal Astronomical Society, 486, 2184

Macri, L. M., Stanek, K. Z., Bersier, D., Greenhill, L. J., & Reid, M. J. 2006, Astrophysical Journal, 652, 1133

Madore, B. F. 1975, Astrophysical Journal Supplement, 29, 219

Madore, B. F. 1977, Monthly Notices of the Royal Astronomical Society, 178, 505

Madore, B. F. 1982, Astrophysical Journal, 253, 575

Madore, B. F. & Freedman, W. L. 1991, Publications of the Astronomical Society of the Pacific, 103, 933

Madore, B. F. & Freedman, W. L. 2020, Astrophysical Journal, 899, 66

Madore, B. F. & Freedman, W. L. 2023, arXiv e-prints, arXiv:2309.10859

Madore, B. F., Freedman, W. L., Hatt, D., et al. 2018, Astrophysical Journal, 858, 11

Madore, B. F., Freedman, W. L., Owens, K. A., & Jang, I. S. 2023, arXiv e-prints, arXiv:2305.06195

Maeder, A. & Meynet, G. 2001, Astronomy & Astrophysics, 373, 555

Maguire, K. 2017, in Handbook of Supernovae, ed. A. W. Alsabti & P. Murdin, 293

Mahmoud, F. & Szabados, L. 1980, Information Bulletin on Variable Stars, 1895, 1

Majaess, D., Turner, D., Moni Bidin, C., et al. 2012, Astronomy & Astrophysics, 537, L4

Malik, M. G. 1965, Astronomical Journal, 70, 94

Mandel, K. S., Thorp, S., Narayan, G., Friedman, A. S., & Avelino, A. 2022, Monthly Notices of the Royal Astronomical Society, 510, 3939

Maoz, D. & Mannucci, F. 2012, Publications of the Astronomical Society of Australia, 29, 447

Marconi, M., Musella, I., & Fiorentino, G. 2005, Astrophysical Journal, 632, 590

Marconi, M., Musella, I., Fiorentino, G., et al. 2010, Astrophysical Journal, 713, 615

Marschall, L. A., Seeds, M. A., & Davis, R. J. 1993, Astronomical Journal, 106, 1123

Martinez, L., Anderson, J. P., Bersten, M. C., et al. 2022, Astronomy & Astrophysics, 660, A42

Matsunaga, N., Feast, M. W., & Menzies, J. W. 2009, Monthly Notices of the Royal Astronomical Society, 397, 933

Mattila, S., Smartt, S., Maund, J., Benetti, S., & Ergon, M. 2010, arXiv e-prints, arXiv:1011.5494

Mauder, H. & Schöffel, E. 1968, Zeitschrift für Astrophysik, 69, 258

McGonegal, R., McAlary, C. W., Madore, B. F., & McLaren, R. A. 1982, Astrophysical Journal Letters, 257, L33

McQuinn, K. B. W., Boyer, M., Skillman, E. D., & Dolphin, A. E. 2019, Astrophysical Journal, 880, 63

McQuinn, K. B. W., Skillman, E. D., Dolphin, A. E., Berg, D., & Kennicutt, R. 2016, Astrophysical Journal, 826, 21

McQuinn, K. B. W., Skillman, E. D., Dolphin, A. E., Berg, D., & Kennicutt, R. 2017, Astronomical Journal, 154, 51

Méndez, B., Davis, M., Moustakas, J., et al. 2002, Astronomical Journal, 124, 213

Meyer, R. 2006, Open European Journal on Variable Stars, 0051, 1

Miller, C. L., Neilson, H. R., Evans, N. R., Engle, S. G., & Guinan, E. 2020, Astrophysical Journal, 896, 128

Miller, J. & Preston, G. 1964, Astrophysical Journal, 139, 1126

Miller, W. J. & Wachmann, A. A. 1973, Ricerche Astronomiche, 8, 367

Millis, R. L. 1969, Lowell Observatory Bulletin, 7, 113

Minkowski, R. 1941, Publications of the Astronomical Society of the Pacific, 53, 224

Mitchell, R. I., Iriarte, B., Steinmetz, D., & Johnson, H. L. 1964, Boletin de los Observatorios Tonantzintla y Tacubaya, 3, 153

Mitchell, R. I., Johnson, H. L., & Iriarte, B. 1961, Astrophysical Journal, 133, 1083

Moffett, T. J. & Barnes, T. G., I. 1984, Astrophysical Journal Supplement, 55, 389

Molnár, L., Joyce, M., & Kiss, L. L. 2019, Astrophysical Journal, 879, 62

Monard, L. A. G. 2002, IAU Circular, 7995, 2

Moore, M., Li, W., & Boles, T. 2003, IAU Circular, 8184, 2

Morokuma, T., Tominaga, N., Tanaka, M., et al. 2014, Publications of the Astronomical Society of Japan, 66, 114

Morozova, V., Piro, A. L., & Valenti, S. 2017, Astrophysical Journal, 838, 28

Mörtsell, E., Goobar, A., Johansson, J., & Dhawan, S. 2022, The Astrophysical Journal, 933, 212

Nagao, T., Mattila, S., Kotak, R., & Kuncarayakti, H. 2023, Astronomy & Astrophysics, 678, A43

Nagao, T., Patat, F., Cikota, A., et al. 2024, Astronomy & Astrophysics, 681, A11

Nakano, S., Kadota, K., & Wells, W. 2008, Central Bureau Electronic Telegrams, 1636, 1

Neilson, H. R. & Ignace, R. 2014, Astronomy & Astrophysics, 563, L4

Neilson, H. R., Langer, N., Engle, S. G., Guinan, E., & Izzard, R. 2012, Astrophysical Journal Letters, 760, L18

Neilson, H. R., Schneider, F. R. N., Izzard, R. G., Evans, N. R., & Langer, N. 2015, Astronomy & Astrophysics, 574, A2

Ngeow, C.-C., Marconi, M., Musella, I., Cignoni, M., & Kanbur, S. M. 2012, Astrophysical Journal, 745, 104

Nijland, A. A. 1935, Bulletin of the Astronomical Institutes of the Netherlands, 7, 248

Nomoto, K. I., Iwamoto, K., & Suzuki, T. 1995, Physics Reports, 256, 173

Nyquist, H. 1928, Physical Review, 32, 110

O'Connor, J. J. & Robertson, E. F. 1998, MacTutor History of Mathematics archive. University of St Andrews

Ofek, E. O., Arcavi, I., Tal, D., et al. 2014, Astrophysical Journal, 788, 154

Oja, T. 2011, Journal of Astronomical Data, 17, 1

Olivares E., F., Hamuy, M., Pignata, G., et al. 2010, Astrophysical Journal, 715, 833

Oort, J. H. 1931, Bulletin of the Astronomical Institutes of the Netherlands, 6, 155

Oosterhoff, P. T. 1935, Harvard College Observatory Bulletin, 900, 9

Oosterhoff, P. T. 1943, Bulletin of the Astronomical Institutes of the Netherlands, 9, 399

Oosterhoff, P. T. 1960, Bulletin of the Astronomical Institutes of the Netherlands, 15, 199

Pan, S. & Yang, W. 2023, arXiv e-prints, arXiv:2310.07260

Parenago, P. P. 1956, Peremennye Zvezdy, 11, 236

Parkhurst, J. A. 1908, Astrophysical Journal, 28, 278

Parrent, J., Branch, D., & Jeffery, D. 2010, SYNOW: A Highly Parameterized Spectrum Synthesis Code for Direct Analysis of SN Spectra, Astrophysics Source Code Library, record ascl:1010.055

Pastorello, A., Sauer, D., Taubenberger, S., et al. 2006, Monthly Notices of the Royal Astronomical Society, 370, 1752

Pastorello, A., Valenti, S., Zampieri, L., et al. 2009, Monthly Notices of the Royal Astronomical Society, 394, 2266

Pastorello, A., Zampieri, L., Turatto, M., et al. 2004, Monthly Notices of the Royal Astronomical Society, 347, 74

Patat, F., Barbon, R., Cappellaro, E., & Turatto, M. 1994, Astronomy & Astrophysics, 282, 731

Pearson, K. F. 1901, The London, Edinburgh, and Dublin Philosophical Magazine and Journal of Science, 2, 559

Peebles, P. J. E. 1993, Principles of Physical Cosmology

Pejcha, O. & Prieto, J. L. 2015, Astrophysical Journal, 799, 215

Pel, J. W. 1976, Astronomy & Astrophysics Supplement, 24, 413

Pel, J. W. 1978, Astronomy & Astrophysics, 62, 75

Pepper, J., Pogge, R. W., DePoy, D. L., et al. 2007, Publications of the Astronomical Society of the Pacific, 119, 923

Percy, J. R., Bezuhly, M., Milanowski, M., & Zsoldos, E. 1997, Publications of the Astronomical Society of the Pacific, 109, 264

Percy, J. R. & Colivas, T. 1999, Publications of the Astronomical Society of the Pacific, 111, 94

Perlmutter, S., Gabi, S., Goldhaber, G., et al. 1997, Astrophysical Journal, 483, 565

Perryman, M. A. C., Lindegren, L., Kovalevsky, J., et al. 1997a, Astronomy & Astrophysics, 323, L49

Perryman, M. A. C., Lindegren, L., Kovalevsky, J., et al. 1997b, Astronomy and Astrophysics, 323, L49

Pesce, D. W., Braatz, J. A., Reid, M. J., et al. 2020, Astrophysical Journal Letters, 891, L1

Pessi, P. J., Anderson, J. P., Folatelli, G., et al. 2023, Monthly Notices of the Royal Astronomical Society, 523, 5315

Pessi, P. J., Folatelli, G., Anderson, J. P., et al. 2019, Monthly Notices of the Royal Astronomical Society, 488, 4239

Phillips, M. M. 1993, Astrophysical Journal Letters, 413, L105

Pietrzyński, G., Graczyk, D., Gallenne, A., et al. 2019, Nature, 567, 200

Pignata, G., Maza, J., Hamuy, M., et al. 2008, Central Bureau Electronic Telegrams, 1587, 1

Pigott, E. 1785, Philosophical Transactions of the Royal Society of London Series I, 75, 127

Pilecki, B., Pietrzyński, G., Anderson, R. I., et al. 2021, Astrophysical Journal, 910, 118

Pineda, J. L., Stutzki, J., Buchbender, C., et al. 2020, Astrophysical Journal, 900, 132

Pingsdorf, F. 1935, Astronomische Nachrichten, 255, 9

Plachy, E., Pál, A., Bódi, A., et al. 2021, Astrophysical Journal Supplement, 253, 11

Planck Collaboration, Ade, P. A. R., Aghanim, N., et al. 2014a, Astronomy & Astrophysics, 571, A23

Planck Collaboration, Ade, P. A. R., Aghanim, N., et al. 2014b, Astronomy & Astrophysics, 571, A16

Planck Collaboration, Aghanim, N., Akrami, Y., et al. 2020, Astronomy & Astrophysics, 641, A6

Pojmanski, G. 2001, in Astronomical Society of the Pacific Conference Series, Vol. 246, IAU Colloq. 183: Small Telescope Astronomy on Global Scales, ed. B. Paczynski, W.-P. Chen, & C. Lemme, 53

Pollacco, D. L., Skillen, I., Collier Cameron, A., et al. 2006, Publications of the Astronomical Society of the Pacific, 118, 1407

Pont, F., Burki, G., & Mayor, M. 1994, Astronomy & Astrophysics Supplement, 105, 165

Poretti, E., Le Borgne, J. F., Rainer, M., et al. 2015, Monthly Notices of the Royal Astronomical Society, 454, 849

Poznanski, D., Butler, N., Filippenko, A. V., et al. 2009, Astrophysical Journal, 694, 1067

Pozzo, M., Meikle, W. P. S., Rayner, J. T., et al. 2006, Monthly Notices of the Royal Astronomical Society, 368, 1169

Pskovskii, I. P. 1977, Soviet Astronomy, 21, 675

R Core Team. 2020, R: A Language and Environment for Statistical Computing, R Foundation for Statistical Computing, Vienna, Austria

Rasmussen, C. E. & Williams, C. K. I. 2006, Gaussian Processes for Machine Learning

Reed, G. F. 1968, Information Bulletin on Variable Stars, 285, 1

Reid, M. J., Pesce, D. W., & Riess, A. G. 2019, Astrophysical Journal Letters, 886, L27

Ribas, I., Jordi, C., Vilardell, F., et al. 2005, Astrophysical Journal Letters, 635, L37

Richmond, M. W., van Dyk, S. D., Ho, W., et al. 1996, Astronomical Journal, 111, 327

Ricker, G. R., Winn, J. N., Vanderspek, R., et al. 2015, Journal of Astronomical Telescopes, Instruments, and Systems, 1, 014003

Riello, M., De Angeli, F., Evans, D. W., et al. 2021, Astronomy & Astrophysics, 649, A3

Riess, A., Anderson, R. I., Breuval, L., et al. 2023, Scrutinizing the Dirtiest Cepheids, a Test of the Hubble Tension, JWST Proposal. Cycle 2, ID. #2875

Riess, A. G., Anand, G. S., Yuan, W., et al. 2024, arXiv e-prints, arXiv:2401.04773

Riess, A. G., Casertano, S., Yuan, W., et al. 2021a, Astrophysical Journal Letters, 908, L6

Riess, A. G., Casertano, S., Yuan, W., et al. 2021b, Astrophysical Journal Letters, 908, L6

Riess, A. G., Casertano, S., Yuan, W., Macri, L. M., & Scolnic, D. 2019, Astrophysical Journal, 876, 85

Riess, A. G., Davis, M., Baker, J., & Kirshner, R. P. 1997, Astrophysical Journal Letters, 488, L1

Riess, A. G., Filippenko, A. V., Challis, P., et al. 1998, Astronomical Journal, 116, 1009

Riess, A. G., Fliri, J., & Valls-Gabaud, D. 2012, Astrophysical Journal, 745, 156

Riess, A. G., Press, W. H., & Kirshner, R. P. 1996, Astrophysical Journal, 473, 88

Riess, A. G., Yuan, W., Casertano, S., Macri, L. M., & Scolnic, D. 2020, Astrophysical Journal Letters, 896, L43

Riess, A. G., Yuan, W., Macri, L. M., et al. 2022, Astrophysical Journal Letters, 934, L7

Rigault, M., Brinnel, V., Aldering, G., et al. 2020, Astronomy & Astrophysics, 644, A176

Rizzi, L., Tully, R. B., Makarov, D., et al. 2007, Astrophysical Journal, 661, 815

Rodríguez, Ó., Clocchiatti, A., & Hamuy, M. 2014, Astronomical Journal, 148, 107

Rodríguez Castillo, G. A., Israel, G. L., Belfiore, A., et al. 2020, Astrophysical Journal, 895, 60

Rodríguez-Segovia, N., Hajdu, G., Catelan, M., et al. 2021, arXiv e-prints, arXiv:2111.03503

Romano, G. 1958, Memorie della Società Astronomia Italiana, 29, 465

Rose, B. M., Dixon, S., Rubin, D., et al. 2020, Astrophysical Journal, 890, 60

Rose, B. M., Rubin, D., Strolger, L., & Garnavich, P. M. 2021, Astrophysical Journal, 909, 28

Rosenfield, P., Marigo, P., Girardi, L., et al. 2014, Astrophysical Journal, 790, 22

Rosenfield, P., Marigo, P., Girardi, L., et al. 2016, Astrophysical Journal, 822, 73

Roy, R., Kumar, B., Benetti, S., et al. 2011, Astrophysical Journal, 736, 76

Rubin, A., Gal-Yam, A., De Cia, A., et al. 2016, Astrophysical Journal, 820, 33

Rust, B. W. 1974, PhD thesis, Oak Ridge National Laboratory, Tennessee

Sahu, D. K., Anupama, G. C., Srividya, S., & Muneer, S. 2006, Monthly Notices of the Royal Astronomical Society, 372, 1315

Sandage, A. 1958, Astrophysical Journal, 127, 513

Sandage, A. & Tammann, G. A. 1968, Astrophysical Journal, 151, 531

Sanders, N. E., Soderberg, A. M., Gezari, S., et al. 2015, Astrophysical Journal, 799, 208

Scargle, J. D. 1982, Astrophysical Journal, 263, 835

Schlafly, E. F. & Finkbeiner, D. P. 2011, Astrophysical Journal, 737, 103

Schlegel, E. M. 1990, Monthly Notices of the Royal Astronomical Society, 244, 269

Schlesinger, F., Palmer, M., Pond, A., & Observatory, Y. U. 1924, General Catalogue of Stellar Parallaxes (Yale University Observatory)

Schmidt, B. P., Kirshner, R. P., & Eastman, R. G. 1992, Astrophysical Journal, 395, 366

Schmidt, E. G. 1974, Monthly Notices of the Royal Astronomical Society, 167, 613

Schmidt, E. G. 2015, Astrophysical Journal, 813, 29

Schmidt, E. G., Chab, J. R., & Reiswig, D. E. 1995, Astronomical Journal, 109, 1239

Schmidt, E. G., Johnston, D., Langan, S., & Lee, K. M. 2004, Astronomical Journal, 128, 1748

Schmidt, E. G., Johnston, D., Langan, S., & Lee, K. M. 2005, Astronomical Journal, 130, 832

Schmidt, E. G. & Reiswig, D. E. 1993, Astronomical Journal, 106, 2429

Schmidt, M. 1963, Nature, 197, 1040

Schulze, S., Sollermann, J., Perley, D. A., et al. 2020, Transient Name Server AstroNote, 99, 1

Scolnic, D., Riess, A. G., Wu, J., et al. 2023, arXiv e-prints, arXiv:2304.06693

Scolnic, D., Smith, M., Massiah, A., et al. 2020, Astrophysical Journal Letters, 896, L13

Seli, B., Oláh, K., Kriskovics, L., et al. 2022, Astronomy & Astrophysics, 659, A3

Serenelli, A., Weiss, A., Cassisi, S., Salaris, M., & Pietrinferni, A. 2017, Astronomy & Astrophysics, 606, A33

Servén, D., Brummitt, C., Abedi, H., & Hlink. 2018, Dswah/Pygam: V0.8.0, Zenodo

Shapiro, P. R. & Sutherland, P. G. 1982, Astrophysical Journal, 263, 902

Shapley, H. 1927, Harvard College Observatory Circular, 314, 1

Shappee, B., Prieto, J., Stanek, K. Z., et al. 2014, in American Astronomical Society Meeting Abstracts, Vol. 223, American Astronomical Society Meeting Abstracts 223, 236.03

Shobbrook, R. R. 1992, Monthly Notices of the Royal Astronomical Society, 255, 486

Shussman, T., Waldman, R., & Nakar, E. 2016, arXiv e-prints, arXiv:1610.05323

Silverman, B. W. 1986, Density estimation for statistics and data analysis

Sim, S. A. 2017, in Handbook of Supernovae, ed. A. W. Alsabti & P. Murdin, 769

Sirianni, M., Jee, M. J., Benítez, N., et al. 2005, Publications of the Astronomical Society of the Pacific, 117, 1049

Slipher, V. M. 1913, Lowell Observatory Bulletin, 2, 56

Slipher, V. M. 1915, Popular Astronomy, 23, 21

Slipher, V. M. 1917, Proceedings of the American Philosophical Society, 56, 403

Slipher, V. M. 1921, Popular Astronomy, 29, 128

Smartt, S. J. 2009, Annual Reviews of Astronomy and Astrophysics, 47, 63

Sobel, I. 2014, Presentation at Stanford A.I. Project 1968

Sollerman, J., Yang, S., Schulze, S., et al. 2021, arXiv e-prints, arXiv:2107.14503

Soltis, J., Casertano, S., & Riess, A. G. 2021, Astrophysical Journal Letters, 908, L5

Soszyński, I., Udalski, A., Szymański, M. K., et al. 2015, Acta Astronomica, 65, 297

Spetsieri et al., Z. 2023, in prep., TBD

Spiro, S., Pastorello, A., Pumo, M. L., et al. 2014, Monthly Notices of the Royal Astronomical Society, 439, 2873

Spreckley, S. A. & Stevens, I. R. 2008, Monthly Notices of the Royal Astronomical Society, 388, 1239

Sterken, C. 2005, in Astronomical Society of the Pacific Conference Series, Vol. 335, The Light-Time Effect in Astrophysics: Causes and cures of the O-C diagram, ed. C. Sterken, 3

Stobie, R. S. 1970, Monthly Notices of the Royal Astronomical Society, 148, 1

Stobie, R. S. & Balona, L. A. 1979, Monthly Notices of the Royal Astronomical Society, 189, 641

Storm, J., Gieren, W., Fouqué, P., et al. 2011, Astronomy & Astrophysics, 534, A94

Strohmeier, W. 1968, Information Bulletin on Variable Stars, 304, 1

Stromberg, G. 1925, Astrophysical Journal, 61, 353

STScI Development Team. 2013, pysynphot: Synthetic photometry software package, Astrophysics Source Code Library, record ascl:1303.023

Stuart, C. 2011, The Big Questions The Universe (Hachette UK)

Süveges, M. & Anderson, R. I. 2018, Astronomy & Astrophysics, 610, A86

Szabados, L. 1976, Information Bulletin on Variable Stars, 1107, 1

Szabados, L. 1977, Communications of the Konkoly Observatory Hungary, 70, 1

Szabados, L. 1980, Communications of the Konkoly Observatory Hungary, 76, 1

Szabados, L. 1981, Communications of the Konkoly Observatory Hungary, 77, 1

Szabados, L. 1983, Astrophysics and Space Sciences, 96, 185

Szabados, L. 1988, Publications of the Astronomical Society of the Pacific, 100, 589

Szabados, L. 1989, Communications of the Konkoly Observatory Hungary, 94, 1

Szabados, L. 1991, Communications of the Konkoly Observatory Hungary, 96, 123

Szabados, L. 1992, in Astronomical Society of the Pacific Conference Series, Vol. 32, IAU Colloq. 135: Complementary Approaches to Double and Multiple Star Research, ed. H. A. McAlister & W. I. Hartkopf, 255

Szabados, L. 1993, in IAU Colloq. 139: New Perspectives on Stellar Pulsation and Pulsating Variable Stars, 406

Szabados, L. 1996, Astronomy & Astrophysics, 311, 189

Szabados, L., Anderson, R. I., Derekas, A., et al. 2013, Monthly Notices of the Royal Astronomical Society, 434, 870

Szabó, R., Buchler, J. R., & Bartee, J. 2007, Astrophysical Journal, 667, 1150

Szalai, T., Vinkó, J., Könyves-Tóth, R., et al. 2019, Astrophysical Journal, 876, 19

Takáts, K. & Vinkó, J. 2006, Monthly Notices of the Royal Astronomical Society, 372, 1735

Takáts, K. & Vinkó, J. 2012, Monthly Notices of the Royal Astronomical Society, 419, 2783

Tammann, G. A., Sandage, A., & Reindl, B. 2003, Astronomy & Astrophysics, 404, 423

Tartaglia, L., Pastorello, A., Sullivan, M., et al. 2016, Monthly Notices of the Royal Astronomical Society, 459, 1039

Taubenberger, S. 2017, in Handbook of Supernovae, ed. A. W. Alsabti & P. Murdin, 317

Teja, R. S., Singh, A., Sahu, D. K., et al. 2022, Astrophysical Journal, 930, 34

Thorp, S., Mandel, K. S., Jones, D. O., Ward, S. M., & Narayan, G. 2021, Monthly Notices of the Royal Astronomical Society, 508, 4310

Tikhonov, N. A., Lebedev, V. S., & Galazutdinova, O. A. 2015, Astronomy Letters, 41, 239

Tinyanont, S., Ridden-Harper, R., Foley, R. J., et al. 2022, Monthly Notices of the Royal Astronomical Society, 512, 2777

Tiwari, P. & Jain, P. 2019, Astronomy & Astrophysics, 622, A113

Tonry, J. & Schneider, D. P. 1988, Astronomical Journal, 96, 807

Tonry, J. L., Dressler, A., Blakeslee, J. P., et al. 2001, Astrophysical Journal, 546, 681

Toomer, G. J. 1974, Archive for History of Exact Sciences, 14, 126

Torres-Arzayus, S., Delgado-Correal, C., Higuera-G., M.-A., & Rueda-Blanco, S. 2023, arXiv e-prints, arXiv:2311.05510

Trabucchi, M. 2023, arXiv e-prints, arXiv:2306.17758

Tripp, R. 1998, Astronomy & Astrophysics, 331, 815

Tully, R. B., Courtois, H. M., Dolphin, A. E., et al. 2013, Astronomical Journal, 146, 86

Tully, R. B. & Fisher, J. R. 1977, Astronomy & Astrophysics, 54, 661

Turner, D. G., Abdel-Sabour Abdel-Latif, M., & Berdnikov, L. N. 2006, Publications of the Astronomical Society of the Pacific, 118, 410

Turner, D. G. & Berdnikov, L. N. 2004, Astronomy & Astrophysics, 423, 335

Turner, D. G., Berdnikov, L. N., Percy, J. R., & Abdel-Sabour Abdel-Latif, M. 2010, Odessa Astronomical Publications, 23, 129

Turner, D. G., Percy, J. R., Colivas, T., Berdnikov, L. N., & Abdel-Latif, M. A.-S. 2009, in American Institute of Physics Conference Series, Vol. 1170, Stellar Pulsation: Challenges for Theory and Observation, ed. J. A. Guzik & P. A. Bradley, 167–169

Turner, D. G., Savoy, J., Derrah, J., Abdel-Sabour Abdel-Latif, M., & Berdnikov, L. N. 2005, Publications of the Astronomical Society of the Pacific, 117, 207

Tutui, Y. & Sofue, Y. 1997, Astronomy & Astrophysics, 326, 915

Udalski, A., Soszynski, I., Szymanski, M. K., et al. 2008, Acta Astronomica, 58, 89

Udalski, A., Szymański, M. K., & Szymański, G. 2015, Acta Astronomica, 65, 1

Ugliano, M., Janka, H.-T., Marek, A., & Arcones, A. 2012, Astrophysical Journal, 757, 69

Usenko, I. A. 1990, Kinematika i Fizika Nebesnykh Tel, 6, 91

Usenko, I. A. 1992, Information Bulletin on Variable Stars, 3784, 1

Usenko, I. A. & Klochkova, V. G. 2015, Astronomy Letters, 41, 351

Utrobin, V. P. 2007, Astronomy & Astrophysics, 461, 233

Utrobin, V. P. & Chugai, N. N. 2009, Astronomy & Astrophysics, 506, 829

van Altena, W. F., Lee, J. T., & Hoffleit, E. D. 1995, The general catalogue of trigonometric [stellar] parallaxes

Van Dyk, S. D. 2017, Philosophical Transactions of the Royal Society of London Series A, 375, 20160277

Vasylyev, S. S., Filippenko, A. V., Vogl, C., et al. 2022, Astrophysical Journal, 934, 134

Verde, L., Treu, T., & Riess, A. G. 2019, Nature Astronomy, 3, 891

Vinkó, J. 1991, Astrophysics and Space Sciences, 183, 17

Vinkó, J. 1993, Monthly Notices of the Royal Astronomical Society, 260, 273

Vinkó, J., Takáts, K., Szalai, T., et al. 2012, Astronomy & Astrophysics, 540, A93

Virtanen, P., Gommers, R., Oliphant, T. E., et al. 2020, Nature Methods, 17, 261

Vogl, C. 2020, PhD thesis, Munich University of Technology, Germany

Vogl, C. 2024, In prep.

Vogl, C., Kerzendorf, W. E., Sim, S. A., et al. 2020, Astronomy & Astrophysics, 633, A88

Vogl, C., Sim, S. A., Noebauer, U. M., Kerzendorf, W. E., & Hillebrandt, W. 2019, Astronomy & Astrophysics, 621, A29

Wachmann, A. A. 1976, Astronomy & Astrophysics Supplement, 23, 249

Walker, W. S. G., Herdman, G. C. D., & Marino, B. F. 1991, Proceedings of the Astronomical Society of Australia, 9, 127

Walraven, J. H., Tinbergen, J., & Walraven, T. 1964, Bulletin of the Astronomical Institutes of the Netherlands, 17, 520

Walraven, T., Muller, A. B., & Oosterhoff, P. T. 1958, Bulletin of the Astronomical Institutes of the Netherlands, 14, 81

Walter, K. 1943, Astronomische Nachrichten, 273, 277

Wang, B., Abdalla, E., Atrio-Barandela, F., & Pavón, D. 2016, Reports on Progress in Physics, 79, 096901

Wang, B., López-Corredoira, M., & Wei, J.-J. 2024, Monthly Notices of the Royal Astronomical Society, 527, 7692

Wang, L. & Wheeler, J. C. 2008, Annual Reviews in Astronomy and Astrophysics, 46, 433

Ward, S. M., Thorp, S., Mandel, K. S., et al. 2023, Astrophysical Journal, 956, 111

Weaver, H. F., Steinmetz, D., & Mitchell, R. 1960, Lowell Observatory Bulletin, 5, 30

Webb, S. 1999, Measuring the universe: the cosmological distance ladder

Welch, D. L., Clayton, G. C., Campbell, A., et al. 2007, Astrophysical Journal, 669, 525

Welch, D. L. & Evans, N. R. 1989, Astronomical Journal, 97, 1153

Wesselink, A. J. 1946a, Bulletin of the Astronomical Institutes of the Netherlands, 10, 91

Wesselink, A. J. 1946b, Bulletin of the Astronomical Institutes of the Netherlands, 10, 91

Wiggins, P. 2017, Central Bureau Electronic Telegrams, 4390, 1

Winkler, C., Courvoisier, T. J. L., Di Cocco, G., et al. 2003, Astronomy & Astrophysics, 411, L1

Wong, K. C., Suyu, S. H., Chen, G. C. F., et al. 2020a, Monthly Notices of the Royal Astronomical Society, 498, 1420

Wong, K. C., Suyu, S. H., Chen, G. C. F., et al. 2020b, Monthly Notices of the Royal Astronomical Society, 498, 1420

Woosley, S. E. 1988, Astrophysical Journal, 330, 218

Woźniak, P. R., Vestrand, W. T., Akerlof, C. W., et al. 2004, Astronomical Journal, 127, 2436

Wray, J. J., Eyer, L., & Paczyński, B. 2004, Monthly Notices of the Royal Astronomical Society, 349, 1059

Wright, B. S. & Li, B. 2018, Physical Review D, 97, 083505

Wu, J., Scolnic, D., Riess, A. G., et al. 2022, arXiv e-prints, arXiv:2211.06354

Yao, Y., De, K., Kasliwal, M. M., et al. 2020, Astrophysical Journal, 900, 46

Yaron, O. & Gal-Yam, A. 2012, Publications of the Astronomical Society of the Pacific, 124, 668

Yoachim, P., McCommas, L. P., Dalcanton, J. J., & Williams, B. F. 2009, Astronomical Journal, 137, 4697

Yuan, W., Macri, L. M., Riess, A. G., et al. 2022, Astrophysical Journal, 940, 64

Zampieri, L., Pastorello, A., Turatto, M., et al. 2003, Monthly Notices of the Royal Astronomical Society, 338, 711

Zanisi, L., Shankar, F., Lapi, A., et al. 2020, Monthly Notices of the Royal Astronomical Society, 492, 1671

Zaritsky, D., Kennicutt, Robert C., J., & Huchra, J. P. 1994, Astrophysical Journal, 420, 87

Zgirski, B., Pietrzyński, G., Gieren, W., et al. 2021, Astrophysical Journal, 916, 19

Zhao, G.-B., Raveri, M., Pogosian, L., et al. 2017, Nature Astronomy, 1, 627

Zwitter, T., Munari, U., & Moretti, S. 2004, Central Bureau Electronic Telegrams, 95, 1